

STATUS OF THESIS

Title of thesis

SYNGAS PRODUCTION VIA DRY REFORMING OF METHANE
OVER Ni-W BIMETALLIC CATALYST SUPPORTED ON Al₂O₃-
MgO

I MOHD YUSUF

hereby allow my thesis to be placed at the Information Resource Center (IRC) of Universiti Teknologi PETRONAS (UTP) with the following conditions:

1. The thesis becomes the property of UTP
2. The IRC of UTP may make copies of the thesis for academic purposes only.
3. This thesis is classified as

☒ Confidential

☐ Non-confidential

If this thesis is confidential, please state the reason:

The contents of the thesis will remain confidential for 10 years.

Remarks on disclosure:

The thesis is confidential since we are looking forward for filing patent application for the work conducted in this doctoral study.

Endorsed by



Signature of Author

Permanent address: Mandi Street, Pul
Kambohaan, Near Masjid Beldaraan,
House No. 11/2067/1, Saharanpur,
247001, U.P., India

Date : 14-02-2022



Signature of Supervisor

Name of Supervisor
Asso. Prof. Dr. Bawadi Abdullah

Date: 14-02-2022

UNIVERSITI TEKNOLOGI PETRONAS

SYNGAS PRODUCTION VIA DRY REFORMING OF METHANE OVER NI-W

BIMETALLIC CATALYST SUPPORTED ON $\text{Al}_2\text{O}_3\text{-MgO}$

by

MOHD YUSUF

The undersigned certify that they have read and recommend to the Postgraduate Studies Program for acceptance this thesis for the fulfillment of the requirements for the degree stated.

Signature:



Main Supervisor:

Assoc. Prof. Dr. Bawadi Abdullah

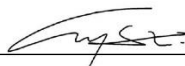
Signature:



Co-Supervisor:

Assoc. Prof. Dr. Lau Kok Keong

Signature:



Head of Department:

Asso. Prof. Ir. Dr. Abd Halim Shah bin Maulud

Date:

24/2/2022

SYNGAS PRODUCTION VIA DRY REFORMING OF METHANE OVER NI-W
BIMETALLIC CATALYST SUPPORTED ON Al₂O₃-MgO

by

MOHD YUSUF

A Thesis

Submitted to the Postgraduate Studies Program

as a Requirement for the Degree of

DOCTOR OF PHILOSOPHY

DEPARTMENT OF CHEMICAL ENGINEERING

UNIVERSITI TEKNOLOGI PETRONAS

BANDAR SERI ISKANDAR,

PERAK

FEBRUARY 2022

DECLARATION OF THESIS

Title of thesis

SYNGAS PRODUCTION VIA DRY REFORMING OF METHANE
OVER Ni-W BIMETALLIC CATALYST SUPPORTED ON Al₂O₃-
MgO

I MOHD YUSUF

hereby declare that the thesis is based on my original work except for quotations and citations which have been duly acknowledged. I also declare that it has not been previously or concurrently submitted for any other degree at UTP or other institutions.

Witnessed by



Signature of Author

Signature of Supervisor

Permanent address: Mandi Street, Pul
Kambohaan, Near Masjid Beldaraan,
House No. 11/2067/1, Saharanpur,
247001, U.P., India

Name of Supervisor
Asso. Prof. Dr. Bawadi Abdullah

Date : [14-02-2022]

Date : [14-02-2022]

DEDICATION

It is with deepest gratitude and love this humble success is dedicated to my family:

*My **mother**, **father**, **loving wife**, **daughter**, **sister**, and my **brothers**.*

This dissertation is dedicated to the love, prayers and moral support of my family that made me capable to get such success and honor.

ACKNOWLEDGEMENTS

Alhamdulillah! The Almighty, Allah Subhanahu Wa Ta'ala, The creator of knowledge, wisdom, power, life, and intelligence. O Allah bless me with benefits of what You have taught me and guide me to the knowledge that is beneficial to me.

I would like to express my sincere gratitude to my supervisor, advisor, and mentor Assoc. Prof. Dr. Bawadi Abdullah. I acknowledge his constant efforts and would like to thank him for esteemed guidance, continuous support, encouragement, and interest throughout my PhD journey. His priceless advice, cool nature and high expectations sparked the momentum and persuaded me to achieve the higher level.

I am highly thankful to my co-supervisor, Assoc. Prof. Dr. Lau Kok Keong, for his continuous guidance, providing the resources that helped me and kept me on track through critical stages of my work. I am also thankful to my field supervisor Prof. Klaus Hellgardt, Imperial College London, U.K. for his insightful comments and suggestions during my research journey.

A special gratitude and love go to my beloved family, my father, my mother, my wife, my daughter, my sister, and my brothers for their prayers and persistent support.

I am thankful to other faculty members Dr. Mohammad Ayoub, Dr. Dzulkarnanin, Dr. Aqsha, Dr. Khairiraihana, and Dr. Oh Pei Ching whose guidance and comments, and support during the BAPC and laboratory access throughout my PhD helped me to plan and groom my work accordingly.

Special thanks to Universiti Teknologi PETRONAS (UTP), Malaysia for this great opportunity and for providing the financial support as graduate assistantship throughout this doctoral research program. I would also like to express my gratitude and thanks to Mr. Khairul Anwar and all the technologist from UTP for their help and support with the equipment and laboratory chores.

I would also like to thank my colleagues and friends with who helped me directly or indirectly during this project: Dr. Mohammed Alnarabiji, Dr. Mukarram Beg, Ms. Nurliyana Masiran, Mr. Mohammad Azad Alam, Mr. Saqib Yar Khan, Ms. Huma Khan, Mr. Parvez Alam Khan, Mr. Faisal Masood, and Mr. Ahmad Salam Farooqi in the ups and downs of my PhD journey.

Finally, I would like to thank all the supportive researchers and scientists in ResearchGate networking site for their time and fruitful discussions.

ABSTRACT

Dry reforming of methane (DRM) is a promising technique for utilization of greenhouse gases (GHGs) to give syngas. The main limitations of DRM are the catalyst deactivation by sintering and coking. This proposes the necessity to find an active and stable catalyst that can confront these issues and facilitate the DRM process. In this doctoral study Ni-based catalysts supported on binary oxide support (i.e., $\text{Al}_2\text{O}_3\text{-MgO}$) were prepared by co-precipitation followed by impregnation method. The catalyst with 12wt.% Ni loading on $\text{Al}_2\text{O}_3\text{-MgO}$ showed the optimum activity and stability for DRM carried out at 800°C, 1 atm, and $\text{CH}_4\text{:CO}_2$ ratio of unity in a fixed-bed tubular reactor. The fresh and spent optimum catalyst were then characterized to analyze the physico-chemical properties and carbon formed during DRM reaction. The effect of W addition on the optimum (12wt.%Ni/ $\text{Al}_2\text{O}_3\text{-MgO}$) catalyst was further investigated. W addition resulted in enhanced catalytic activity and stability, and the Ni-W bimetallic catalyst with 4wt.% W exhibited most steady performance (with 88.8% and 91.5% conversion of CH_4 and CO_2 and syngas ratio of 0.9 respectively), even after 24 h of reaction. The fresh and spent Ni-W catalysts were characterized and the corresponding textural properties, crystallinity, morphology, basicity, enhanced physico-chemical properties, and the type of carbon formed on the catalysts are analyzed. The amorphous carbon-nanosheets were formed on monometallic Ni catalyst, whereas the MWCNTs on Ni-W catalyst. Further, the process parameters for DRM over optimum Ni-W catalyst were optimized using response surface methodology (RSM), within temperature range of 600°C-800°C and $\text{CH}_4\text{:CO}_2$ of 0.5-1.5 via CCD of RSM. It has been found that a temperature of 777.29°C and $\text{CH}_4\text{:CO}_2$ of 1.11 is optimum for the proposed catalyst. Finally, the reaction kinetics of DRM over optimum Ni-W catalyst was investigated via four typical kinetic models i.e., Power-Law, Langmuir-Hinshelwood, Eley-Rideal I, and Eley-Rideal II models. The analysis showed that Langmuir-Hinshelwood model showed the best fitting between experimental and estimated reaction rates with R^2 value of 0.983.

ABSTRAK

Proses pembentukan semula pengeringan metana (DRM) merupakan satu teknik menjamin penghasilan sintesis gas menggunakan gas rumah hijau. Namun demikian, cabaran utama dalam proses ini adalah penyahaktifan pemangkin disebabkan oleh pembentukan karbon dan penggubalan iaitu proses sintering. Hal ini menjadi antara salah satu sebab kepada keperluan kajian ini dijalankan adalah untuk mencari dan mengkaji pemangkin yang stabil dan aktif sekali gus yang boleh mengatasi masalah yang dihadapi dalam proses DRM. Oleh itu, dalam kajian falsafah ini, pemangkin yang berasaskan Nikel menggunakan binari oksida seperti Al_2O_3 - MgO disintesis menggunakan kaedah kepemendakan kimia dan diikuti oleh kaedah pengisitepuan. Pemangkin dengan peratusan 12wt% Nikel pada Al_2O_3 - MgO telah menunjukkan optimum aktiviti dan stabiliti ketika proses DRM dijalankan pada suhu 800°C , 1 atm, dan berserta nisbah $\text{CH}_4:\text{CO}_2$ yang sama di dalam reaktor tiub katil tetap. Kemudian ciri-ciri pemangkin yang baru dan pemangkin optimum telah dianalisis untuk mengetahui fizik-kimia pemangkin dan pembentukan karbon semasa proses DRM dijalankan. Penambahan bahan kimia W pada pemangkin optimum (12wt.%Ni/ Al_2O_3 - MgO) telah dikaji secara terperinci. Keputusan kajian menunjukkan bahawa kehadiran W meningkatkan aktiviti pemangkin dan kestabilan pemangkin dan pemangkin Ni-W dengan peratusan 4% wt. W menunjukkan prestasi yang tinggi (88.8% dan 91.5% penukaran kepada CH_4 dan CO_2 berserta nisbah sintesis gas iaitu 0.9) walaupun selepas 24 jam tindak balas. Ciri-ciri tekstur, kehabluran, morfologi, keasaman, fiziki-kimia pemangkin dan jenis karbon yang terbentuk pada pemangkin telah dikaji dan analisis menggunakan pemangkin Ni-W yang baru dan yang telah digunakan. Lembaran-nano karbon amorfus terbentuk pada monometal Ni pemangkin, manakala MWCNTs pada pemangkin Ni-W. Selain itu, proses parameter dalam proses DRM telah dioptimumkan menggunakan kaedah tindak balas permukaan (RSM) menggunakan julat suhu antara 600°C - 800°C dan $\text{CH}_4:\text{CO}_2$ nisbah antara 0.5 hingga 1.5 menggunakan reka bentuk komposit berpusat (CCD) dalam kaedah tindak balas permukaan (RSM). Hasil keputusan daripada reka bentuk komposit berpusat (CCD) mendapati bahawa optimum suhu dan nisbah $\text{CH}_4:\text{CO}_2$ adalah 777.29°C dan 1.11 bagi pemangkin yang telah dicadangkan. Akhir sekali, kadar tindak balas RSM proses menggunakan pemangkin optimum iaitu Ni-W pemangkin telah dikaji menggunakan empat jenis kinetik model iaitu Power-Law, Langmuir-Hinshelwood, Eley-Rideal I, dan Eley Rideal II model. Keputusan analisis telah menunjukkan bahawa "Langmuir-Hinshelwood" model yang paling sesuai kerana anggaran nilai kadar tindak balas dengan eksperimen adalah R^2 0.983.

In compliance with the terms of the Copyright Act 1987 and the IP Policy of the university, the copyright of this thesis has been reassigned by the author to the legal entity of the university,

Institute of Technology PETRONAS Sdn Bhd.

Due acknowledgement shall always be made of the use of any material contained in, or derived from, this thesis.

© MOHD YUSUF, 2022

Institute of Technology PETRONAS Sdn Bhd

All rights reserved.

TABLE OF CONTENT

ABSTRACT.....	viii
ABSTRAK.....	ix
Institute of Technology PETRONAS Sdn Bhd.....	x
TABLE OF CONTENT	xi
LIST OF FIGURES	xv
LIST OF TABLES	xvii
LIST OF ABBREVIATIONS	xviii
CHAPTER 1	1
1. INTRODUCTION	1
1.1 Background and Motivation.....	1
1.2 Problem Statement	4
1.3 Research Hypothesis	5
1.4 Research Objectives.....	5
1.5 Scope of Study	6
1.6 Significance of the Study	7
1.7 Thesis Organization	7
CHAPTER 2	9
2. LITERATURE REVIEW	9
2.1 Chapter overview	9
2.2 Dry Reforming of Methane (DRM)	9
2.3 Thermodynamic overview	10
2.4 Catalyst support	13
2.5 Catalyst Promoters	15
2.6 Bimetallic catalyst.....	18
2.7 Trimetallic catalyst.....	33
2.8 Study of spent catalysts.....	35
2.9 Optimization study using Response Surface Methodology	37
2.10 Reaction Kinetics of dry reforming of methane.....	39
2.11 Research Gap	46
CHAPTER 3	48
3. MATERIALS AND METHODS.....	48

3.1	Chapter Overview	48
3.2	Materials	49
3.3	Catalyst Preparation	50
3.4	Screening of catalysts.....	52
3.5	Catalyst Characterization	52
3.5.1	Crystallite phases and size analysis.....	52
3.5.2	Surface area and pore analysis	53
3.5.3	Morphology Analysis.....	54
3.5.4	Elemental Composition and Mapping.....	54
3.5.5	Catalyst Active Sites Behavior	54
3.5.6	Catalyst's Basicity Analysis.....	54
3.5.7	Quantitative Analysis of Carbon Formed	55
3.5.8	Analysis of Binding Energy and Oxidation States.....	55
3.5.9	Structure and Morphology Analysis	55
3.5.10	Qualitative analysis of Carbon formed	56
3.6	Catalyst testing for DRM reaction	56
3.7	Turnover Frequency (TOF).....	58
3.8	Optimization of process parameters using RSM.....	58
3.9	Kinetic studies for DRM.....	61
CHAPTER 4		63
4.	RESULTS AND DISCUSSION	63
4.1	Chapter Overview	63
4.2	Screening for Ni loading.....	63
4.2.1	Performance Evaluation of catalysts for DRM	64
4.2.2	Catalyst Characterizations.....	65
4.2.2.1	X-Ray diffraction	65
4.2.2.2	Textural Properties	66
4.2.2.3	FESEM.....	68
4.2.2.4	TEM	69
4.2.2.5	EDX and Elemental Mapping	70
4.2	Effect of W addition.....	72
4.3.1	Catalyst Characterizations.....	72
4.3.3.1	X-Ray diffraction	72

4.3.3.2	Textural Properties	74
4.3.3.3	FESEM.....	76
4.3.3.4	EDX and Elemental Mapping	78
4.3.3.5	TPR-H ₂	79
4.3.3.6	TPD-CO ₂	81
4.3.2	Performance Evaluation of catalysts for DRM	82
4.3.3	Stability test for optimum performance Ni-W (W _b) catalyst	86
4.3.4	Characterizations of catalysts post DMR reaction	88
4.3.4.1	XPS analysis	88
4.3.4.2	XRD of spent catalyst	91
4.3.4.3	FESEM of spent catalyst.....	92
4.3.4.4	EDX and Elemental Mapping of spent catalyst	93
4.3.4.5	TPO-O ₂ of spent catalyst.....	94
4.3.4.6	RAMAN Analysis.....	97
4.3.4.7	TEM of spent catalyst	98
4.4	Process Optimization Using RSM	100
4.4.1	Effect of reaction parameters on reactant's conversion	101
4.4.1.1	Effect of reaction parameters on CH ₄ conversion.....	101
4.4.1.2	Assessment of observed and predicted conversion of CH ₄	103
4.4.1.3	Effect of reaction parameters on CO ₂ conversion.....	104
4.4.1.4	Assessment of observed and predicted conversion of CO ₂	105
4.4.1.5	Effect of reaction parameters on H ₂ :CO ratio	106
4.4.1.6	Assessment of observed and predicted values of H ₂ :CO ratio.....	107
4.4.2	Response surfaces interaction of RSM model	107
4.4.3	Optimization of the process parameters for DRM over Ni-W catalyst.....	109
4.4.4	Verification of optimized condition and percentage error	111
4.5	Kinetic Modelling Analysis	112
4.5.1	Reaction Mechanism.....	113
4.5.2	Kinetics testing for DRM.....	114
4.5.3	Effect of process variables on reaction rate	119
4.5.4	General applicable kinetic models	120
4.5.4.1	Power-Law Model.....	120
4.5.4.2	Langmuir-Hinshelwood Model.....	121

4.5.4.3	Eley Rideal Models	122
4.6	Summary	124
CHAPTER 5	125
5	CONCLUSION AND RECOMMENDATION	125
5.1	Conclusion	125
5.2	Recommendations	126
REFERENCES	128
LIST OF PUBLICATIONS	161
APPENDIX A	164
APPENDIX B	172
APPENDIX C	178
APPENDIX D	180
APPENDIX E	183
APPENDIX F	192

LIST OF FIGURES

Figure 1.1. (a) Surface average atmospheric CO ₂ concentration (ppm), (b) Globally-averaged, monthly mean atmospheric CH ₄ abundance [6].....	2
Figure 2.1. Carbon containing product for the various reactions: (a) CH ₄ decomposition (CH ₄ = 100%), (b) Boudouard reaction (CO = 100%), (c) Reforming of CH ₄ with CO ₂ (CH ₄ = 50% and CO ₂ = 50%) [69].	13
Figure 2.2. (a, b) TEM images and (c–h) EDX mapping of spent SiO ₂ @Ni@ZrO ₂ catalyst after dry reforming reaction [133].	35
Figure 2.3. The pictorial illustration of effect of position of active metal (Ni) on the performance of catalyst [140].....	36
Figure 2.4. Reaction scheme of Ni/DFSBA-15 over DRM. (a) bidentate carbonate, (b) unidentate carbonate, (c) linear carbonyl [130].....	43
Figure 2.5. Energy pathways and profiles for the three different pathways in CO ₂ activation: (I) CO ₂ * + * → CO* + O*; (II) CO ₂ * + H* → COOH* + * → CO* + OH*; (III) CO ₂ * + H* → mono-HCOO* + * → bi-HCOO* + * [CO ₂ * + H* → bi-HCOO* + *] → CHO* + O* [162].	44
Figure 2.6. Energy profiles for the two pathways in CH oxidation by O: (A) CH* + O* → CHO* + * → CO* + H*; (B) CH* + O* → COH* + * → CO* + H [162].	44
Figure 2.7. Energy profiles for the two different pathways in CH oxidation by OH: (C) CH* + OH* → CHO* + * → CHO* + H*; (D) CH* + OH* → COH* + * → COH* + H [162].	45
Figure 3.1. Research workflow for synthesis, characterization, and performance evaluation, optimization, and kinetic studies of catalysts.....	48
Figure 3.2 Schematic diagram for DRM reactor setup.	57
Figure 4.1. Performance in terms of (a) Percentage CH ₄ conversion (b) Percentage CO ₂ conversion and (c) Syngas ratio, for different Ni content catalysts supported on Al ₂ O ₃ -MgO with 1:2 ratio.	65
Figure 4.2. X-ray diffraction patterns of fresh (Ni ₁₂) and spent (Ni _{12Sp}) optimum catalysts.....	66
Figure 4.3. (a) Nitrogen adsorption-desorption isotherms for optimum CS and Ni ₁₂ catalyst, and (b) Pore-size distribution curves for optimum CS and Ni ₁₂ catalyst.	68
Figure 4.4. FESEM images of (a) fresh (Ni ₁₂) and (b) spent (Ni _{12Sp}) catalysts.....	69
Figure 4.5. TEM images of (a) fresh (Ni ₁₂) and (b) spent (Ni _{12Sp}) catalyst.....	70
Figure 4.6. EDX spectrum of (a) fresh (Ni ₁₂) and (b) spent (Ni _{12Sp}) catalyst.....	71
Figure 4.7. Elemental mapping of optimum fresh and spent (Ni ₁₂ and Ni _{12Sp}) catalyst.....	71
Figure 4.8. XRD pattern of monometallic Ni and series of Ni-W bimetallic catalysts (Ni _f , W _a , W _b , W _c , W _d).	73
Figure 4.9. N ₂ adsorption-desorption isotherms for catalyst support (CS), and different prepared catalysts (Ni _f , W _a , W _b , W _c , W _d).	75
Figure 4.10. Pore size distribution curves for catalyst support (CS), and different prepared catalysts (Ni _f , W _a , W _b , W _c , W _d).	75
Figure 4.11. FESEM images of catalysts samples (a) Ni _f , (b) W _a , (c) W _b , (d) W _c , (e) W _d	78
Figure 4.12. Elemental mapping of different freshly synthesized catalyst samples (Ni _f , W _a , W _b , W _c , and W _d)	79
Figure 4.13. TPR-H ₂ profile of different synthesized catalysts.	81
Figure 4.14. TPD-CO ₂ profile of different synthesized catalysts.	82
Figure 4.15. Performance evaluation (a) CH ₄ conversion (b) CO ₂ conversion (c) H ₂ :CO vs. time, (d) H ₂ yield (%) (e) CO yield (%) for synthesized catalysts for 6h reaction.	85

Figure 4.16. Stability test for W_b catalyst for 24h of DMR reaction.	87
Figure 4.17. XPS spectra for Ni 2p (a) Ni_f and (b) W_b catalysts (c) Narrow scan for W 4f of W_b catalyst and (d-e) XPS narrow scan for O 1s of fresh Ni_f and W_b catalysts, respectively.	89
Figure 4.18. XRD pattern for spent (Ni_{Sp} and $W_{b,Sp}$) catalysts after 6h of DMR reaction.	92
Figure 4.19. FESEM images of spent catalysts with different magnifications showing (a-b) Ni_{Sp} catalyst with carbon nanosheets formed and (c-d) $W_{b,Sp}$ with formed CNT during the 6h of DMR reaction.	93
Figure 4.20. The elemental dot mapping of spent (Ni_{Sp} and $W_{b,Sp}$) catalysts after 6h of DMR reaction. ..	94
Figure 4.21. The proposed reaction mechanism for DRM on Ni-W bimetallic catalyst [96].	96
Figure 4.22. TPO- O_2 profiles of spent (Ni_{Sp} and $W_{b,Sp}$) catalysts after 6h of DMR reaction at 800°C.	97
Figure 4.23. Raman analysis of spent (Ni_{Sp} and $W_{b,Sp}$) catalysts after 6h of DMR reaction at 800°C.	98
Figure 4.24. TEM analysis of spent (Ni_{Sp} and $W_{b,Sp}$) catalysts after 6h of DMR reaction for at 800°C.	99
Figure 4.25. The actual vs predicted value plots obtained from RSM.	104
Figure 4.26. 3-D response surface and contour plots displaying the effects of reaction temperature and feed ratio on (a) CH_4 conversion, (b) CO_2 conversion, and (c) H_2 : CO	108
Figure 4.27. 3-D and contour desirability plots obtained from the multi-response desirability analysis.	110
Figure 4.28. Modified reaction rates $PCH_4.PCO_2/R$ vs partial pressure of (a) CH_4 and (b) CO_2 for LH model, at 600°C-800°C.	116
Figure 4.29. Arrhenius plots to determine the apparent E_a and E_{CH_4} and E_{CO_2} over Ni-W bimetallic catalyst.	117
Figure 4.30. The rate of consumption as a function of temperature vs. partial pressure of (a) CH_4 and (b) CO_2 from experimental data of Ni-W bimetallic catalyst. The curve fitting carried out by employing the LH model.	120
Figure 4.31. Comparison between experimental and estimated reaction rates of DRM based on Power-Law model.	121
Figure 4.32. Comparison between experimental and estimated reaction rates of DRM based on Langmuir-Hinshelwood model.	122
Figure 4.33. Comparison between experimental and estimated reaction rates of DRM based on (a) ERI and (b) ERII models.	123

LIST OF TABLES

Table 2.1. The enthalpy (ΔH), gibbs free energy (ΔG) and entropy (S) of different materials in DRM process [60][61][62][63].	11
Table 2.2. Catalysts developed in the last decades and their performance at different operating conditions with major findings for DRM reactions.	21
Table 2.3: Summary of literature on optimization of syngas production from catalytic reforming of CH_4 and CO_2 using RSM.	38
Table 2.4. Recent kinetic studies and their key outcomes for DRM reaction.	42
Table 3.1. List of precursor salts used in the catalyst synthesis.	49
Table 3.2. The synthesized catalysts along with their preparation method, and name coding.	51
Table 3.3. The input process parameters for CCD with their coded representation.	59
Table 3.4. The DOE suggested by CCD along with responses obtained.	59
Table 4.1. Textural properties of the synthesized catalyst support and optimum catalyst.	67
Table 4.2. Textural properties of synthesized support, monometallic and bimetallic catalyst.	76
Table 4.3. The elemental composition obtained by EDX analysis of prepared catalysts (Ni_f , W_a , W_b , W_c , W_d).	78
Table 4.4. TOF of the monometallic and optimum bimetallic catalyst calculated via TPR- H_2 chemisorption analysis [171].	86
Table 4.5 Comparison of performance and stability of catalysts for DRM reaction in the recent studies employing composite catalysts.	87
Table 4.6. Average crystal sizes of the spent monometallic and optimum bimetallic catalyst with TPO- O_2 results.	91
Table 4.7. The elemental composition obtained by EDX analysis of spent catalysts (Ni_{sp} , $\text{W}_{b,sp}$) after 6 h of DRM reaction.	94
Table 4.8. The DOE suggested by CCD along with responses obtained.	100
Table 4.9. ANOVA table for CH_4 conversion obtained from (CCD) RSM.	102
Table 4.10. ANOVA table for CO_2 conversion obtained from (CCD) RSM.	105
Table 4.11. ANOVA table for H_2 : CO obtained from (CCD) RSM.	106
Table 4.12. Goals and responses of the input process variables and their responses.	109
Table 4.13. Optimum experimental values vs predicted values and corresponding percentage error.	111
Table 4.14. The activation energies (E_A) over different catalysts for DRM reaction.	118
Table 4.15. Kinetic parameters attained by the applied kinetic models.	122

LIST OF ABBREVIATIONS

BBD	Box-Behnken design
BET	Brunauer, Emmett, and Teller
BMD	Boehlert Matrix Design
CCD	Central Composite Design
CCS	Carbon Capture and Storage
CCU	Carbon Capture and Utilization
CNT	Carbon Nanotubes
DRM	Dry Reforming of Methane
DFT	Density Functional Theory
EDX	Energy Dispersion X-ray
ER	Eley Rideal
ESRL	Earth System Research Laboratory
FESEM	Field Emission Scanning Electron Microscopy
F-T	Fischer–Tropsch
GC-TCD	Gas Chromatography- Thermal Conductivity Detector
GHG	Greenhouse Gas
GHSV	Gas Hourly Space Velocity
ICDD	International Centre for Diffraction Data
IUPAC	International Union of Pure and Applied Chemistry
LH	Langmuir-Hinshelwood
MWCNT	Multiwalled Carbon Nanotubes
PBD	Plackett Burman design
PL	Power Law
POM	Partial Oxidation of Methane
PPB	Parts per billion
PPM	Parts per million
RDS	Rate Determining Step
RSM	Response Surface Methodology
DOE	Design of Experiments
RWGSR	Reverse Water Gas Shift Reaction
SMSI	Strong Metal-Support Interaction
SRM	Steam Reforming of Methane
TEM	Transmission Electron Microscopy

TPD-CO ₂	Temperature Programmed Desorption of CO ₂
TPO-O ₂	Temperature Programmed Oxidation of O ₂
TPR-H ₂	Temperature Programmed Reduction of H ₂
TOF	Turnover Frequency
WGSR	Water Gas Shift Reaction
XPS	X-ray Photoelectron Spectroscopy
XRD	X-ray Diffraction
E _a	Activation Energy
o	Vacant site
C _s	Carbide Surface
*	Educt/Intermediate specie
<i>k</i>	Rate Constant
K _{CH₄}	Adsorption Equilibrium Constant for CH ₄
K _{CO₂}	Adsorption Equilibrium Constant for CO ₂

CHAPTER 1

INTRODUCTION

1.1 Background and Motivation

The world population is increasing at a fast pace and is expected to reach 8.5 billion in 2030 and around 10 billion in 2050 as per the reports of United Nations [1]. The escalation of human population at this rate is posing a great challenge for energy industries to meet the simultaneous growth in its demand [2]. The upsurge in world's population is not only posing a burden on consumption of fossil fuels, but also leading to intensification of greenhouse gases (GHGs, i.e. CO₂ and CH₄) in the atmosphere [3, 4]. Carbon dioxide is the most abundant GHG that is present in atmosphere and its concentration is continuously rising by human activities such as burning fossil fuels and by natural processes such as respiration and volcanic eruptions. Apart from consumption of fossil fuels a large amount of greenhouse gases are flared into the atmosphere worldwide from natural gas and other sources. For example, Malaysia is one of the major natural gas producers in the world, with estimated natural gas reserves of 88.0 tscf and some of these reservoirs contain very high CO₂ concentration (as high as 87%) [5]. As per the latest data from Earth System Research Laboratory (ESRL), USA, the global CO₂ concentration increased from 315.00 ppm to 419.13 ppm, since 1959 to 2021 (shown in Figure 1.1) [6], which is highest recorded CO₂ concentration level in last two centuries. The global CO₂ emission touched all time high mark by emitting 33.1 billion tons of CO₂ in the atmosphere [7, 8]. The concentration of CH₄ in atmosphere is lower than CO₂ comparatively [9], however it still contributes to 20% of overall global warming [10], because it is 28 times more effective to the greenhouse effect than CO₂ [11]. The CH₄ concentration has risen from 1650 ppb in 1985 to 1893 ppb in June 2021 as per the latest data from ESRL, USA (shown in Figure 1.1) [6].

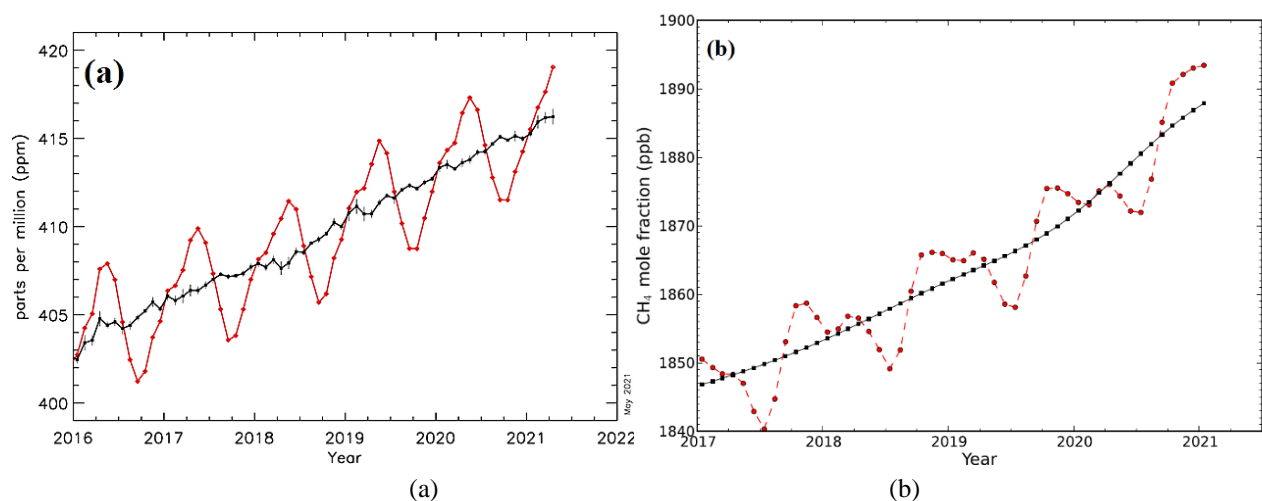


Figure 1.1. (a) Surface average atmospheric CO₂ concentration (ppm), (b) Globally-averaged, monthly mean atmospheric CH₄ abundance [6].

Besides natural gas exploration and processing, the grasslands, termites, lakes, wildfires, wetlands are the natural sources of CH₄ emission apart from human activities such as oil and gas processing, coal mining and landfills [12]. The excess of GHGs in the atmosphere results in rise of global temperature and interferes with the global climate cycle, giving rise to droughts and flooding in different parts of the globe [13]. These changes in climatic cycles due to rising GHGs in atmosphere pose a burden on ecosystem which ultimately leads to loss of biodiversity [14]. Hence it becomes critically important at this alarming situation to look and explore more carbon capture and storage (CCS) along with carbon capture and utilization (CCU) techniques. Also to minimize the dependency on fossil fuels and exterminate its harmful effects on environment, an alternative clean fuel needs to be explored [15, 16].

Gas reforming is the commercial technique used by industries for syngas production. The reforming of methane can be done by employing different techniques which are; steam reforming of methane (SRM), partial oxidation of methane (POM) and dry reforming of methane (DRM) [17]. DRM, also known as CO₂ reforming of CH₄ is one of the promising techniques both for fixing the CO₂ and for getting value added product. DRM has continuously attracted and gained the interest of researchers in the last decade due to its encouraging response for CO₂ and CH₄ fixation DRM [18]. Additionally DRM provides a technique to utilize natural gas from gas fields having elevated CO₂ concentrations, which may reach up to more than 80% in some cases [5], thus providing an economic alternative for high cost separation processes.

Steam Reforming of Methane (SRM):-



Partial Oxidation of Methane (POM):-



Dry Reforming of Methane (DRM):-



Generally, the DRM reaction (eqn. 1.3) can be catalyzed by d-block elements, which are noble metal-based (i.e., Pt, Pd, Rh, Ru, Ir etc.) and non-noble metal-based (such as Ni, Co, Fe etc.). However, regardless of better coke resistance and better capacity towards splitting C-H bond the active metals (mostly Ni based) are preferred over the noble metal-based catalysts due to their easy availability, equivalent activity and reduced cost [19]. The main problems related to Ni-based catalysts are coking and sintering of catalyst at high temperatures [20, 21]. Hence, Ni-based catalysts are broadly studied to minimize coking and sintering, and thus to improve its durability. The catalytic activity and stability can be improved by doping with suitable metals, which may be noble, alkaline or corresponding d-block metals [22–24]. The activity and stability of catalyst is subjected to the nature of the support, since it affects the active metal dispersion and support interactions throughout the catalyst [25]. The support also provides large surface area, anchorage to the active metals dispersed on it, and basicity. The support may acts as Lewis base, which instigate strong CO₂ adsorption and prevents coke formation via high CO₂ adsorption on the catalyst surface, which speed up the CO₂ conversion with carbon to give CO [26]. It has been also been reported by several researchers that by using bimetallic catalysts system the coke formation can be reduces to a large extent [27–29]. Several researchers also studied that the use of rare earth elements either as supports or promoters, and other d-block elements with Ni improved the reaction conversions, since both the metals work synergistically [30–32].

Besides the above-mentioned factors, the catalyst stability and DRM reaction also depends on active metal doping, the type or support used, and the synthesis technique employed for catalyst preparation.

A comparative study has been done by Bagheri-Mohagheghi [33] conducted a comparative study in which they concluded that the method of catalyst preparation plays the key role in the functioning and performance of the catalyst. They displayed that amongst catalysts synthesized by sol-gel methods and conventional co-precipitation, the catalyst synthesized by co-precipitation showed elevated BET surface area and produces almost spherical and hexagon α -powder. The preparation method affects the crystal size, active metal dispersion and morphology of the catalyst [34]. Apart from physicochemical properties of catalyst, the operating variables such as accompanying side reactions, reactant partial pressure, reaction temperature are the vital factors that needs to be evaluated for optimum catalytic performance and durability throughout the DRM reaction [35, 36].

1.2 Problem Statement

In the process of CO₂ reforming of methane, the noble metals meet the purpose since they possess both high activity and resistant against coke formation; however noble metals are highly costly; hence it is not economic to commercialize them [37]. Therefore, emphasis of researcher has been shifted towards d-block metals especially Ni and Co, due to their economic price, ease of availability and high activity [38]. Nevertheless, coke deposition on the Ni-based catalyst during the DRM reaction is still the major limitation.

The main hurdles for Ni-based catalysts in DRM reaction are coking and sintering, which disables the catalysts for longer duration of time. The key factors that need to be considered for better functioning of catalyst are selection of appropriate support, optimum metal loading on catalyst support, and a bimetal that can form a thermally stable alloy to give enhanced durability to the overall catalyst. The primary roles of the catalyst support are to provide thermal stability, basicity, high surface area, uniform metal dispersion, and a strong grip to the active metal particles. The optimum loading analysis of active metal (Ni) on catalyst support is essential to avoid the formation of bigger agglomerates of Ni at higher temperatures during DRM reaction, and hence avoid high coking. Further, another problem associated with the monometallic Ni-based catalysts is carbon deposition and hence rapid deactivation. Tungsten (W) is reported to forms thermally stable alloys with Ni [39–41] which can result in enhanced durability of Ni-W bimetallic catalysts. Also, Ni-W catalyst is reported to inhibit the RWGS reaction [42] which is a side reaction that takes place with the DRM reaction, and hence can enhance the process

efficiency. Thus, investigating the effect of Tungsten (W) as a bimetal with Ni seems to be a promising approach to enhance catalytic stability and performance. The proposed Ni-W/Al₂O₃-MgO catalysts has not yet been studied for DRM reaction. There are very limited studies for the optimization of input process parameters (i.e., reaction temperature and feed gas ratio) for DRM reaction for bimetallic catalysts. Also, no combined experimental and kinetic analysis for the proposed Ni-W bimetallic catalyst in DRM reaction has been carried out yet to understand the insight of reaction.

1.3 Research Hypothesis

Ni is the commercial catalyst that is being used in gas reforming reactions. Whereas Tungsten (W) is a metal with highest melting point (3,422 °C). The reason of investigating Tungsten (W) as bimetal in the bimetallic Ni-W catalyst is that it inhibits the reverse water gas shift (RWGS) reaction and favors water gas shift (WGS) reaction [42]. Hence it is supposed to enhance the DRM process. Another reason of using W is that it inhibits coke formation due to high redox potential of tungsten oxide [27]. The metals with high redox potential are reported to aid in reduced coke formation in DRM reaction, due to formation of different metal complexes depending on the catalyst [43]. However, a detailed study of the catalytic behavior of Ni-W bimetals, effect of its concentration and interaction with the support at high and low temperatures still needs to be studied. W is also reported to form alloys with Ni which are thermally very stable at high temperatures [39–41]. Therefore, the effect of W metal loading on the Ni based catalysts in terms of coke formation, morphology, long term activity and kinetics has been analyzed for DRM reaction in the present research.

1.4 Research Objectives

The ultimate objective of this research is to synthesize an effective catalyst, i.e., both active and durable for the dry reforming of methane. The following are the specific objectives:

1. To synthesize and characterize Al₂O₃-MgO supported Ni, and Ni-W bimetallic catalysts.
2. To evaluate the performance of synthesized catalysts and investigate the effect of W addition on catalytic performance and stability for DRM.
3. To optimize the process parameters for the optimum Ni-W bimetallic catalyst for DRM via RSM.

4. To study reaction kinetics for DRM reaction using the PL, ER I, ER II and LH models.

1.5 Scope of Study

This research spotlights conversion of two main green-house gases (i.e., CH₄ and CO₂) into value-added product viz. syngas. The key factor in this conversion is the catalyst, that assist the reaction at low reaction temperatures and hence make the process economic. The parameters used along with their range has been specified and explained below:

1. To achieve the first objective the monometallic (i.e., Ni/Al₂O₃-MgO) and bimetallic (Ni-W/Al₂O₃-MgO) catalysts were synthesized via two step synthesis technique. The catalyst support is prepared by co-precipitation method followed by impregnation of Ni and W. The two step technique is employed since it results in formation of catalyst with better activity compared to the one step technique (i.e., co-precipitation) [44]. The optimum Al₂O₃:MgO ratio of 1:2 was taken from literature [45] and also verified during synthesizing of catalysts. The Ni-metal loading (in wt.%) was varied as 10-16 wt.% on the catalyst support. The metal loading on the support depends on the surface area of catalyst support and the metal support interactions. This range of metal loading is chosen as per the available literature. The lower metal loading results in very less conversion and selectivity, whereas a high loading of active metal cause sintering and agglomeration along with elevated coke formation [46]. Further, the Ni-W bimetallic catalyst with varying W concentration of 2-8 wt.% have been synthesized. This range of W loading has been taken by carefully analyzing the available literature [32, 47]. Furthermore, the catalysts have been characterized by employing various techniques such as XRD, BET, FESEM-EDX, TPD, TPO, TPR (with temperature range up to 800°C), TEM, XPS and RAMAN spectroscopy to determine the physicochemical properties like, phases present, surface area, morphology, elemental composition, basicity, hydrogen affinity, binding energy oxidation states and type of carbon formed.
2. To achieve the second objective, the performance evaluation of the prepared monometallic Ni and bimetallic Ni-W catalysts has been done at a constant atmospheric pressure, in a fixed bed catalytic reactor. The atmospheric pressure is used since low pressure favors the DRM reaction as per Le Chatelier's principle and reported in most of the literatures [3, 37]. The tubular reactor was fabricated from stainless steel and jacketed

with furnace regulated by control panel to maintain the high reaction temperatures. A total flow rate of 60 mL/min has been used for carrying out the performance evaluation and stability test for the catalyst [48], since it is the optimum flow rate for the reactor with ID of 10mm (c.f. APPENDIX D).

3. To achieve the third objective, the optimization of process parameters i.e., temperature and feed ratio (i.e., CH₄: CO₂) at a constant pressure (atmospheric pressure i.e., 1.01325 bar) has been done using RSM statistical tool from design expert software. The reaction temperature has been varied in the range from 600°C-800°C and the CH₄: CO₂ was varied from 0.5 to 1.5, respectively [49, 50].
4. Finally, to achieve the fourth objective, the kinetic analysis of DRM for the optimum Ni-W bimetallic catalyst has been investigated. The four basic models i.e., Power-Law (PL), Langmuir-Hinshelwood (LH), Eley Rideal I (ERI), Eley Rideal II (ERII) models [3], [51], were used in the partial pressure range of 0.2-0.6 and temperature range 600°C-800°C to study the reaction kinetics.

1.6 Significance of the Study

This study will focus on the effect of different parameters such as effect of catalyst's preparation route, bimetal on the performance of catalyst. The stability study of the optimum catalyst is expected to provide a durable catalyst for DRM reaction. Further, the optimization of process parameters will provide the optimum reaction conditions (i.e., the temperature and feed gas ratio). Finally, the kinetic study will provide an overview of the reaction mechanism for Ni-W bimetallic catalyst, and the most appropriate approach for modelling via existing kinetic models. The proposed optimum catalyst will bridge the gap and contribute for a stable DRM reaction catalyst in the journey for an ideal catalyst.

1.7 Thesis Organization

This doctoral thesis includes five chapters along with appendices covering the supplementary data information. The individual chapter explains the different vital parts of the investigation. The research work comprehends the description on the associated subjects i.e., carried out for this research. A brief description of thesis organization as per different chapters is as follows:

1. Chapter 1 presents a current scenario of global warming due to the emission of GHGs into the atmosphere. It includes the issues related to production of sustainable green fuels, gas reforming and catalysts. Hence, it provides an outlook for the corresponding problem statements, research objectives and hypothesis along with the scope of the study.
2. Chapter 2 provides a very comprehensive and rich literature review of latest trends in catalysis for DRM. It focuses on a wide range of issues related with catalyst such as, thermodynamic overview, effect of catalyst support, promoters, bi-metals, and tri-metals. It also highlights the optimization studies using RSM and the reaction kinetics of DRM reaction. The chapter after a thorough literature review yields with a research gap stated at the end.
3. Chapter 3 illustrates the detailed methodology and deployment of materials during the experimental study. The experimental procedure employed for catalyst synthesis, catalyst's characterization, catalyst testing for DRM using the fixed bed reactor has been explained in detail. Further, the optimization study using the RSM software, and the kinetic models used to study reaction kinetics for DRM have also been elucidated in detail.
4. Chapter 4 includes the comprehensive discussion of the results obtained from catalyst's characterization and the experimental analysis for DRM. A meticulously researched discussion on the physicochemical properties, morphology, phases present, coke formed along with the performance evaluation of catalyst has been reported. The optimization of parameters for the best performance and stable catalyst has also been evinced. Finally, the reaction kinetics of the DRM reaction has been studied employing the four different kinetic models.
5. Chapter 5 summarizes all the obtained research findings and contributions of the present study. It concludes and recommends the future endorsements for the associated research field and its analysis.

CHAPTER 2

LITERATURE REVIEW

2.1 Chapter overview

This chapter provides a comprehensive overview about the DRM process and role of catalyst in the DRM reaction. The different sections cover the thermodynamic overview of DRM along with the effect of catalyst support, promoters, bi-metal, tri-metal on the catalyst. The effects of all these mentioned factors have been summarized in Table 2.2. The study also includes the investigations of the different spent catalysts to examine the types of carbon formed during the DRM reaction. Further, the different optimization studies using RSM carried out by different researchers are also discussed and summarized in Table 2.3. Finally, the kinetic studies for DRM reaction, conducted by several researchers via several kinetic models have been analyzed and illustrated in Table 2.4.

2.2 Dry Reforming of Methane (DRM)

Gas reforming is the conventional method that is being employed in industries for syngas production. The methane reforming is done by any of the three processes, i.e. by SRM (steam reforming of methane), POM (partial oxidation of methane), and DRM (dry reforming methane) [17].

SRM:



POM:



DRM:



Among the existing gas reforming techniques DRM is a promising alternative for syngas production, due to several technical and thermodynamic aspects. An elevated syngas ratio is obtained from SRM (i.e., $\text{H}_2:\text{CO} = 3:1$), which is high than the required value for F-T synthesis

(i.e., $\text{H}_2:\text{CO} = 2:1$) [52]. SRM demands rigorous energy input due to its endothermic nature and hence a high-priced process [53]. Additionally, an elevated feed ratio (of $\text{H}_2\text{O}:\text{CH}_4$) is needed to obtain an increased H_2 yield. This further makes SRM process energetically unfavorable and fast-tracks catalysts deactivation [54]. Furthermore, the SRM process encounter corrosion problems and thus needs an attached desulphurization unit [55]. The POM process is appropriate for producing the long chain hydrocarbons and naphtha [56]. With very short residence time, the POM process deliver high conversion rates and selectivity [57]. However, the exothermic nature of the reaction results in generation of hot spots on the catalyst, and thus it becomes a grueling task to control the operation [17]. Moreover, POM also requires an additional cryogenic unit to separate O_2 from the air [55]. Hence it can be inferred that among the existing techniques DRM is the most promising approaches, since it consumes two major GHGs (i.e., CO_2 and CH_4) to produce a value-added product, i.e., syngas which is the main product of gas reforming. Syngas has widespread uses and works as a feedstock in the manufacture of hydrogen, methanol, methyl ethers and Fischer-Tropsch synthesis (F-T synthesis) [58, 59] and also a promising solution to reduce the greenhouse gases emissions from the environment [60]. DRM yields a ratio of H_2/CO equal to one which can be easily employed not only for synthesizing oxygenated chemicals but the long chain hydrocarbons as well for F-T synthesis [53]. Furthermore apart from natural gas reserves, biogas (comprising of CO_2 , CH_4) can be used as a feedstock for the production of green fuels [61].

2.3 Thermodynamic overview

DRM is endothermic in nature and requires high operating temperatures; however, the use of catalyst can reduce the temperature, energy requirement and optimize the reaction considerably. For efficient syngas production by DRM, the simultaneous study of associated side reactions [62] is equally important. The side reactions accompanied by the main reaction are as follows:

Reverse water-gas-shift (RWGS)



Decomposition of CH_4



Disproportionation of CO



Hydrogenation of CO₂



Hydrogenation of CO



Table 2.1. The enthalpy (ΔH), gibbs free energy (ΔG) and entropy (S) of different materials in DRM process [63]–[66].

Materials	$\Delta G_{298}^0(\text{kJ/mol})$	$\Delta H_{298}^0(\text{kJ/mol})$	$S_{298}^0(\text{kJ/K.mol})$	$E_{a.w}(\text{kJ/mol})$	$E_{a.wo}(\text{kJ/mol})$
CH _{4(gas)}	-50.5	-74.5	0.1863	208-131	450-312
CO _(gas)	-137.2	-110.5	0.1976	-	-
CO _{2(gas)}	-394.4	-393.5	0.2137	100-13	302-250
H _{2(gas)}	0	0	0.1306	-	-
H _{2O(gas)}	-228.6	-214.8	0.1887	-	-
O _{2(gas)}	0	0	0.205	-	-
C _(solid)	0	0	0.0057	-	-

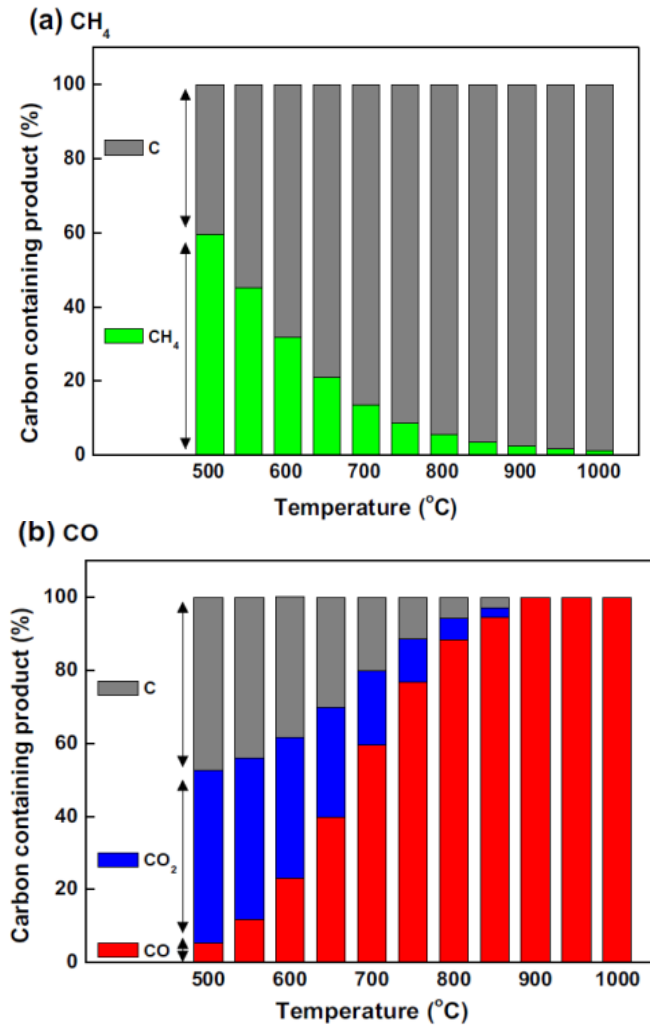
$E_{a.w}$: Activation Energy with Ni based catalyst

$E_{a.wo}$: Activation without catalyst

Chen et al. [67] demonstrated in their work that the spontaneity and the direction of DRM reaction and its side reactions can be determined by calculating its Gibbs free energy (ΔG) through the desire's equation expression using the values from Table 2.1. Further, it can be clearly seen from Table 2.1 that the catalyst provides an alternative path for the reaction to take place. There is a huge difference between the activation energy (E_a) ranges with and without catalysts. This catalyst provides an energy pathway with lower activation energy barrier [64–66].

The main reaction (eqn. 2.3) is favorable at a temperature higher than 700 °C for DRM although simultaneous RWGS reaction as shown in eqn. 2.4 may reduce H₂ to CO ratio. Apart from RWGS reaction, additional side reactions that may occur and interfere with DRM

efficiency are CH_4 decomposition, hydrogenation of CO_2 , disproportionation of CO , and CO reactions. These side reactions (eqns. 2.5-2.8) can have a significant effect on the DRM process efficiency and their dominance change with feed gas ration and reaction conditions. Reactions as shown in eqns. 2.6-2.8 are dominant at lower temperature range below 527 °C and hence coke formation may occur by side reactions whereas the CH_4 decomposition reaction (eqn. 2.5) which is an endothermic reaction generally favored at higher temperatures [19]. As displayed in Figure 2.2, the coke deposition during DRM reaction occurred due to decomposition of CH_4 (eqn. 2.5) and Boudouard reaction or CO disproportionation (eqn. 2.6) [68].



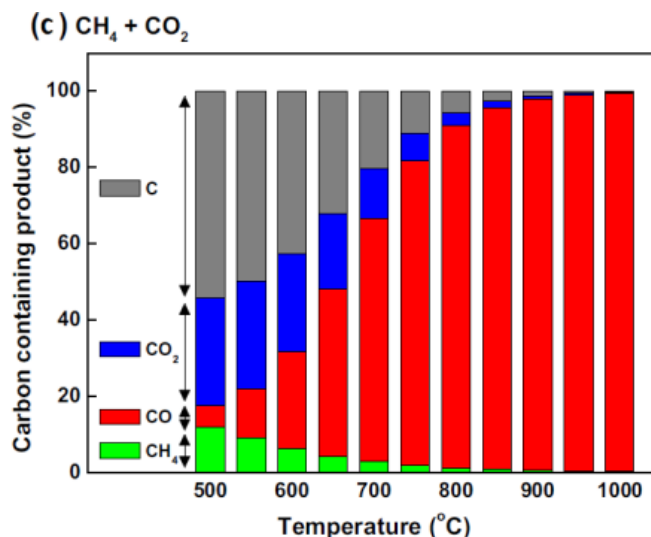


Figure 2.1. Carbon containing product for the various reactions: (a) CH_4 decomposition ($\text{CH}_4 = 100\%$), (b) Boudouard reaction ($\text{CO} = 100\%$), (c) Reforming of CH_4 with CO_2 ($\text{CH}_4 = 50\%$ and $\text{CO}_2 = 50\%$) [69].

Wang et al. [70] confirmed that breakdown of CH_4 occurs beyond 557°C , whereas Boudouard reaction happens below 700°C . An optimum temperature that ranged from 870 to 1040°C was recommended in the research for $\text{CO}_2:\text{CH}_4$ feed ratio of 1:1 considering the coke formation and conversion. Numerous investigations have been carried out on the thermodynamic simulations for different temperature, pressure, CO_2 to CH_4 ratio, additional oxidant, and coke formation reactions. Nevertheless, most of the studies deduced that DRM at high temperature, beyond 850°C and low pressure is necessary for high conversion of CH_4 and CO_2 [62, 68, 70]. Besides that, minimizing the coke formation yield is principally vital in a stable DRM process since the coke formation strongly relying on catalyst type used and difficult to generalize its formation by calculating the operating condition thermodynamically. Therefore, DRM studies were reviewed with a focus on the use of catalysts and several factors that affect the catalytic performance are discussed below.

2.4 Catalyst support

Usually, a heterogeneous catalyst comprises of more than one constituent. The active metal component is enclosed in a solution of catalyst support substance to yield a supported metal catalyst. The catalyst support plays a substantial role in boosting the surface area of the active sites, on which active metal is scattered. Also, the proper anchorage and suitable geometry

are provided by the catalyst support to enhance the durability and resistance towards sintering [57]. Chaudhary et al. [71] studied Ni metal catalyst supported on Al_2O_3 and MgAl_2O_4 for DRM and oxidized DRM (ODRM) and found the existence of strong metal-support interactions between both alumina and mixed magnesia-alumina supports. However, enhanced dispersion of Ni metal for MgAl_2O_4 support was observed as compared to Al_2O_3 and greater CH_4 and CO_2 conversion was noted for Ni/ MgAl_2O_4 than Ni/ Al_2O_3 with similar coke formation. Recent study by Tanios et al. [72] indicated that $\text{Co}_2\text{Ni}_2\text{Mg}_2\text{Al}_2$ catalyst calcined at 800°C showed better catalytic activity and stability for 20h on stream than commercial catalyst 50%Ni/ Al_2O_3 due to strong interaction between Ni and Co. This mutual interaction amongst Ni and Co is due to formation of Ni-Co alloys which leads to restricted particle size (Co and Ni) and superior dispersion as elucidated by characterization studies. To study the metal and support interactions Al-swai et al. [73], synthesized different compositions of CeO_2 -MgO support with fixed Ni metal composition and the authors found that Ni supported on 15% CeO_2 -MgO showed the excellent performance with higher conversion of 95.2% and 93.7% for CO_2 CH_4 respectively. This enhanced functioning of the catalyst is due to the existence of an excess amount of active Ni sites and the elevated $\text{Ce}^{3+}/\text{Ce}^{4+}$ ratio that affirmed the formation of oxygen vacancies. In general, it can be deduced that CeO_2 caused elevated oxygen movement and better reducibility of catalyst. In another study by Zhu et al. [74], Ni/MgAl mixed oxides with an elevated ratio of Mg/Al were reported to be more efficient in terms of coke resistance and catalytic activity where the best activity and stability were shown by Ni/MgAl with Mg/Al ratio of one for DRM reaction. This enhanced activity and stability is due to compelling interaction between Ni and magnesia. NiO with MgO forms a solid solution as are highly miscible due to their identical crystalline structure.

Rong-jun et al. [75] studied the effect of different supports (i.e. SiO_2 , TiO_2 , Al_2O_3 , magnesia-alumina, ZrO_2 , MgO) on the catalytic performance of Ni-based catalyst in DRM. The mixed support MgO- Al_2O_3 was found to have high interactions with NiO and exhibited superior catalytic performance in DRM even under high gas hourly space velocity (GHSV) and showed extended stability with more than 100h due to spinel NiAl_2O_4 formation of and NiO-MgO solid solution. Another research by Djaidja et al. [76] revealed that without Mg, a very slight increase in coke formation was noted and in contrast by increasing the Mg amount in the catalyst support,

the coke formation was minimized. The findings indicated that the prominent basicity of MgO, analogous crystal structure is highly favorable for Ni-based catalysts.

A study that evaluated impregnated NiO/MgO-600 and NiO/MgO-800 catalysts that were calcined at various temperatures of 600°C and 800°C, respectively. The study revealed that NiO/MgO-800 catalyst exhibited enhanced catalytic performance, solid metal support interaction (SMSI) and more CO₂ adsorption sites than NiO/MgO-600 catalyst. This was due to the elevated binding energy and interaction of Ni²⁺ ions with the support in NiO/MgO-800 catalyst. It was also found that CO₂ did not directly dissociate and the dissociation of a hydrogen ion from CH₄ stimulated the dissociation of CO₂ into CO [77]. Various supported (single, mixed oxide) catalysts were studied at low temperature (400 °C) for DRM reaction [78]. The supported catalysts are Ni/Al₂O₃, Ni/MgO, Ni/TiO₂, Ni/SiO₂, Ni/ZrO₂, Ni/La₂O₃-ZrO₂, Ni/doped alumina Sira110 and Ni/promoted magnesium oxide PuralMG30. Among various supports, La₂O₃-ZrO₂ showed highest stability and CO/H₂ yield close to equilibrium. The improved stability of Ni/La₂O₃-ZrO₂ catalyst was due to SMSI and imprisonment of metal on the pores of the support. Whereas there was no entrapment of active metal for other supports as a result graphitic carbon formation took place and hence resulted in low stability. Besides that, Fauteux-lefevre et al. [79] investigated NiAl₂O₄ supported on Al₂O₃-ZrO₂ reported that the NiAl₂O₄/Al₂O₃-YSZ-1 and NiAl₂O₄/Al₂O₃-YSZ-2 catalysts gave better conversions and elevated H₂ concentrations. An insignificant amount of coke formation was observed on the catalyst even after operating at drastic conditions for an extended time. This is due to formation of stable spinel type structure which inhibits the coke formation. Also, for hexadecane SRM the H₂, CO, CO₂ and CH₄ amount were all near the intended values as from theoretical thermodynamic equilibrium calculations.

As evidenced in the available literature (summarized in Table 2.2), catalyst support plays a vital role in its activity, stability, and performance. This is mainly due to various interactions such as metal support interactions, morphology, and comparative the lattice structure in case of mixed oxide supports to form a stable metal solution.

2.5 Catalyst Promoters

Doping of catalyst by alkaline or alkaline earth metals is also one of the notable methods to enhance the catalytic properties. Promoter improves catalyst efficiency by altering and stabilizing catalyst structure, increasing the oxygen storage capacity, enhancing its reducibility,

and reducing the formation of coke. The selection of promoter and its amount of concentration to be added depends on the catalytic system used for the reforming reaction [18]. To study the impact of promoter on catalytic efficiency recently [80] doped the Ni (5 wt%) / γ -Al₂O₃ catalyst with Pt (0-2.8 wt%) and found that alloy which is rich in Ni and formed by electroless deposition showed a maximum activity in Pt loading (0.4 monolayers of Pt) on Ni. At low temperatures (525 °C - 600 °C) it showed a synergistic effect on noticeable activation energies related to an increase in CH₄ conversion rates whereas, at high temperature (700 °C) the separation of nano-particulate alloy phases was observed. This converse performance is due to compensation effect; in which a group of material if surpasses the isokinetic temperature, the performance of catalyst exhibits an opposite fashion. Hence, the increasing temperature will escalate the pre-exponential factor to counterbalance the reduced E_A. In the same year Salam et al. [48] studied the influence of CeO₂ (10 wt%) and La₂O₃ (10 wt%) doping on Ni/Al₂O₃ catalyst. In the nanocatalysts synthesized through sol-gel technique the observed that doping Ni/Al₂O₃ with CeO₂ improved the CO₂ and CH₄ conversions, whereas, doping Ni/Al₂O₃ with La₂O₃ did not show any effect on conversion. However, La₂O₃ showed a steady conversion rate during 8h of dry reforming reaction. This is because CeO₂ boosted the dispersion of active metal throughout the catalyst and increased its basicity and reducibility. In another study, Zhang et al. [81] investigated on Ni metal catalyst supported on ZrO₂ catalyst and doped with Ce, La, Sm and Y. The results showed that superior methane dissociations and CO₂ activation with promoted catalysts. The order of activity of the doped catalyst was found to be in Y > Sm > La > Ce sequence. This enhanced performance is due to the consequences of doping on surface adsorbing capacity for oxygen with more coke deposition at temperatures below 700 °C. In one more study, Sun et al. [82] prepared and studied Ce and Ca promoted Ni-MSiC catalysts (Ni- xCe (5-x) Ca-MSiC) for DRM reaction. Synergistic effect between Ce and Ca was observed which resulted in the reduction of coke formation and sintering of the catalyst. Additionally, the Ce doped catalyst increased the oxygen storage capacity of catalysts by facilitating the conversion of Ce⁺⁴/Ce⁺³ and Ni⁺²/Ni⁰. The catalyst which is only doped with Ca showed poor performance. This is because of the inadequate active metal scattering which results in limited active spots (compared to the one doped with both Ce and Ca) and higher CO₂ conversion than CH₄ (due to RWGS reaction).

Yttrium-promoted nickel-KIT-6 mesoporous silica catalysts were synthesized by Swirk et al. [83]. The yttrium doped catalyst showed better reducibility of NiO and improved dispersion

in KIT-6 support. The (Ni-8Y)/ KIT-6, with a molar ratio of Y/Si = 0.05 presented the highest activity and structural stability in DRM from 600 °C to 750 °C. Another type of supported catalyst, doped Ni-based SBA-15 with titanium nitride was developed and tested for DRM by Chotirach and Tungasmita [84]. The findings showed that for Ni/SBA-15 catalyst, doping with TiN enhanced the performance with high catalytic activity and improved coke resistance at 700 °C. This enhanced performance is because of enriched basic sites in the doped Ni-based catalyst with TiN when compared to non-doped Ni catalyst. The mutual interactions between Ni and TiN on SBA-15 morphology resulted in higher binding energy as described in its XPS analysis. Two more related research were published in the year 2018. Maina et al. [85] reported that the stability and performance of Na and K promoted iridium metal supported on alumina catalyst and long-term exposure to DRM resulted in iridium catalysts with elevated sintering resistance. This is mainly due to the non-stop wipe out mechanism (for Ir doped catalyst), which removes the carbon formed during the decomposition of CH₄. As a result, the metallic surface continues to be free from carbon deposition for long durations of time at 750 °C. Catalysts such as Ni/Al₂O₃, Ni-Co/Al₂O₃-MgO and Ni-Co/Al₂O₃-MgO for DRM reactions as synthesized by Azeanni et al. [86] showed that Nb-Zr promoted Ni-Co/Al₂O₃-MgO catalyst has more uniform and well-dispersion of metal than Ni-Co/Al₂O₃-MgO. Moreover, improved conversion for both CH₄ (86.96%) and CO₂ (87.84%) were observed. This happened due to increased BET surface area of catalyst after doping with Nb-Zr. Also due to the formation of spinel MgAl₂O₄ structure the coke resistance of the overall catalyst improved to a large extent.

On the contrary, Mo-promoted Ni/Al₂O₃ catalyst for DRM caused a considerable reduction in the catalytic activity compared to the non-promoted Ni/Al₂O₃ catalyst that showed high catalytic activity as reported by Yao et al. [87]. This was primarily due to set up of a distinct Ni^o phase that disconnected from Mo and hence decreased the overall basicity of the catalyst. Another research was carried out with Ni(3%)/ZrO₂ and Na (0.6%) promoted Ni(3%)/ZrO₂ catalysts where Na-promoted Ni/ZrO₂ showed significantly higher activity, stability, water gas shift reaction (WGS) promotion and SMSI [88].

Earlier, Yang Cao et al. [89] studied the effect of rare earth metals on the prepared NiMgAl catalyst by doping it with 0.15 wt% of Sc, Y, Ce and Pr. The authors concluded that rare earth elements modified with catalysts enhanced CO₂ adsorption sites, improved catalytic stability and coke resistance especially with Ce or Pr as the promoters. This is mainly due to

elevated quantity of strong basic spots and co-occurrence of redox pairs (i.e., $\text{Ce}^{3+}/\text{Ce}^{4+}$ or $\text{Pr}^{3+}/\text{Pr}^{4+}$) that is responsible for enriched oxygen vacancies and enhanced redox properties. In another study, two different zeolite supports with La and Ca promoted Ni-based catalysts were prepared by Alotaibi et al. [90]. The BET surface area of the two supports i.e., ZL(A) and ZL(B) were $925 \text{ m}^2/\text{g}$, and $730 \text{ m}^2/\text{g}$ respectively. The findings showed that ZL (B) promoted with Ni and Ca catalysts exhibits better performance which results in the highest CH_4 conversion of 60% and stability with reduced time on stream compared to promoted Ni on ZL (A). In another study Radlik et al. [91] investigated the optimum loading of Ni metal for ceria and zirconia support (Ni/CZ) for low temperature (550°C) DRM. The optimum CH_4 and CO_2 conversions and H_2/CO ratio of unity are obtained by the catalyst loaded with 10 wt% Ni. It has also been concluded from the results that, although high metal loading gives elevated conversions; but lower dispersion and agglomeration of Ni particles has been observed which leads to higher coke formation resulting in limited stability. The effect of promoters was summarized and presented in Table 2.2.

In conclusion, the addition of promoters boosted the main metal dispersion by synergistic interactions and reduced the required temperature to obtain the optimized performance. The role of a promoter and its effect depends on the metal system (i.e., the support used, the active metal and promoter interactions, the lattice structure of dopant etc.). A promoter may alter the catalytic structure which influence catalytic performance, or it may also change the metal support interactions and hence the overall acidity and basicity of the catalyst, which directly affects the performance and selectivity of the reaction. Meanwhile, bimetallic catalysts are equivalent to the metal promoted catalyst but contradicted in the magnitude of interactions of metal with support and metal to metal interactions. However, selecting a suitable co-metal can be difficult and the actual reaction mechanism still needs to be explored.

2.6 Bimetallic catalyst

One of the primary aspects of the performance of the bimetallic catalyst is its preparation technique. Strong metal-support interaction was observed in the samples calcined at high temperatures, which also bring about spinel-type structure [3]. Recently, Turap et al. [92] studied the effect of bimetallic catalysts for Co-Ni metals by varying the Co: Ni ratio from 0-1.0 and tested for DRM. They found that Co-Ni/ CeO_2 alloy exhibited enhanced performance in comparison to that of Ni/ CeO_2 . The catalyst with the composition of Co-Ni(0.8)/ CeO_2 displayed

the highest catalytic activity and stability with the least carbon formation even after 10h of experimental run. This enhanced performance is due to selective adsorption of O_2 that facilitated removal of carbon and feeble adsorption of hydrogen that restricted RWGS reaction. The Co-Ni alloy formation is solely responsible for these improved characteristics of the catalyst that is formed following the reduction phase. Besides that, several combinations and structural forms of bimetallic nickel-cobalt catalysts for DRM activity were tested by Aybuke and Ramazan [93]. The researchers observed that Ni (8 wt%) – Co (2 wt%)/MgO wash-coated monolith catalyst showed elevated activity, stability (48h), reduced coke formation (from 41 wt% to 13.3 wt% at 3% O_2 feed). This may be attributed to the fact that catalyst in the form of monolithic improved the surface area-volume relation and heat transfer as compared to powdered form of catalyst.

Apart from this, a sol-gel technique was utilized to prepare three nano-catalysts which were Ni/ Al_2O_3 (as catalyst-1), Ni-Co/ Al_2O_3 (as catalyst-2) and Ni-Co/ Al_2O_3 -MgO (as catalyst-3) by Azeanni et al. [86] and catalyst-3 was found to have good catalyst functioning compared to the other synthesized catalysts owing to SMSI, elevated stability and considerable resistance to carbon deposition during the DRM reaction mainly because of the formation of $MgAl_2O_4$ spinel structure.

Another technique, the ultrasonic-assisted co-precipitation method was used by Shamskar et al. [94] to synthesize mesoporous nano-crystalline bimetallic catalyst (25wt %) Ni-M- Al_2O_3 (M = CeO_2 , La_2O_3 , and ZrO_2) and tested for DRM. They observed that the addition of 5 wt% La_2O_3 and ZrO_2 increased the overall surface area of catalyst and the use of the same content of CeO_2 showed an inverse effect. The authors also found that promoted catalyst showed lower coke deposition and decreased activity, unlike the Ce promoted catalyst. The superior performance of catalyst with CeO_2 is due to its distinctive redox property, which allows it prompt swapping amid Ce^{3+} and Ce^{4+} types. Synthesis of Ni/CNT, Ni/SBA-15 and a series of Ni-based bimetallic catalysts (Cu, Ca, Mg, Mn, Co-Ni/SBA-15) by Y. Dai et al. [95] revealed that Ni/SBA-15 exhibited improved conversion efficiency than that of Ni/CNT whereas spent catalyst (Ni/SBA-15 at 600 °C) showed no catalytic deterioration and negligible coke deposition. Also, the catalysts activity was spotted to follow the order as Cu–Ni alloy > Mg–Ni alloy > Co–Ni alloy > Ca–Ni alloy > Mn–Ni alloy. This superior performance of Cu–Ni and Mg–Ni alloy is due to availability of more active spots on their surface, reduced particle size and better dispersion due to compatible crystal lattice. In another comparative study, comparison between

Ni/SiO₂ catalyst and Ni₁₇W₃/SiO₂ (Ni=10.7wt%, W=5.7wt%) bimetallic catalyst indicated that the Ni₁₇W₃/SiO₂ catalyst was superior to Ni/SiO₂ catalyst for the DRM reaction due to the formation of Ni₁₇W₃ alloy and α -WC, which is very stable alloy [96]. In an alternate study, Ni–Ce/MgAl₂O₄ bimetallic catalyst was used in bi-reforming of methane (BRM) for syngas production by Young et al. [97]. It was found that Ni–Ce/MgAl₂O₄ (Ce/Ni = 0.25) catalyst showed better activity and hindrance to coke formation for BRM due to the improved metal dispersion, outstanding reducibility, and effective surface oxygen transfer.

Analysis on Ni–Mo₂C catalyst with Ni/Mo molar ratios of 1/3, 1/2, and 1/1 showed that Ni–Mo₂C (1/1) and Ni–Mo₂C (1/3) were deactivated due to the coke formation and bulk oxidation Mo₂C to MoO₃, respectively. For Ni/Mo molar ratio of 1/2, catalytic oxidation-reduction cycle was established and Ni–Mo₂C catalyst showed typical bi-functional catalyst characteristic for DRM Shi et al.[98]. Earlier, a study on Ni-Mo/SBA-15 bimetallic catalyst for DRM reactions by Huang et al. [99] showed lower initial activity of Ni-Mo compared to Ni. However, Mo/Ni atomic ratio of 1/2 revealed an elevated activity, superior stability, and the lowest carbon deposition rate at 800 °C. Since, increasing Mo/Ni ratio further result in diminished reduction of NiO and hence lowered conversion.

Hence it can be established that, when a bimetallic catalyst was used, both metals were active and functioned synergistically in contrast to the promoted catalyst, where the activity of metal was promoted by the addition of doping metal. Bimetallic catalysts largely displayed improved performances compared to corresponding monometallic catalysts mainly due to improved stable structure, enhanced reducibility, increased surface area and better oxygen storage capacity. Method of preparation, reaction conditions and major findings of bimetallic catalysts are presented in Table 2.2.

Table 2.2. Catalysts developed in the last decades and their performance at different operating conditions with major findings for DRM reactions.

Catalyst Used	Reaction Conditions	Preparation method	Coke deposition	Major finding/Conclusions	Conversion (%)		H ₂ :CO	References
					CH ₄	CO ₂		
Monometallic Catalysts								
Ni(50%)/Al ₂ O ₃ and Co ₂ Ni ₂ Mg ₂ Al ₂ 800	500°C-800°C, Fr =1:1, GHSV=32,000 h ⁻¹	HT	N.R.	Catalyst calcined at 800°C, showed superior activity due to interaction between Ni and Co. Co ₂ Ni ₂ Mg ₂ Al ₂ 800 showed better activity and stability than commercial catalyst Ni(50%)/Al ₂ O ₃ at 800°C.	~ 96	~ 92.5	~ 0.82	[72]
Ni@HSS	800°C, Fr = 1, GSHV=144,000 mL h ⁻¹ g ⁻¹	FOP	N.R.	Ni@HSS showed excellent performance with elevated CH ₄ and CO ₂ conversions; also, high stability for DRM reaction	94.4	95	0.88-0.93	[100]
Ni on MgO and mixed (CeO ₂ -MgO)	800°C, Fr = 1:1, GHSV = 36000cm ³ /gcat.h	CP+IMP	N.R.	The utmost durability and conversion have been exhibited by Ni/(15%)CeO ₂ -MgO catalyst.	93.7	95.2	0.85-1.2	[25]
Ni/DFSBA-15	600-900°C, Fr =1:3, GHSV=15000-35000 mL/g.h)	MAME	N.R.	Factors affecting CO ₂ and CH ₄ conversions for DRM are, CH ₄ : CO ₂ > Temperature > GHSV. Optimum conditions are, T = 794°C, GHSV = 23815 mL/g.h, CH ₄ /CO ₂ = 1.199.	93.48	95.67	0.983	[101]
Ni impregnated on MgO	800 °C, 1atm	IMP	N.R.	The Ni-based catalyst (calcined at 600°C and 800°C), calcined at higher temperature displayed SMSI, enhanced activity and extra CO ₂ adsorption spots comparatively.	85-93	90-94	N.R.	[102]
Ni/Mg (Al)O	600- 800 °C, Fr = 1:1, Feed flow rate = 100 mL min ⁻¹	CP	Varies from 0.6 to 4.5 wt% depending on Ni particle size	Elevated activity, resistance against carbon formation and stability has been observed with the catalyst i.e., reduces at 700°C compared to the one reduced at 650°C.	45-93	58-90	0.68-0.9	[103]

Table 2.2. (Continued)

Catalyst Used	Reaction Conditions	Preparation method	Coke deposition	Major finding/Conclusions	Conversion (%)		H ₂ :CO	References
					CH ₄	CO ₂		
Ni on (SA-6175) and (SA-5239)	500°C to 800°C Fr =1:1, SV=680 ml/h g.cat	IMP	17.65% and 8.80% on α -Al ₂ O ₃ (SA-5239) at 600°C	Coke formation was reported at reduced temperatures for all catalysts. However, γ -Al ₂ O ₃ (SA-6175) showed better coke resistance than α -Al ₂ O ₃ (SA-5239). At 800°C, α -Al ₂ O ₃ (SA-5239) showed high stability at feed composition fraction (CO ₂ :CH ₄) of 1.3.	90.8-90.9	76.9-76	0.83	[104]
Ni nanoclusters dispersed on modified alumina (with Ce, Mg)	500°C to 700°C, GHSV=5000 to 50,000 mL/g h, Fr = 1:1	TAST	N.R.	Catalyst synthesized by template-assisted solvo-thermal method showed better resistivity toward sintering and low coke formation. Also enhanced the catalyst activity with CO ₂ and CH ₄ conversion of >90% each has been noticed.	>90	>90	~1	[105]
Ni on 5 μ m spherical CeO ₂ flowers	750°C, Fr = 1:1, GHSV=2300 h ⁻¹	HTH+IMP	N.R.	The obtained PSC samples possessed a great porosity, uniformity, excellent catalytic stability. 3.4% of Ni was found to be optimum with only 3.1% degradation of CH ₄ conversion.	~ 87-90	~ 60-87	~ 0.85	[106]
Ni-based on SiO ₂ , TiO ₂ , Al ₂ O ₃ , MA, ZrO ₂ , MgO support	750°C, Fr =1, 60,000(ml/h gcat).	IMP	NiO/SiO ₂ = 3.0 NiO/TiO ₂ =24.7 NiO/Al ₂ O ₃ =16.3 NiO/MA=1.7 NiO/ZrO ₂ =21.0 NiO/MgO=4.2 [/(mgc.(gcat.h) ⁻¹]	MgO-modified Al ₂ O ₃ exhibits superior catalytic performance in DRM even under very high GHSV and stable because of the formations of NiAl ₂ O ₄ spinel and NiO-MgO solid solution.	~88	~90	N.R.	[75]
Ni-SiO ₂	400-900°C, Fr = 1:1, Flow rate = 70cm ³ /min	MDS and IIMP	N.R.	The catalyst synthesized by modified direct synthesis showed less coke deposition and elevated Ni dispersion as compared to the one synthesized by incipient impregnation.	80-87	86-94	1-1.2	[107]

Table 2.2. (Continued)

Catalyst Used	Reaction Conditions	Preparation method	Coke deposition	Major finding/Conclusions	Conversion (%)		H ₂ :CO	References
					CH ₄	CO ₂		
Ni/Al ₂ O ₃ and Ni/MgAl ₂ O ₄	600-750°C, Fr = 1:1:1 Gas flow rate = 60ml/min	IWI	Max. 53.3% C for DRM at 600°C, (for 10% Ni/MgAl ₂ O ₄)	SMSI for Ni/Al ₂ O ₃ and Ni/MgAl ₂ O ₄ , better dispersion of Ni metal for MgAl ₂ O ₄ support. CH ₄ and CO ₂ conversion is higher for Ni/MgAl ₂ O ₄ than Ni/Al ₂ O ₃ with similar coke formation.	~ 85	75-79	~ 0.73	[71]
Ni/DMS	700°C, Fr =1:1, WHSV = 18 000 mL gcat ⁻¹ h ⁻¹	OPS	N.R.	Ni/DMS catalyst showed outstanding performance with stable CH ₄ conversion of 76% at 700°C. Also, negligible coke formation and sintering is observed due to its surface morphology in which the Ni NPs are caged in 3-D layers.	~ 76	83	0.9-0.95	[108]
Ni on CNT, SBA-15, and doped Ni/SBA-15	600°C-700°C , Fr = 1:1, (SV) = 5000–20000 h ⁻¹	HTH+CVD	N.R.	Ni/SBA-15 displayed improved performance in terms of conversion compared to Ni on CNT. Catalyst showed anti sintering property and negligible coke deposition.	75	77	N.R.	[95]
Ni-MCM	700°C, Fr =1:1, 1 atm, flow rate = 30 mL/min	OPS and IWI	N.R.	Ni-MCM catalyst (synthesized by OPS technique) remained active and structurally stable due to smaller Ni particles, with low coke deposition.	~ 72	~ 80	~ 0.9	[109]
Ni/MFI zeolite	800°C, Fr=1:1, 50 mLmin ⁻¹	MZSC + IMP	N.R.	The highest activity and stability are reported for wetness impregnation catalyst. Also, the extent of catalyst deactivation was low for corresponding conventional zeolite catalysts comparatively.	~70	~ 72	~ 1	[110]
Ni/Ce _{0.62} Zr _{0.38} O ₂	800 °C, , Fr= 1:1, GHSV=20,000 h ⁻¹	IWI	N.R.	Among the three samples (i.e, Ni loading of 2, 4 and 10 wt%), Ni(10%)/CZ catalyst showed superior CH ₄ and CO ₂ conversion, uniform H ₂ :CO ratio of unity but highest coke formation.	~40	~38	1	[91]

Table 2.2. (Continued)

Catalyst Used	Reaction Conditions	Preparation method	Coke deposition	Major finding/Conclusions	Conversion (%)		H ₂ :CO	References
					CH ₄	CO ₂		
Ni/Al ₂ O ₃	600 °C, Fr = 1:1, Flow rate = 60ml/min	SG,HTH	N.R.	Ni supported on MA, produced by the sol–gel route (Ni@SGA) exhibited utmost activity for DRM at 600 °C.	~35-37	50-47	1.25	[32]
Ni/ZrO ₂ , Ni/ZrO ₂ –MgO	600°C, Fr =1:1, 200mLmin ⁻¹	CP+IMP	N.R.	MgO addition to the zirconia support displayed superior properties. This resulted in stable tetragonal morphology of catalyst and enhanced thermal stability. Ni/ZrO ₂ –0.4%Mg showed optimum stability at 600°C.	~27	~33	N.R.	[23]
Promoted/Bimetallic Catalysts								
Ce/Ca promoted Ni- MSC	850 °C, Fr = 1:1, flow rate = 120 mL/min	ST+CIMP	N.R.	Simultaneous loading of Ce and Ca resulted in prohibition of coke growth and sintering of catalyst owing to synergistic effect between the promoters, whereas only Ca or Ce promoted catalyst showed coke deposition and poor performance.	Max.96	Max.97	~ 1	[82]
Pd-CeO ₂ nanocrystals	300–800 °C, WHSV =30,000 ml h ⁻¹ g ⁻¹ , 1 atm	SFI	N.R.	Owing to elevated Pd dispersion the catalyst showed activity at low temperatures. The catalyst also showed improved activity, coke resistance and very less sintering during DRM.	Max~93	Max~95	0.8-1.1	[111]
Ni-SiO ₂ , Ni-CeO ₂ and Ni NP sandwiched between CeO ₂ and SiO ₂	600°C, Fr =3:2, GHSV=200 Lh ⁻¹ gcat ⁻¹ , 1 atm	NPSN+IMP	N.R.	The sandwiched Ni catalyst was found stable at 600 °C for DRM (biogas), whereas Ni-SiO ₂ catalyst displayed comparatively elevated carbon deposition causing obstruction in reactor in 22 h. Also, very insignificant activity has been shown by Ni-CeO ₂ .	~94	~87.25	~0.5	[112]

Table 2.2. (Continued)

Catalyst Used	Reaction Conditions	Preparation method	Coke deposition	Major finding/Conclusions	Conversion (%)		H ₂ :CO	References
					CH ₄	CO ₂		
SmCoO ₃ perovskite	700°C-800°C, Fr = 1:1, WHSV =30,000 ml h ⁻¹ g ⁻¹ , 1 atm	SGC	N.R.	High conversion for both reactants has been achieved at stoichiometric point. Also, considerable yield of hydrogen and carbon mono-oxide (67% and 65% respectively) has been noticed.	Max.93	Max.93	0.8-1.6	[113]
[Ni-Mo/Al ₂ O ₃]	550 °C to 850 °C, Fr = 1:1, GHSV=20,000 h ⁻¹	IMP	N.R.	The utmost catalytic activity has been shown by un-doped Ni/Al ₂ O ₃ catalyst; however, Mo doped catalyst proved out to be substantially inactive. Maximum conversions are obtained at 850°C.	Max.91.1	Max.93.4	Max.0.93	[87]
Ni–Mo/SBA-15	800 °C, 1 atm, GHSV=4000 ml/gcat.h Fr = 1:1	IWCIMP	(0.00073gm. C/gm.cat.h)	Bimetallic Ni–Mo showed reduced activity when compared to mono-metallic Ni catalyst. However, elevated activity, least coke formation and prolonged stability has been achieved when Mo:Ni ratio tuned to 1:2.	~90	N.R.	~1.17	[99]
Ni/Al ₂ O ₃ doped with Ce ₂ O and La ₂ O ₃	800°C, Fr=1:1, flow rate = 60mLmin ⁻¹	SG	N.R.	Doping with Ce ₂ O ₃ (10 wt%) enhanced the dispersion, basicity, and reducibility of the catalyst, whereas adding La ₂ O ₃ (10 wt%) had almost no effect on conversion but gave the stable reaction for 8 h.	89.6	91.2	0.86-0.95	[48]
La _{0.8-x} Sr _x Cr _{0.85} Ni _{0.15} O ₃ (x = 0, 0.1, 0.2 and 0.3)	600- 800 °C, Fr = 1:1. 1 atm, GHSV between 3000- and 12000-ml g ⁻¹ h ⁻¹	SM	N.R.	La _{0.6} Sr _{0.2} Cr _{0.85} Ni _{0.15} O _{3-δ} showed highest catalytic performance with stability. An increase in oxygen vacancy and basicity has been observed on adding Sr.	~ 89	~ 89	~ 1	[114]

Table 2.2. (Continued)

Catalyst Used	Reaction Conditions	Preparation method	Coke deposition	Major finding/Conclusions	Conversion (%)		H ₂ :CO	References
					CH ₄	CO ₂		
NiMgAl catalyst promoted with (0.15 wt%) Sc, Y, Ce and Pr	Fr = 1:1, Gas flow rate= 45 mL/min, 750 °C	CP	N.R.	Rare earth elements modified catalysts possess enhanced CO ₂ adsorption sites, improved catalytic stability, conversion, and coke resistance (especially with Ce as the promoter).	86-88	95-96	0.97-0.98	[89]
Ni–Mg–Al (Varying Ni concentrations)	500-800 °C, Fr= 1:1 and WHSV = 60,000 mL g ⁻¹ h ⁻¹	CIMP	Varied from 2.7-43.8 wt% gcat	It has been concluded that at soaring temperatures (750°C) rise in active metal loading stabilize catalyst and vice versa. 12 wt% of Ni showed optimum activity.	87	92	~0.92	[115]
Ni-Y doped KIT-6 MCM	Fr = 1:1, 600°C to 750 °C, (GHSV = 20,000 h ⁻¹)	IWI	N.R.	(Ni-8Y)/ KIT-6, (molar ratio Y/Si = 0.05) displayed peak activity in DRM from 600°C to 750°C, Structural stability shown by TEM.	Max~87	Max~90	0.87-1	[83]
Ni and Ni-Co on different Al ₂ O ₃ , MgO supports	800°C, Fr =1, 1 atm	SG	N.R.	Nb-Zr promoted Ni-Co/Al ₂ O ₃ -MgO has consistently dispersed metal than Ni-Co/Al ₂ O ₃ -MgO.	86.96	87.84	~1.1	[86]
Sr promoted Ni+Co (5% each) on γ-Al ₂ O ₃	500-700 °C, Fr = 1:1, 1 atm, F/W= 60 mL/min g _{cat}	IMP	Varied between 5.8-9.1 wt% for Sr promoted catalysts	On doping the bimetallic catalyst with Sr resulted in reduced activity but boosted stability. Utmost stability obtained by 5Ni5CoSr0.75 catalyst with least carbon deposition.	84.9	82.3	N.R.	[116]
Ni-Co/MgO over monoliths	600-800 °C, Fr =1:1, GHSV= 42000 and 84000 mlgcat ¹ h ⁻¹	IWI	41 wt% to 13.3 wt% in absence and presence of 3% O ₂	Ni (8wt%) – Co (2wt.%)/MgO catalyst showed elevated activity, stability, reduced coke formation (at 3% O ₂ feed) at 750°C.	83	89	0.95	[93]

Table 2.2. (Continued)

Catalyst Used	Reaction Conditions	Preparation method	Coke deposition	Major finding/Conclusions	Conversion (%)		H ₂ :CO	References
					CH ₄	CO ₂		
Ir on Al ₂ O ₃ doped with (Na, K) and (Ba, Ca and Mg).	750 °C, Fr = 1:1, flow rate = 20 mL min ⁻¹	IWI	N.R.	Long time dry reforming reactions showed that iridium catalysts have elevated sintering resistance. Ir(1%)/Al ₂ O ₃ -Mg(10%) showed finest performance.	81.2	93.5	0.75	[85]
Ni-based on Al ₂ O ₃ -CeO ₂ , Mo (monometallic), Fe-Mo, Pt-Mo (bimetallic) and Pt-Fe-Mo (trimetallic)	550°C -700°C, GHSV=12,000 mLg _{cat} ⁻¹ h ⁻¹	IWI	N.R.	Performance of Ni/Al ₂ O ₃ -CeO ₂ catalyst enhanced extensively on adding Pt. Fe and Mo metals. The utmost conversions of CH ₄ and CO ₂ , highest stability with coke resistance, elevated selectivity regarding H ₂ /CO ratio has been observed over Pt/Fe-Mo/Ni/Al ₂ O ₃ -CeO ₂ trimetallic catalyst.	>80%	85%	0.79-0.91	[117]
Ce (III) promoted Pt, Pd, Ni/MgO trimetallic	700°C-900°C, Fr = 1:1 and 2:1, GHSV = 30ml min ⁻¹ , 1 atm,	CP	2.4 wt%	Pt, Pd, Ni/MgO (trimetallic) catalyst gave very effective conversions for DRM at 900°C, little coke formation. Doping with Ce ₂ O ₃ further improved stability of the MgO cubic phase; enhanced its thermal stability, elevated basicity of support, reduced coke formation, and decreased reducibility of Ni ²⁺ , Pd ²⁺ , and Pt ²⁺ ions.	80	99	~1.1	[118]
Co-Ni alloy on CeO ₂	600-850°C, Fr = 0.3:0.3, 1 atm, flow rate = 100 mL min ⁻¹	IWI, CIMP	N.R.	Co:Ni of 0.8 supported over CeO ₂ showed highest activity and stability at 800°C with least coke formation even after 10 h.	80	85	0.72-0.80	[92]
Pt (0.2-0.5%) promoted Ni/(10%)/Al ₂ O ₃	750°C, Fr =1:1, 1 atm	ESIMP	N.R.	It has been noticed that 0.5% Pt doped catalyst exhibited superior performance and durability with reduced coke formation comparatively.	~79	~97	~0.63	[119]

Table 2.2. (Continued)

Catalyst Used	Reaction Conditions	Preparation method	Coke deposition	Major finding/Conclusions	Conversion (%)		H ₂ :CO	References
					CH ₄	CO ₂		
Ni–Mo ₂ C (varying Ni:Mo molar ratios)	500°C, Fr =1:1, W/F = 0.3 gscm ⁻³	AQC	N.R.	During DRM Ni–Mo ₂ C (1:1) got deactivated owing to carbon deposition and Ni–Mo ₂ C (1:3) because of Mo ₂ C bulk oxidation. Therefore 1:2 molar ratio of Ni/Mo, oxidation–reduction cycle was deduced showing it as a typical stable bi-functional catalyst.	~80	~90	~0.5	[98]
Ni/Al ₂ O ₃ , Ni-Co/Al ₂ O ₃ and Ni–Co/Al ₂ O ₃ –MgO	800°C, Fr = 1, 1 atm	SG	N.R.	Superior performance has been reported by CAT-3 in terms of better SMSI, coke resistance and durability for DRM.	~78	~87	~0.9	[120]
Ni/Al ₂ O ₃ promoted with (3 wt.%) MgO, CaO, and BaO	700°C Fr from 1:2 to 4:1, GHSV = 12,000(ml/h gcat).	IMP	N.R.	Doping with MgO, CaO, and BaO reduced SBET but enhanced the catalytic activity. MgO showed highest activity by making it easy for Ni to get reduced and also reduced reduction temperature.	~76	~78	~0.91	[24]
Ni/ZrO ₂ doped with (Ce, La, Sm and Y)	700°C, Fr =1:1, GHSV= 24000 mlgcat ⁻¹ h ⁻¹	IMP	N.R.	Improved CH ₄ dissociations and CO ₂ activation was observed with promoted catalysts with more coke deposition at temperatures below 700°C.	38-74	45-79	0.66-0.96	[81]
Ni/SiO ₂ and Ni ₁₇ W ₃ /SiO ₂ (Ni=10.7wt%, W=5.7 wt%)	800 °C, F/W = 96,000 ml/g·h, 800 °C, 1atm	IMP	N.R.	Tungsten enriched catalyst showed superior performance and durability then mono-metallic Ni catalyst because α-WC is formed, which is very stable alloy.	60-70	69-75	N.R.	[96]
TiN promoted Ni-based SBA-15	700 °C, Fr = 1:1, 1atm	HTH	N.R.	Merging Ni/SBA-15catalyst with TiN resulted in enhanced activity of catalyst and resistance against coke formation due to increase in basic sites. 10Ni/5TiN-SBA-15 showed appreciable stability for over 12 h.	~66	~71	0.8	[84]

Table 2.2. (Continued)

Catalyst Used	Reaction Conditions	Preparation method	Coke deposition	Major finding/Conclusions	Conversion (%)		H ₂ :CO	References
					CH ₄	CO ₂		
Ni–Ce/MgAl ₂ O ₄	F _b = 1:0.8:0.4, GHSV of 530,000 ml/h-gcat, 600°C to 650°C	CIMP	8.0% at Ce/Ni=0.25	In CSCRM enriched dispersion of metal, outstanding reducibility, superior coke hindrance and prolonged activity has been obtained by Ni–Ce/MgAl ₂ O ₄ .	Max.~66	Max.~35	~2.5	[97]
La and Ca promoted Ni/ZL(A) and Ni/ZL (B)	700°C, Fr = 1:1, 1 atm, Flow rate=40 ml/min.	IWI	N.R.	The ZL-B support showed superior results with both Ni and Ca doped Ni catalysts (with boosted CH ₄ conversion and elevated endurance) when compared to ZL-A support.	Max. 60	Max. 65	N.R.	[90]
MNC Ni-M-Al ₂ O ₃ * (M =CeO ₂ , La ₂ O ₃ , and ZrO ₂)	600 °C, Fr = 1, 1 atm	USCP	N.R.	Zirconia and lanthanum (5 wt%) proved out to be favorable whereas ceria was unfavorable for surface area of catalyst. Promoted catalyst displayed lower coke deposition, decreased activity unlike the Ce promoted catalyst.	52-55	74-77	~0.75	[94]
Na-doped Ni/ZrO ₂ and Ni/ZrO ₂	600 °C, Fr = 70:30	IWI	(2.08 wt% for Ni/ZrO ₂ , 0.11 wt% for Na-Ni/ZrO ₂)	Na-promoted Ni/ZrO ₂ showed significantly higher activity, stability, WGSR promotion and SMSI.	~15	~50	0.71-0.78	[88]
(0-2.8 wt%) Pt promoted Ni (5 wt%) / γ -Al ₂ O ₃	575-625 °C , Fr =1:1, GHSV from 33,000-49,500 h ⁻¹ , 1atm	DIED	3.54-7.21(mmol C/g _{cat})	Ni rich alloy formed by electroless deposition showed a maximum activity for Pt loading on Ni. An interactive outcome on E _A is observed at 525–600 °C for methane conversion. Although, at elevated temperature (700 °C) nano-particulate alloy phases gets dispersed.	Max.12	N.R.	~ 0.3-0.5	[80]

Table 2.2. (Continued)

Catalyst Used	Reaction Conditions	Preparation method	Coke deposition	Major finding/Conclusions	Conversion (%)		H ₂ :CO	References
					CH ₄	CO ₂		
Trimetallic Catalysts								
LaNi _{0.34} Co _{0.33} Mn _{0.33} O ₃	800 °C, Fr =1:1.05, nearly 1 atm	MWP	N.R.	Co improved the reaction rate whereas an SMSI was facilitated by MnO due to a synergistic effect of the tri-metals. Also, considerably elevated activity and stability has been observed with small carbon deposition for trimetallic catalyst in DRM.	Max~94	Max~92	~1.15-1.2	[121]
NiCoMn/ZrO ₂ doped with Ce, La, Ca, K	800 °C, Fr = 1:0.8, 1atm	CP	Lowest for Ni–Co–Mn–Ce–ZrO catalyst, Highest for Ni–Co–Mn–ZrO =13.78wt%	Doped tri-metallic (Ni-Co-Mn) catalyst noticeably improved conversions (of CH ₄ and CO ₂) and selectivity to H ₂ and CO comparatively. Ce and La showed stable and elevated conversions. Doped catalysts showed enhanced activity, durability, and low coking. Ce doping resulted in best activity.	N.R.	~95.5 and 89.9%	N.R.	[122]
Ni-Co-Ru/ MgO-Al ₂ O ₃	800°C, Fr=1:1, 10-30 mLmin ⁻¹ , 1 atm	ASG, BSG, NSG and CP	N.R.	Ni-Co-Ru/MgO-Al ₂ O ₃ synthesized by NSG route displayed elevated and optimum stability and activity then the monometallic (Ni) catalyst with very less carbon formation.	~ 92	~ 93	~ 1	[123]
Ni-Au-Pt trimetallic catalyst supported on alumina and Alumina-X (X = ceria or magnesia)	400-800 °C, Fr: = 1:1, WHSV=60, 000 mLg ⁻¹ h ⁻¹	SG+IMP	19 wt. % for the Ni-Al sample and 9 mass% for Ni-Au-Pt-Al sample	The composite (bi and tri-metallic) catalysts proved out to be better than monometallic catalysts. Enrichment of Ni with minute amount of Au and Pt gave synergistic interaction, which easily reduces NiO species and enhance its stability, performance, and coke resistance at 750°C.	87.5-85	93-92	N.R.	[22]

Table 2.2. (Continued)

Catalyst Used	Reaction Conditions	Preparation method	Coke deposition	Major finding/Conclusions	Conversion (%)		H ₂ :CO	References
					CH ₄	CO ₂		
BaZr _{0.8649} Ru _{0.1351} O ₃ , CaZr _{0.91087} Ru _{0.08913} O ₃ and SrZr _{0.88729} Ru _{0.11271} O ₃	500-800 °C, Fr =1:1, GHSV= 35,800 h ⁻¹	MCAC	(0.0049, 0.028 and 0.0097) g _{coke} g _{catyst} ⁻¹ h ⁻¹ respectively	Catalysts synthetized by auto-combustion technique displayed advanced reducibility, better surface area, excellent thermal strains, and thus improved performance in DRM. SrZrRUO ₃ gave the finest performance as per long durability and conversion.	~ 70-75	~ 80	0.8-0.97	[124]

Note: Table 2.2 summarize the effect of catalyst support, promoters, bimetal and trimetal on the performance for DRM reaction.

*Fr is the molar ratio of the feeding reactants for DRM (CH₄: CO₂- mol/mol)

*F_b is the molar ratio of the feeding reactants for BRM (CH₄: CO₂: H₂O- mol/mol/mol)

*N.R is not reported

*MFI (Mesoporous fibrous)

*MCM (mesoporous silica)

*NP (Nanoparticles)

*MNC (Mesoporous nanocrystalline)

*MA- magnesia-alumina

*MZSC (microemulsion zeolite seed crystallization)

*SG (Sol Gel), SGC (Sol-gel citrate), ASG (Acidic sol-gel), BSG (Basic sol-gel), NSG (neutral sol-gel)

* MAME (microwave-assisted micro-emulsion)

*CP (Co-precipitation)

*IMP (Impregnation), CIPM (Co- Impregnation)

*ESIMP (excess-solution impregnation)

*IWI (incipient wetness impregnation)

*IWCIMP (incipient wetness co-impregnation)

*SM (Solution Method)

*MDS and IIMP (Modified direct synthesis and incipient impregnation)

*OPS (one- pot synthesis)

*DIED (Dry Impregnation and electroless deposition)

*MCAC (modified citrate and auto-combustion)

Table 2.2. (Continued)

- *NN (Ni nanoparticles with surface area: 55m²/g; particle size: 20 nm) by Loba Chemie, Mumbai, India).
- *ST (Soft template method)
- *HT (Hydrotalcite route)
- *EPG (epoxide- initiated gelation method)
- *HTH (hydrothermal method)
- *WCS (wet chemistry synthetic route)
- *MWP (microwave assisted Pechini method)
- *FOP (facile one-pot micelle method)
- *NPSN+IMP (Ni-phyllsilicate precursor route and SiO₂ nanospheres followed by impregnation method)
- *USCP (ultrasonic assisted co-precipitation method)
- *SFI (surfactant induced method)
- *CVD (chemical vapor deposition)
- *TAST (template-assisted solvo thermal method)
- *AQC (Aqueous solution followed by carburization)

2.7 Trimetallic catalyst

The synthesis of complex trimetallic catalysts was reported recently [22, 117, 125] to achieve surplus performance for ideal catalyst identification for DRM. In the last decade, various research evaluated the trimetallic catalysts which are summarized in Table 2.2 and the details as follows.

Recently, Aramouni NAK et al. [123] studied the Ni-Co-Ru trimetallic catalyst via different (acidic/basic/neutral sol-gel and co-precipitation) synthesis routes and compared their performances. They found that the trimetallic (Ni-Co-Ru) catalyst displayed elevated stability and activity then the monometallic (Ni) catalyst. It has also been reported that the catalyst support synthesized by neutral sol-gel route gave the optimum performance compared to other catalysts. This may be due to the fine pores size in case of catalyst synthesized by neutral sol-gel method which inhibited the thick whisker carbon formation on its surface.

Another trimetallic catalyst (Ni-based Pt-Fe-Mo) was synthesized by Jawad et al.[126] using incipient wetness impregnation technique and the catalytic performance of Ni/Al₂O₃-CeO₂ improved drastically on adding metals such as Pt, Fe and Mo. The best conversions of CH₄ with >80% and CO₂ approximately 85%, utmost stability and coke resistance, elevated selectivity concerning H₂/CO ratio were observed over Pt/Fe-Mo/Ni/Al₂O₃-CeO₂ trimetallic composite catalyst. The enhanced performance of this complex trimetallic catalyst is pertinent to an electronic amelioration of the surface Ni atoms due to FeO_x/Ni and MoO_x/Ni interactions.

Trimetallic LaNi_{0.34}Co_{0.33}Mn_{0.33}O₃ catalyst for better activity and stability from the perovskite LaNiO₃ was developed by Yong et al. [121] which is prone to acute coke formation microwave-assisted Pechini method. It was observed that on the introduction of Mn, the stability of the catalyst improved, and the addition of Co increased the reaction rate. A strong metal-support interaction was aided by MnO due to a synergistic effect of the tri-metals; high activity and stability with minute coke formation were observed at drastic conditions of DRM for the trimetallic catalyst.

Wu *et al.* [22] also synthesized bi and trimetallic (Ni, Au, Pt) catalysts supported on Al₂O₃ and Al₂O₃-MO_x (M = Ce or Mg) oxides by classical sol-gel technique for support preparation followed by impregnation of the active metal. It was noted that the composite (bi and tri-metallic) catalysts (Ni-Au, Ni-Pt, Ni-Au-Pt) showed better performance than monometallic catalysts. Introduction of a small amount of Au and Pt to Ni catalyst gave better

synergistic interactions, which easily reduced the NiO species and decreased the particle size thereby enhancing its stability, performance, and resistance against carbon formation.

Apart from classical sol-gel technique, co-precipitation method was used to synthesize Pt-Pd-Ni trimetallic catalyst supported on MgO and MgO-Ce₂O₃ Al-doghachi and Hin [118]. The findings indicated that Pt, Pd, Ni/MgO (trimetallic) catalyst resulted in very effective conversions with CO₂ equal to 99% and CH₄ of about 80% for DRM at 900 °C. Reduced coke formation was noted, and the catalyst showed impressive thermal stability due to SMSI between Ce₂O₃ and MgO. Furthermore, doping with Ce₂O₃ improved the stability of the MgO cubic phase and enhanced its thermal stability and basicity of support besides reducing the coke formation and decreasing the reducibility of Ni²⁺, Pd²⁺, and Pt²⁺ ions. Similar co-precipitation method was used by Bhavani et al. [122] to synthesize trimetallic NiCoMn/ZrO₂ catalyst doped with alkaline and rare earth metals (Ce, La, Ca, K). The findings showed that doped NiCoMn/ZrO₂ catalyst exhibited improved conversions of CH₄ and CO₂ and enhanced selectivity to H₂ and CO. Besides that, doped catalysts also showed enhanced activity and better stability with negligible coke deposition; meanwhile, Ce-promoted Ni-Co-Mn/ZrO₂ catalyst displayed the highest activity with minute reduction in activity even after the reaction. This is due to increase in the number of very strong basic sites (53.14 μmol/g) on doping with alkaline earth metals as per the TPD analysis of catalyst. Rare earth metals such as Ce and La were comparatively more efficient than alkaline metals such as Ca and K. The promoters affected the catalyst in numerous ways i.e., increased the active sites, reduced the crystal size, and enhanced the metal dispersion as per the characterization results. Moreover, the reason quoted for the enhanced performance of this composite catalyst is the proposed reaction mechanisms on the catalytic surface, i.e., firstly, the breakdown of CH₄ on the metallic surface and then decay of CO₂ at the interface of metal–support to yield CO. The catalytic activity relies greatly on CH₄ activation on metallic sites, that may be somewhat impeded by carbon. Another proposed correlation for DRM is the association between the catalytic activity and number of basic sites measured by CO₂-TPD. However, still the mechanism of auto-thermal reaction for supported composite catalysts (for example NiCoMn/ZrO₂) is still under debate.

Hence for trimetallic catalyst it may be inferred that the properties such as dispersion of metals, oxygen vacancies and transportability within the catalyst, resistance to coke formation and morphology can be enhanced to a large extent by appropriate selection of metals that will fit

in the crystal lattice of the catalyst to improve its overall stability. However, still the knowledge of reaction mechanism pertinent to composite catalyst system is necessary.

2.8 Study of spent catalysts

The study of spent catalyst is of vital importance because it provides the evidence and better insight into the reaction mechanism [110, 127]. The investigation of spent catalyst also draws curtains and provides the information of the amount and type of carbon formed during the DRM reaction [128–130]. This helps in inference of a better catalyst and hence its desirability. Several studies independently proposed that apart from the amount of carbon formed, the type of carbon plays a key role in the prolonged activity of catalyst [100, 107, 108]. The type and amount of carbon formed during the reaction can be easily characterized via SEM, TEM, TPO and RAMAN analysis [109, 131]. Thereby, categorizing it into amorphous, filamentous, graphitic, carbon nanosheets, carbon nanotubes (CNTs), multiwalled carbon nanotubes (MWCNTs) [106], [132]. For an instance, recently Dou et al. [133], sandwiched $\text{SiO}_2@\text{Ni}@\text{ZrO}_2$ and $\text{SiO}_2@\text{Ni}$ catalyst by wet chemistry synthetic route was used and tested for DRM.

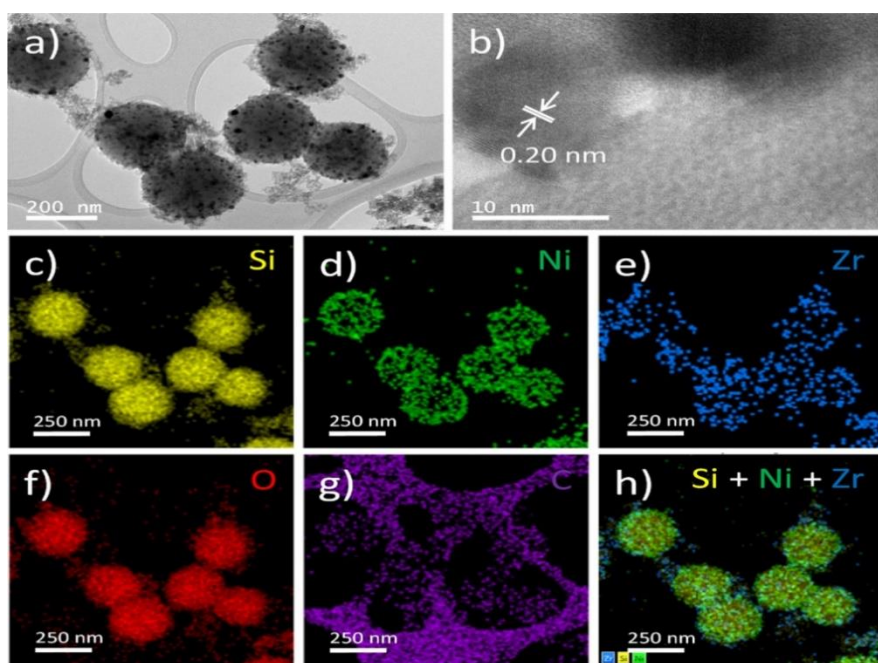


Figure 2.2. (a, b) TEM images and (c–h) EDX mapping of spent $\text{SiO}_2@\text{Ni}@\text{ZrO}_2$ catalyst after dry reforming reaction [133].

The spent catalyst characterized by transmission electron microscopy (TEM) to examine carbon deposition has been shown in Figure 2.2. The dispersion of Ni nanoparticles along with

the different other existing elements and carbon (Figure 2.2 (g)) can be seen clearly in the elemental mapping of the spent catalyst.

The type of carbon formed also depends on the morphology and hence the preparation technique of the catalyst [113, 134]. Recently, Bagheri-mohagheghi [135], and Jeong et al. [136] independently stated that the method of catalyst synthesis plays a decisive role in the structural characteristics and performance of catalyst. It has been concluded by recent investigations that the type of carbon formation greatly influences catalytic performance. If the coke formed during the DRM reaction is of the form of amorphous and carbon nanosheets, they will shroud the active sites of the catalyst [73]. This will result in the lower activity and hence the degraded performance of the catalyst. However, if the coke formed is of CNTs and MWCNTs type, the catalyst will remain active for extended duration of time [137, 138]. This is due to the fact that CNTs/MWCNTs does not stick to the catalyst surface, but grow on the catalyst surface either by tip of base growth mechanism [139]. Further, it has also been investigated and inferred by Q. Ma et al. [140] that the site position of active metal in the CNTs also influence the performance of the catalyst (cf. Figure 2.3).

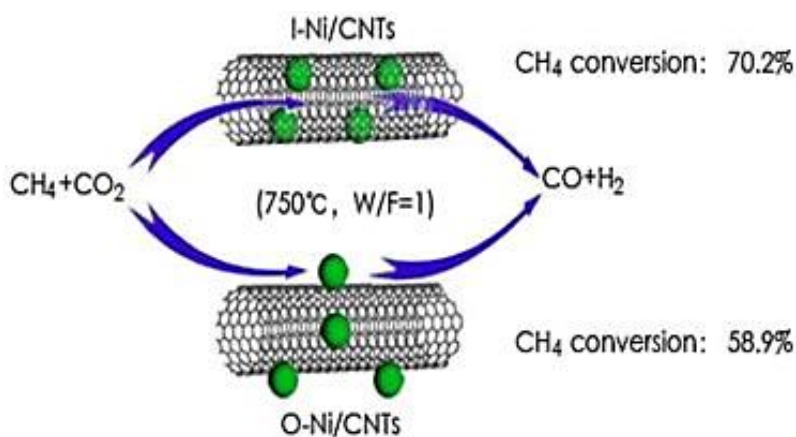


Figure 2.3. The pictorial illustration of effect of position of active metal (Ni) on the performance of catalyst [140].

The life of the catalyst in DRM process depends on the operating conditions such as reaction temperature, feed gas ratio, composition, or percentage doping of the active metal in the catalyst. The deactivation of catalyst can be due to thermal degradation resulting in sintering or by coking. Hence it is tough to predict life period of a catalyst. However it has been studied that the phenomenon of coking occurs due to Boudouard reaction, which takes place at lower ranges of

temperature Jang et al. [68]. The carbon formed owing to methane decomposition blocks the active sites of the catalyst Ochoa et al. [141].

2.9 Optimization study using Response Surface Methodology

Apart from catalyst's physicochemical properties, the operating parameters i.e., reaction temperature and the reactants partial pressure are the key factors, that needs to be considered for the optimum performance and durability of the catalyst during DRM [142]. A few studies reported the conventional practice of optimization by varying one variable at a time while keeping others as constant. However, this approach is time-consuming and does not consider the interaction between the studied variables. Hence, it is unable to reach the true optimum. Therefore, Response surface methodology (RSM) is employed for efficient and simple optimization with a fewer number of experiments. RSM is a very convenient statistical analysis tool developed by Box and Wilson in 1951, employed for process optimization and design of experiments (DOE) [143]. The tool is useful in relating various independent input variables with one or more responses [144]. Several RSM analysis have been carried out by different researchers for optimization study of DRM. However, many disparities in results have been reported, which could be due to the different behavior, mechanism and side reactions taking place with different catalysts [145].

The RSM interface requires a set of experimental data as input and response variables to generate the three-dimensional (3-D) plots using the generated polynomial equation from DOE. The DOE obtained by RSM is advantageous since it significantly reduces the experimental time, operation cost and increases the process efficiency [146, 147]. RSM has several interface tools such as central composite design (CCD), Box-Behnken design (BBD), Boehlert Matrix design (BMD), and Plackett Burman design (PBD) which can be used for process optimization purposes. The various optimization studies conducted by researchers for DRM has been summarized in Table 2.3. The effect of various input process parameters i.e., reaction temperature and feed ratio (CH_4 : CO_2) and GHSV on the conversion of CH_4 , CO_2 and syngas (H_2 : CO) ratio, have been investigated using RSM. However, CCD has been extensively used for DRM applications due to its better fit with quadratic models and two input variable [148]. Further, the significance of CCD is its capability of processing a reduced number of experiments and to forecasting both the quadratic and linear parameters interaction [149, 150].

Table 2.3: Summary of literature on optimization of syngas production from catalytic reforming of CH₄ and CO₂ using RSM.

Optimization Approach (RSM)	Catalyst	Factors	Responses	Optimum Conditions		
				Factors	Responses	Reference
CCD	Ni/SiO ₂	Temp. (600 °C-800°C), CH ₄ : CO ₂ (0.25-4)	Conversions (%CH ₄ and %CO ₂), H ₂ :CO, Carbon content	Temp = 800°C, CH ₄ : CO ₂ = 2.125	%CH ₄ conv.= 79.6, %CO ₂ conv.= 84.2, H ₂ :CO=0.4, Carbon content =51.1 gm	[151]
CCD	Ni-Co/MgO-ZrO ₂	Temp. (700 °C-800°C), CH ₄ : CO ₂ (1-5), GHSV (8,400-200,000), O ₂ concentration (3-8)	Conversion (%CH ₄) and H ₂ yield (%)	Temp = 749°C, CH ₄ : CO ₂ = 0.33, O ₂ conc. = 7 mol%	%CH ₄ conv.= 88 H ₂ yield (%) = 86	[152]
CCD	Ni-Co/MSN	Temp. (700 °C-800°C), CH ₄ : CO ₂ (1-5), GHSV (10,000-60,000 mL g ⁻¹ h ⁻¹)	Conversion (%CH ₄)	Temp = 783°C, CH ₄ : CO ₂ = 3, GHSV= 38,726 mL g ⁻¹ h ⁻¹	%CH ₄ conv.= 79.6	[153]
CCD	Ni-La@KCC-1	Temp. (680°C-820°C), CO ₂ :CH ₄ (0.5-4.5), GHSV (5000-55000 mLg ⁻¹ h ⁻¹)	Conversions (%CH ₄), CO ₂ :CH ₄ , GHSV	Temp = 810°C, CO ₂ : CH ₄ =1, GHSV= 35,500 mL g ⁻¹ h ⁻¹	%CH ₄ conv.= 96.46,	[154]
CCD	15%Ni / CaFe ₂ O ₄	Temp. (700 °C-800°C), CH ₄ : CO ₂ (1-5), GHSV (8,400-200,000)	Conversions (%CH ₄ and %CO ₂), H ₂ and CO yield (%)	Temp = 832.45°C, CH ₄ : CO ₂ = 0.96, GHSV=35,000 mL g ⁻¹ h ⁻¹	%CH ₄ conv. = 85, %CO ₂ conv. =88, H ₂ yield (%) = 75.76, CO yield (%) = 77.82	[49]
BBD	Co/Sm ₂ O ₃	Partial pressures (CH ₄ and CO ₂ from 10-50), Temp. (650 °C-750°C)	H ₂ and CO yield (%)	Partial pressures (CH ₄ = 47.9kPa, CO ₂ =48.9kPa), Temp = 735°C	H ₂ yield (%) = 79.4, CO yield (%) = 79.0	[155]
BBD	Co/CeO ₂	Partial pressures (CH ₄ from 10-50), Temp. (650 °C-750°C), CH ₄ : CO ₂ (0.4-1)	Conversions (%CH ₄ and %CO ₂), H ₂ :CO	Partial pressures (CH ₄ = 46.85kPa), Temp = 727°C, CH ₄ : CO ₂ =0.6	%CH ₄ conv.= 74.85, %CO ₂ conv.= 76.49, H ₂ :CO=0.97	[156]
BBD	Co/α-Al ₂ O ₃	Partial pressures (CH ₄ and CO ₂ 10-50), Temp. (650 °C-750°C)	H ₂ yield (%)	Partial pressures (CH ₄ = 50 kPa, CO ₂ =32 kPa), 750°C	H ₂ yield (%) = 71.38	[157]

2.10 Reaction Kinetics of dry reforming of methane

Kinetic studies for reforming of CH₄ were performed to acquire an appropriate reaction rate, as this is the main area of concern for both industries and academia. It can be an experimental or theoretical based mechanism of the reaction, whichever that is consistent with the corresponding experimental statistics for curve fitting and depicts the reaction rate of the process Wang and Lua [158]. Since the last decade, SRM has attracted a lot of consideration regarding mechanistic studies. Nevertheless, when DRM was introduced as the potential green alternative for both GHG's reduction and syngas production, numerous studies were carried out for DRM kinetics and mechanistic which are essential to optimize DRM process, reactor, and catalyst design.

Generally, power-law of model was used for estimating the initial guesses about activation energy, rate constant and order of the reaction (see eqn. 2.9). However, this model was unable to signify the overall kinetics of the reaction since it does not consider all the elementary steps involved in the reaction Kathiraser et al. [65]. The main advantage of this model is its easier execution in methane reforming reaction. To get a better insight of all the mechanistic steps or elementary reaction involved in the reaction, various rigorous models such as Langmuir-Hinshelwood (LH) and Eley-Rideal models (i.e., ERI and ERII) were applied in the literature.

Initial studies performed by Zhang and Verykios [159] for understanding the kinetics of nickel-based catalysts for DRM. They computed the apparent activation energy for nickel-based catalysts supported on Al₂O₃, CaO and Al₂O₃/CaO. The results revealed that the apparent activation energy of Al₂O₃ supported nickel catalyst was 72.7 kJ mol⁻¹ and considerably decreased to 35.0 kJ mol⁻¹ for Ni/ Al₂O₃/CaO catalyst, owing to the better dispersion and high reducibility. Moreover, LH was also applied by considering the effect of basicity of CaO and methane cracking as the rate-determining step (see eqn. 2.9). The model reasonably fitted to the data, this study did not provide kinetic parameters and adsorption values.

$$R = \frac{aP_{CH_4}P_{CO_2}^2}{(P_{CO_2} + bP_{CO_2}^2 + cP_{CH_4})^2} \quad (2.9)$$

Similarly, Mark et al. [160] performed kinetics over Ir/Al₂O₃ catalyst and applied various rate models by fitting the data to the experimental data. They proposed that during dissociative adsorption of methane, the rate-determining step is the methane decomposition at the surface of Ir/Al₂O₃ catalyst to hydrogen and carbon. Whereas the carbon when combine with CO₂ gets

converted to 2CO by fast conversion. The rate equations were formulated according to the LH and Eley-Rideal models (see eqns. 2.10 – 2.14).

The catalytic dry reforming reaction basically proceeds in three main steps, mainly adsorption, formation of educts and finally desorption. In the first step the reactant gases (i.e., mainly CH₄ and CO₂) get chemisorbed on the catalyst's surface. The second step proceeds with the formation of educts or intermediate species at the catalyst surface. Finally, the educts form the product (i.e., CO and H₂) that gets desorbed from the catalyst's surface. The ER I and ERII models (eqns 2.13-2.14) provides a comparatively better approach of reaction mechanism compared to the PL model. The Eley-Rideal models (i.e., ERI and ERII) assumes that one of the reactant gases (CH₄ in case of ERI and CO₂ in case of ERII) gets adsorbed on the surface of the catalyst. Whereas another gas does not get adsorbed and remains in the gaseous phase. The adsorbed gas then forms educt which reacts with the free gas present in its vicinity. Finally, the product gases are desorbed from the catalyst's surface. On the other hand, the LH model (eqn. 2.14) gives the most realistic approach for the reaction mechanism and hence most applicable for DRM reactions. The LH model assumes that in the first step, both the gases get adsorbed on the surface of the catalyst. In the second step, both the adsorbed species forms educts, which finally forms products and gets desorbed from the surface of the catalyst. The LH model gives the best fit between the experimental and predicted reaction rates.

Basic Reaction:



Power Law (PL):

$$R = k[\text{P}_{\text{CH}_4}]^m[\text{P}_{\text{CO}_2}]^n \quad (2.11)$$

Eley Rideal I (ERI):

$$R = \frac{k \cdot K_{\text{CO}_2} \cdot \text{P}_{\text{CH}_4} \cdot \text{P}_{\text{CO}_2}}{1 + K_{\text{CO}_2} \cdot \text{P}_{\text{CO}_2}} \quad (2.12)$$

Eley Rideal II (ERII):

$$R = \frac{k \cdot K_{\text{CH}_4} \cdot \text{P}_{\text{CH}_4} \cdot \text{P}_{\text{CO}_2}}{1 + K_{\text{CH}_4} \cdot \text{P}_{\text{CH}_4}} \quad (2.13)$$

Langmuir-Hinshelwood (LH):

$$R = \frac{k \cdot K_{\text{CH}_4} \cdot K_{\text{CO}_2} \cdot \text{P}_{\text{CH}_4} \cdot \text{P}_{\text{CO}_2}}{(1 + K_{\text{CH}_4} \cdot \text{P}_{\text{CH}_4} + K_{\text{CO}_2} \cdot \text{P}_{\text{CO}_2})^2} \quad (2.14)$$

Numerous other studies using various Ni-based catalysts have shown different activation energy values of carbon dioxide and methane in DRM which indicated that CH₄ molecules are much more stable than CO₂ due to its steady tetrahedral structure and hence resulted in higher activation energy than CO₂ Nagaoka et al. [161]. Furthermore, Kathiraser et al. [65] studied and demonstrated that basicity of catalyst support, bimetallic interactions and promoters have a great influence on the activation energy barrier of the DRM. The summary of the kinetic studies carried out recently with major outcomes is shown in Table 2.4.

Recently, Cheng et al. [130] performed a mechanistic study using an in-situ IR adsorbed CH₄, CO₂ and CO₂+CH₄ for DRM. The findings confirmed that DRM reaction occurred at 300°C by the formation of transition species which are unidentate and bidentate carbonate through the pathway of CO₂ dissociation and CO₂ adsorption reactions. The intended mechanism of syngas production by DRM using the 10Ni/DFSBA-15 catalyst is displayed in Figure 2.4. DRM activity was instigated by adsorption of the feed gases which are CH₄ and CO₂ against Ni/DFSBA-15 surface. CO₂ gets dissociated into CO and O against the oxygen vacant positions of Ni/DFSBA-15. Simultaneously, the CH₄ also gets dissociated over the active Ni metal site to form CH_x and H groups. The H₂ and CO gases were produced by the contact of transition species with CH₄ molecules. The catalyst exhibited good regeneration abilities with very insignificant catalyst deactivation.

Table 2.4. Recent kinetic studies and their key outcomes for DRM reaction.

Catalyst	Reactor Type	Modeling Method	Key findings	Reference
Ni/DFSBA-15	Continuous tubular stainless steel (ID=11 mm)	Quadratic Model	The mechanism study proved that the transition species (unidentate and bidentate) are formed by dissociative and adsorption process of CO ₂ . The FTIR analysis also verified it. Further, syngas was formed when the transition species interact with methane during the DRM reaction at 300°C.	[130]
Pt	N.R.	DFT	Kinetics results concluded that CH dissociative adsorption on Pt (1 1 1) surface is the rate-controlling step; and the principal reaction follows route (C) for CH oxidation.	[162]
Ni-Fe-MgO	Fixed-bed quartz reactor (ID=10 mm)	Kinetic modeling (Arrhenius plot and modified Wigner-Polanyi equation)	Kinetic results revealed that Fe slow down the degree of CH ₄ split-up, which is the regulatory step for the reaction. Elevated oxygen concentration was observed over Ni-Fe alloy catalysts with greater Fe loadings, slightly intensifying slight surface oxygen. Furthermore, the gasification of surface carbon was observed by gas phase CO ₂ kinetically.	[163]
Ni	Fixed bed plug flow reactor	DFT	Kinetic study result showed that the successive dissociation of CH ₄ succeeded by oxidation of carbon by atomic O ₂ is the governing pathway for reaction. Also, at low concentration of CH ₄ and CO ₂ , the overall reaction rate will be governed by dissociative adsorption of CH ₄ and oxidation of carbon, whereas at elevated pressures oxidation of C is proposed as the rate governing step for DRM.	[164]
Pt–Ni	Fixed bed down-flow tubular quartz reactor	Kinetic modeling (power-law rate expression)	Results showed that elevated Ni:Pt loading ratio inhibited CO and CO ₂ consumption dominated on the catalyst. Whereas at low Ni:Pt loading ratio feeble CH ₄ adsorption is noticed and CO limiting effect is almost diminished.	[165]

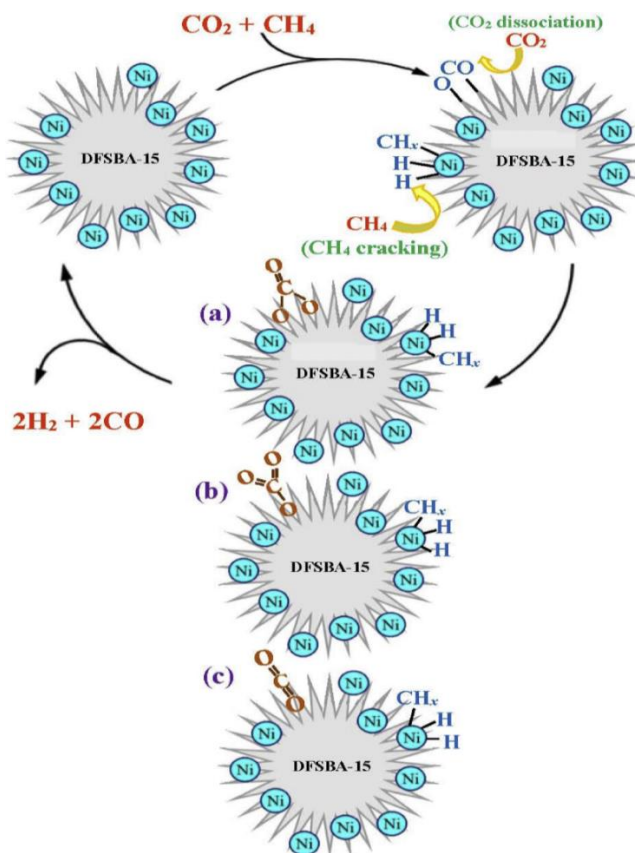
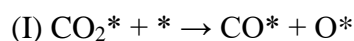


Figure 2.4. Reaction scheme of Ni/DFSBA-15 over DRM. (a) bidentate carbonate, (b) unidentate carbonate, (c) linear carbonyl [130].

Niu *et al.* [162] worked on density functional theory analysis (DFT) using a micro-kinetic model to compute the reaction mechanism of Pt catalyst for DRM. The energies of adsorption for the reactants, products, intermediates a in the DRM process are computed over the Pt (1 1 1) surface. For CO_2 activation method, three viable reaction pathways were studied for CO_2 decomposition as shown in Figure 2.5:



The path I require activation hindrance of 1.809 eV and the forward reaction is strongly endothermic). Furthermore, the kinetic results showed that the process is resilient to proceed on Pt (1 1 1) surface. Meanwhile, path II is a simple step which can be carried out with the lower activation barrier of 0.746 eV. Path III compels an elevated activation barrier hence highly

endothermic, which leads to the minimal forward rate constant. Hence it has been concluded that Path II is the dominant reaction pathway in CO₂ activation.

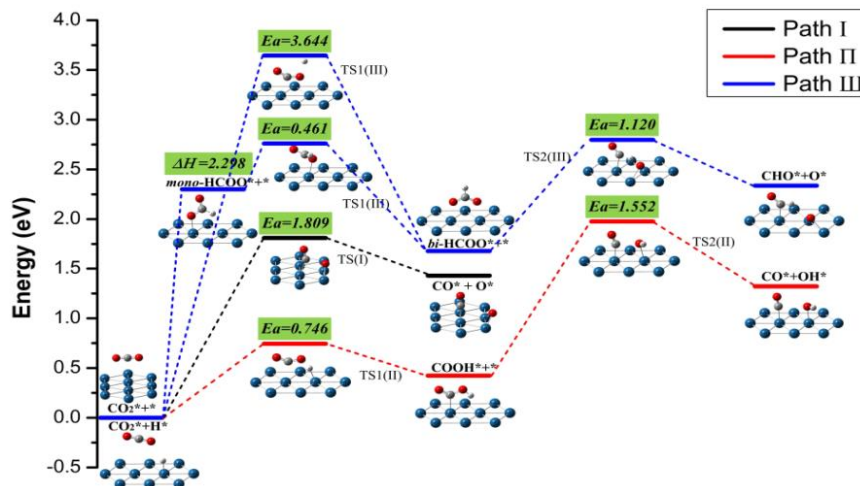


Figure 2.5. Energy pathways and profiles for the three different pathways in CO₂ activation: (I) CO₂* + * → CO* + O*; (II) CO₂* + H* → COOH* + * → CO* + OH*; (III) CO₂* + H* → mono-HCOO* + * → bi-HCOO* + * [CO₂* + H* → bi-HCOO* + *] → CHO* + O* [162].

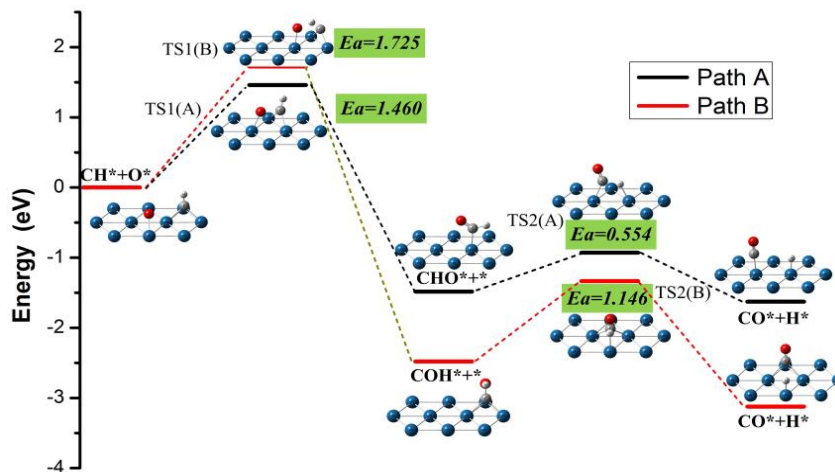


Figure 2.6. Energy profiles for the two pathways in CH oxidation by O: (A) CH* + O* → CHO* + * → CO* + H*; (B) CH* + O* → COH* + * → CO* + H [162].

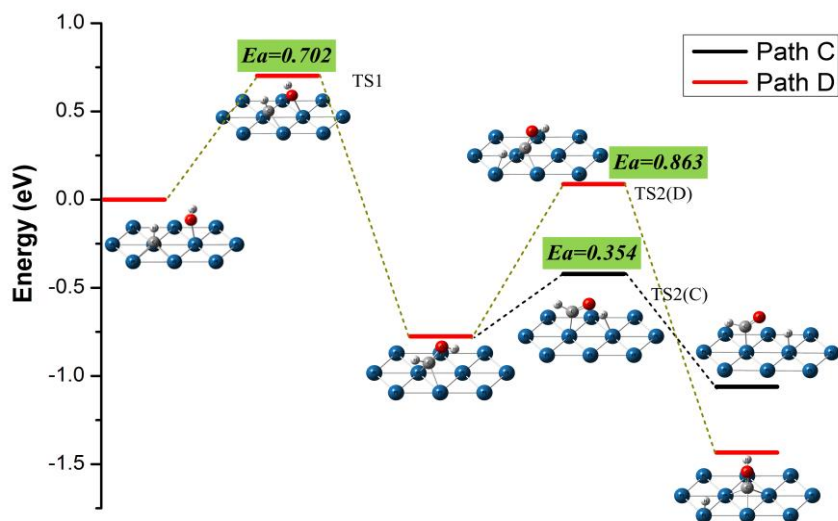


Figure 2.7. Energy profiles for the two different pathways in CH oxidation by OH: (C) $\text{CH}^* + \text{OH}^* \rightarrow \text{CHOH}^* + * \rightarrow \text{CHO}^* + \text{H}^*$; (D) $\text{CH}^* + \text{OH}^* \rightarrow \text{CHOH}^* + * \rightarrow \text{COH}^* + \text{H}$ [162].

The dissociative adsorption of CH on Pt (1 1 1) surface was found to be the rate-controlling step. CH group was present in a high amount on Pt (1 1 1) surface, which suggested that coke formation from dehydrogenation of CH_4 is difficult corresponding to the Pt (111) surface. The chief pathway for CH oxidation as shown in Figure 2.6 and Figure 2.7 can be summarized as: $\text{CH}^* + \text{OH}^* \rightarrow \text{CHOH}^* + * \rightarrow \text{CHO}^* + \text{H}^* \rightarrow \text{CO}^* + 2\text{H}^*$. It was also deduced that Ni catalysts can be improved by introducing novel metals like platinum (Pt) to increase its resistive ability to avoid deactivation in industrial production processes.

According to T. Zhang et al. [163], for MgO supported Fe-Ni alloy catalyst, the addition of Fe reduced the activity of Ni metal surface while increasing the coke resistant property, enhanced durability and enriched surface coke gasification. Its kinetics showed that Fe slows down the rate of CH_4 dissociation, which is the rate-controlling step for coke deposition and reforming reaction, thereby slowing down the formation of coke and deactivation of the catalyst surface. Alternatively, Fan et al. [164] developed a thorough micro-kinetic model centered on DFT calculations to find new horizons of reaction mechanism in DRM for Ni catalyst. The principal pathway was found to be the consecutive methane dissociation followed by oxidation of carbon from atomic oxygen. This model also showed that at low partial pressures of CH_4 and CO_2 , both oxidation of carbon and dissociative adsorption of methane cooperatively dominated the whole rate of reaction, whereas, at higher pressure, oxidation of carbon is proposed as the rate-controlling step of reaction which was in contradiction with the general experimental results.

Aksoylu and Özkara [165] performed a comparative study on the kinetics of DRM over Pt–Ni supported on Al_2O_3 catalyst. The authors observed that power-law model rate expression attained for 0.3%Pt-10% Ni/ Al_2O_3 have reaction order of unity for CH_4 and 0.87 for CO_2 whereas for 0.2%Pt-15% Ni/ Al_2O_3 , reaction orders of 1.09 and 1.40 for CH_4 and CO_2 , respectively. An elevated Ni: Pt loading ratio was reported to inhibit CO and CO_2 consumption dominated on the catalyst, whereas at low Ni: Pt loading ratio weaker CH_4 adsorption was noticed and hence the consuming ability of CO_2 as the oxygen source increased and CO inhibition effect is almost eliminated.

2.11 Research Gap

DRM is a promising technique to convert these two GHG's (i.e., CO_2 and CH_4) into syngas with H_2 :CO ratio of unity. This syngas can be directly utilized in Fischer-Tropsch synthesis. However, still DRM is not commercialized due to several limitation in the process. The DRM process demands the use of catalyst due to its highly endothermic nature. The noble metal-based (i.e., Pt, Pd, Rh, Ir, Ru, and Au) catalysts cannot be commercialized due to its very high price, whereas the Ni-based catalysts which have shown the comparable activities have stability problem. The main problems associated with Ni-based catalysts is high coking and sintering. The coking blocks the active sites of the catalyst and deactivates it whereas due to sintering the morphology of catalyst gets ruptured. The catalyst stability depends on several factors such as MSI, durability of catalyst support at elevated temperatures, thermal stability of catalyst, surface area, and dispersion of active metal in the catalyst support. The Al_2O_3 support has a high surface area, but coke formation is its main limitation due to its acidic nature. The MgO has high coke resistance, due to formation of solid solution between Ni and MgO (as Ni–Mg–O). However, Ni/MgO has low activity then Ni/ Al_2O_3 , under the similar reaction conditions. Its (MgO) elevated thermal stability and high basicity is a promising feature that encourage researcher to use MgO into highly endothermic DMR reaction. The introduction of MgO as a support also helps in better Ni dispersion within the catalyst surface, which ultimately results in elevated activity and low deactivation of catalyst [166]. Hence a mixed oxide support (Al_2O_3 and MgO) is a promising approach. The method of catalyst synthesis also plays a key role on the performance and durability of the catalyst as per the studies of Bagheri-Mohagheghi et al. [135] and Jeong et al. [136]. The mixed bimetallic oxide support, with Al_2O_3 :MgO of 1:2 has shown the optimum performance as per the works of Zhu et al.[74]. To the best of author's knowledge, the analysis

for optimum Ni loading and the effect of tungsten (W) addition as bimetal on $\text{Al}_2\text{O}_3\text{-MgO}$ support employing the proposed methodology, has not yet investigated.

Hence in the present study a series of Ni loaded on $\text{Al}_2\text{O}_3\text{-MgO}$ catalysts are synthesized and characterized for screening of optimum Ni loading. The effect of W addition as bimetal was then investigated on optimum Ni loaded catalyst. Finally, the optimization of parameters for optimum the optimum Ni-W/ $\text{Al}_2\text{O}_3\text{-MgO}$ catalyst has been carried out using RSM; followed by micro kinetic modelling using the available kinetic models.

CHAPTER 3

MATERIALS AND METHODS

3.1 Chapter Overview

This chapter covers the description of materials used, the methodology adopted for catalyst synthesis, equipment involved, the characterization techniques used and the analysis of catalysts activity. Figures 3.1 display the research flowchart for different activities carried out along with optimization and kinetic study.

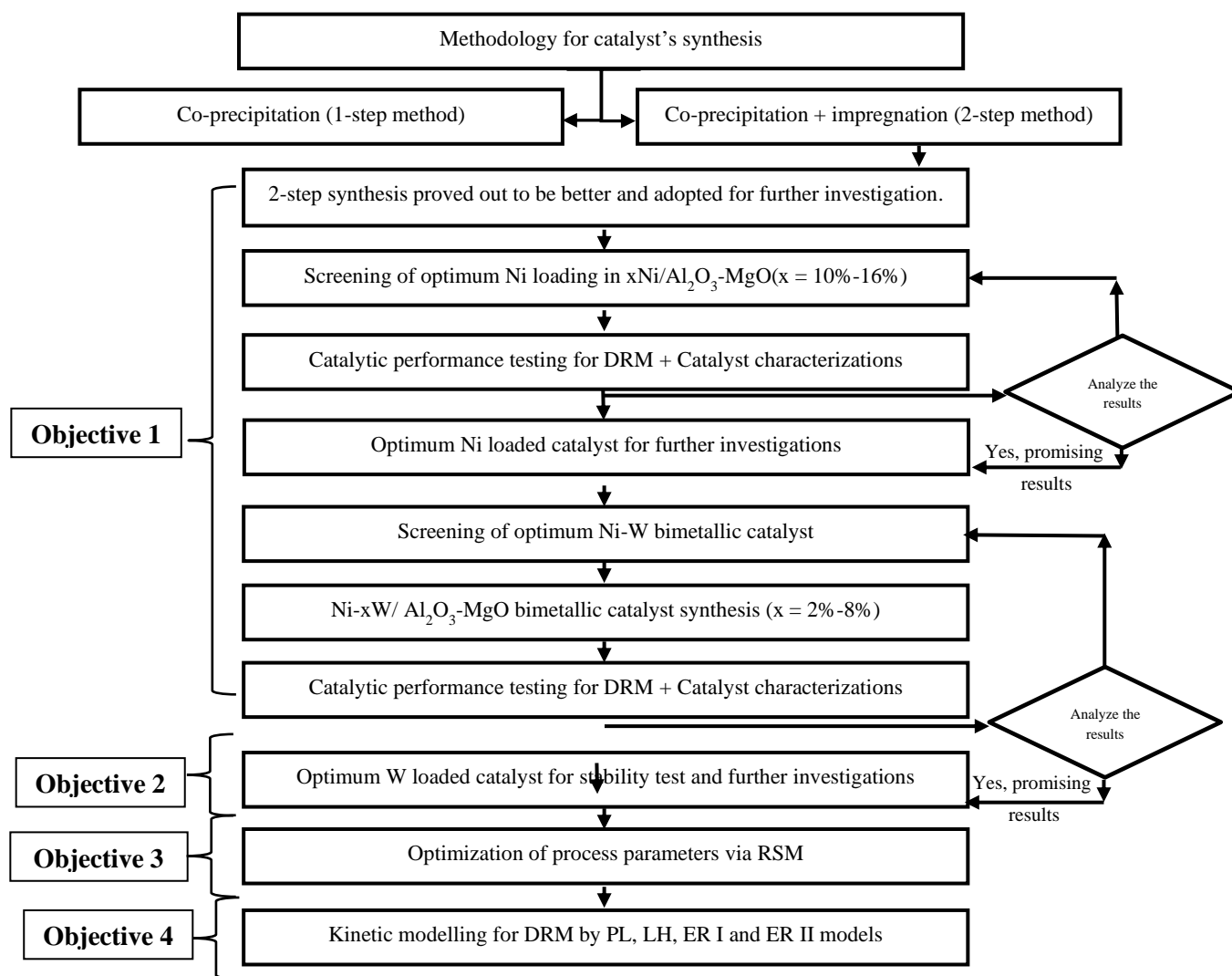


Figure 3.1. Research workflow for synthesis, characterization, and performance evaluation, optimization, and kinetic studies of catalysts.

3.2 Materials

The different precursor chemical salts were obtained from Sigma Aldrich for this research work. Nickel Nitrate Hexahydrate ($\text{Ni}(\text{NO}_3)_2 \cdot 6\text{H}_2\text{O}$), Ammonium Tungstate $((\text{NH}_4)_{10}(\text{H}_2\text{W}_{12}\text{O}_{42}) \cdot 4\text{H}_2\text{O})$, Magnesium Nitrate Hexahydrate ($\text{Mg}(\text{NO}_3)_2 \cdot 6\text{H}_2\text{O}$), Aluminum Nitrate Hexahydrate ($\text{Al}(\text{NO}_3)_3 \cdot 9\text{H}_2\text{O}$) were used as precursor salts for catalyst synthesis. The ammonia solution was also obtained from Sigma Aldrich to carry out the catalyst synthesis. The chemical salts and the gases used along with their purity has been displayed in Table 3.1.

Table 3.1. List of precursor salts used in the catalyst synthesis.

Chemical Name	Linear Formula	Uses	Supplier	Mass Fraction Purity
Nickel Nitrate Hexahydrate	$\text{Ni}(\text{NO}_3)_2 \cdot 6\text{H}_2\text{O}$	Impregnation of Ni metal in support	Sigma Aldrich	>99.9%
Ammonium Tungstate	$((\text{NH}_4)_{10}(\text{H}_2\text{W}_{12}\text{O}_{42}) \cdot 4\text{H}_2\text{O})$	Impregnation of W metal in support	Sigma Aldrich	>99.9%
Magnesium Nitrate Hexahydrate	$\text{Mg}(\text{NO}_3)_2 \cdot 6\text{H}_2\text{O}$	Provide MgO in support preparation via co-precipitation	Sigma Aldrich	>99%
Aluminium Nitrate Nonahydrate	$\text{Al}(\text{NO}_3)_3 \cdot 9\text{H}_2\text{O}$	Provide Al_2O_3 in support preparation via co-precipitation	Sigma Aldrich	>99%
Ammonia solution	NH_4OH	Maintain basic pH of solution during support preparation	Sigma Aldrich	28 wt%
Methane	CH_4	Reactant gas for DRM	Linde Malaysia	99.5%
Carbon dioxide	CO_2	Reactant gas for DRM	Linde Malaysia	99.99%
Hydrogen	H_2	Activates catalyst pre-DRM reaction and GC gas supply	Linde Malaysia	99.5%
Nitrogen	N_2	Purging Gas	Linde Malaysia	99.99%
Argon	Ar	GC gas supply	Linde Malaysia	99.99%
Helium	He	GC gas supply	Linde Malaysia	99.99%

3.3 Catalyst Preparation

The catalysts were prepared by employing the two-step synthesis method, i.e., co-precipitation followed by impregnation. The two-step synthesis technique proved out to be better than the single step (co-precipitation) method, in terms of catalytic performance and activity [44]. The mixed metal oxide alumina-magnesia ($\text{Al}_2\text{O}_3\text{-MgO}$) support with $\text{Al}_2\text{O}_3\text{:MgO}$ of 1:2 was prepared by co-precipitation method employing $\text{Al}(\text{NO}_3)_3 \cdot 9\text{H}_2\text{O}$ and $\text{Mg}(\text{NO}_3)_2 \cdot 6\text{H}_2\text{O}$ salts from Sigma Aldrich as precursor chemicals. The $\text{Al}_2\text{O}_3\text{:MgO}$ of 1:2 is used since it provided the most stable performance throughout the reaction as per our study and the investigations of Zhu et.al [45]. Stoichiometric quantity of precursor chemicals was dissolved in distilled water at constant stirring on a hot plate magnetic stirrer at a temperature of 80°C until a clear solution is obtained. Thereafter, ammonia solution (28 wt.% in water) is added dropwise to the mixture as a precipitating agent with constant stirring while maintaining the pH at about 9-9.5 throughout the stirring. The reaction mixture is aged for 10h with continuous stirring at 80°C . The precipitate formed is washed and filtered with distilled water. The slurry obtained was dried at 110°C for 12h and then calcined at 850°C for 4h in the furnace under static air (ramping rate of $5^\circ\text{C}/\text{min}$) [167, 168]. The calcination temperature for the catalyst is chosen as 850°C to avoid the weight loss of catalyst during the DRM reaction since the reaction is carried out at 800°C . The Further it has also been reported in a study by Al Fatesh et al. [167] that a catalyst calcined at highest temperature displayed highest conversion. Similarly in another study by Feng et al. [102] explained that the catalyst calcined at highest temperature showed stronger and more active sites for the adsorption of CO_2 and that the presence of surface H would promote the dissociation of CO_2 into CO. Also in a recent study by Bao et al. [169] the DRM catalyst has been calcined at 850°C for 4 hours, hence in the light of above available literatures the calcination temperature has been chosen for the catalyst preparation. The stoichiometric amounts of Ni ($\text{Ni}(\text{NO}_3)_2 \cdot 6\text{H}_2\text{O}$) salt was weighed and mixed with distilled water to the known weight of the support to obtain the different monometallic Ni catalysts. Similarly, stoichiometric amounts of Ni ($\text{Ni}(\text{NO}_3)_2 \cdot 6\text{H}_2\text{O}$) and W ($(\text{NH}_4)_{10}(\text{H}_2\text{W}_{12}\text{O}_{42}) \cdot 4\text{H}_2\text{O}$) salts were weighed and mixed with distilled water to the known weight of the support to obtain the different bimetallic Ni-W catalysts. The procedure is conducted by addition of water on the support until the first drop of water appeared on the surface of the support, which indicated that the catalyst support is saturated and cannot absorb water anymore. The mixture is aged for 6h under constant stirring at 80°C . The excess water is

then evaporated and dried at 110°C for 12h, and the catalyst is calcined at 850°C for 4h in static air. Hence, a series of differently Nickel loaded catalysts (i.e., 10 wt.% (Ni₁₀), 12 wt.% (Ni₁₂), 14 wt.% (Ni₁₄) and 16 wt.% (Ni₁₆)) were obtained. The 12 wt% Ni loaded catalyst has shown the optimum performance and hence used for further investigation for bimetallic catalysts. Thereafter, a series of catalysts having fixed Ni amount (i.e., 12wt%Ni/Al₂O₃-MgO) and varying W concentration (in wt%) has been prepared as 12%Ni/Al₂O₃-MgO, 12%Ni-2%W/Al₂O₃-MgO, 12%Ni-4%W/Al₂O₃-MgO, 12%Ni-6%W/Al₂O₃-MgO, and 12%Ni-8%W/Al₂O₃-MgO and named as Ni_f, W_a, W_b, W_c, and W_d, respectively. The corresponding spent catalysts are also named as Ni_{Sp}, W_{a,Sp}, W_{b,Sp}, W_{c,Sp}, and W_{d,Sp} respectively, and the catalyst support (i.e., Al₂O₃-MgO) as CS. The prepared Al₂O₃-MgO support and various impregnated catalysts has been arranged along with their preparation techniques and name coding in table 3.2.

Table 3.2. The synthesized catalysts along with their preparation method, and name coding.

S.No.	Catalysts	Preparation method	Codes
Screening for optimum Ni loading			
1.	Al ₂ O ₃ -MgO	CP	CS
2.	10%Ni/ Al ₂ O ₃ -MgO	CP + IMP	Ni ₁₀
3.	12%Ni/ Al ₂ O ₃ -MgO	CP + IMP	Ni ₁₂
4.	14%Ni/ Al ₂ O ₃ -MgO	CP + IMP	Ni ₁₄
5.	16%Ni/ Al ₂ O ₃ -MgO	CP + IMP	Ni ₁₆
Screening for optimum W loading			
6.	12%Ni/ Al ₂ O ₃ -MgO	CP + IMP	Ni _f
7.	12%Ni-2% W/ Al ₂ O ₃ -MgO	CP + IMP	W _a
8.	12%Ni-4% W/ Al ₂ O ₃ -MgO	CP + IMP	W _b
9.	12%Ni-6% W/ Al ₂ O ₃ -MgO	CP + IMP	W _c
10.	12%Ni-8% W/ Al ₂ O ₃ -MgO	CP + IMP	W _d

*CP = Co-precipitation, IMP = Impregnation.

3.4 Screening of catalysts

The screening of the synthesized catalysts is done by testing the catalyst's performance in DRM reactor (as explained in section 3.6) and by determining their various physicochemical properties. There are ample of characterizations that were carried out to confirm the features of the synthesized catalysts which helped in assessment of optimum catalyst. The DRM reaction tests were carried out at 800°C, 1 atm a total flowrate of 60 ml/min (i.e., CH₄:CO₂:N₂ = 1:1:1). The reactant's conversion is analysed via the GC unit equipped with TCD. The percent conversion of CH₄, CO₂ along with H₂:CO is plotted vs time in three different plots. The stability, activity, and coke formation in the spent catalyst was then analysed accordingly. Finally, the best performing catalyst is chosen for further stability, optimization, and kinetic studies.

3.5 Catalyst Characterization

Characterization techniques play a crucial role in investigating the physicochemical, compositional, structural, and morphological properties of catalysts. These properties are essential to understand the reaction mechanism on the catalyst's surface, and thus helps in screening of the optimum catalyst for DRM reaction. Characterization techniques performed to analyse the catalysts morphology, crystallite size, reduction temperature, crystalline structure, the amount, and type of carbon deposited, dispersion of active metal and surface compositional properties. The crystallite phases, elemental composition, and metal dispersion has been confirmed by XRD, EDX, and elemental dot mapping analysis. The surface area has been investigated by BET analysis and the morphology via FESEM and TEM analysis. The active sites and basicity and oxidation states of the elements along the binding energy of the freshly synthesized catalysts were conformed via TPR-H₂ and TPD-CO₂ and XPS analysis. Finally, the amount and type of carbon formed on the spent catalyst was confirmed by TPO-O₂, RAMAN, and TEM analysis. The various characterizations carried out along with the respective instruments used is described in the following section.

3.5.1 Crystallite phases and size analysis

The powder X-Ray diffraction (XRD) patterns of the calcined catalysts were recorded using a Bruker D8B Advance X-ray diffractometer. The phases existing in the powdered catalyst

samples were detected by correlating the patterns with the standard International Centre for Diffraction Data (ICDD) database's reference.

The analyzer chamber was placed to the diffractometer, and the monochromatic synchrotron emission was targeted on the catalyst surface. The scans were taken over a range of $5^\circ < 2\theta < 90^\circ$ with a scan rate of $4^\circ/\text{min}$. The X-ray beams strike the face of the crystallite structure, resulting in a constructive interference at the specific angles. These angles were calculated from the wavelength of incident X-rays beam and area between the crystalline facets, as described by the Bragg's Law (Eqn. 3.1):

$$n\lambda = 2d \sin\theta \quad (3.1)$$

where the value of n is 1, λ is the wavelength of the incident X-rays, d is the distance between the crystal facets and θ is the incident angle. The average crystallite size is calculated by the Debye-Scherrer equation (Eqn. 3.2).

$$D = \frac{K\lambda}{\beta \cos\theta} \quad (3.2)$$

where K is the Scherrer's constant factor (with a value = 0.9), β is the full width of half maximum, λ is the wavelength of the X-ray beam, and θ is the Bragg's diffraction angle.

3.5.2 Surface area and pore analysis

The Brunauer-Emmett-Teller (BET) technique in a relative pressure range (p/p°) of 0.02–0.30 is employed to determine the surface area. The BET surface area method is based on the principle of adsorption and desorption of N_2 i.e., inferred and executed with multiple points N_2 analyzer. The N_2 physisorption isotherms were employed to determine the textural properties of synthesized catalysts at -195.80°C by a gas adsorption analyzer (Tristar 3020, Micromeritics). Further, the pore volume was determined by the amount of N_2 adsorbed at a relative (p/p°) of 0.99. The liquid nitrogen temperature was arranged with an automatic volumetric adsorption unit (Tristar 3020, Micromeritics). The mean pore diameter, pore volume and the pore size distribution were determined by Barrett-Joyner-Halenda (BJH) analysis. The pre-treatment for each sample was performed via 0.2-0.3 g of samples placed into the filler rods. Each sample was treated with degassing at 300°C under vacuum for 6 h before the analysis.

3.5.3 Morphology Analysis

The FESEM apparatus fitted with EDC (Zeiss Supra 55VP) was employed to investigate the morphology of freshly synthesized and the spent catalyst samples. The sample was loaded on a disc coated with carbon and finely tuned using an internal camera. The high-resolution images were captured at a high voltage of 15 kV to produce highly magnified images (i.e., 1kx-50kx) at a high vacuum. The high electron beam is sourced to perceive the image of the sample at a very high magnification. The gun emitting electrons discharge very intense beam of electrons. Due to this high intensity impact of electron beams, the photons are generated from the sample material which is observed through the detector. The signals are then sent to the screen for final imaging.

3.5.4 Elemental Composition and Mapping

The Electron Dispersive X-ray (EDX) coupled with FESEM (Zeiss Supra 55VP) was employed to verify the elemental composition (wt.%) of synthesized and spent catalyst. Further the dot mapping analysis was obtained to investigate the uniform dispersion of elements present throughout the catalyst samples. EDX and elemental provides the quantitative analysis of the elements present in the material along with the particle distribution.

3.5.5 Catalyst Active Sites Behavior

The Temperature Programmed Reduction (H_2 -TPR) analysis of the catalysts was performed to study the catalyst's active sites behavior using a Thermo Finnigan TPDRO 1100 instrument equipped with a thermal conductivity detector (TCD) and a mass spectrometer with heating rate range up to 800°C. In a typical analysis, about 0.05 gm of the catalyst was placed in a reactor and pre-treated at 150°C (at a ramping rate of 40°C/min) for 60 min in N_2 . The catalyst samples were then degassed under a hydrogen flow (5.06% in N_2) under heating from 20°C-800°C. The H_2 -TPR analysis of the fresh catalysts was also performed using the same instrument and followed identical procedures, i.e., 0.1 gm of fresh catalyst samples pretreatment at 250°C (with He) for 30 mins followed by treatment with CO_2 while keeping the oven off.

3.5.6 Catalyst's Basicity Analysis

The Temperature Programmed Desorption of CO_2 (TPD- CO_2) analysis of the catalyst samples was also carried out using the same apparatus (i.e., Thermo Finnigan TPDRO 1100 instrument)

as TPR-H₂ and followed identical procedures. The 0.1 gm of fresh catalyst samples pretreatment at 250°C (with He) for 30 mins followed by treatment with CO₂ while keeping the oven off.

3.5.7 Quantitative Analysis of Carbon Formed

The Temperature Programmed Oxidation (TPO-O₂) analysis of the catalyst samples was also carried out using the same apparatus (i.e., Thermo Finnigan TPDRO 1100 instrument) as TPR-H₂ and followed identical procedures. The 0.1 gm of the spent catalyst sample, and 5% O₂ was supplies to the gas mixture. Moreover, before the TPO analysis, the spent catalysts were finely crushed and homogenized in an agate mortar. The amount and type of coke formed is indicated by the amount of O₂ utilized and the temperature at which it is consumed.

3.5.8 Analysis of Binding Energy and Oxidation States

The X-Ray Photoelectron Spectroscopy (XPS) analysis is used to investigate the surface chemistry of the prepared catalysts. The surface compositional oxidation states of the synthesized catalysts were determined using the XPS spectra. XPS analysis of freshly prepared catalyst (non-activated) was conducted on an XSAM800 spectrometer with Al K α (h ν = 1486.6 eV). The binding energy (BE) scale was standardized initially via position of the peaks for the Cu 2p (3/2) (932.62 eV) and Au 4f (7/2) (83.96 eV) core levels corresponding to pure metallic copper and gold. The powdered samples were then fixed on a vessel mounting a double-sided adhesive tape.

The regions corresponding to Ni 2p, W 4f, and O 1s were examined under a narrow scan, and the photoelectron signals were recorded. The pass energy of 200 eV radiation (with 400-microns x 700-microns aperture) are employed to collect the spectra. Charging effects were rectified by tuning the binding energies using the C 1s peak at 284.8 eV from carbon contamination.

3.5.9 Structure and Morphology Analysis

The TEM analysis of the freshly prepared and the spent catalysts were carried out by an electron microscope (Hitachi H7100 TEM system, 100keV). The powdered catalyst was consistently dispersed in isopropyl alcohol and placed on a carbon coated copper grid (400 meshes). Furthermore, the sample was dried in vacuum for 12 h prior to the analysis. The powdered catalysts (both fresh and spent) were then examined by TEM to further study the morphology

and type of carbon formed during DRM reaction. The ImageJ software is also used to determine the particle size.

3.5.10 Qualitative analysis of Carbon formed

Raman spectroscopy is an outstanding characterization technique to determine the structure and type of carbon deposited over the spent catalyst during the DRM reaction. It is one of the prime spectroscopic techniques for the characterization of carbonaceous materials, including graphene, carbon nanotubes, and graphite [170]. The prime first order Raman peaks in graphite are optical phonons at 1582 cm^{-1} corresponding to the E_{2g} mode, called the graphite band (G-band) and at 1349 cm^{-1} corresponding to the A_{1g} mode, called the disorder band (D-band) [171]. Raman spectra were obtained using a spectrometer (LabRAM) equipped with a 514 nm Andor CCD laser beam under ambient conditions. The morphology of the spent catalyst has been further analyzed by TEM, using a transmission electron microscope (Hitachi TEM system) at different magnifications.

3.6 Catalyst testing for DRM reaction

The DRM catalytic reaction test was carried out in a jacketed furnace tubular reactor as shown in Figure 3.2. The reactor tube is fabricated from quartz with an internal diameter of 10 mm, and a wired mesh in the middle of the reactor tube. A sample of 100 mg of each catalyst sample is retained on the fixed wired mesh sandwiched in a thin quartz wool layer. This arrangement is used to keep the catalytic bed in the middle position for constant heating throughout the reaction. The catalyst is activated by a mixture of 50% H₂ with N₂ at a total flow rate of 60 mL/min at 800°C for 1 h before the actual reaction. The catalyst is reduced at 800°C, since as per the available literature, the catalyst reduced/activated at higher temperatures showed better performance in terms of activity and durability compared to the catalyst's reduced at lower temperatures [172]. Then an equimolar gaseous mixture of CH₄, CO₂, and N₂ (i.e., 20 mL/min each) is fed into the reactor, and the activity of the catalyst is recorded at 800°C [4, 8, 25, 72, 48]. Any inert gas (such as Ar, He) can be used as a purging gas for reforming reactions, which is a standard practice even by industries, to wipe out the combustible gases from the reactor by inert gases. Here N₂ is used since it is inert and economic compared to the noble gases. By mixing nitrogen with the input gases, the effective displacement of gases from reactor (without reacting chemically with the substrates) takes place. Further, for the optimization and kinetic modelling

the DRM reaction is carried out at temperature ranges from 600-800°C. The feed gas conversions are recorded for 6 h of reaction test, using online gas chromatography (GC). The GC unit used was fitted with a thermal conductivity detector (TCD) from Agilent Technologies (model 7820A).

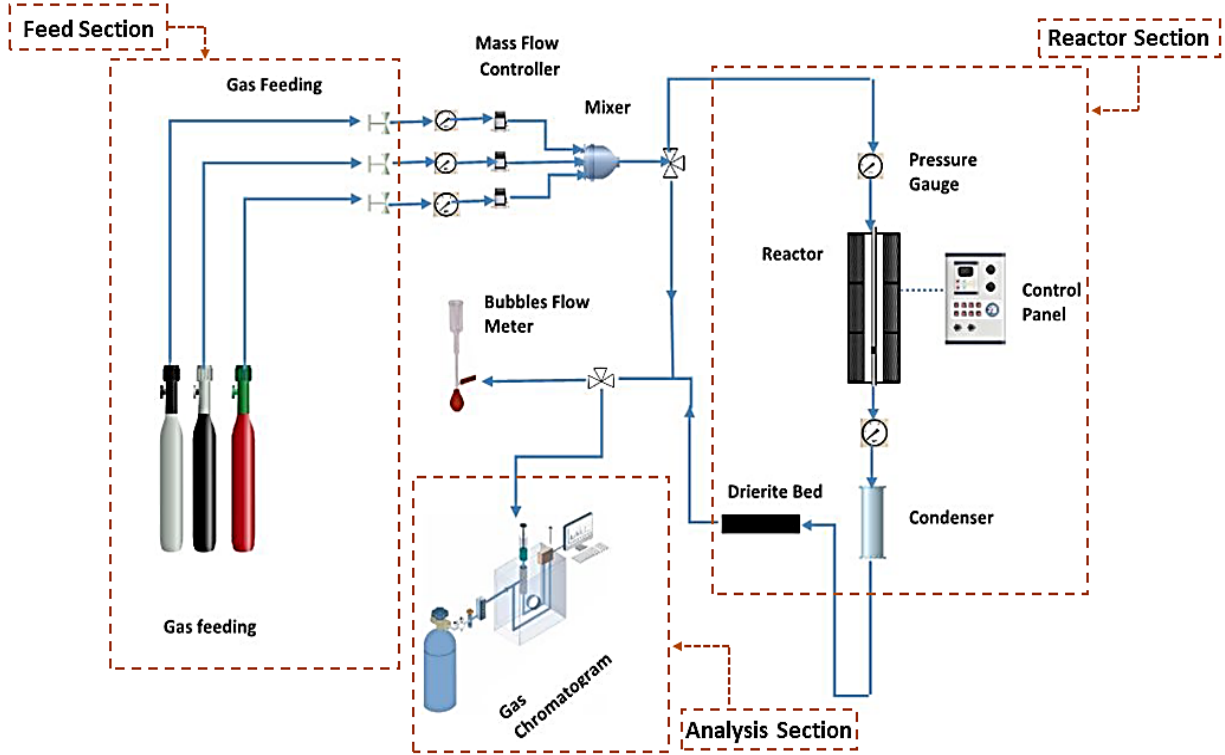


Figure 3.2 Schematic diagram for DRM reactor setup.

To achieve accurate results the calibration of GC has been carried out. The calibrations are performed for H₂, N₂, CO, CH₄, and CO₂, utilizing standard calibration gas cylinders with N₂ as the balance gas. The initial injection temperature was 50°C, and the detector temperature was 200°C. The oven temperature program has an initial 25°C holding time for 0 min, ramping rate of 15 °C/min to 200°C and a holding time of 1 minute. The CH₄ and CO₂ conversions and syngas ratio were calculated by using the following expressions (Eqns. 3.3-3.7)

$$\text{CH}_4 (\%) = \left\{ \frac{F_{\text{CH}_4\text{in}} - F_{\text{CH}_4\text{out}}}{F_{\text{CH}_4\text{in}}} \right\} \times 100 \quad (3.3)$$

$$\text{CO}_2 (\%) = \left\{ \frac{F_{\text{CO}_2\text{in}} - F_{\text{CO}_2\text{out}}}{F_{\text{CO}_2\text{in}}} \right\} \times 100 \quad (3.4)$$

$$\text{H}_2:\text{CO} = \frac{F_{\text{H}_2\text{out}}}{F_{\text{COout}}} \quad (3.5)$$

$$\text{H}_2 \text{ Yield (\%)} = \frac{\text{Moles of H}_2 \text{ produced}}{2 (\text{Moles of CH}_4 \text{ in feed})} \quad (3.6)$$

$$\text{CO Yield (\%)} = \frac{\text{Moles of CO produced}}{(\text{Moles of CH}_4 \text{ in feed} + \text{Moles of CO}_2 \text{ in feed})} \quad (3.7)$$

The optimum performance catalyst was then tested for stability test and then for optimization of process parameters via RSM. Finally, the kinetic study of the optimum performance bimetallic catalyst is carried out. The four main kinetic models are fitted for the experimental and predicted reaction rates as explained in section 3.8.

3.7 Turnover Frequency (TOF)

The concept of turn over frequency (TOF) was proposed by Michel Boudart in the year 1968. The main principal of TOF is comparison of activity of catalysts via chemisorption. The TOF may be expressed as the molar rate consumed per mole of active sites of the catalyst [173], [174]. The TOF of methane for the DRM reactions, were also calculated for the optimum monometallic and bimetallic catalysts. The number of active surface metal sites were calculated from the data obtained from TPR-H₂ analysis. The TOF for the catalysts were determined via following Eqn 3.8:

$$\text{TOF} = \frac{\text{Flow rate of CH}_4}{\text{gm}_{\text{cat}}} \times \frac{\% \text{ CH}_4 \text{ Conversion}}{100} \times \frac{1}{A_s} \quad (3.8)$$

where, the flow rate of CH₄ was taken in mol/s, the weight of catalyst (i.e., gm_{cat}) is taken in grams, and the active surface metal sites (A_s, in mol/gm_{cat}) was calculated from the TPR-H₂ analysis [175]. The methodology was adopted from the latest TOF investigation conducted by K. Ray et al. [176] and Sengupta et al. [175]. TOF gives a relative overview of catalysts performance, however the performance further depends on and varies with the catalyst's particle size, basicity, morphology, and surface area. The TOF of metallic catalyst varies in the range 10² s⁻¹ to 10⁷ s⁻¹, whereas for enzymes it varies between 10³ s⁻¹ to 10⁷ s⁻¹ [177].

3.8 Optimization of process parameters using RSM

The process parameters for DRM reaction over the optimum performance catalyst was determined by central composite design (CCD) tool of RSM. The CCD interface is employed since it is well suited for quadratic models and two input parameters and is extensively used in the DRM process's optimization study [148, 178]. The 3-D response surface plots are obtained,

depicting the interaction of the input process parameters (i.e., temperature and feed ratio) on the percentage conversion of CH₄ and CO₂, and H₂:CO ratio. The two input process parameters (i.e., temperature and feed ratio) are chosen for optimization, since the temperature and feed ratio have a dominant effect on the performance of DRM reactions [157, 179]. The other parameter which may be studied is the effect of pressure on the efficiency of DRM process. However due to the available reactor limitations this parameter cannot be studied since the available reactor can operate at 1 atm pressure only. The experimental data were fitted in the quadratic model equation obtained by CCD tool to give 3-D response surface plots.

Table 3.3. The input process parameters for CCD with their coded representation.

Input process parameter	Symbol	Coded values		
		-1	0	+1
Temperature (°C)	A	600	700	800
Feed Ratio (CH ₄ : CO ₂)	B	0.5	1	1.5

The outcome of input process parameters (i.e., A: reaction temperature and B: feed ratio (CH₄: CO₂)) on the process responses (i.e., % CH₄ conversion, % CO₂ conversion and H₂:CO ratio) were examined for DRM process over the optimum catalyst by employing the CCD interface. The input process parameters and the responses have been outlined with the coded values in Table 3.3. The DOE obtained as per the CCD interface for optimization study and the reactions have been précised in Table 3.4. The input process parameters have been represented in coded notations from Table 3.3. Further, the reaction temperature range studied is 600°C-800°C and the feed gas ratio range considered is 0.5-1.5, since it agrees well with the literature available for DRM process [25, 37, 101].

Table 3.4. The DOE suggested by CCD along with responses obtained.

Input Process Parameters (Coded values)		
Run	A: Temperature	B: Feed Ratio (CH ₄ : CO ₂)
1	+1	0
2	0	+1
3	0	-1

4	0	0
5	-1	+1
6	+1	+1
7	0	0
8	-1	-1
9	+1	-1
10	0	0
11	0	0
12	-1	0
13	0	0

Desirability function is a contemporary technique for optimization of different parameters, explained by Derringer and Suich [180]. The key approach for desirability function is that, since different parameters are measured at different scales, the main hurdle is comparing them. Therefore, this contrary limitation of comparing "apple to orange" outcomes has been addressed by ascribing them a desirability score. The objective is firstly converted into a distinct desirability function (i.e., d_i), that varies within the span of 0 and 1 as Eqn. 3.9:

$$0 \leq d_i \leq 1 \quad (3.9)$$

If the aim is at its objective, then $d_i = 1$, whereas if the response is beyond the acceptable area, $d_i = 0$. In this manner, the "finest" outcome for each criterion is attained (i.e., $d_i = 1$), likewise the inappropriate is also score (as $d_i = 0$). Finally, to achieve optimum desirability, the maximized combination of outcomes is chosen by the desirability function [181].

R_2 represents the goodness of fit between the obtained experimental data and the predicted data by CCD tool of RSM. The acceptable value of R_2 should be at least 0.6 (60%) or 0.7 (70%). A significant relationship between the independent and dependent variables exists if regression significance (F) value $< \alpha = 0.05$. The p-value for each regression coefficient demonstrate about the possibility of the coefficient for that independent variable emerged by chance and does not describe a real relationship. The claim should be rejected if $p < 0.05$. which means the null hypothesis is true. Further, the confidence limits are the 95% probability that the true value of the coefficient lies between the lower and upper 95% values: estimated value of Y for the given X value.

3.9 Kinetic studies for DRM

The four main reaction kinetic models (i.e., Langmuir-Hinshelwood (LH), Power Law (PL), and Eley-Rideal (ERI and ERII)) were used to understand DRM kinetics [51, 182, 183]. PL model is the simplest of all reaction kinetic models, and it can be used to make a rough inference for kinetic parameters [37]. The ER model proposes that one gas (either CH₄ or CO₂) gets adsorbed on the catalyst active sites at thermodynamic equilibrium, whereas the other remains in the gas phase. The adsorbed gas then forms the educt and reacts with the non-adsorbed gas (by ER I or ER II mechanism). The RDS step is the one comprising the reaction of adsorbed gas with another reactant [182, 183]. Whereas, in LH model, it has been claimed that both the reactant gases get absorbed on the active sites of the catalyst. The educts formed react with each other, during this phenomenon some elementary reactions are at thermodynamic equilibrium whereas some are the RDS. The decomposition of CH₄ and CO₂ decomposition are supposed as elementary reactions in DRM reaction. The LH model is the most applicable and widely used for DRM reactions, since it provides more realistic approach for reaction mechanism, and explain the mechanistic steps more accurately [183, 184]. The equations employed for kinetic studies are Eqns. (3.10-3.13):

Power Law (PL):

$$R = k[P_{CH_4}]^m[P_{CO_2}]^n \quad (3.10)$$

Eley Rideal I (ERI):

$$R = \frac{k \cdot K_{CO_2} \cdot P_{CH_4} \cdot P_{CO_2}}{1 + K_{CO_2} \cdot P_{CO_2}} \quad (3.11)$$

Eley Rideal II (ERII):

$$R = \frac{k \cdot K_{CH_4} \cdot P_{CH_4} \cdot P_{CO_2}}{1 + K_{CH_4} \cdot P_{CH_4}} \quad (3.12)$$

Langmuir-Hinshelwood (LH):

$$R = \frac{k \cdot K_{CH_4} \cdot K_{CO_2} \cdot P_{CH_4} \cdot P_{CO_2}}{(1 + K_{CH_4} \cdot P_{CH_4} + K_{CO_2} \cdot P_{CO_2})^2} \quad (3.13)$$

To carry out the kinetic modelling analysis for the DRM reaction, the flow rate is tuned from 30-150ml/min to study the influence of external diffusion on reaction at 800 °C. For the fixed bed reactor used to carry out this study (with ID =10mm) the conversion is constant in the range 60 ml/min to 90 ml/min (APPENDIX D). The kinetic testing is done by varying the input gaseous flowrate (i.e., CH₄, CO₂ and N₂) into the reactor at atmospheric pressure.

Table 3.5. The reaction parameters and the corresponding range used for kinetic study.

S.No.	Reaction Parameter	Range
1.	Partial Pressure (P _{CH₄})	0.2-0.6
2.	Partial Pressure (P _{CO₂})	0.2-0.6
3.	Temperature	600°C-800°C

The total flow rate was maintained at 70 ml/min and the reaction temperature is varied from 600°C-800°C. The partial pressure of both the reactant gases was varied from 0.2 to 0.6 as shown in Table 3.5. Then by applying the rate equation the adsorption equilibrium constants (i.e., K_{CH₄} and K_{CO₂}) and rate constant (*k*) were obtained via linear regression analysis. The obtained K_{CH₄}, K_{CO₂} and *k* values were then fitted in the Arrhenius plot for calculation of activation energy (E_a). Finally, the experimental reaction rate vs the estimated reaction was plotted for all the kinetic models (APPENDIX F).

CHAPTER 4

RESULTS AND DISCUSSION

4.1 Chapter Overview

This chapter includes the comprehensive discussions on performances, characterizations, optimization, and kinetic studies of the prepared catalysts. This chapter is divided into four main sections; whereby section 4.2 confers the screening of optimum Ni loading on Al_2O_3 -MgO support, validated by the performance evaluation and respective catalyst characterizations. Section 4.3 discusses about the effect of W addition on the optimum Ni loaded catalyst. The textural properties, morphology, compositional characteristics along with other characterizations has been reported. The performance and stability test of the optimum Ni-W bimetallic catalyst is also reported in this section. Further, section 4.4 deals with the optimization study for the obtained optimum Ni-W bimetallic catalyst for DRM. The RSM tool of 'Design Expert Version-12' is used for optimization of reaction parameters. Finally, the kinetic study has been carried out and discussed in section 4.5. The various kinetic models such as Power-Law, Langmuir-Hinshelwood, Eley-Rideal (I and II) has been employed for the data fitting. The best fitting model has been reported recommended for the optimum performance Ni-W bimetallic catalyst.

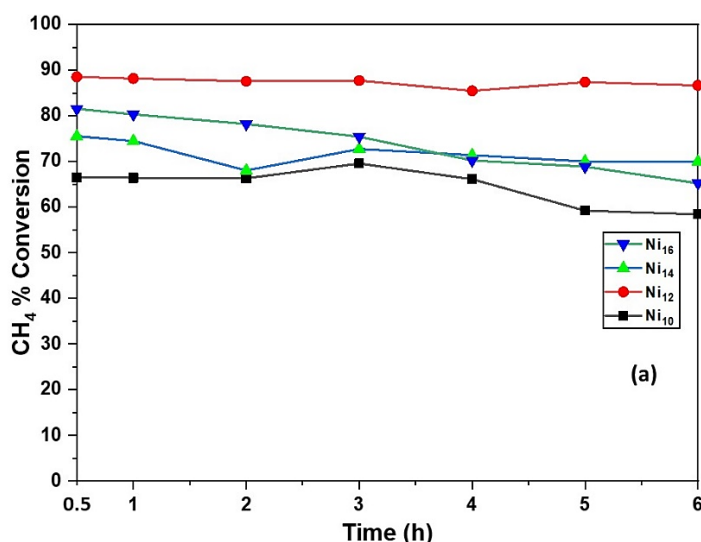
4.2 Screening for Ni loading

The catalysts are prepared via two step synthesis process, i.e., co-precipitation of catalyst support followed by impregnation of Ni metal. The precursor chemical salts are weighted in stoichiometric amount and mixed as per the detailed methodology explained in section 3.3 above. The catalyst support is prepared This section studies the Ni loading analysis on the prepared optimum Al_2O_3 -MgO support. The Al_2O_3 -MgO support with different composition ratio (i.e., Al_2O_3 :MgO of 1:1, 1:2 and 2:1) were prepared and it has been verified that Al_2O_3 :MgO of 1:2 showed most stable performance [74]. Further, four Ni loaded catalyst samples with Ni content of 10, 12, 14 and 16wt% on Al_2O_3 -MgO (1:2) were prepared. The performance evaluation of the prepared catalysts was carried out for DRM reaction. The optimum performance Ni catalyst has been characterized by XRD, BET, FESEM, TEM, EDX and elemental mapping. Finally, the spent catalyst has been characterized by XRD, FESEM, TEM, EDX and elemental mapping to study the amount and type of carbon formed during the

DRM reaction. It has been observed that on increasing Ni loading the catalyst's performance increased (from 10 wt.% to 12 wt.%). However, on further increasing the Ni loading (i.e., 14 wt%-16 wt.%) the quick deactivation of catalyst has been observed. Further on characterizing the spent catalyst, the formation of amorphous carbon on the active sites of catalyst is observed, which has been verified as the reason for declined catalytic activity.

4.2.1 Performance Evaluation of catalysts for DRM

The different Ni loaded catalysts $x\text{Ni}/\text{Al}_2\text{O}_3\text{-MgO}$ (where, $x= 10, 12, 14$ and $16\text{wt}\%$) were tested for DRM in the reactor. The catalysts were named as Ni_{10} , Ni_{12} , Ni_{14} and Ni_{16} , respectively as discussed in section 3.3 above. The catalyst testing for DRM was carried out for 6h of experimental run and the outcomes, i.e., percentage CH_4 and CO_2 conversions and $\text{H}_2:\text{CO}$ ratio has been calculated using the equations 3.3, 3.4, and 3.5 respectively. It has been observed that the catalyst with 12wt.% Ni loading showed elevated activity both for CO_2 and CH_4 conversions. The CH_4 percentage conversion remained almost stable between 88% to 84% and CO_2 conversion between 96% to 90% respectively for 6h of DMR reaction. Further, it can be clearly seen that 12wt.% Ni loaded catalyst showed most stable syngas ratio (varied from 0.96-0.9) compared to other catalysts for the conducted DRM test for 6h. The performance evaluation of the synthesized catalysts is shown in Figure 4.1 (a-c). The catalysts with higher Ni loading (i.e., 14wt.% and 16wt.%) showed high initial activities, however the activities declined over the span of time. This decline in activity may be due to agglomeration of Ni particles to form bigger Ni particles for high doping. The results are in agreement with the concluding remarks made by Abdullah et al.[3] and Aramouni et al. [185].



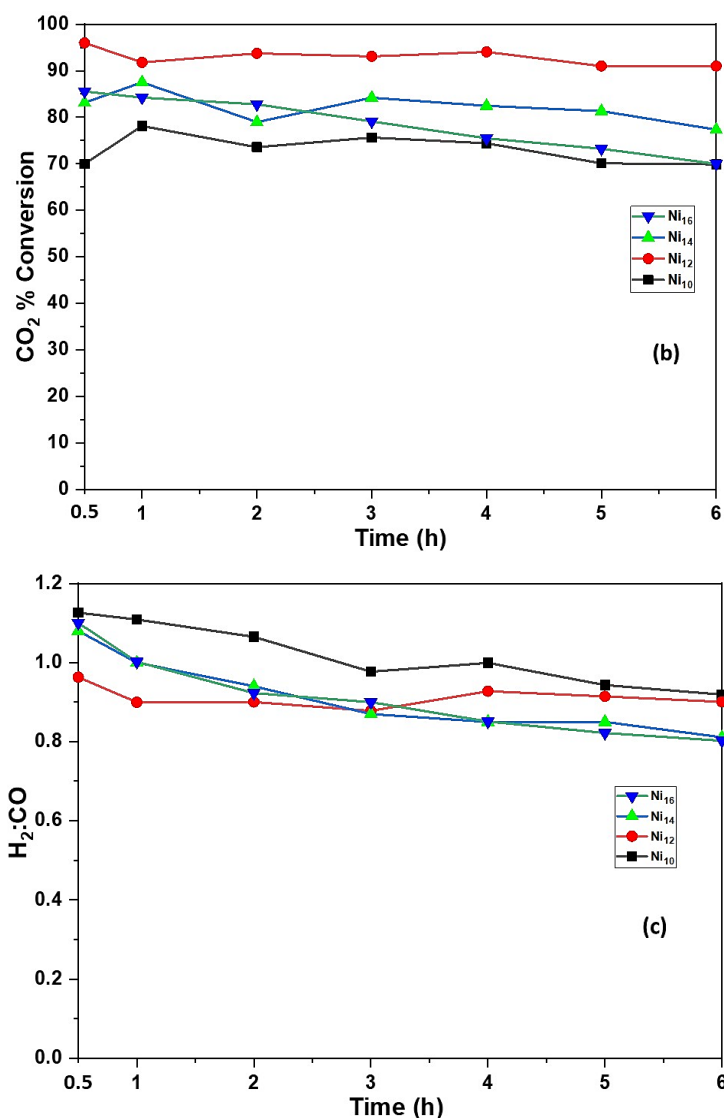


Figure 4.1. Performance in terms of (a) Percentage CH₄ conversion (b) Percentage CO₂ conversion and (c) Syngas ratio, for different Ni content catalysts supported on Al₂O₃-MgO with 1:2 ratio.

This optimum performance catalyst (i.e., Ni₁₂, both fresh and spent) were further characterized to study its surface area, morphology and the type of carbon deposited during 6h of DRM reaction.

4.2.2 Catalyst Characterizations

4.2.2.1 X-Ray diffraction

The XRD pattern has been recorded for fresh and spent Ni₁₂ catalyst, since it showed the optimum performance during the DMR reaction. The crystallite peak of cubic MgO has been seen corresponding to the 2-theta value of 36.9°, 43.1°, 62.4° [ICDD file no. 03-065-0476] and

found consistent with literature [186]. Also, the diffraction peaks for 2 theta values of 26°, 44°, 52° and 76° are observed corresponding to NiAl_2O_4 phase [ICDD 01-078-6961] and in agreement with Bach. et al. [187]. Moreover, the Al_2MgO_4 spinel phase peaks have been found corresponding to the 2-theta value of 31°, 36° and 65° [ICDD 01-077-3527]. In the spent catalyst, the carbon deposited has been indicated by the peaks corresponding to 2-theta value of 26.6°, and 51° [ICDD 03-065-6212] and can be clearly seen in Figure 4.2. The results agree with Zhu et al. [45] and Zhan et al. [103].

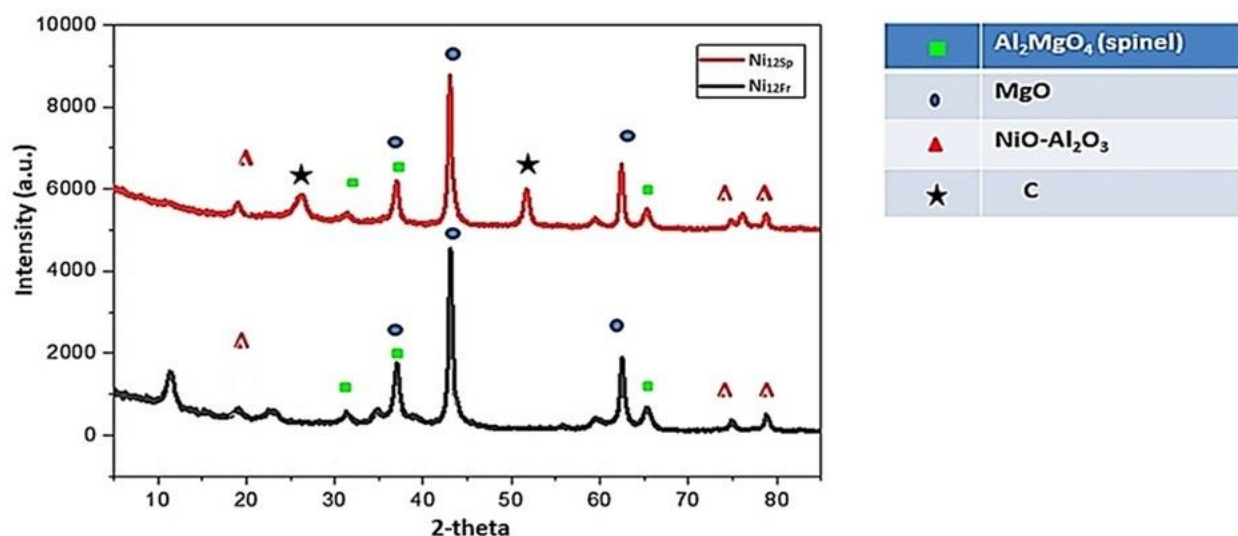


Figure 4.2. X-ray diffraction patterns of fresh (Ni_{12}) and spent ($\text{Ni}_{12\text{Sp}}$) optimum catalysts.

4.2.2.2 Textural Properties

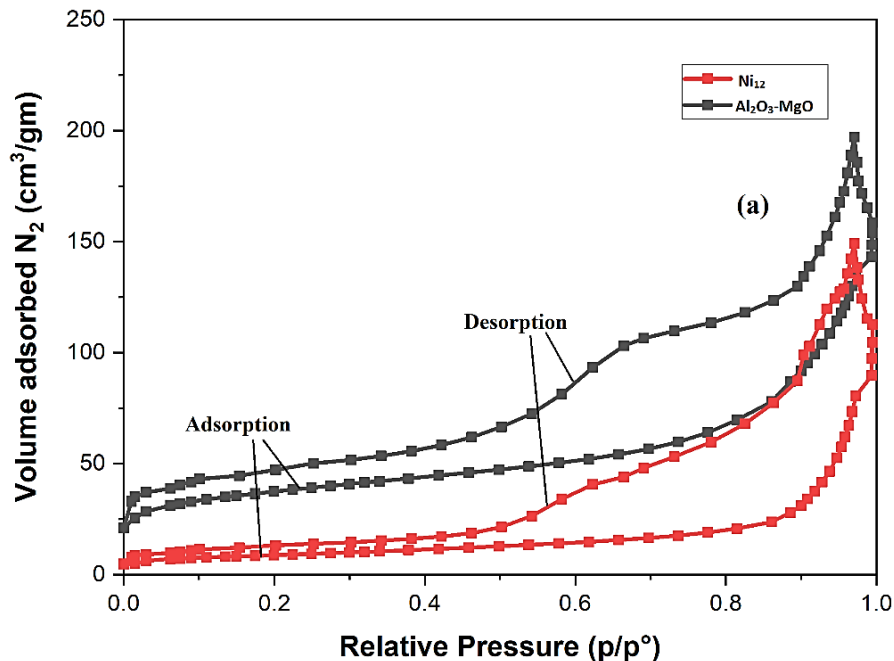
The textural properties of catalyst support (CS) and the optimum loaded Ni_{12} has been determined by BET analysis in Table 4.1. The BET surface area of Al_2O_3 -MgO support is found to be $96.1 \text{ m}^2/\text{g}$ whereas on impregnation of 12wt.% of Ni into the Al_2O_3 -MgO support the surface area reduced to $29.3 \text{ m}^2/\text{g}$ [73]. The reverse trend is observed in BJH average pore size of the support after active metal impregnation as reported in Table 4.1. These results are in agreement with the literature [18, 19]. The associated N_2 adsorption-desorption isotherms for the catalyst support i.e., Al_2O_3 -MgO and for Ni_{12} catalyst has been displayed in Figure 4.3(a). These isotherms are categorized as of group IV isotherms, which represents the characteristics of mesoporous materials (i.e., 2–50 nm) as per IUPAC [188].

Table 4.1. Textural properties of the synthesized catalyst support and optimum catalyst

Catalyst	BET surface area (m ² /g)	BJH average pore size (nm)	Pore volume (cm ³ /g)	Average crystal size ^a (nm)	
				Fresh	Spent
Al ₂ O ₃ -MgO (support, Al ₂ O ₃ :MgO=1:2)	96.1	12.5	0.26	-	
Ni ₁₂	29.3	26.5	0.21	46.1	54.3

^a calculated through Debye–Scherrer equation from XRD peaks of MgO at 43.1° and (200) plane.

Further, the adsorption-desorption hysteresis curves are obtained for the p/p° range of 0.05-0.98 and fits to class hysteresis loop. It can be elucidated, that the catalyst contains highly uniform and mesoporous channels, also the cumulations are almost uniform spheres. In the further investigation, the pore size distribution has been analyzed and shown in Figures 4.3(b). The pore size of catalyst support increased on doping of Ni into it from 12.5nm to 26.5 nm. On loading the catalyst support with active metal, the surface area of the support decreased due to the blockage of pores, whereas the pore diameter increased.



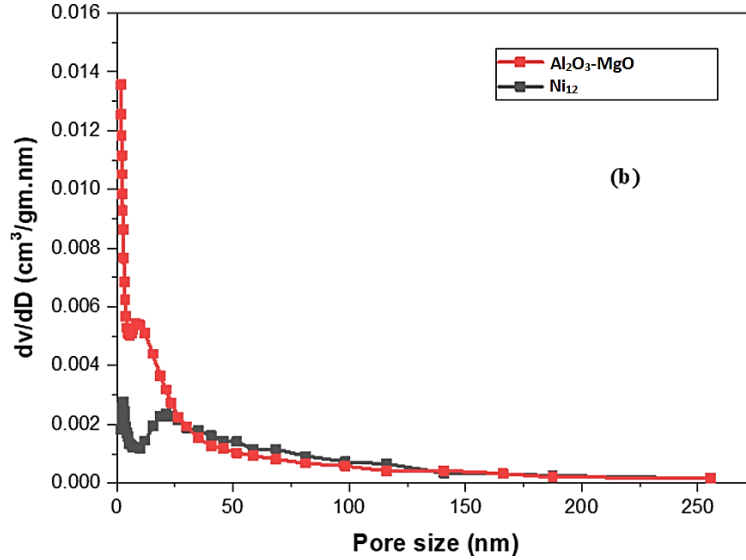


Figure 4.3. (a) Nitrogen adsorption-desorption isotherms for optimum CS and Ni₁₂ catalyst, and (b) Pore-size distribution curves for optimum CS and Ni₁₂ catalyst.

4.2.2.3 FESEM

The FESEM analysis of the freshly prepared and spent Ni₁₂ catalyst has been conducted to study the morphology of the prepared catalyst. The surface morphology has been observed at different magnifications and been depicted in Figure 4.4(a-b). The FESEM images showed minute grained surface for freshly prepared catalyst, whereas for the spent catalyst the carbon nanosheets has been observed. This reveals the reason for reduced activity of the catalyst after 6h of DRM reaction at 800°C. The carbon nanosheets encapsulated the active sites on the catalyst's surface and hence reduced its activity. The comparable results for this type of amorphous carbon formation has been reported by Farooqi et al. [189].

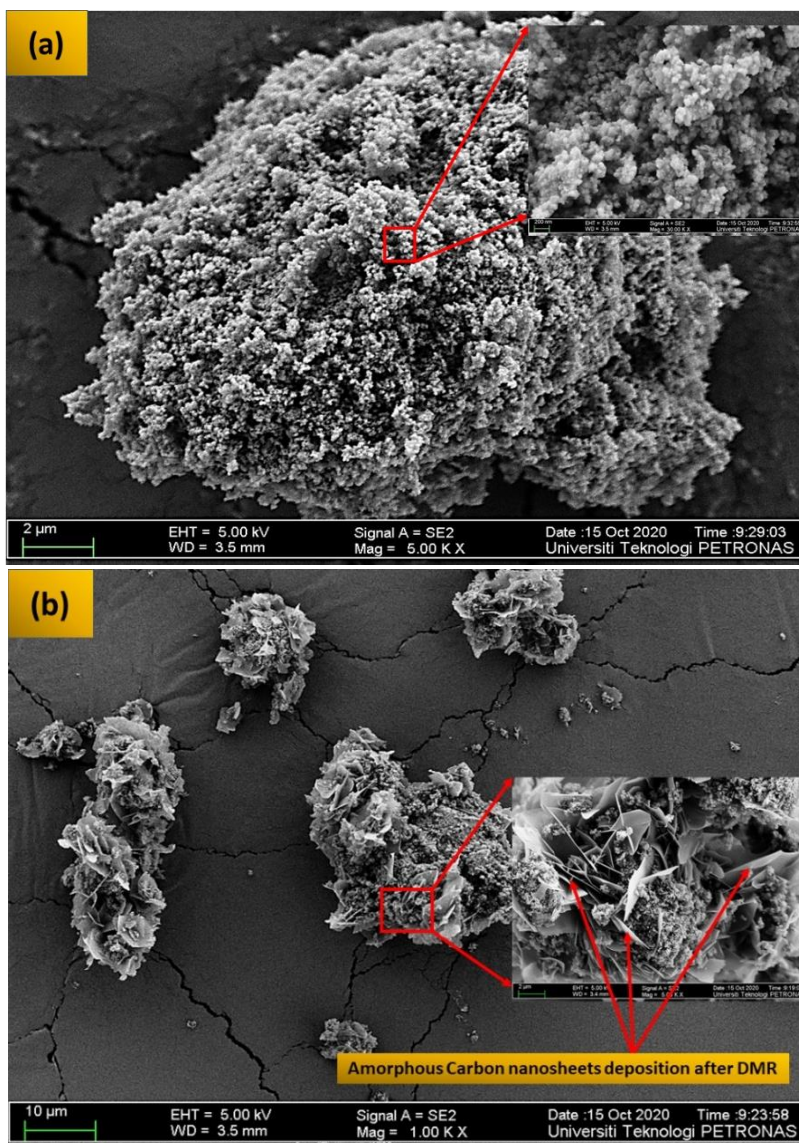


Figure 4.4. FESEM images of (a) fresh (Ni_{12}) and (b) spent ($\text{Ni}_{12\text{Sp}}$) catalysts.

4.2.2.4 TEM

The FESEM done in the previous section confirms the formation of carbon nanosheets. To get further insight of the carbon formation the TEM analysis of the optimum fresh and spent catalyst has been conducted. The octahedral morphology of the synthesized Ni particles is seen clearly in the freshly synthesized catalyst, Figure 4.5(a). The comparable octahedral morphology of Ni particles has been reported in the literature for Ni-based catalyst by Jiang et al. [190] and Ali et al. [191]. The amorphous carbon spots deposition covering the catalyst surface can also be seen clearly in the TEM images as shown in Figure 4.5(b). Similar amorphous carbon spots formation has been reported for DRM reaction over Ni-based catalyst conducted by Xu et al. [192].

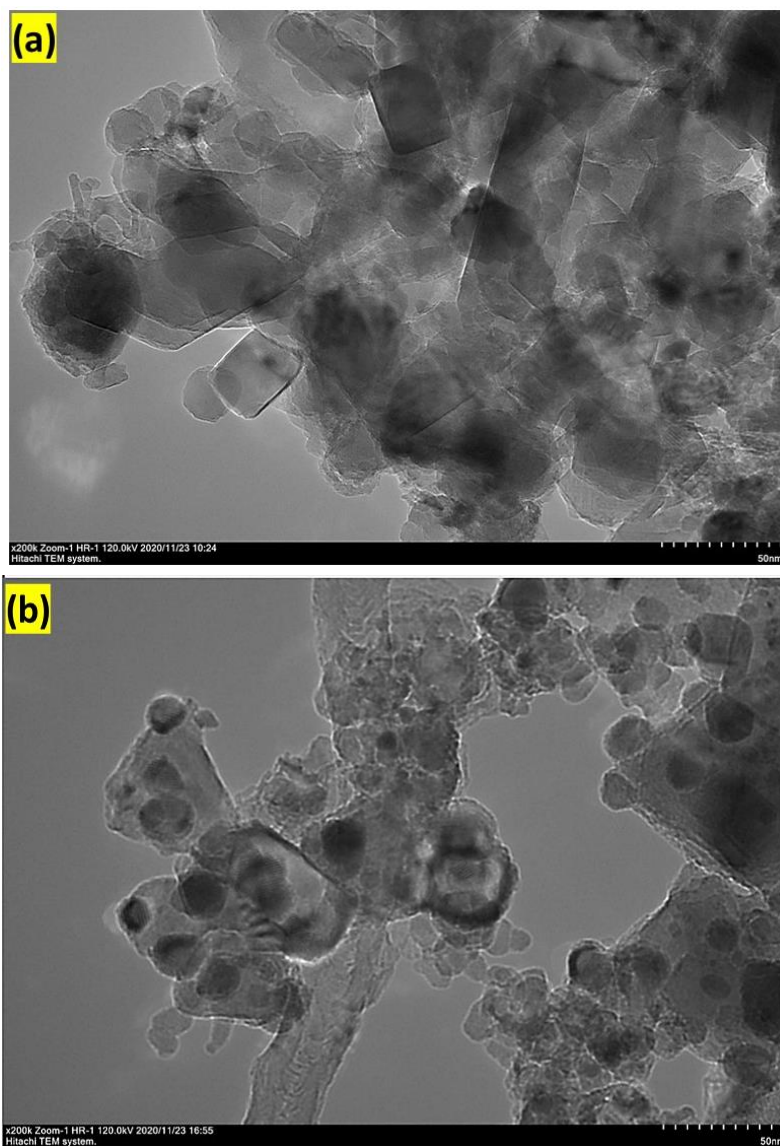


Figure 4.5. TEM images of (a) fresh (Ni_{12}) and (b) spent ($\text{Ni}_{12\text{Sp}}$) catalyst.

4.2.2.5 EDX and Elemental Mapping

The EDX analysis has been conducted to confirm the catalyst composition of the synthesized and spent catalyst. The existence of the elements such as Ni, Mg, Al, and O has been detected in the EDX analysis of fresh catalyst, as shown in Figure 4.6(a). Further apart from the above constituents the elemental carbon has also been detected in the EDX spectrum of the spent catalyst (i.e., $\text{Ni}_{12\text{Sp}}$) as displayed in figure 4.6(b). There was significant coke formation for 6 h of DRM test for 12wt.% Ni loaded catalyst (i.e., about 26%). This also agree with the above XRD, FESEM and TEM analysis where the carbon has been detected in the spent catalyst. Further, the

elemental map sum spectrum can also be seen in the figures showing the percentage of each element in the synthesized and spent catalysts. On the other hand, for the spent catalyst (i.e., Ni_{12Sp}) was observed. This further verify the presence of C in the spent catalyst sample as shown in Figure 4.6(b).

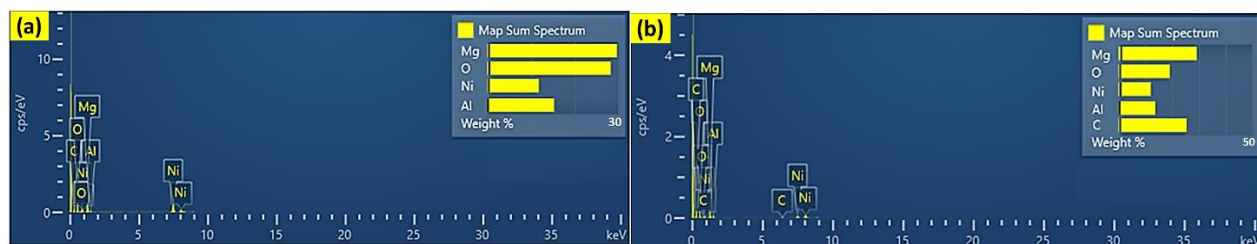


Figure 4.6. EDX spectrum of (a) fresh (Ni₁₂) and (b) spent (Ni_{12Sp}) catalyst.

The elemental mapping of the synthesized fresh and spent nano-catalyst has also been carried out. It can be seen clearly that in the fresh catalyst a more uniform distribution of elements is present, compared to the spent catalyst. After undergoing DRM reaction for 6h at 800°C, the elemental distribution gets disturbed as evident from Figure 4.7. This may be due to sintering effect and due to the deposition of carbon over the spent catalyst (as evident from TEM results, Figure 4.5(b)). The amorphous carbon distribution throughout the catalyst active sites can also be seen clearly in elemental mapping of C in Figure 4.7 for the spent catalyst. These obtained results are in the agreement of the recent investigations of Li et al. [193].

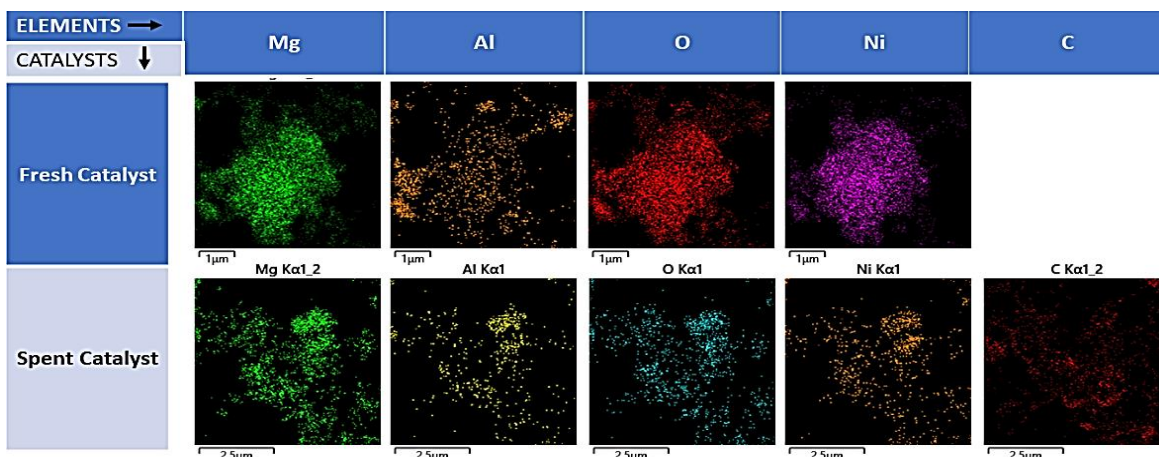


Figure 4.7. Elemental mapping of optimum fresh and spent (Ni₁₂ and Ni_{12Sp}) catalyst.

The experimental analysis showed that a loading of 12 wt.% Ni on Al₂O₃-MgO support (with ratio of 1:2) is optimum both in terms of reactant conversions and stable syngas ratio for DRM reaction. The catalyst with 12wt.% Ni loading showed highest activity both for CH₄ and CO₂ conversions. The CH₄ conversion varied from 88% to 84% and the CO₂ conversion varied from

96% to 90%, respectively during 6 h of DRM reaction. The other catalysts with higher Ni content showed high initial activities, but the performance declined over time. Further in this study, various characterizations carried out for optimum Ni catalyst has inferred the formation of amorphous carbon nanosheets during the DRM reaction as evident from FESEM and TEM results.

4.2 Effect of W addition

The optimum Ni loaded catalyst (named as Ni_f i.e., 12wt.% Ni) with best performance is further studied with tungsten (W) as a bimetal. The effect of W addition on Ni/Al₂O₃-MgO catalyst for DRM reaction is studied in this section. A series of W loaded catalysts Ni-xW/Al₂O₃-MgO were prepared (x = 2, 4, 6, 8wt.%) by the methodology described in section 3.3 above. The freshly prepared bimetallic catalysts (named as W_a, W_b, W_c, and W_d) were characterized with BET, XRD, FESEM, EDX, elemental mapping, TPR-H₂ and TPD-CO₂. The performance evaluation of the prepared bimetallic catalyst is carried out in the reactor for DRM. The XPS analysis of the optimum performance catalyst and the reference (Ni_f) catalysts was also carried out to determine the oxidation state of the elements present in the catalysts. Finally, the spent optimum W loaded catalyst with best performance has been characterized with XRD, FESEM, EDX, elemental mapping, TPO-O₂, RAMAN and TEM analysis. The characterization of spent catalyst helped in the analysis of amount and type of carbon formed and its durability during the DRM reaction. Finally, the stability test was conducted for optimum Ni-W/Al₂O₃-MgO bimetallic catalyst.

4.3.1 Catalyst Characterizations

4.3.3.1 X-Ray diffraction

The XRD pattern of fresh supported monometallic (Ni) and different bimetallic (Ni-W) catalysts with varying W content has been shown in Figure 4.8. Different peaks have been observed corresponding to NiO, NiO-MgO, Al₂O₃-MgO, and NiWO₄. For the reference monometallic (Ni_f) and the bimetallic (W_a, W_b, W_c, and W_d), the characteristic peaks of bulk phase cubic MgO has been observed at the 2-theta value of 36.9°, 43.1°, 62.4°, and 78.7° [ICDD file no. 03-065-0476] corresponding to the miller indices of (111), (200), (220) and (222), respectively. The XRD peaks of NiO coincides with MgO, and hence it is difficult to differentiate the two; this result is in agreement with previously reported work [194]. Whereas, the spinel Al₂MgO₄ crystals have been observed at the 2-theta values of 19.1°, 31.3°, 44.8°, 59.4°, and 65.3° [ICDD

file no. 01-077-3527] corresponding to the miller indices of (111), (220), (400), (511) and (620), respectively and found consistent with the literature [45, 195]. Moreover, the tiny peaks for NiWO_4 alloy have been observed for bimetallic W_b , W_c , and W_d catalysts at 2-theta values of 46.4° and 72.6° corresponding to miller indices (103) and (302) respectively [ICDD file no. 01-072-0480], these results are also found consistent with the literature [196–198]. This Ni-W alloy (i.e., NiWO_4) has a melting point of 1400°C and is thermally very stable [199]. It has also been reported in the literature that at 800°C the NiWO_4 crystals are highly stable with very negligible weight loss [200]. The Ni-W alloy peaks were not observed for the W_a catalyst; this may be due to the fact of uniform mixing of the minute amount of W throughout the catalyst (in W_a sample), which was beyond the detectable limit of XRD. However, no characteristic peaks for WO_3 in the solid solution appeared. This may be again due to very homogeneously dispersed W within the catalyst and hence beyond the detectable limit of the XRD. But the NiO-MgO peaks got a little broadened and diminished on increasing the W concentration indicating the crystalline phase and reduced crystal size on the loading of W (cf. Table 4.2). The results obtained are in agreement with the literature [201].

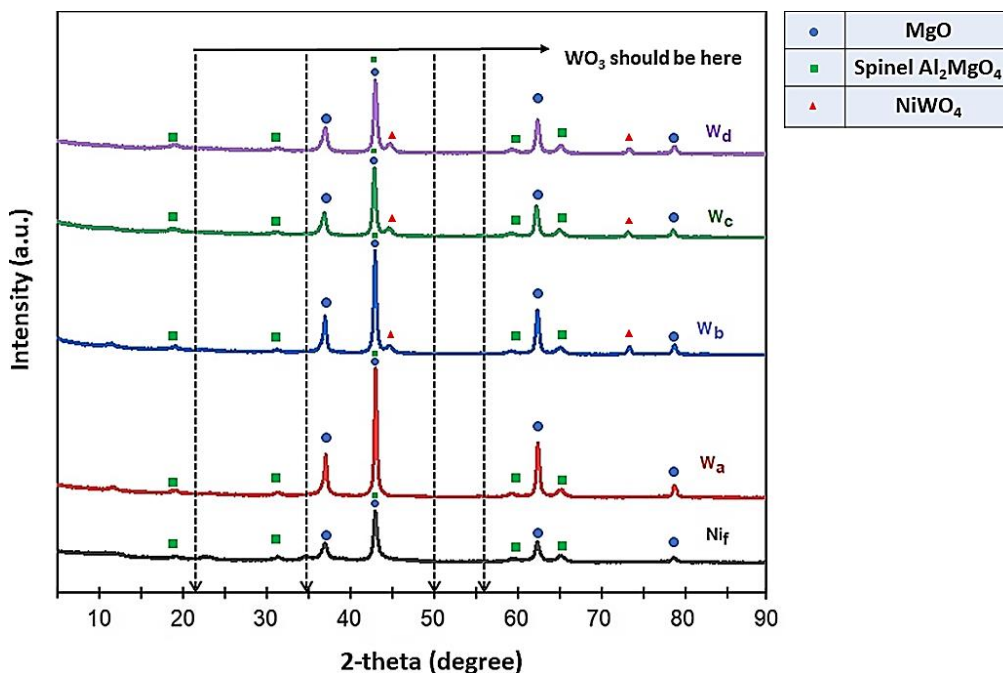


Figure 4.8. XRD pattern of monometallic Ni and series of Ni-W bimetallic catalysts (Ni_f , W_a , W_b , W_c , W_d).

4.3.3.2 Textural Properties

The physicochemical properties of the monometallic catalyst (Ni_f) and the different bimetallic catalysts (i.e., W_a , W_b , W_c , and W_d) with varying tungsten addition (i.e., 2wt%-8wt% respectively) has been analyzed and reported in Table 4.2. The initial surface area of the support decreased due to impregnation of Ni metal into the support from 96.1 m^2/g to 29.3 m^2/g as evident from BET surface area analysis, indicating the shutting of pores of catalyst support by Ni metal impregnation. However, the BET surface area increased on the addition of W into the catalyst and has shown a rising trend with percentage addition of W into the catalyst (from 29.3 m^2/g for Ni_f catalyst to 37.3 m^2/g and 48 m^2/g for W_a and W_b , respectively). Nevertheless, on further adding W into the catalyst, a slight drop in BET surface area is observed, i.e., the surface area of 45.3 m^2/g and 43.6 m^2/g for W_c and W_d , respectively, have been witnessed. This is due to the formation of bigger Ni crystallites in Ni_f catalyst as compared to bimetallic catalysts by adding W. The Ni_f catalyst has a bigger crystallite size when compared to bimetallic catalysts (shown in Table 4.2, calculated by Scherrer equation). The crystal size decreased on the addition of W to the monometallic catalyst, which further reduced on increasing W (beyond 4wt.%) content in the catalyst. This may be due to Ni-W alloy's formation and synergistic effect between different oxides in the solid solution and has been found consistent with the literature [202]. Similarly, the surface area also increased accordingly and was found consistent with the literature [96]. Moreover, the reverse trend has been seen in the pore size of the powdered catalyst. The supporting media's pore size increased on doping of Ni into it from 12.5nm to 26.5 nm. On adding W into the Ni-based monometallic catalyst, the pore size decreased (from 26.5nm for Ni_f to 18.6 nm for W_a). On further addition of W (i.e., for W_b , W_c , and W_d), the pore size increased to 19.4 nm, 22.8 nm, and 23.1 nm, respectively. Also, the pore volume followed a similar trend as that of pore size. These obtained results are in accordance with the literature [203]. The N_2 adsorption-desorption isotherms associated with the different catalysts have been shown in Figure 4.9(a). The isotherms for catalyst support (i.e., $\text{Al}_2\text{O}_3\text{-MgO}$ as CS) and all the freshly prepared catalyst (i.e., Ni_f , W_a , W_b , W_c , and W_d) has been displayed in Figure 4.9. The obtained isotherms are classified as group IV isotherms, representing the characteristics of mesoporous materials (i.e., 2–50 nm) as per IUPAC.

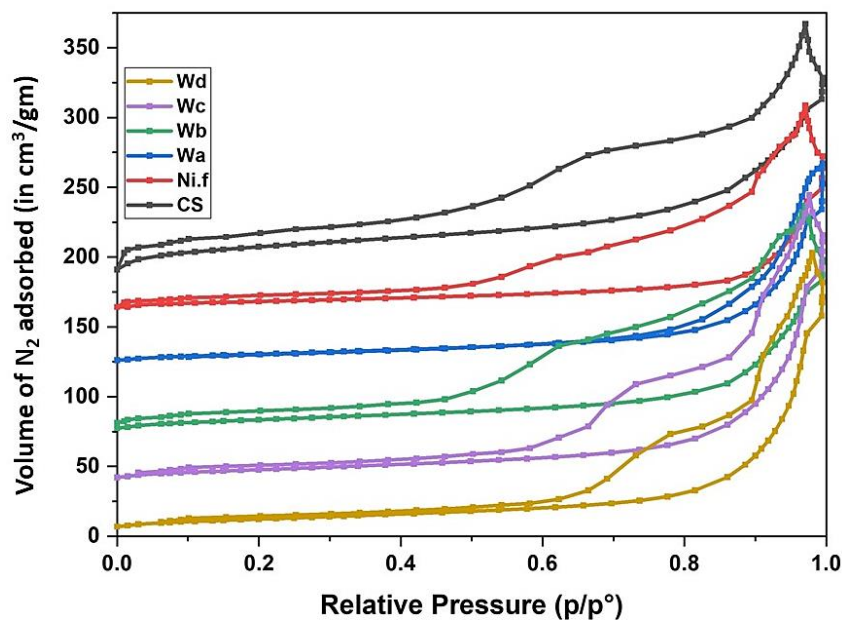


Figure 4.9. N₂ adsorption-desorption isotherms for catalyst support (CS), and different prepared catalysts (Ni_f, W_a, W_b, W_c, W_d).

Further, the adsorption-desorption hysteresis curves are obtained for the p/p^o range of 0.05-0.96 and fit to class H3 hysteresis loop. It can be illuminated that the catalysts contain highly uniform and mesoporous channels; also the cumulations are almost uniform spheres [188].

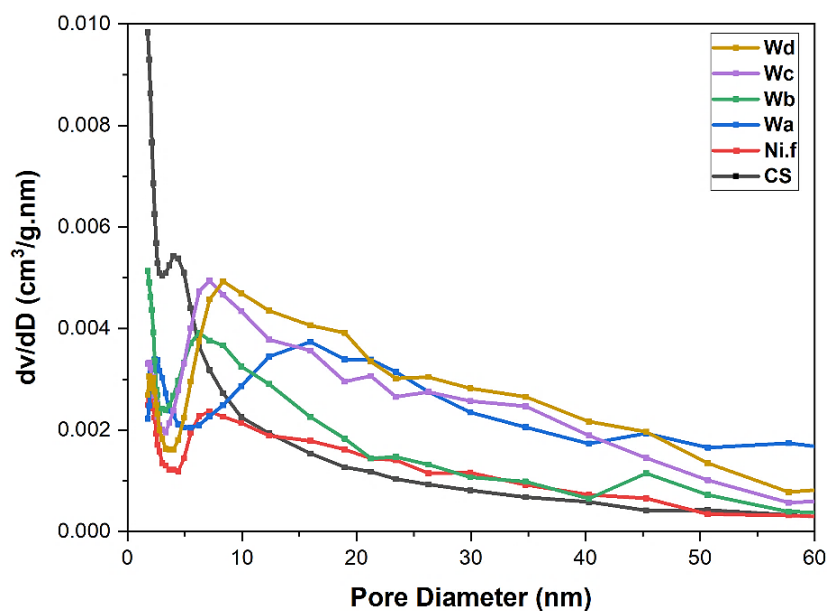


Figure 4.10. Pore size distribution curves for catalyst support (CS), and different prepared catalysts (Ni_f, W_a, W_b, W_c, W_d).

Table 4.2. Textural properties of synthesized support, monometallic and bimetallic catalyst

Catalyst	BET surface area ^a (m ² /g)	BJH average pore size (nm)	Pore volume (cm ³ /g)	Average crystallite size ^b (nm)	H ₂ consumed (μmol g _{cat} ⁻¹) _c
Al ₂ O ₃ -MgO (support)	96.1	12.5	0.25	-	-
12% Ni/Al ₂ O ₃ -MgO (Ni _f)	29.3	26.5	0.20	46.1	274.08
12% Ni-2% W/Al ₂ O ₃ -MgO (W _a)	37.3	18.6	0.18	25	572.8
12% Ni-4% W/Al ₂ O ₃ -MgO (W _b)	48.0	19.4	0.24	22.9	769.55
12% Ni-6% W/Al ₂ O ₃ -MgO (W _c)	45.3	22.8	0.28	19.7	738.2
12% Ni-8% W/Al ₂ O ₃ -MgO (W _d)	43.6	23.1	0.31	19.5	679.99

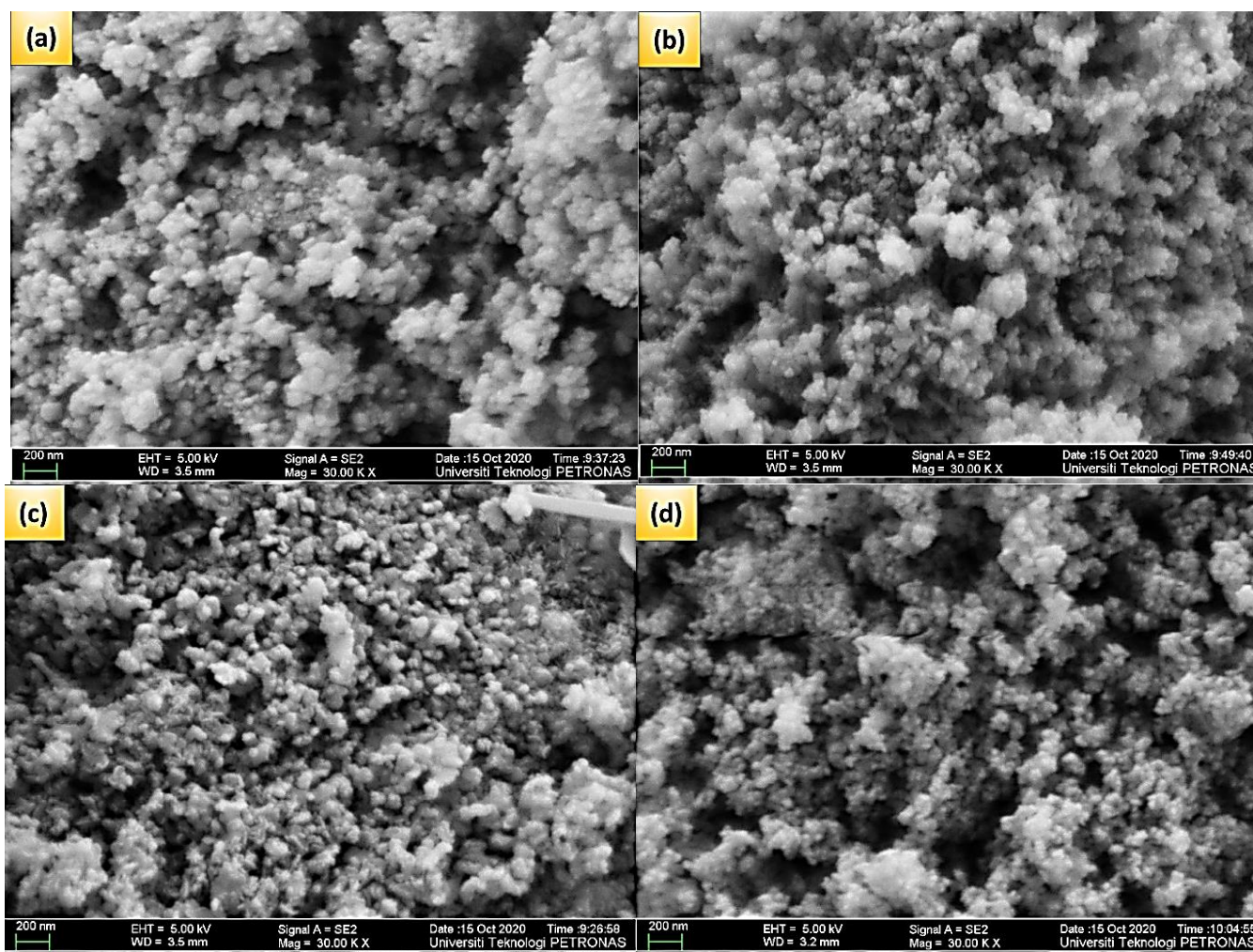
^a surface area computed by the BET method. ^b calculated through Debye–Scherrer equation from XRD peaks of MgO at 43.1° and (200) plane. ^c Determined from H₂-TPR analysis of freshly prepared catalysts.

The pore size distribution for the catalyst support and different catalysts has been analyzed (shown in Figure 4.10). The BJH pore size distribution of prepared catalyst support and that of Ni_f catalyst shows a relatively constricted distribution for the peak values of around 5 nm and 8 nm, respectively. Further culmination of peaks at around 18 nm for W_a and 10 nm for different W loaded bimetallic catalysts (i.e., W_b, W_c, and W_d), respectively, have been observed (Figure 4.10). The BJH pore size analysis confirms the formation of mesoporous materials [73].

4.3.3.3 FESEM

The FESEM images of all the freshly prepared catalysts have been analyzed, and surface morphology at the constant magnification (200nm) has been shown in Figure 4.11. The W_d sample shows an apparent change in the surface morphology on intensifying the W addition to the monometallic Ni_f. The Ni_f catalyst is composed of clustered and linked particles that are dense and have low porosity of the residual pores comparatively. Catalysts formed by W's addition got shifted into the minute grained morphology, which is composed of comparatively consistent shaped crystals (from 20-50 nm). However, throughout the catalyst, only Ni aggregates are visible, and no W agglomerates are visible due to W's very good dispersion within

the catalyst. The reduction of crystal size on W's addition due to its dispersive character catalyst has also been reported in the investigation by Sheng et al.[201]. The small size collection of sphere masses is observed in the Figure 4.11 (a-e), which may be formed during the heat treatment of the catalyst. The particles clump together to each other on the catalyst surface, engendering pores, and due to which a porous textured morphology is developed. The structure of all the samples resembles that of Pacific-elkhorn corals like morphology. The similar morphology has been reported by a recent investigation conducted by Al-Fatesh et al. [204]. Increasing the content of W showed a reduction in grain size of the catalysts and hence increased surface area, which is also verified by BET surface area analysis in Table 4.2. This also agrees with the studies of Khajeh et al. [205].



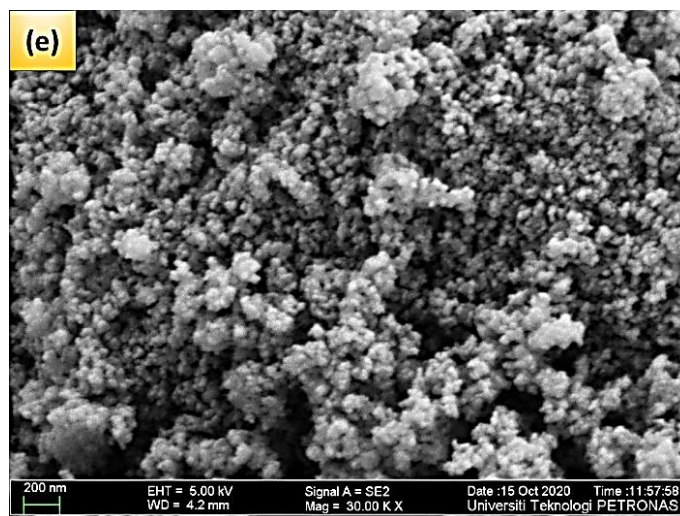


Figure 4.11. FESEM images of catalysts samples (a) Ni_f, (b) W_a, (c) W_b, (d) W_c, (e) W_d

4.3.3.4 EDX and Elemental Mapping

The EDX analysis of the synthesized nanocatalysts Ni_f, W_a, W_b, W_c, and W_d catalysts has been done and shown in Table 4.3. The spectrum of different elemental species has confirmed the elemental composition of all the catalysts (c.f. APPENDIX E). The characteristics peaks of Mg, Al, Ni, and O have been detected in all the samples. However, the W peak has not been detected for the W_a catalyst sample (with 2 wt.% W content). This may be due to W's uniform dispersion throughout the sample, leading to the extremely minute concentration of W in the sample, i.e., beyond the detectable limit of the EDX spectrum. The precision of EDX and EDXRF techniques is vulnerable while measuring the concentration of minute concentrations, it also agrees with the existing literature [206, 207]. For all the other bimetallic samples (i.e., W_b, W_c, and W_d), Tungsten (W) peak is observed clearly with its composition along with the other existing elemental peaks (i.e., Mg, Al, Ni, and O). Moreover, the small crystals of W are dispersed on the catalyst support, which would result in strong metal support interactions (MSI).

Table 4.3. The elemental composition obtained by EDX analysis of prepared catalysts (Ni_f, W_a, W_b, W_c, W_d).

Elements (wt.%) → Catalyst ↓	Mg	Al	O	Ni	W
Ni _f	41.5	20	27	11.5	-
W _a	41	19.6	27.9	11.5	N.D.
W _b	40	19.6	25	11.5	3.9
W _c	38	18	26.5	11.5	6
W _d	36.9	18	25.6	11.6	7.9

The elemental mapping of the synthesized nanocatalysts has been displayed in Figure 4.12. The dot mapping of constituent elements of catalysts confirms their existence in the prepared samples. It has also been observed that the W is very well and uniformly dispersed throughout the catalyst. Further, the better Ni dispersion can be seen clearly in bimetallic (W_a , W_b , W_c , and W_d) catalysts after adding W into the catalyst compared to monometallic Ni (Ni_f) catalyst. The enhanced Ni dispersion is proved by H_2 -TPR results, showing more H_2 consumption and hence making more active sites available for the reaction after the addition of W in the catalyst (cf. Table 4.2). The superior dispersion of active metal ultimately results in its enriched availability and enhanced the catalyst's activity [205].

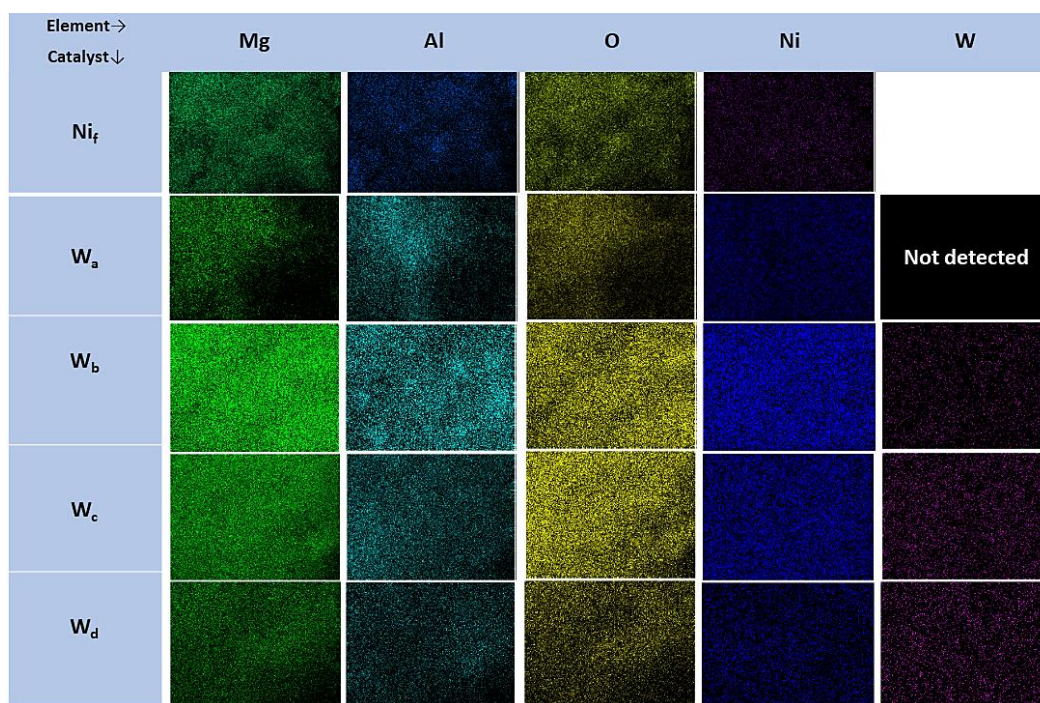


Figure 4.12. Elemental mapping of different freshly synthesized catalyst samples (Ni_f , W_a , W_b , W_c , and W_d)

4.3.3.5 TPR- H_2

The H_2 -TPR analysis is carried out via Thermo Finnigan TPDRO 1100 instrument with heating rate range up to 800°C . The H_2 -TPR profile of the prepared catalysts (i.e., Ni_f , W_a , W_b , W_c , and W_d) has been displayed in Figure 4.13. The wide reduction peaks corresponding to the NiO reduction can be seen for all the synthesized catalysts. However, there is a difference in the reduction fashion of the catalysts. The three peak maxima regions i.e., at around 223°C - 400°C (region I), 423°C - 500°C (region II) and 700°C - 800°C (region III) were observed. The peaks in

the low temperature were accredited to non-amalgamated NiO species. In contrast, the peaks at higher temperatures were ascribed to Ni's composite oxides with W and the catalyst support. As per the existing literature, the peaks at low temperatures correspond to free NiO species due to inadequate MSI [208]. On the other hand, the peaks around 500°C and 800°C correspond to comparatively strong interaction species of NiO_x. Further, the reduction peak between 600°C and 800°C could be associated with the reduction of Ni²⁺ dispersed in the inner layers of the catalyst's support lattice [209, 210]. As per the temperature range of the instrument (i.e., up to 800°C) the peaks within the temperature range of 800°C are analyzed, which also agree with the existing literature [183, 211, 212]. As per the results obtained for the catalysts, it has been observed that on adding more W, the binding energy gets reduced, and the catalyst gets reduced at a lower temperature range. However, there was a significant increase in the hydrogen consumption on adding W to the monometallic Ni catalyst. The H₂ uptake was minimum for the Ni_f catalyst, indicating its lowest activation of sites available for DMR reaction. Whereas, for bimetallic catalyst, the H₂ consumption enhanced to a large extent since the surface area and the available active sites increased by the addition of W (cf. Table1). W_b catalyst showed maximum consumption of H₂ (i.e., 769.55 µmol/g) optimum activity. The H₂ intake by different samples can be arranged in decreasing order as: W_b (769.55 µmol/g) > W_c (738.2 µmol/g) > W_d (679.99 µmol/g) > W_a (572.8 µmol/g) > Ni_f (274.08 µmol/g). This trend of H₂ consumption can be directly correlated with the BET surface area of the prepared catalyst (cf. Table 4.2). This justifies that more NiO was reduced to active metallic Ni, making more active sites available for DMR reaction to occur.

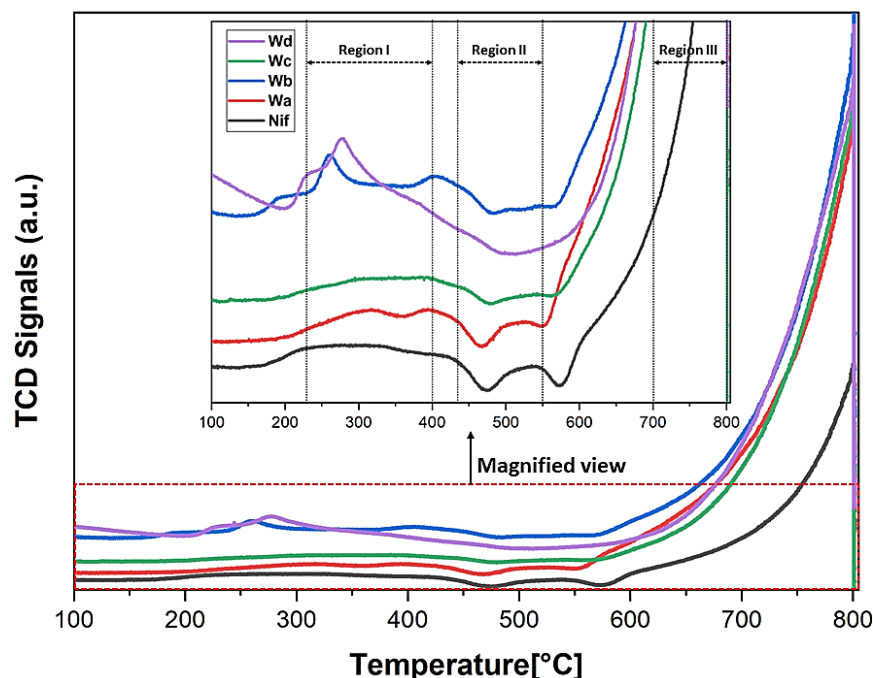


Figure 4.13. TPR-H₂ profile of different synthesized catalysts.

4.3.3.6 TPD-CO₂

The CO₂-TPD profiles of catalyst correspond to the degree of linkage of CO₂ with the catalyst's surface and the basicity of catalyst surface [213]. CO₂-TPD profiles of monometallic Ni (Ni_f) catalyst and different prepared bimetallic catalysts (i.e., W_a, W_b, W_c, and W_d) have been depicted in Figure 4.14. As per the available literature, there exist three types of basic sites i.e., attributed to the low-temperature range (i.e., 50°C-200°C), intermediate temperature range (i.e., 200°C-450°C), and high-temperature range (i.e., 450°C-800°C) corresponding to weak Brønsted basic sites, Lewis acid-base sites, and Lewis basic sites associated with oxygen anions respectively [214]. Generally, a catalyst's CO₂ adsorption ability indicates its basicity, i.e., higher CO₂ adsorption corresponds to the more basic catalyst. The higher catalyst basicity results in less catalyst deactivation and lowers coke formations [215]. Oxides of W are acidic; hence a decrease in the basicity of monometallic Ni_f can be observed clearly on the addition of W [216]. The catalysts can be sequenced in the increasing order of basicity as 136.68, 137.84, 142.25, 190.69, 237.78 $\mu\text{mol g}_{\text{cat}}^{-1}$, i.e., $W_d < W_c < W_b < W_a < \text{Ni}_f$ according to the CO₂ adsorbed by different catalysts. On the other hand, the addition of W resulted in the slight shift of the strong basic site peak (i.e., Lewis basic sites associated with oxygen anions, Figure 4.14) from 440°C to 419°C (evident in the curve corresponding to W_d when compared to Ni_f curve) due to acidification of

catalyst. During DMR reaction, CH_4 will decompose instead of reacting with CO_2 since firmly adsorbed carbon dioxide will not react with methane easily as per Le Chatelier's principle [217]. As far as W addition's influence is concerned, there appears a direct correlation between increasing W content and the basic sites of the catalyst [32]. However, the catalyst's performance may not solely depend on the basicity of the catalyst but also on other physicochemical properties such as surface area, active metal sites, and metal dispersion [37].

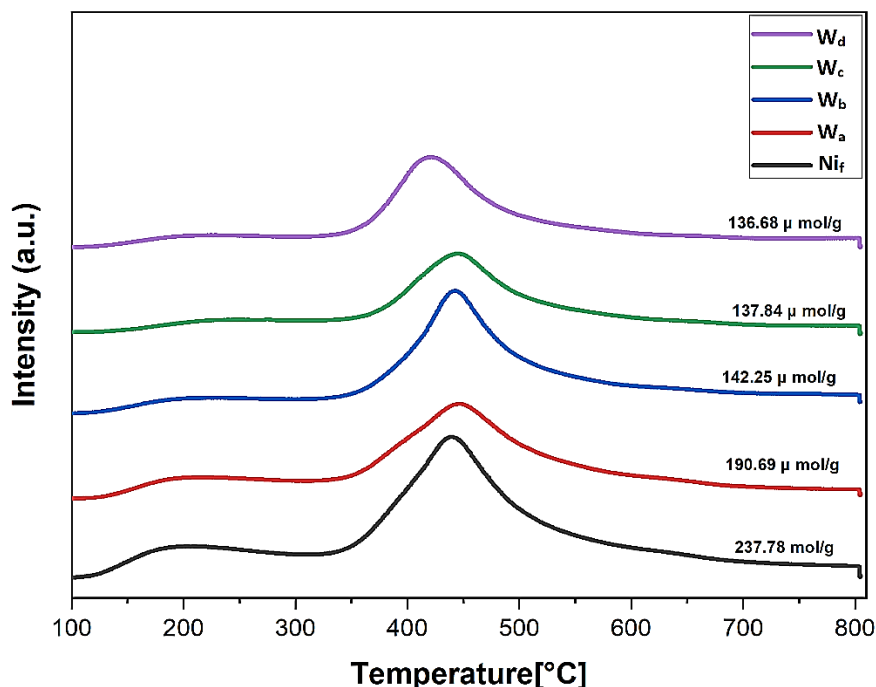


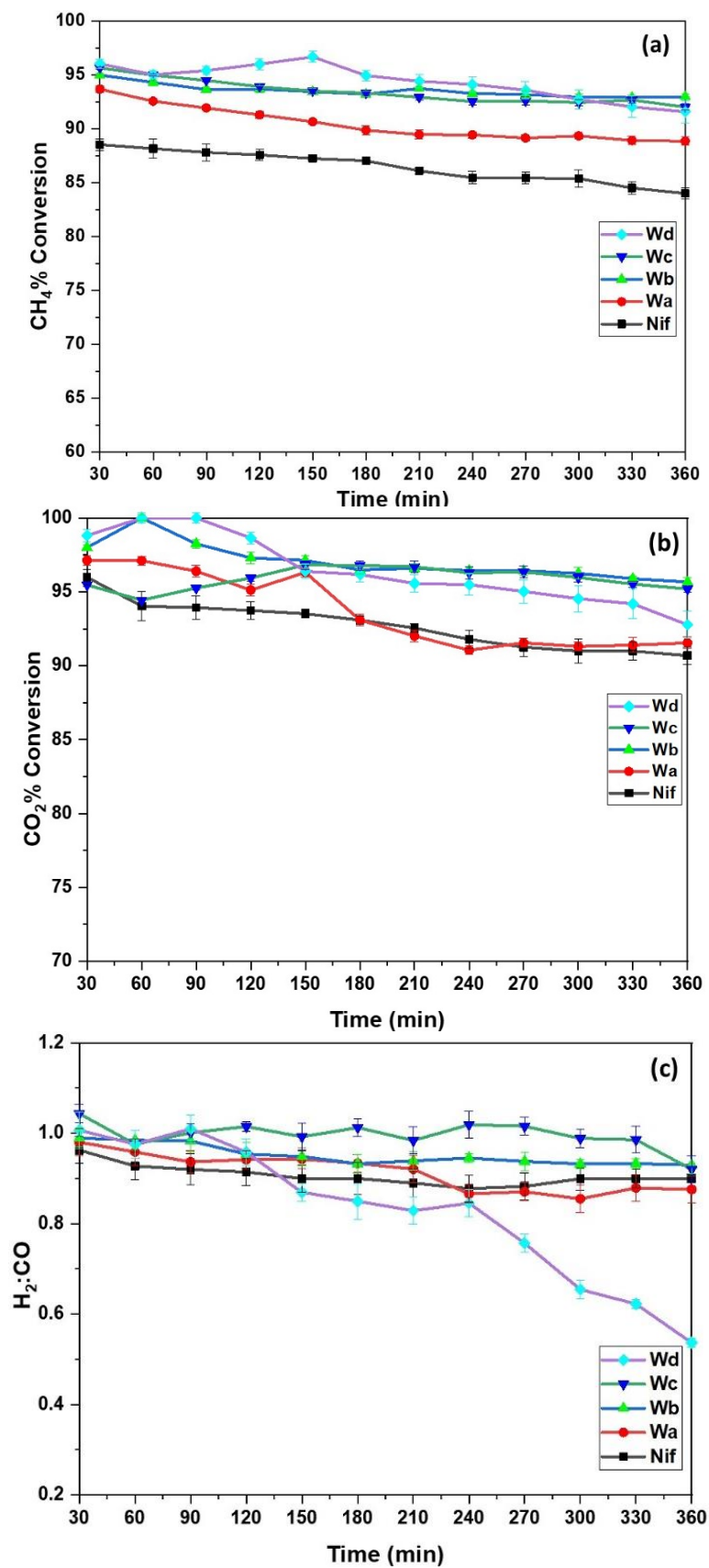
Figure 4.14. TPD- CO_2 profile of different synthesized catalysts.

4.3.2 Performance Evaluation of catalysts for DRM

The activity and stability performance of the prepared catalysts (i.e., Ni_f , W_a , W_b , W_c , and W_d) are tested for DMR reaction in the tubular fixed bed reactor. The reaction was carried out for 6h at 800°C at GHSV of $36000 \text{ cm}^3 \text{ gmcat}^{-1} \text{ h}^{-1}$. The conversions of CH_4 , CO_2 along with H_2 :CO are calculated from eqns. 3.2, 3.3, and 3.4, respectively. The bimetallic Ni-W catalysts have shown significantly elevated conversion compared to monometallic Ni catalyst (Ni_f). It can be seen clearly from Figure 4.15(a-b) that CH_4 and CO_2 conversions improved on increasing the W content from 2% to 8%. However, the initial conversion drops down over 6h of the DMR reaction test. The Ni_f catalyst showed lower conversions comparatively, which dropped from 88.5% to 84% and 95.9% to 90.6% for CH_4 and CO_2 , respectively. However, for the bimetallic catalysts, the CH_4 conversion dropped from 93.7% to 88.8% for W_a , 94.9% to 92.9% for W_b ,

95.6% to 95% for W_c , and 96% to 91.5%, respectively. Likewise, the CO_2 conversion also dropped from initial conversions of 97.1%, 97.9%, 95.4%, and 98.8% to final values of 91.5%, 95.6%, 95.1%, and 92.7% for W_a , W_b , W_c , and W_d , respectively. This enhanced conversion trend is due to enhanced surface area and enriched morphology of bimetallic catalysts, as shown in the surface area and porosity study of the synthesized catalysts. However, it is noticeable for W_b catalyst that it performed quite stably over the 6h of DMR reaction test when compared to other bimetallic catalysts. There is only a slight drop of conversion of W_b catalyst for both CH_4 and CO_2 , respectively, portraying it as the optimum catalyst amongst all the prepared catalysts. Moreover, looking at the $H_2:CO$ results, W_b proved to be the most stable catalyst (varied from 0.98 to 0.93) throughout the reaction. The analysis also showed that coke formed during the reaction was reported to be minimum for W_b catalysts. The CO_2 conversions are always slightly higher than the CH_4 conversions. This may be due to the RWGS reaction taking during DMR reaction. Nonetheless, despite giving the highest initial conversions, the W_d catalyst showed maximum carbon deposition. The $H_2:CO$ dropped drastically from 1 to 0.53 (Figure 4.15 (c)). The 6h reaction tests are repeated thrice to reduce the possible errors and confirm the optimum performance catalyst. It has been noted that a uniform activity has been obtained with a maximum error deviation of 1.25%.

Further, the percentage H_2 and CO yield has been calculated using the eqn. 3.5 and eqn.3.6. and has been depicted in Figure 4.15(d-e) respectively. The bimetallic Ni-W catalysts showed improved yield both for H_2 and CO when compared to monometallic Ni catalyst. The percentage H_2 and CO yields varied from 45.2% to 38.5% and 47.5% to 42% respectively during 6h of DMR reaction monometallic Ni catalyst (Ni_f). The percentage H_2 yield for bimetallic catalysts varied from 49.2% to 44%, 52% to 47%, 51.5% to 41.3% and 53.5% to 25.1% for W_a , W_b , W_c and W_d , respectively. Whereas the percentage CO yield for bimetallic catalysts varied from 50.3% to 45.6%, 54% to 47%, 51.8% to 44.5% and 53.6% to 33.1% for W_a , W_b , W_c and W_d , respectively. Among the bimetallic Ni-W catalysts, the W_b catalyst not only showed comparative superior percentage yield for both H_2 and CO, but also showed maximum stability with least variance in percentage yield during 6h of DMR reaction.



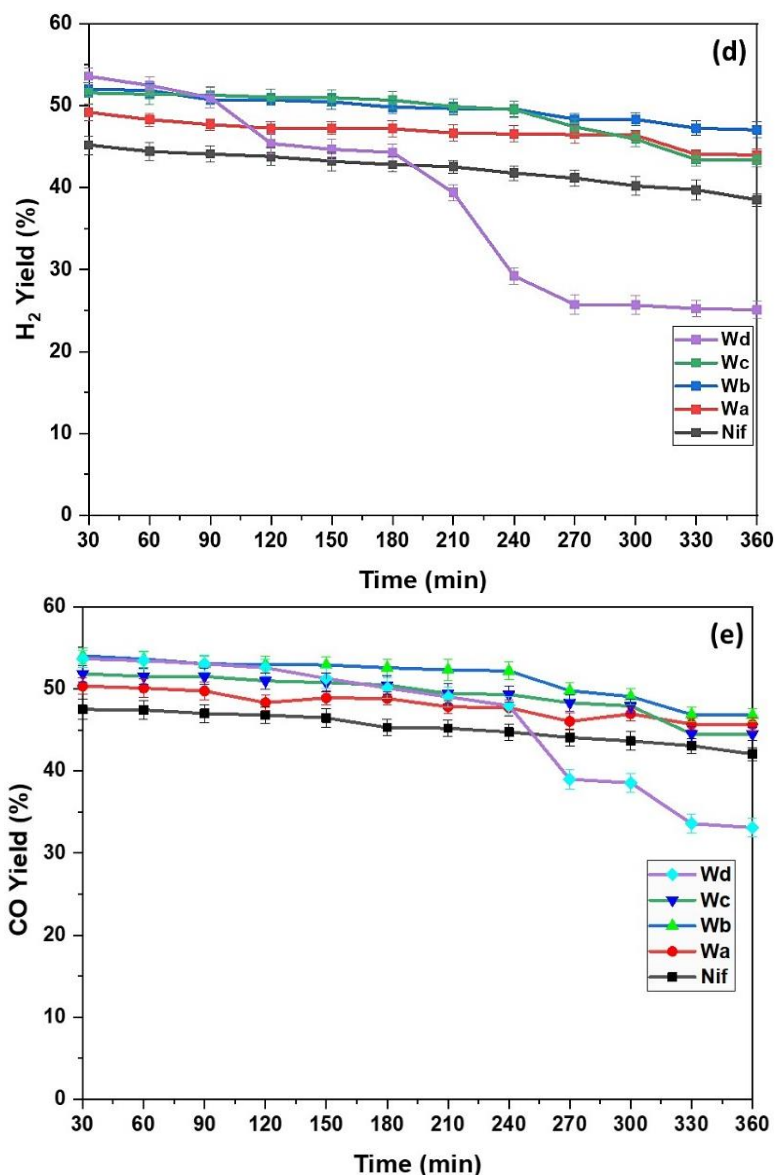


Figure 4.15. Performance evaluation (a) CH₄ conversion (b) CO₂ conversion (c) H₂:CO vs. time, (d) H₂ yield (%) (e) CO yield (%) for synthesized catalysts for 6h reaction.

As evident from the catalytic testing above, the W_b catalyst proved out to be the optimum bimetallic catalyst. Hence the reference monometallic (Ni_f) and optimum bimetallic (W_b) has been used further to determine their TOF by using Eqn. 3.8. The TOF for W_b catalysts has been found to be 15.41 s⁻¹, whereas for Ni_f it is found to be 5.98 s⁻¹. This further supports the superior performance of W_b catalyst over the Ni_f catalyst. The obtained TOF values are compared with the recent research and found to be in the range of reported literature (c.f. Table 4.4).

Table 4.4. TOF of the monometallic and optimum bimetallic catalyst calculated via TPR-H₂ chemisorption analysis [176].

Sr. No.	Catalyst	TOF (s ⁻¹)	Reference
1.	12 wt.% Ni/MgO-Al ₂ O ₃ (Ni _f)	5.98	(This Work)
2.	12 wt.% Ni- 4 wt.% W/MgO-Al ₂ O ₃ (W _b)	15.41	(This Work)
3.	75 wt.% Ni- 25 wt.% Fe/ Al ₂ O ₃	5.80	[176]
4.	75 wt.% Ni- 25 wt.% Co/ Al ₂ O ₃	15.30	[176]
5.	Ru/ Al ₂ O ₃	4.0	[177]
6.	Pt/ Al ₂ O ₃	3.8	[177]
7.	Ni/SiO ₂	15.1	[218]

4.3.3 Stability test for optimum performance Ni-W (W_b) catalyst

The W_b catalyst was further tested further for performance evaluation since it proved to be most stable in activity and performance during the 6h of the DMR reaction test. The stability test of W_b is conducted for 24h of reaction under a similar feed rate and identical reaction condition, as explained above. The catalyst showed high conversion and excellent stability throughout the reaction. The CH₄ and CO₂ conversions dropped insignificantly, i.e., from 95% to 88.8% and 98% to 91.5%, respectively. The syngas ratio was also plausible since it varied from 0.99 to 0.9, even after 24h of DMR reaction (Figure 4.16). The W_b catalyst's high stability can be correlated to various parameters observed during its post DMR reaction characterization. The factors like 'reducibility, type and amount of carbon formed, surface area, the elevated number of active metal sites available for reaction, and stable bimetallic alloy formation,' which hindered the coke formation, have been discussed in the characterization results obtained below.

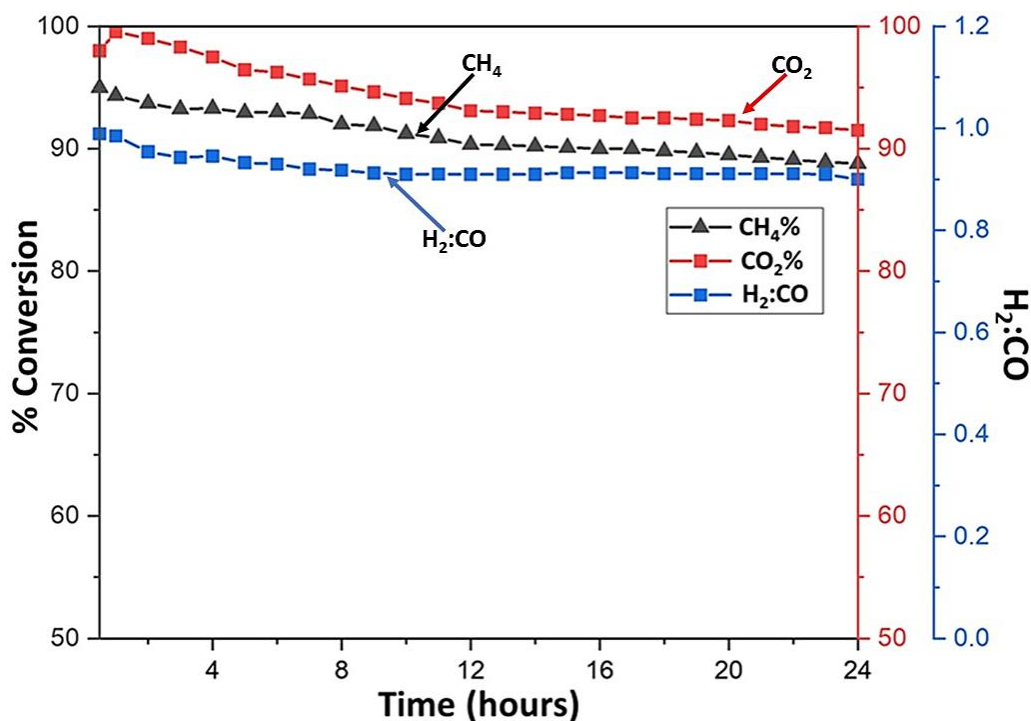


Figure 4.16. Stability test for W_b catalyst for 24h of DMR reaction.

The results obtained in the above analysis is compared with the recent literature and it has been found that the Ni-W catalyst proved out to be superior in terms of its high performance and better stability even after 24 h of DRM reaction. This highly elevated and stable performance of the Ni-W catalyst is due to formation of thermally stable NiWO₄ alloy which restrained the sintering of Ni-W catalyst. The performance of Ni-W catalyst was superior when compared to the other Ni-based catalysts as reported in the literature (arranged in the Table 4.5).

Table 4.5 Comparison of performance and stability of catalysts for DRM reaction in the recent studies employing composite catalysts.

Catalyst	Reaction Temperature (°C)	% Conversion (Maximum)		Major Finding	Reference
		CH ₄	CO ₂		
Ni-Au-Pt/ Al ₂ O ₃	750	87.8	93.3	The catalyst showed stable performance for 6 h of DRM test. Around 9.5 wt.% of coke formation has been reported.	[22]
Ni-Mo/ Al ₂ O ₃	800	79.8	85.9	In corporation of Mo in Ni based catalyst reduced the performance of catalyst for 6 h of DRM test.	[87]

Catalyst	Reaction Temperature (°C)	% Conversion (Maximum)		Major Finding	Reference
		CH ₄	CO ₂		
Ni-Co/CeO ₂	800	80	85	Stable performance of DRM reaction for 10 h of stability test.	[92]
Ni-Ce/MgAl ₂ O ₄	650	66	35	Stable performance has been obtained for 5 h of reaction with 8 wt.% of coke depositions on the catalyst.	[97]
Ni-Mg/Al ₂ O ₃	800	90	93	At 800 °C the high conversions are recorded which reduced gradually with time. The 8.4 wt.% of coke formation has been reported for 6 h of DRM reaction test.	[115]
Ni-Co/Al ₂ O ₃	700	86.1	84.5	The conversion dropped drastically only in 7.5 h of DRM reaction test. The 9.4 wt.% of coke formation has been reported.	[116]
Ni-W/Al ₂ O ₃ -MgO	800	95	98	The catalyst showed high activity and stability for 6 h of reaction. The coke deposited during DRM reaction test is 7.5 wt.%. The catalyst showed around 90% conversion even after 24 h of stability test.	This Study

4.3.4 Characterizations of catalysts post DMR reaction

4.3.4.1 XPS analysis

The XPS spectrum of Ni 2p_{3/2} for both freshly prepared Ni_f and W_b catalysts has been recorded. The characteristic stepped spectra of XPS obtained have been treated, and baseline corrections have been made to plot the binding energy finally (i.e., BE in eV) vs. intensity, as shown in Figure 4.17(a-b). The Ni 2p_{3/2} level spectrum of the complex catalyst can be divided into two main regions. The primary peak for Ni 2p_{3/2} can be seen simulating the charge transfer in the range 859.13-860.18 eV and its satellite peak at 866.20-867.41 eV, respectively. It has been witnessed that BE of Ni 2p_{3/2} for both the catalysts is superior to pure NiO (i.e., BE of Ni 2p_{3/2} for NiO lies in the range 853.8-854.5 eV) [40, 96, 201]. This clearly supports the MSI of Ni²⁺ with the alumina-magnesia (Al₂O₃-MgO) support. Further, it has been evidenced that BE of Ni 2p_{3/2} for Ni_f catalyst is 860.18 eV whereas, BE for W_b catalyst is 859.13 eV.

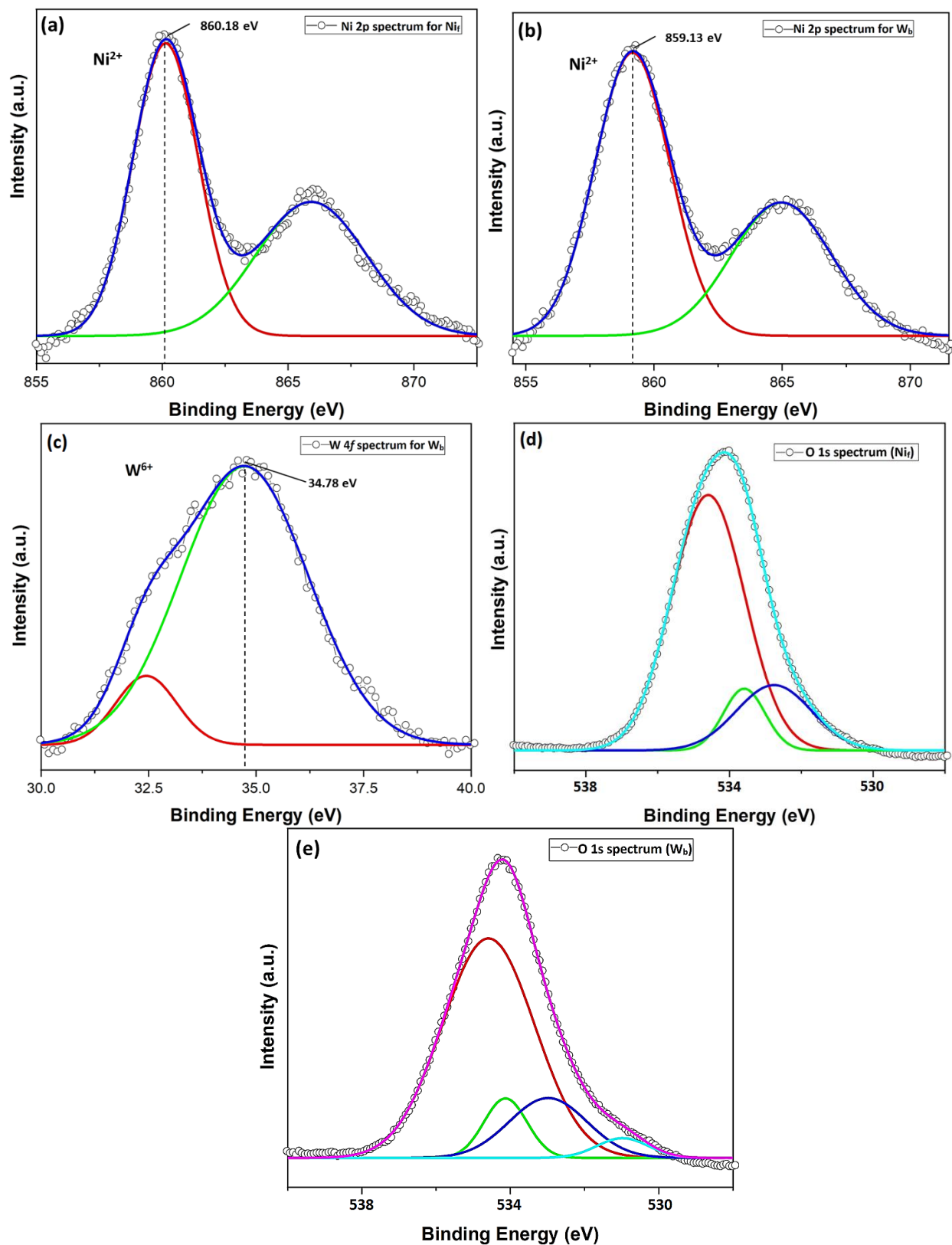


Figure 4.17. XPS spectra for Ni 2p (a) Ni_f and (b) W_b catalysts (c) Narrow scan for W 4f of W_b catalyst and (d-e) XPS narrow scan for O 1s of fresh Ni_f and W_b catalysts, respectively.

This result agrees well with the TPR analysis (c.f. Table 4.2), where the easy reduction at lower temperatures has been witnessed for W_b catalyst compared to Ni_f catalysts indicating low MSI in the case of W_b . This reduction in BE maybe because, when the loosely bound outer shell electrons of W encounter the Ni^{2+} ion, it (the electrons) tries to normalize its charge by intensifying some δ^- charge to it. Hence, the overall electron cloud endeavours to normalize the charge comparatively (i.e., compared to Ni_f catalyst where W is absent), and therefore the overall binding energy gets reduced. The obtained results are in agreement with the previous literature [219]. Further, the narrow scan for W has been conducted for W_b catalyst. The W 4f XPS spectrum for W_b catalyst has been shown in Figure 4.17(c). The BE energy for W 4f_{7/2} in the spectra (corresponding to the chemical environment of W_b catalyst) has been depicted as 34.78 eV. The BE obtained for W 4f_{7/2} suggests the existence of W^{6+} state as reported in the literature [4]. The presence of W^{6+} ion existing in the solid solution (i.e., Ni-W-Al-Mg) creates the possibility of the existence of Ni-W alloy ($NiWO_4$) and oxide of W (WO_3) [41, 220]. This holds good with the XRD analysis of both the catalysts (i.e., W_b and W_{bSp} in Figure 4.8 and Figure 4.18, respectively). It is also evident from the literature that this range of BE obtained for W 4f_{7/2} favours specifically for W^{6+} ions bordered by oxide ions [221]. Therefore, it can imply that the electron transfer between Ni and W has improved their mutual interaction and the synergistic effect leads to the formation of thermally stable Ni-W alloy [220, 221]. The Ni-W alloy has intensified crystallinity further during 6h of DMR reaction, and sharp peaks have been detected in XRD analysis of spent catalyst comparatively.

Figure 4.17(d-e) depicts three different species of oxygen for O 1s scan on the surface of the catalysts (i.e., Ni_f and W_b). The three overlapping peaks observed in the O 1s BE region of Ni_f catalyst are located at 532.5 eV, 533.7 eV, and 535.1 eV, respectively, whereas for W_b catalyst, the peaks are observed at 532.9 eV, 534.2 eV, and 534.8 eV, respectively. The first peak at around BE of 532 eV is ascribed to the lattice oxygen, and the other overlying peaks (at 533 eV and 535 eV) are corresponding to the surface adsorbed oxygen and hydroxyl species, respectively [73]. The intensity of the peak attributed to 535 eV look prominent on Ni_f catalyst when compared to W_b catalyst, which contains W. the high affinity between the surface may explain this behavior chemisorbed OH and MgO, which remains with fraction even after thermal treatment at high temperatures [41, 222, 223]. Furthermore, one additional peak observed at

530.8 eV is ascribed to NiWO₄ (i.e., O-[Ni-W] bond) and WO₃ (i.e., W-O bond) and is found consistent with the literature [220, 224].

4.3.4.2 XRD of spent catalyst

The XRD pattern of both spent catalysts (i.e., Ni_{sp} and W_{b.sp} after undergoing DMR reaction) has been recorded and displayed in Figure 4.18. Some new XRD peaks have been observed for the post-reaction catalyst samples due to some new crystals forming during the reaction. The characteristic peak of carbon deposited during the reaction can be seen clearly on both spent catalysts at the 2-theta value of 26.5°, corresponding to the miller indices of (002) [ICDD file no. 03-065-6212]. The sharp carbon peak for Ni_f and a diminished peak for W_b have been recorded, which has been found consistent with the literature [73, 74, 225]. For the spent bimetallic catalyst (W_b), the Ni-W alloy peak observed at 2-theta values of 46.4° and 72.6° got sharpened and more prominent (compared to the XRD analysis of freshly prepared catalyst). This may be due to the increase in crystallinity of NiWO₄, during the DMR reaction at 800°C. The Ni-W alloy formed is responsible for the stable morphology and performance of W_b catalysts, and the results are in agreement with the literature [226]. Similarly, it has been seen that the peaks corresponding to the spinel Al₂MgO₄ phase at 19.1°, 31.3°, 44.8° and MgO phase at 36.9° and 62.4° (for both catalysts) have shown sharp intensity peaks compared to the fresh catalysts due to the same above reason. The peak for Ni is also observed in both spent catalysts at the 2-theta value of 51.9°C and miller indices of (200). Further a new phase of WC has been detected at 2-theta values of 31.9° and 75° corresponding to miller indices of (001) and (200), respectively for spent Ni-W catalyst and the results are in accordance with the literature [227]. The crystallite size remained almost constant before and after the reaction for the bimetallic W_b catalysts (cf. Table 4.6) because the alloy formed did not allow the Ni to agglomerate into bigger lumps.

Table 4.6. Average crystal sizes of the spent monometallic and optimum bimetallic catalyst with TPO-O₂ results

Catalyst	Average crystal size ^a (nm)	O ₂ consumed (μmol g _{cat} ⁻¹) ^b
Ni _{sp}	54.3	5961.1
W _{b.sp}	23.1	480.2

^a Calculated by Debye-Scherrer equation from XRD peaks for MgO (200) plane. ^b obtained from O₂-TPO analysis of freshly prepared catalysts

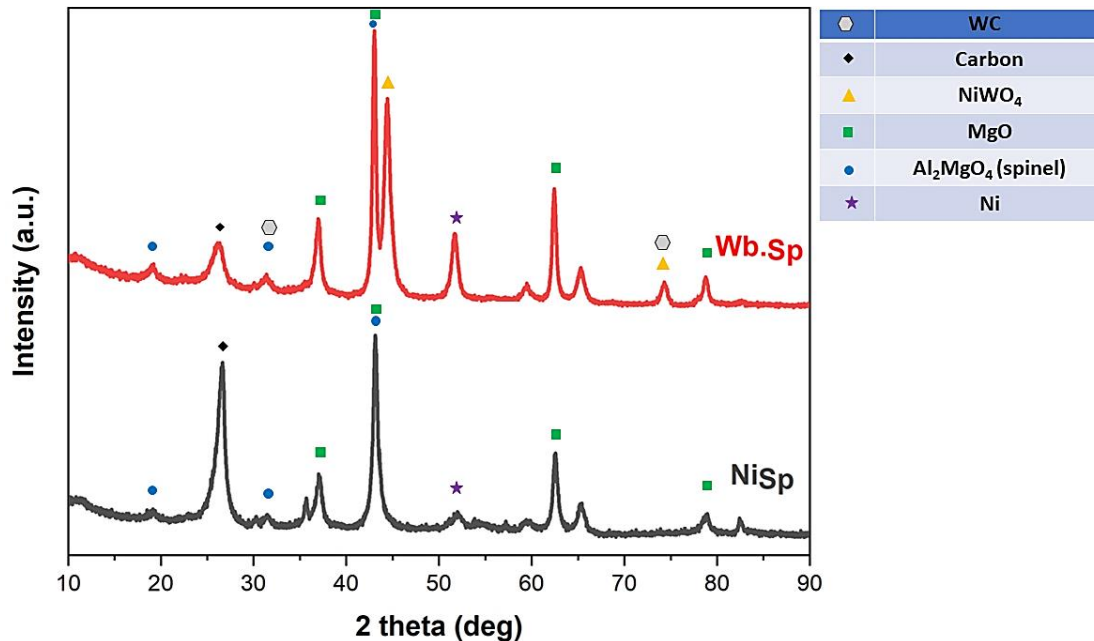


Figure 4.18. XRD pattern for spent (Ni_{Sp} and $\text{W}_{\text{b.Sp}}$) catalysts after 6h of DMR reaction.

4.3.4.3 FESEM of spent catalyst

The FESEM analysis of the spent monometallic (Ni_{Sp}), and the optimum performance bimetallic (W_{b}) catalyst has also been performed to investigate the coke formation further. The FESEM images confirmed the filamentous type of carbon formation for the monometallic Ni_{Sp} catalyst (Figure 4.19(a-b)). The carbon sheets formed during the DMR reaction resembled that of rose petals as depicted in the Figure 4.19(a-b). This type of carbon formation has an inhibitory effect on catalyst performance since it encapsulates the active sites of catalyst. The inferior performance of monometallic Ni catalysts can be evidenced due to the formation of this type of carbon [104, 228]. The TPO results also confirm the amorphous type of carbon formation for the monometallic Ni catalyst.

On the contrary, for the spent bimetallic ($\text{W}_{\text{b.Sp}}$) catalysts, the carbon formed after the DMR reaction was in the form of carbon nanotubes. The carbon nanotubes' morphology is an entangled network of fine ducts, as shown in Figure 4.19(c-d). Various pieces of literature are available regarding the postulates for the CNT growth mechanism on the catalyst surface. However, the breakdown of the feedstock carbon source on the catalyst surface to form carbon nanotube may be illustrated by diffusion precipitation mechanism [229].

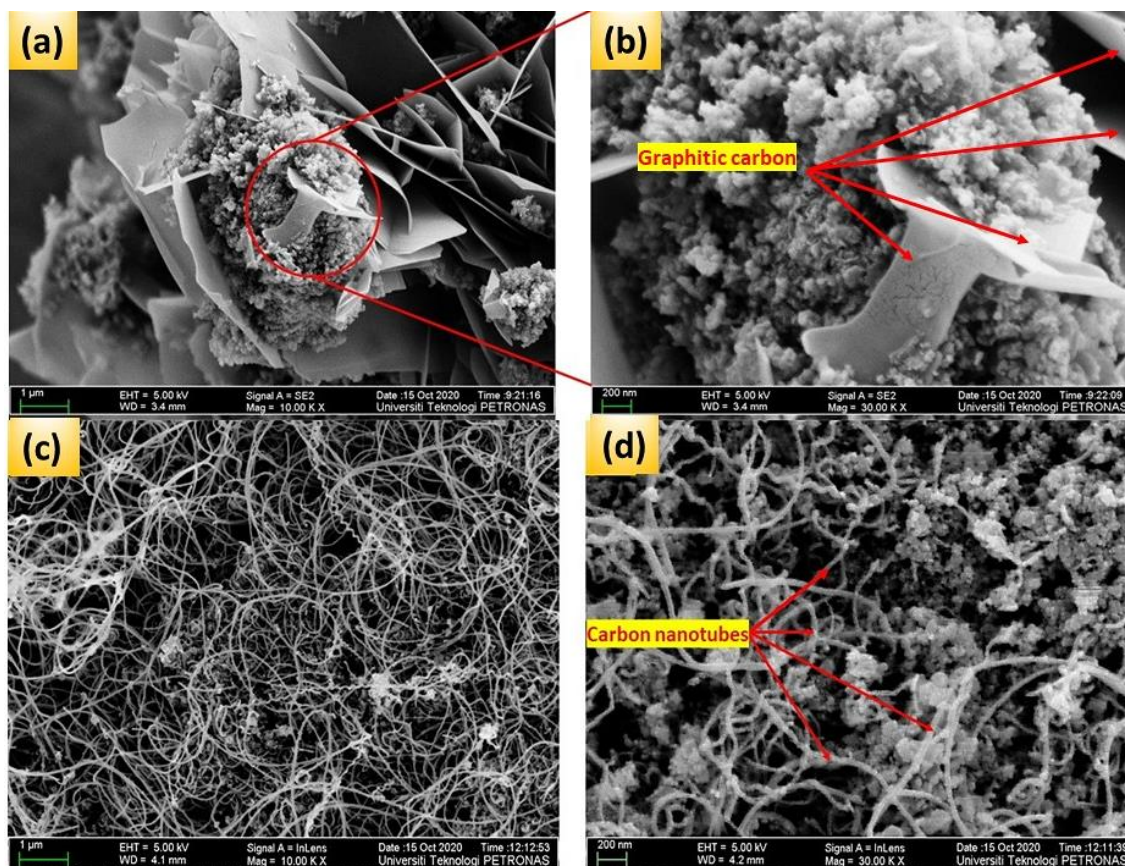


Figure 4.19. FESEM images of spent catalysts with different magnifications showing (a-b) Ni_{Sp} catalyst with carbon nanosheets formed and (c-d) $\text{W}_{\text{b,Sp}}$ with formed CNT during the 6h of DMR reaction.

Furthermore, it has also been reported that MSI also plays a crucial role in the phenomenon of CNT formation (i.e., either through tip growth in case of fragile interaction or growth by the base for strong interactions) [230].

4.3.4.4 EDX and Elemental Mapping of spent catalyst

The EDX analysis of the spent Ni_{Sp} and $\text{W}_{\text{b,Sp}}$ catalysts have been done and arranged in Table 4.7. The spectrum of different elemental species has confirmed the elemental composition of the spent catalysts (c.f. APPENDIX-E). Apart from the elemental peaks of Mg, Al, Ni, and O an additional peak of carbon formed post DMR reaction has been in both the samples. The obtained spectrum confirmed that more coke is formed (about 26% C) for monometallic Ni_{Sp} catalyst, when compared to bimetallic $\text{W}_{\text{b,Sp}}$ catalyst (i.e., about 7.5%) after undergoing DMR reaction.

Table 4.7. The elemental composition obtained by EDX analysis of spent catalysts (Ni_{sp}, W_{b.sp}) after 6 h of DRM reaction.

Elements (wt.%) → Catalyst ↓	Mg	Al	O	Ni	W	C
Ni _{sp}	34.9	17	11	11.1	-	26
W _{b.sp}	39	18.5	19.8	11.4	3.8	7.5

The elemental mapping of the spent catalysts (Ni_{sp} and W_{b.sp}) has been conducted and depicted in Figure 4.20. The dot mapping of constituent elements of catalysts confirms their existence in the prepared samples. It has also been observed that the carbon formed is more prevalent for Ni_{sp} catalyst, whereas a very minute amount of coke is formed for W_{b.sp} catalyst, as displayed by dot mapping of C.

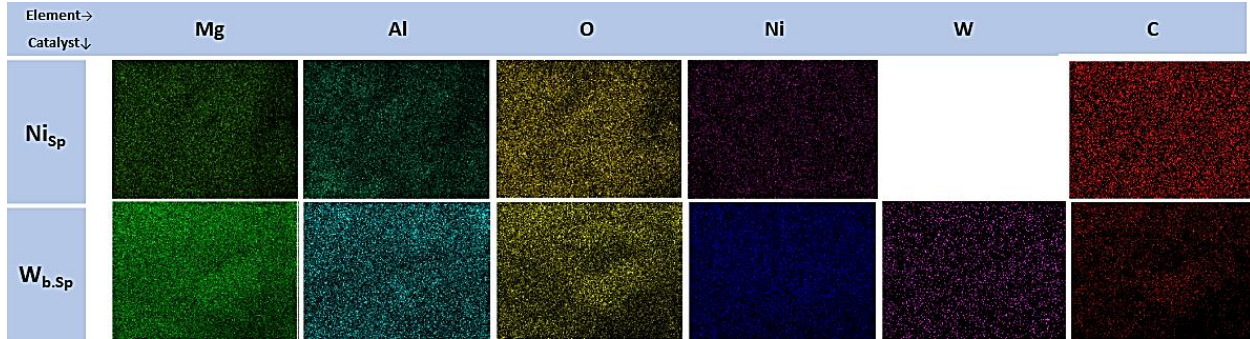
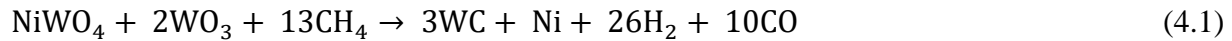


Figure 4.20. The elemental dot mapping of spent (Ni_{sp} and W_{b.sp}) catalysts after 6h of DMR reaction.

4.3.4.5 TPO-O₂ of spent catalyst

The DMR reaction is affected by active metal/metals and depends on metal support interfacial regions [231, 232]. As per the results obtained from XRD analysis of spent catalysts, the WC's formation has been observed along with the Ni-W alloy during the DMR reaction. This may be due to in-situ carburization of WO₃ with the assistance of Ni for CH₄ dissociation, and found consistent with the literature [51, 226]. The reaction taking place on catalyst's can thus be explained by the following equations :



During the DRM reaction the phenomenon occurring on the catalyst in the above equations can be illustrated as the following steps. In the first step (eqn.4.1), the existing Ni-W alloy (evident from XRD and XPS results above) have undergone the reaction with methane [233]. The oxides of tungsten were carbonized by the aid of nickel for dissociation of methane to give tungsten carbide (eqn.4.1) during DMR reaction performed at 800°C. The formation of tungsten carbide follows and assists in the activation of carbon dioxide and thus hinders the coke formation (eqns.4.2 and 4.3). Hence, it finally resulted in diminished coke formation when compared to monometallic Ni catalyst (evident from EDX results in Table 4.7).

The activation of CO₂ by WC formed can be explained further by the elementary reactions shown in eqns. (4.4-4.7). The CO₂ gets adsorbed on catalyst to dissociate into CO and O*. The educt O* then combines the carbon on the metal carbide surface (i.e., C_s) and a vacant site (⁰) is created. This vacancy is then further occupied by either O* which oxidize the carbide into the metal oxide, or by C* from the carbon adsorbed from CH₄ forming the carbide again.



This above elementary reaction steps are also found consistent with the literature [51]. The TPO-O₂ profiles of the spent catalysts (i.e., Ni_{sp} and W_{b,sp}) have been displayed in Figure 4.22. The signal intensity of O₂ consumed depicts the quantity of accumulated carbon. The three main types of carbons are ascertained and named as C_α, C_β, and C_γ [232]. The carbon species (C_α) that gets oxidized at and below 400°C is amorphous type carbon shrouding the metal surface. The carbon species (C_β) at around 600°C is somewhat graphitic, and the peaks at and above 650°C are ascribed to (C_γ) carbon nanotube [25, 232]. The reaction mechanism form DRM can be sketched as depicted in Figure 4.21 below.

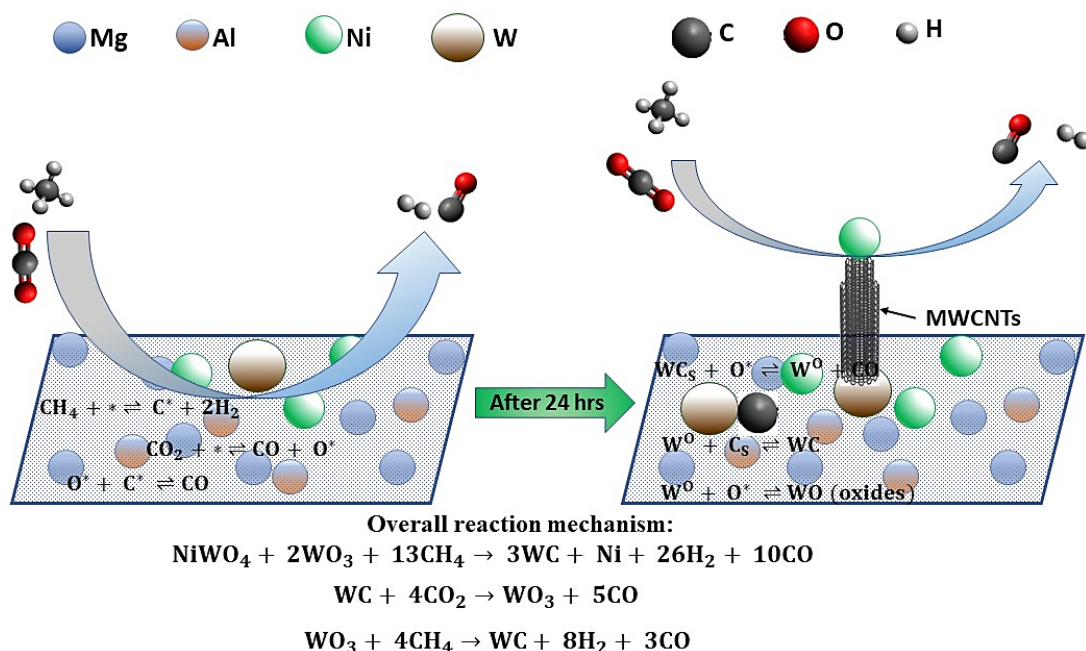


Figure 4.21. The proposed reaction mechanism for DRM on Ni-W bimetallic catalyst [96].

The spent monometallic Ni_{Sp} shows a big central peak at around 400°C , which indicated the existence of $\text{C}\alpha$ species. The formation of amorphous ($\text{C}\alpha$) carbon may be the reason for the lower catalytic activity of the monometallic catalyst. Whereas the spent bimetallic catalyst W_{bSp} showed a single sharp peak at around 650°C , depicting $\text{C}\gamma$ type carbon deposition. The small intensity peak is shown by W_{bSp} catalyst, convey diminished coke formation comparatively. The signal depicts the formation of carbon nanotubes ($\text{C}\gamma$), which is also confirmed by FESEM images of the spent catalyst (Figure 4.19(c-d)). Hence it can be concluded from the above analysis that catalyst W_{bSp} showed comparatively less carbon formation (in the form of carbon nanotubes) than Ni_{Sp} for 6h of DMR reaction. The amount of O_2 consumed by each spent catalyst (i.e., Ni_{Sp} and W_{bSp}) sample has been displayed in Table 4.6. It has been reported in the literature that $\text{C}\alpha$ type carbon is formed primarily by CH_4 decomposition at the early stage of DMR reaction. The oxides of W are Brønsted acids, and hence they are very good oxidizing agents [234]. Therefore, W easily reacts with the amorphous carbon ($\text{C}\alpha$), whereas it is hard to reform carbon nanotubes due to their high crystallinity [235].

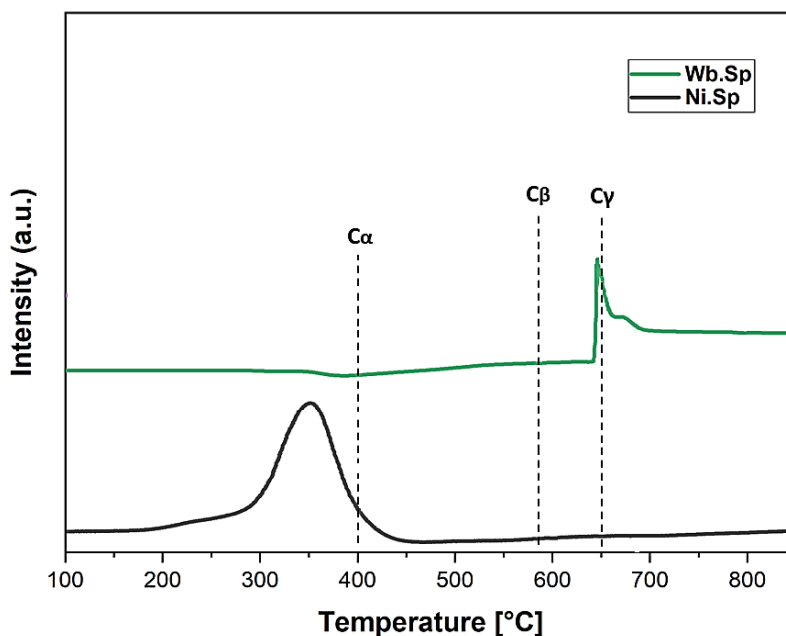


Figure 4.22. TPO-O₂ profiles of spent (Ni_{Sp} and W_{b.Sp}) catalysts after 6h of DMR reaction at 800°C.

4.3.4.6 RAMAN Analysis

The spent catalysts (i.e., Ni_{Sp} and W_{b.Sp}) are further characterized by employing Raman spectroscopy to study the graphitization of the carbon deposited during the DMR reaction. The results obtained by Raman analysis verified the formation of different types of carbon deposited on Ni_{Sp} and W_{b.Sp} catalysts. The two peaks obtained (for Ni_{Sp}) at 1341 cm⁻¹ and 1587 cm⁻¹ are corresponding to D-band and G-band, respectively, and are found consistent with the literature [236]. The peak at G-band is associated with lateral stretching of all sp² pairs of atoms corresponding to graphitic carbon structure. Conversely, the D-band is ascribed to sp² sited and denotes disarranged carbon structure (generally amorphous carbon or disordered lattice carbon) [232]. The ratio of intensities of D and G band (i.e., I_D/I_G) is used to assess the characteristics of carbon nanotubes. The lower values of ratio (i.e., I_D/I_G < 1) implies superior grade graphitization with rare defects in the crystal lattice, whereas higher values of ratio (i.e., I_D/I_G > 1) denote amorphous carbon with no or very small, the ordered arrangement of the lattice. The Lorentzian line shape method is used to fit the spectra, and the I_D/I_G ratio is determined by taking the ratio of the integrated areas under the peaks. It can be easily established from Figure 4.23 that I_D/I_G ratios of 1.72 and 0.47 are obtained for catalysts Ni_{Sp} and W_{b.Sp} respectively. Hence, it indicates that carbon nanotubes may have formed on the surface of W_{b.Sp} catalyst due to higher peak intensity

of G-band. The results are found consistent with the FESEM and TPO analysis above (Figure 4.19 and Figure 4.22). Furthermore, the peak at 2696 cm^{-1} is allocated as a G' band corresponding to second-order Raman scattering, which is generally associated with the purity of carbon nanotubes. Hence, it can be established that on adding W to the Ni catalyst, the morphology of the carbon formed on the catalyst has been modified, i.e., composite catalysts promoted the formation of CNT appreciably.

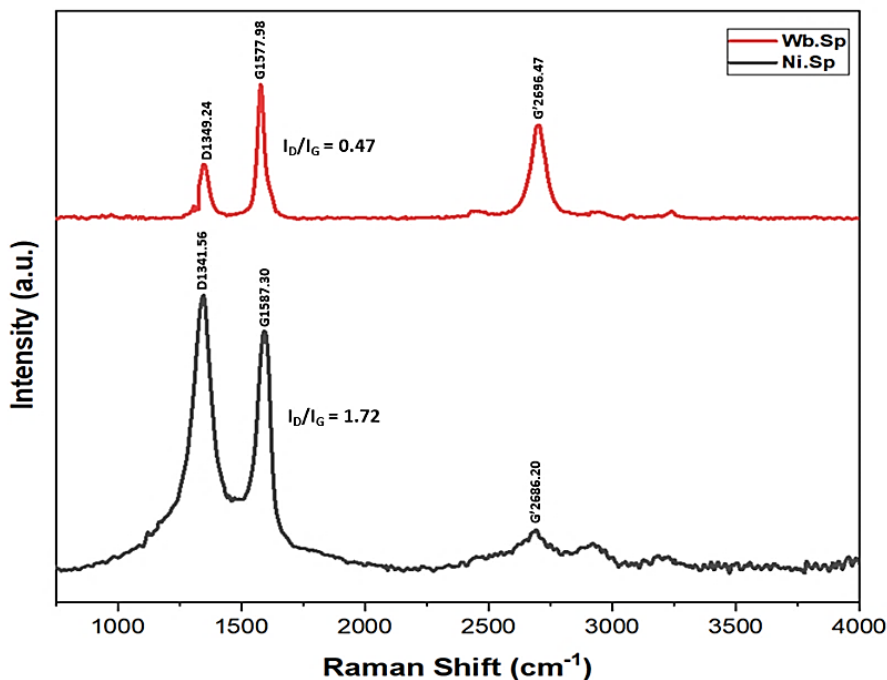


Figure 4.23. Raman analysis of spent (Ni_{Sp} and $\text{W}_{\text{b.Sp}}$) catalysts after 6h of DMR reaction at 800°C .

4.3.4.7 TEM of spent catalyst

TEM analysis of the spent catalysts (Ni_{Sp} and $\text{W}_{\text{b.Sp}}$) is conducted to get further insight into the carbon deposition. The FESEM images of the spent catalysts (Figure 4.19) depicted the formation of carbon nanosheets for Ni_{Sp} catalyst and CNT for $\text{W}_{\text{b.Sp}}$ catalyst, respectively. The Ni_{Sp} catalyst surface was shrouded by amorphous carbon nanosheets, due to which the contact of CH_4 reactants with the active sites of the catalyst is hindered. This type of carbon deposition verifies the low activity of the monometallic catalyst. Conversely, the bimetallic catalyst ($\text{W}_{\text{b.Sp}}$) forms a carbon nanotube, validating the result of TPO (as evident from Figure 4.22). TEM analysis shows a composite network of amorphous carbon (as dark spots all over the sample) for Ni_{Sp} catalyst in Figure 4.24(a). Nonetheless, for $\text{W}_{\text{b.Sp}}$ the TEM results confirmed the formation

of multi-walled carbon nanotubes (MWCNTs) as they are thick and composed of tubed piled one over the other as depicted in Figure 4.24(b). The comparable results for MWCNT formation has been reported by Al Swai et al. [25] and Charisiou et al. [237]. These MWCNT can be utilized in several industrial and eco-friendly applications and may help to enhances the process economy [238]. The MWCNTs can significantly be used in the field of nano electronics for making diodes and transistors. Recently MWCNT's have been proposed for their efficient applications in energy storage and production in fuel cells. Further, MWCNTs can be efficiently employed in water treatment, drug delivery, and sensing [239], [240].

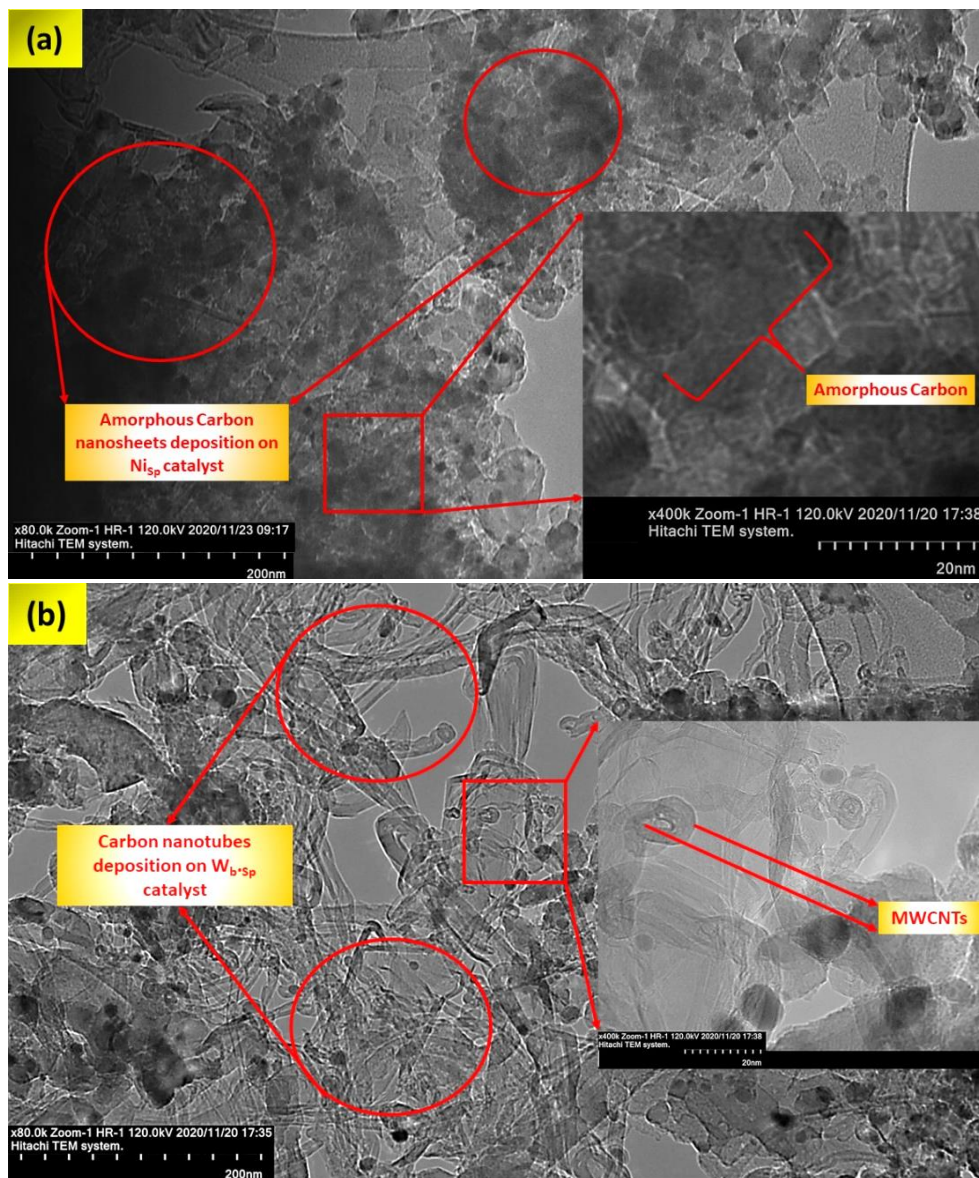


Figure 4.24. TEM analysis of spent (Ni_{sp} and $W_{b,sp}$) catalysts after 6h of DMR reaction for at 800°C.

Hence, it may be inferred from the above analysis that addition of W as a bimetal has an enhancing effect on the performance and stability of catalyst and with 12wt.% Ni-4wt.% W loading showed the best performance. This high-performance catalyst is further analyzed for optimization studies.

4.4 Process Optimization Using RSM

In this section, the outcome of input process parameters (i.e., A: reaction temperature and B: feed ratio [CH₄: CO₂]) on the process responses (i.e., % CH₄ conversion, % CO₂ conversion and H₂:CO ratio) were examined for DRM process over the optimum performance Ni-W bimetallic catalyst by employing the CCD interface. From the section 4.2 and 4.3 the screening of catalysts leads to Ni-W/MgO-Al₂O₃ catalyst, with 12wt.% Ni and W (4wt.%) on Al₂O₃-MgO (with Al₂O₃: MgO of 1:2). The DOE obtained as per the CCD interface for optimization study and the reactions have been précised in Table 4.8. The input process parameters have been represented in coded notations from Table 3.3. The reaction was carried out for 6 h each over a temperature range of 600 °C – 800 °C, a feed ratio (CH₄:CO₂) range of 0.5-1.5 at constant GHSV of 36000 cm³gm_{cat}⁻¹ h⁻¹. This range for input process parameters has been taken and studied keeping in view about the endothermic nature of DRM reaction and as per available literature [130], [154]. Further, this constant GHSV is used since for the reactor used maximum conversion achieved is at a flow rate of 60 ml min⁻¹ or GHSV of 36000 cm³gm_{cat}⁻¹ h⁻¹. The conversion increased from GHSV of 12000 cm³gm_{cat}⁻¹ h⁻¹ to 36000 cm³gm_{cat}⁻¹ h⁻¹ and remained constant on further increasing the GHSV.

Table 4.8. The DOE suggested by CCD along with responses obtained.

Input Process Parameters (Coded values)			Response		
Run	A: Temperature	B: Feed Ratio (CH ₄ : CO ₂)	CH ₄ Conversion (%)	CO ₂ Conversion (%)	H ₂ :CO Ratio
1	+1	0	93.5	97.5	0.96
2	0	+1	65	77.5	1.17
3	0	-1	80.4	49.5	0.65
4	0	0	75.2	78.1	1.13
5	-1	+1	58.3	69	1.1

6	+1	+1	89	98	1.1
7	0	0	74.2	77.8	0.99
8	-1	-1	68.9	36.2	0.59
9	+1	-1	98.9	64	0.6
10	0	0	73.4	76.6	0.96
11	0	0	74.8	75.2	0.92
12	-1	0	64.3	62.3	0.98
13	0	0	75.2	74.8	0.88

4.4.1 Effect of reaction parameters on reactant's conversion

The effect of input reaction parameters (i.e., CH₄ and CO₂ feed ratio and the temperature) on the output (i.e., percentage conversions of CH₄ and CO₂ along with the syngas ratio) has been studied in detail in this section.

4.4.1.1 Effect of reaction parameters on CH₄ conversion

The experimental data attained from DRM reaction over Ni-W/MgO-Al₂O₃ catalyst is fitted into the quadratic model obtained from RSM (CCD) as per equation 4.8. The RSM model attained for the percentage conversion of CH₄ has been scrutinized on a 95% confidence level for its algorithmic significance. The ANOVA results (i.e., degrees of freedom (DOF), the sum of the square, F- values, mean square and P-values) have been summarized in Table 4.9. The ANOVA result confirmed that the RSM models for CH₄ conversion to be significant statistically since the p-value < 0.05. Furthermore, the RSM model's significance is ratified by the obtained F-value. The F-value of 167.36 attained from the assay denotes that model is significant and there is only a 0.01% probability that this large "Model F-Value" may occur due to noise. Hence, the obtained model has less noise interference. The ANOVA findings also show that, since the p-value is around 5%, hence the lack of fit is not significant. This confirms the meticulous fitting of data by the RSM model.

Table 4.9. ANOVA table for CH₄ conversion obtained from (CCD) RSM.

Response	Model Terms	Sum of squared	DOF	Mean square	F-value	P-value	
CH ₄ Conversion (%)	Model	1638.88	5	327.78	167.36	<0.0001	significant
	A-Temperature	1347.00	1	1347.00	687.76	<0.0001	
	B-Feed Ratio	214.80	1	214.80	109.68	<0.0001	
	AB	0.12	1	0.12	0.06	0.8097	
	A ²	74.04	1	74.04	37.80	0.0005	
	B ²	2.89	1	2.89	1.47	0.2640	
	Residual	13.71	7	1.96			
	Lack of Fit	11.36	3	3.79	6.44	0.0519	not significant
	Pure Error	2.35	4	0.58			
	Cor Error	1652.59	12				

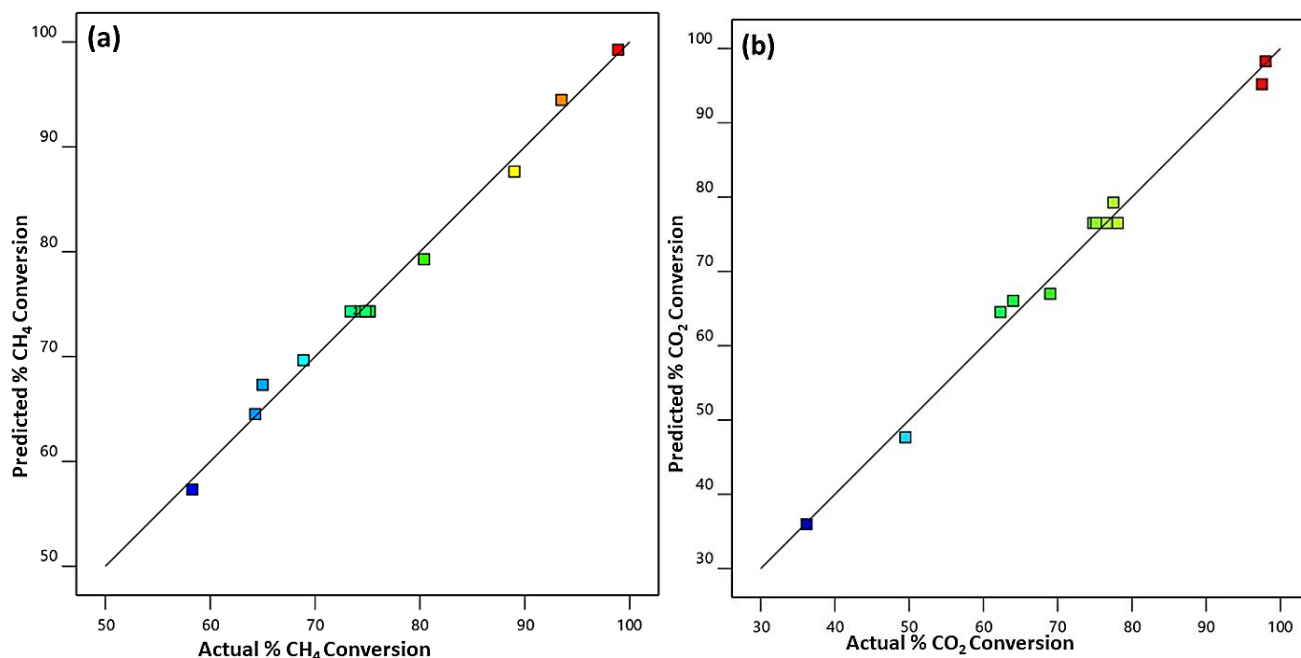
The ANOVA assay findings further exhibit that the process parameter terms (i.e., A, B and A²) are significant (due to p-values<0.05). However, the terms AB and B² are not substantial (due to p-values>0.05) but still show interaction amid reaction temperature and feed ratio, as per the quadratic model equation. It shows that the input parameters (i.e., reaction temperature and feed ratio) significantly influence CH₄ conversion. It is evident from the obtained F-value chart that temperature has a major effect on CH₄ conversion because it has the greatest F-value. This trend is found consistent with the literature, where it has been concluded that temperature has the most significant influence on methane conversion for DRM process [49], [152].

The quadratic model (in coded process parameter terms) obtained after ANOVA can be written as:

$$\text{CH}_4 \text{ conversion (\%)} = 74.32 + 14.98A - 5.98B + 0.175AB + 5.18A^2 - 1.02B^2 \quad (4.8)$$

4.4.1.2 Assessment of observed and predicted conversion of CH_4

The RSM model's reliability for CH_4 conversion has been checked by placing the experimental data in the model. The experimental data are then compared with the predicted data obtained from the analysis, as shown in Figure 4.25 (a). It has been witnessed that predicted value points are well scattered and in close proximity to the parity line. This further validates the robustness of the model. The statistical analysis of the actual vs predicted values had been conducted using design expert version 12. The results obtained exhibits that the coefficient of determination (i.e., R^2) and the adjusted R^2 value are 0.992 and 0.986, respectively, whereas a standard error of 1.84% is obtained. A highly precise correlation between the actual and the predicted CH_4 conversions is indicated by the higher R^2 and adjusted R^2 values. The reduced value of error suggests insignificant inconsistency amongst the actual and predicted values of CH_4 conversion.



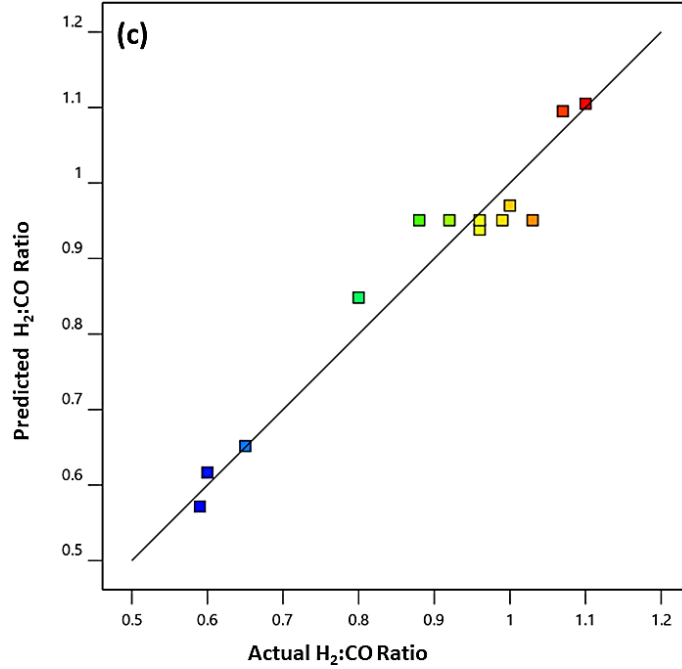


Figure 4.25. The actual vs predicted value plots obtained from RSM.

4.4.1.3 Effect of reaction parameters on CO₂ conversion

The RSM model for percent conversion of CO₂ attained is represented by equation 4.9. Consequently, the model for CO₂ conversion is examined by ANOVA as a précised in Table 4.10. The outcome of ANOVA showed the significance of the model used to forecast the conversion of CO₂ (since its p-values < 0.05). The lack of fit (with p-value > 0.05) further supported that the model is significant. This implies that the experimental data fit well into the model, and the lack of fit is insignificant for the model used. The outcomes of ANOVA summarized in Table 4.10, depicts that all the process parameters terms (coded terms expect AB) are significant (due top-value < 0.05). This indicates that the process parameters (i.e., temperature and feed ratio) have a considerable effect on the conversion of CO₂. Further, it is evident from the obtained F-value chart that feeds ratio and temperature have a major effect on CO₂ conversion (since the F-values are 308.56 and 290.60, respectively). Subsequently from the above effect, the square of feed ratio (i.e., B²) have a prominent influence on the conversion of CO₂ (F-value 96.87) compared to other interaction effects. The quadratic model (in coded process parameter terms) obtained after ANOVA can be written as:

$$\text{CO}_2 \text{ conversion (\%)} = 76.51 + 15.33A + 15.80B + 0.3AB + 3.35A^2 + 13.05B^2 \quad (4.9)$$

Table 4.10. ANOVA table for CO₂ conversion obtained from (CCD) RSM

Response	Model Terms	Sum of squared	DOF	Mean square	F-value	P-value	
CO ₂ Conversion (%)	Model	3387.57	5	677.51	139.57	< 0.0001	significant
	A-Temperature	1410.67	1	1410.67	290.60	< 0.0001	
	B-Feed Ratio	1497.84	1	1497.84	308.56	< 0.0001	
	AB	0.3600	1	0.3600	0.0742	0.7932	
	A ²	31.03	1	31.03	6.39	0.0393	
	B ²	470.24	1	470.24	96.87	< 0.0001	
	Residual	33.98	7	4.85			
	Lack of Fit	25.14	3	8.38	3.79	0.1153	not significant
	Pure Error	8.84	4	2.21			
	Cor Total	3421.55	12				

4.4.1.4 Assessment of observed and predicted conversion of CO₂

The RSM model (i.e., attained from equation 4.9) has been consequently examined by the actual (experimental) and predicted conversion values. The actual (experimental) values of the reaction parameters were inserted in the RSM model, and the predicted values were obtained as depicted in Figure 4.25(b). It has been observed that the observed and the predicted values are dispersed nearby and fits well with the parity line. Additionally, the model has been inspected statistically to validate its sturdiness. The results obtained shows that the coefficient of determination (i.e., R^2) and the adjusted R^2 value are 0.9901 and 0.9830, respectively, whereas a standard error of around 2.2 % is observed. Hence, it shows no significant difference between the actual and predicted values of CO₂ conversion. The obtained results are in agreement with the existing literature [152].

4.4.1.5 Effect of reaction parameters on H₂:CO ratio

The final RSM model for H₂:CO ratio attained in terms of coded parameters is displayed as equation 4.10. The ANOVA was successively employed to check the significance of the model. The quadratic model obtained for H₂:CO was reliable for predicting its (H₂:CO ratio) values since the p-value for the model is less than 0.05 (p-value = 0.0002). Furthermore, the ANOVA results for lack of fit support the model's sturdiness (due to its p-value>0.05). The ANOVA results (summarized in Table 4.11) convey the model's significance and suggest that the feed ratio (evident from F-value) has a prominent effect on the H₂:CO ratio compared to temperature. It agrees with the performance evaluation results of DRM reaction conducted, which showed that the H₂:CO ratio increased significantly on increasing the feed ratio.

$$\text{H}_2\text{:CO} = 0.9507 - 0.045A + 0.2217B - 0.0577A^2 - 0.0774B^2 \quad (4.10)$$

Table 4.11. ANOVA table for H₂: CO obtained from (CCD) RSM.

Response	Model Terms	Sum of squared	DOF	Mean square	F-value	P-value	
H ₂ :CO	Model	0.3499	5	0.0700	26.02	0.0002	significant
	A- Temperature	0.0121	1	0.0121	4.52	0.0711	
	B-Feed Ratio	0.2948	1	0.2948	109.62	< 0.0001	
	AB	0.0020	1	0.0020	0.7530	0.4143	
	A ²	0.0091	1	0.0091	3.39	0.1084	
	B ²	0.0166	1	0.0166	6.15	0.0422	
	Residual	0.0188	7	0.0027			
	Lack of Fit	0.0051	3	0.0017	0.4962	0.7044	not significant
	Pure Error	0.0137	4	0.0034			
	Cor Total	0.3688	12				

4.4.1.6 Assessment of observed and predicted values of $H_2:CO$ ratio

The statistical capability of the RSM model (i.e., attained from equation 12) have been tested by putting the actual (experimental) and predicted ratio values. The plot between actual and predicted outcomes for $H_2:CO$ has been depicted in Figure 4.25(c). It can be elucidated that the predicted and actual data points are dispersed nearby the parity line and agree well with the model. Furthermore, the model's reliability can be evidenced by its R^2 value, i.e., greater than 0.8 (i.e., 0.9490). Therefore, the difference between the actual and predicted values is insignificant and goes well with RSM's model. The obtained trend is in agreement with the literature [241], [242].

4.4.2 Response surfaces interaction of RSM model

The 3-D response along with the contour plots displaying the of the interaction of temperature (A) and feed ratio (B) on percentage conversion of CH_4 , CO_2 and $H_2:CO$ for DRM process over Ni-W/ Al_2O_3 catalyst are shown in Figure 4.26. The conversion of CH_4 and CO_2 is noticed to increase from the initial minimum values of 58.3% and 49.5% to a maximum value of 98.9% and 97.5% respectively. The $H_2:CO$ ratio has risen from a minimum of 0.6 to 1.1 as the maximum obtained value. It is evident from the plots corresponding to CH_4 and CO_2 conversion (Figure 4.26(a-d)) that both temperature and feed ratio significantly influence the conversion. Whereas the feed ratio has a major effect on the $H_2:CO$ ratio compared to temperature input (Figure 4.26 (e-f)). Further, it can be seen from the obtained plots for CH_4 conversion, the temperature in the dominating factor compared to the feed ratio. On the other hand, feed ratio dominates the temperature comparatively for CO_2 conversion, as indicated in the red-colored response. The response surface interactions obtained are in accordance with the ANOVA results and were found to be consistent with the literature [242, 243].

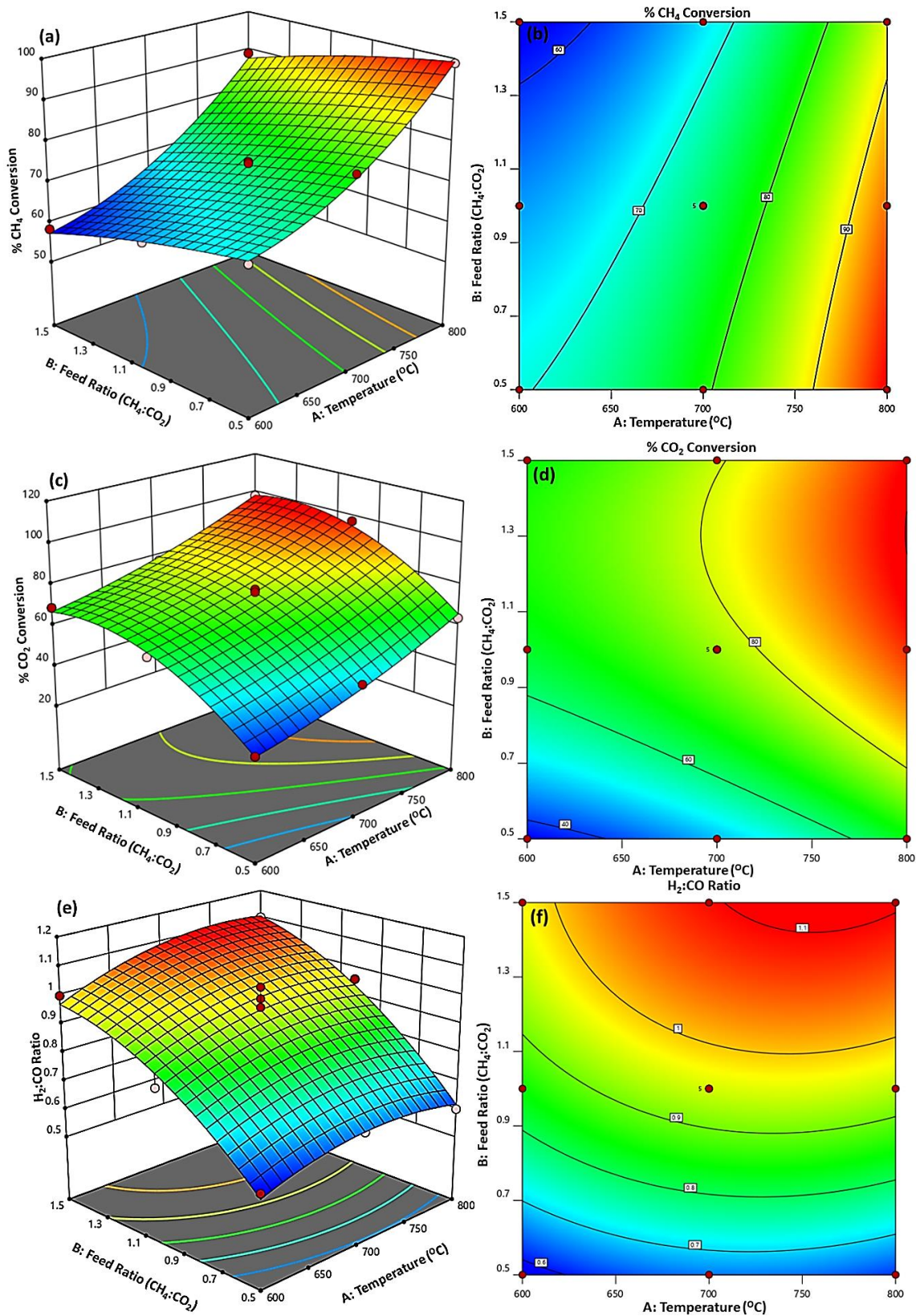


Figure 4.26. 3-D response surface and contour plots displaying the effects of reaction temperature and feed ratio on (a) CH_4 conversion, (b) CO_2 conversion, and (c) $\text{H}_2:\text{CO}$.

4.4.3 Optimization of the process parameters for DRM over Ni-W catalyst

In the present study, the optimization of process parameters for the DRM process over the optimum performance Ni-W/Al₂O₃-MgO catalyst has been carried out by employing the RSM tool of Design-Expert version 12 software. The range of high and low levels of the input process parameters (reaction temperature and feed ratio) and their responses (CH₄, CO₂ conversion and H₂:CO) have been specified and summarized in Table 4.12. The main objective is to maximize the responses (i.e., maximize CH₄ and CO₂ conversions while targeting H₂:CO at 1) and minimize the reaction temperature while keeping the feed ratio between 0.5 to 1.5.

Table 4.12. Goals and responses of the input process variables and their responses.

Name	Goal	Lower Limit	Upper Limit
Process variables			
A: Temperature (C)	Minimize	600	800
B: Feed Ratio	In range	0.5	1.5
Responses			
CH ₄ conversion (%)	Maximize	60	98.9
CO ₂ conversion (%)	Maximize	60	97.5
H ₂ :CO	Target=1	0.7	1.2

The desirability of individual responses was obtained by employing the desirability estimation profiler. This desirability forecast function can handle simultaneous optimization of different responses by exercising a separate model for them. The effect of input process variables on desirability has been depicted in Figure 4.27, along with its overall 3-D and contour plots. The plots obtained (shown in Figure 4.27) illustrates that the optimum conditions are desired at the temperature range of 700-800 °C and feed ratio of 0.7-1.2 at the constant GHSV of 36,000 cm³gcat⁻¹h⁻¹ with desirability varying between 0.6-0.8. This suggests that the optimum parameters

(i.e., maximized conversions of CH_4 , CO_2 and $\text{H}_2\text{:CO}$) could be achieved within the above-specified range of parameters. The algorithm adopted by RSM came out with the optimum solution with recommended desirability value of 0.723 (depicted in Figure 4.27). The analysis carried out by the RSM suggested a reaction temperature of 777.29°C , a feed ratio of 1.11 and the percentage conversion of CH_4 as 87.6%, CO_2 as 93.3% $\text{H}_2\text{:CO}$ value of 1, respectively.

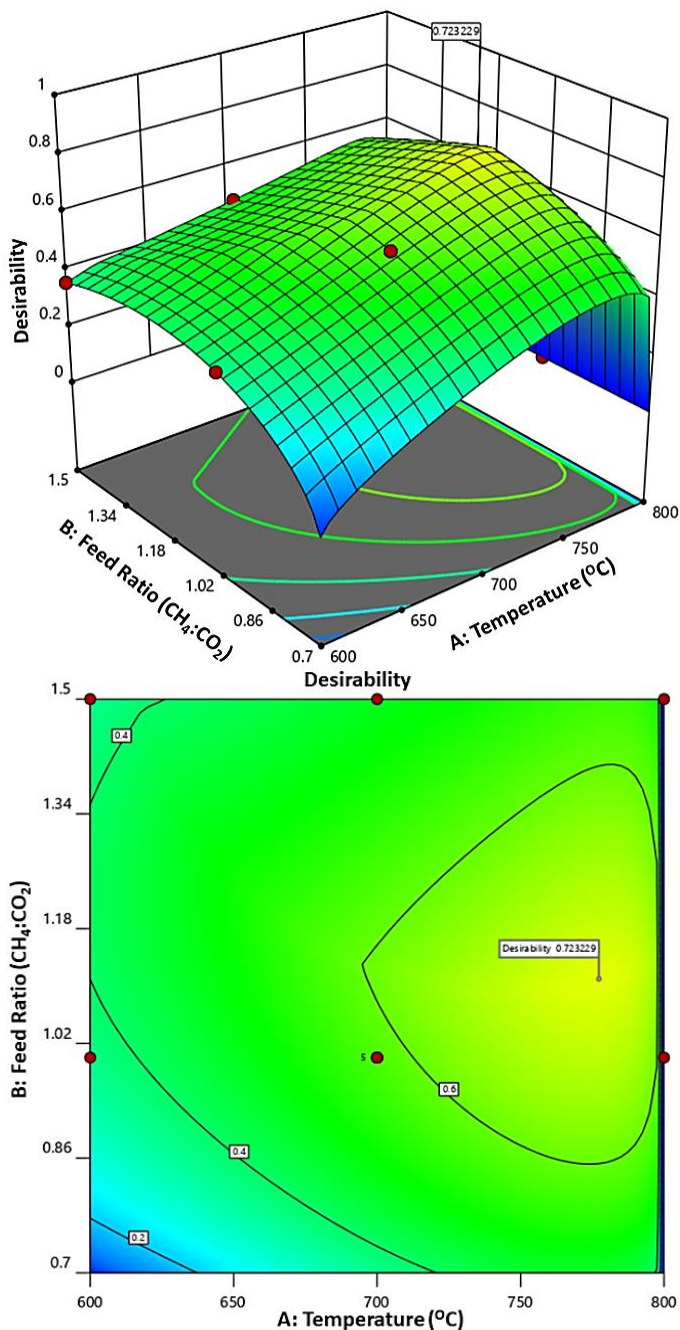


Figure 4.27. 3-D and contour desirability plots obtained from the multi-response desirability analysis.

4.4.4 Verification of optimized condition and percentage error

The recommended set of optimum conditions were then further verified by carrying out experimental DRM test over Ni-W/Al₂O₃-MgO catalyst at the specified conditions. The experiment is repeated thrice to minimize the mean error while comparing the predicted data (i.e., CH₄, CO₂ conversions and H₂:CO). The DRM reaction carried out at the obtained optimum conditions showed stable performance for 12h of reaction test. The actual experimental and the RSM predicted values of the responses had been summarized in Table 4.13.

Table 4.13. Optimum experimental values vs predicted values and corresponding percentage error.

Run	CH ₄ Conversion (%)			CO ₂ Conversion (%)			Syngas Ratio		
	Experimental	Predicted	% Error	Experimental	Predicted	% Error	Experimental	Predicted	% Error
1	85.41	87.65	2.62	90.22	93.25	3.35	0.97	1	3.09
2	84.83	87.65	3.32	89.17	93.25	4.5	0.96	1	4.16
3	86.14	87.65	1.75	91.83	93.25	1.55	0.99	1	1.01
Mean	85.5		2.56	90.1		3.13	0.96		2.75

The obtained experimental data are compared with the predicted data, and hence the percentage error was calculated (cf. Table 4.13). Further, the mean errors were utilized to justify the optimization results. The average errors for CH₄, CO₂ conversions and H₂:CO were 2.56%, 3.13% and 2.75%, respectively. Since the software forecast the data with 95% confidence (i.e., with a 5% probability of error); therefore, errors were counted as insignificant. This demonstrates that the statistical analysis carried out by RSM was a reliable method for DRM process optimization. The actual value may differ from the predicted value for the CCD (RSM).

The minute fluctuations (i.e., within 5% error range) in the experimental and predicted values is a normal trend and agrees with the existing literature [151–153, 179, 244].

Hence, from this study it can be inferred that the quadratic model suggested by CCD tool of RSM is best suited for the experimental design of optimization studies (as obtained from ANOVA). After carrying out a set of 13 experiments for optimization study at different reaction conditions (i.e., the temperature of 600°C - 800°C and CH₄: CO₂ of 0.5-1.5); it has been found that the optimum input conditions for temperature and feed ratio were 777.29°C and of 1.11 with the desirability of 0.723.

4.5 Kinetic Modelling Analysis

The kinetic and mechanistic studies of DRM is important to profoundly cognize the process and optimize the process parameters for industrial applications [245]. However, there are discrete views on the DRM reaction mechanism and its RDS. Wei et al. [246] described methane decomposition as RDS for DRM, whereas Lou et al.[247] reported decomposition of educts like CH_xO as RDS. The difference in reaction mechanism of reforming reactions is mainly due to different catalysts and different operating temperatures [248]. There are numerous kinetic and mechanistic studies conducted by researchers over Ni-based catalysts for DRM. Bodrov and Apel'baum proposed the first reaction mechanism for DRM in 1967. According to their findings they reported that the rate of DRM over Ni surface may be explained by the same kinetic equation as that for steam reforming of methane (SRM). The main assumption made in the Bodrov's model is that CH₄ react with steam and not with CO₂ [249]. Further, Zhang and Verykios [250] derived a Langmuir-Hinshelwood (LH) model for DRM over Ni/CaO-Al₂O₃ catalyst, taking in account that CH₄ is the rate determining step (RDS). Later, Slagtern et al.[251] described that RDS is the one comprising of CH₄ dissociation to give carbon species and CO₂ dissociation to give oxygen adsorbed educt, respectively. Hu and Ruckenstein [252] also came out with a similar outcome and concluded that surface reactions between oxygen and carbon educts are RDS over Ni catalysts. In another study, Tsipouriari and Verykios [253] reported a kinetic model. They assumed the methane cracking and the surface reaction between C and oxygen-carbonate species are RDS over Ni/La₂O₃ catalyst. Although different RDS are proposed in reaction mechanism studies, LH model has been commonly used in the kinetic studies of DRM. Recently, most of the investigations for reaction mechanism of DRM were derived based on LH

model. These were mainly recommended from the general LH steps presented by Xu and Froment [254] from their study on Ni based catalyst supported on MgAl_2O_4 for SRM reactions.

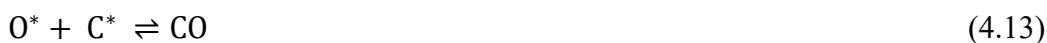
In this section, the three main reaction kinetic models (i.e., Langmuir-Hinshelwood (LH), Power Law (PL) and Eley-Rideal (ER)) are used to understand DRM kinetics [51, 182, 183]. PL model is the simplest of all reaction kinetic models, and it can be used to make a rough inference for kinetic parameters [37]. The ER model proposes that one gas (either CH_4 or CO_2) gets adsorbed on the catalyst active sites at thermodynamic equilibrium, whereas the other remains in the gas phase. The adsorbed gas then forms the educt and reacts with the non-adsorbed gas (by ER I or ER II mechanism). The RDS step is the one comprising the reaction of adsorbed gas with another reactant [182, 183]. Whereas, in LH model, it has been claimed that both the reactant gases get absorbed on the active sites of the catalyst. The educts formed react with each other, during this phenomenon some elementary reactions are at thermodynamic equilibrium whereas some are the RDS. The decomposition of CH_4 and CO_2 decomposition are supposed as elementary reactions in DRM reaction. The LH model is the most applicable and widely used for DRM reactions, since it provides more realistic approach for reaction mechanism, and explain the mechanistic steps more accurately [183, 184]. The kinetics of DRM reaction for the optimum Ni-W bimetallic catalyst is examined in a fixed bed tubular reactor over a temperature range from 600°C - 800°C at the standard atmospheric condition. The obtained data was then examined by employing different kinetic models (i.e., PL, ERI, ER II and LH). Finally, the adsorption energies of different reaction gases and the activated energy were also estimated by Arrhenius equation.

4.5.1 Reaction Mechanism

Several step-wise reaction mechanism have been proposed so far by researchers [65]. Wang et al. [255] conducted a theoretical study for DRM reaction and concluded that reactant gases gets adsorbed on the active sites of catalysts to form some educts. The educts formed then give CO and H_2 finally, which gets desorbed from the active sites. As per the investigations made by researchers the three rudimentary type of catalysts were considered, i.e., supported Ni-based, supported noble metal-based, and the carbide catalyst [51]. However, the XRD results (in section 4.3.4.2) confirms the existence of Ni-W alloy (NiWO_4) and WC in the spent catalyst, and the analysis suggested the pathway for DRM reaction (in section 4.3.4.5) as eqns. (4.1-4.3). The

suggested mechanism holds good with the reported literature and our findings [226]. Further the elementary reaction steps have been described (in section 4.3.4.5) as eqns. (4.4-4.7).

The WC activates CO₂, and the elementary reactions may be proposed as eqns. (4.4-4.7). The CO₂ molecule is then adsorbed to catalyst surface and dissociate into CO and O*. The intermediate O* then join with the carbon on the metal carbide surface (i.e., C_s) and a vacant site (°) is created. This vacancy is then further occupied by either O* which oxidize the carbide into the metal oxide, or by C* from the carbon adsorbed from CH₄ forming the carbide again [233]. Moreover, Iyer et al.[51] also reported for the noble metal-based catalyst mechanism. They demonstrated that the O* formed from the splitting of CO₂ combines with the C* formed from CH₄ splitting. The proposed reaction mechanism steps can be shown as eqns:



Further, it is broadly accepted that CO₂ gets adsorbed on the active site and react with H dissociated by CH₄. However, still there exist an ambiguity regarding reaction pathways of CO₂ methanation [255, 256].

4.5.2 Kinetics testing for DRM

The overall flow velocity is varied from 30-150ml/min to determine the effect of external diffusion for DRM reaction at 800 °C. It has been observed that the conversion of reactant gases increased with time when the inlet gas flow rate increased from 30 ml/min to 60 ml/min. The conversion remained constant till the flow rate was raised to 90 ml/min, and started to decrease slightly on further increasing the flow rate from 90ml/min to 150ml/min. This may be ascribed to the fact that external mass transfer of the reactant is barely influenced when the gas flow rate exceeds a particular limit. This further reveal that the external diffusion process of reactant gases (i.e., CH₄ and CO₂) through the catalytic bed was faster than the reaction on catalyst surface. Hence, it infers that the chemical reaction was the rate-determining step in DRM process. The kinetic testing is carried out the by altering the amount of gaseous feed (i.e., CH₄, CO₂ and N₂) i.e., being fed into the reactor at atmospheric pressure. In the kinetic analysis of DRM, firstly the

flow rate of CH₄ is kept constant (i.e., 24 ml/min) whereas the flowrate of CO₂ is varied (in the range 6-36ml/min.) to vary the partial pressure of CO₂ in the range of 0.2-0.6, keeping partial pressure of CH₄ as constant (i.e., 0.3). Similarly, in the other run the pressure of CH₄ is varied in the range of 0.2-0.6 and partial pressure of CO₂ is kept constant (i.e., 0.3). The N₂ is used as a balance gas to maintain a total flow rate of 70 ml/min, however it does not participate in the reaction. The reaction temperature is varied as 600°C, 700°C and 800°C. The rate of CO production can be determined as:

$$R_{CO} = F_{out} \cdot x_{CO} \quad (4.14)$$

The rate of CH₄ consumption can be determined as:

$$R_{CH_4} = F_{CH_4} - F_{out} \cdot x_{CH_4} \quad (4.15)$$

The rate of CO production is double than that of CH₄ consumption, and can be written as:

$$R_{CO} = 2F_{CH_4} \cdot x_{CO} / (x_{CO} + 2x_{CH_4}) \quad (4.16)$$

Hence, the rate of reaction for DRM can be expressed as:

$$R = \frac{R_{CO}}{V} = 2F_{CH_4} \cdot x_{CO} / [(x_{CO} + 2x_{CH_4}) \cdot V] \quad (4.17)$$

where R is rate of the reaction, x is the molar fraction of production, F is the molar flow rate and V is the volume of Ni-W bimetallic catalyst.

The rate equations for DRM reaction deduced from three main kinetic models are represented as [51], [182], [183]:

Power Law (PL):

$$R = k[P_{CH_4}]^m[P_{CO_2}]^n \quad (4.18)$$

Eley Rideal I (ERI):

$$R = \frac{k \cdot K_{CO_2} \cdot P_{CH_4} \cdot P_{CO_2}}{1 + K_{CO_2} \cdot P_{CO_2}} \quad (4.19)$$

Eley Rideal II (ERII):

$$R = \frac{k \cdot K_{CH_4} \cdot P_{CH_4} \cdot P_{CO_2}}{1 + K_{CH_4} \cdot P_{CH_4}} \quad (4.20)$$

Langmuir-Hinshelwood (LH):

$$R = \frac{k \cdot K_{CH_4} \cdot K_{CO_2} \cdot P_{CH_4} \cdot P_{CO_2}}{(1 + K_{CH_4} \cdot P_{CH_4} + K_{CO_2} \cdot P_{CO_2})^2} \quad (4.21)$$

The eqn. (4.21) was used to determine the equilibrium constants and the rate constant by applying linear regression correlation analysis. Hence, for LH model the eqn. (4.22) is attained.

$$\sqrt{\frac{P_{CH_4} \cdot P_{CO_2}}{R}} = \frac{1}{\sqrt{k \cdot K_{CH_4} \cdot K_{CO_2}}} + \sqrt{\frac{K_{CH_4}}{k \cdot K_{CO_2}}} P_{CH_4} + \sqrt{\frac{K_{CO_2}}{k \cdot K_{CH_4}}} P_{CO_2} \quad (4.22)$$

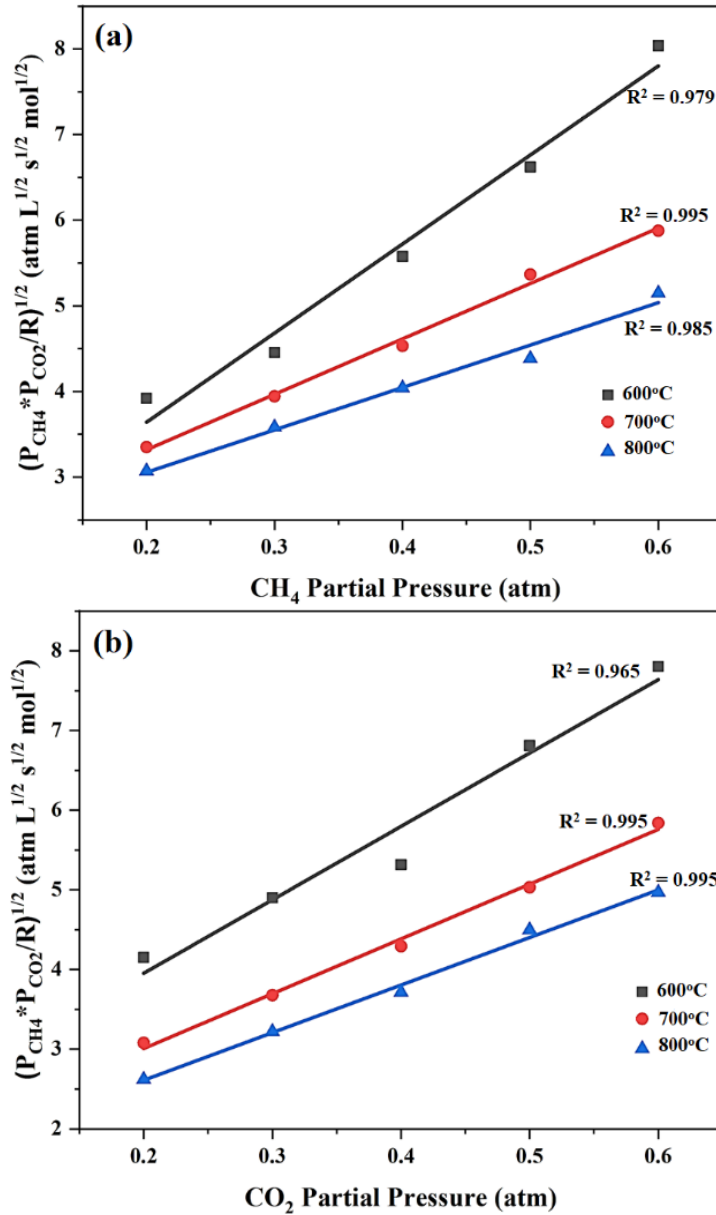


Figure 4.28. Modified reaction rates $\sqrt{P_{CH_4} \cdot P_{CO_2} / R}$ vs partial pressure of (a) CH_4 and (b) CO_2 for LH model, at 600°C-800°C.

By maintaining a constant partial pressure of CH₄ or CO₂, a linear plot of $\sqrt{P_{CH_4} \cdot P_{CO_2} / R}$ vs. partial pressure of reactant gases is obtained. The rate constant (k) along with the adsorption equilibrium constants (i.e., K_{CH₄} and K_{CO₂}) were attained through linear regression of the graph. The approximated rate expressions were also attained by fitting of the experimental data. The Newton-Raphson minimization algorithm is used to calculate the kinetic parameters of catalyst. The LH model was employed to investigate the reaction kinetics of DRM over Ni-W bimetallic catalyst over a temperature range of 600°C-800°C. The LH model is used for this aspect since it provides most realistic approach and preferred over other existing models [257]. The effect of partial pressure of reactant gases on $\sqrt{P_{CH_4} \cdot P_{CO_2} / R}$ has been shown in Figure 4.28. The calculations done to determine the value of $\sqrt{P_{CH_4} \cdot P_{CO_2} / R}$ from rate of the experimental rate of reaction has been given in APPENDIX F (cf. Tables A.9 and A.10). It has been observed that the plot obtained between the partial pressure of gases (i.e., CH₄ and CO₂) and $\sqrt{P_{CH_4} \cdot P_{CO_2} / R}$ is fairly linear. The rate constant (k) and the adsorption equilibrium constants (i.e., K_{CH₄} and K_{CO₂}) were obtained from fitted curves. Further, the activation energy of the reaction (E_a) and the pre-exponential factors were obtained by using the Arrhenius equations (eqn. 4.23).

$$\ln k = E_a / RT + \ln A \quad (4.23)$$

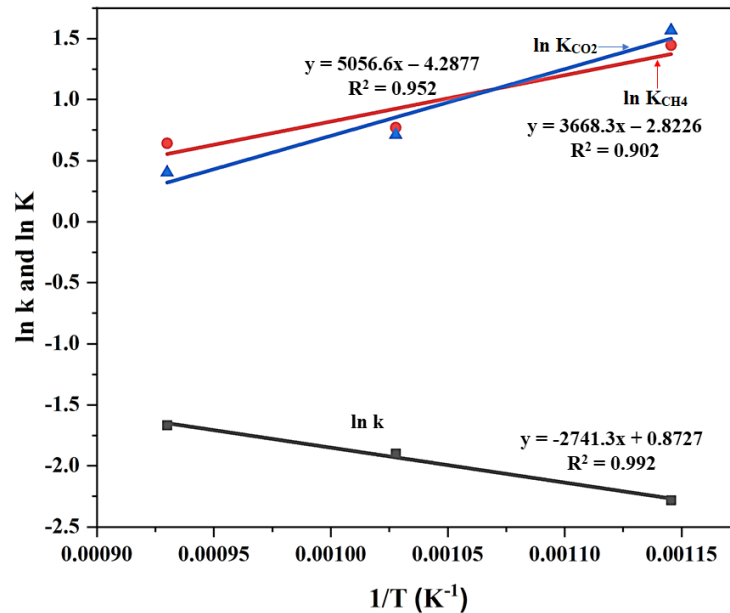


Figure 4.29. Arrhenius plots to determine the apparent E_a and E_{CH₄} and E_{CO₂} over Ni-W bimetallic catalyst.

The K_{CH_4} , K_{CO_2} and k values were calculated from the data fitting plot shown in Figure 4.28. Further, the Arrhenius plot has been obtained and shown in Figure 4.29, from the k values calculated from slope and intercept analysis of Figure 4.28. The calculated values have been tabulated in APPENDIX F (cf. Tables A.11). The activation energies were then calculated from the slope of straight lines plotted in Figure 4.28. The results obtained have shown the elevated adsorption activation energy for CH_4 (i.e., $E_{CH_4} = 45.94$ kJ/mol), whereas a lower value for CO_2 (i.e., $E_{CO_2} = 31.92$ kJ/mol). This shows the higher susceptibility of CH_4 towards temperature, then CO_2 comparatively. This trend obtained is found in agreement with the literature and validates that activation rate of CO_2 is swifter compared to that of CH_4 [258](cf. Table 4.14). Further the overall activation energy is calculated as 24.03 kJ/mol. The obtained trend of activation energies is quite close to that of the previous investigations conducted by Takano et al.[259] and Pichas et al.[248]. Thus, the relationship equations between the rate constant and equilibrium constants with temperature can be written as:

$$k = 2.29 \exp(-24030/RT) \text{ mol/L.s} \quad (4.24)$$

$$K_{CH_4} = 2.66 \times 10^1 \exp(45939.8/RT) \text{ atm}^{-1} \quad (4.25)$$

$$K_{CO_2} = 8.91 \times 10^1 \exp(31919.9/RT) \text{ atm}^{-1} \quad (4.26)$$

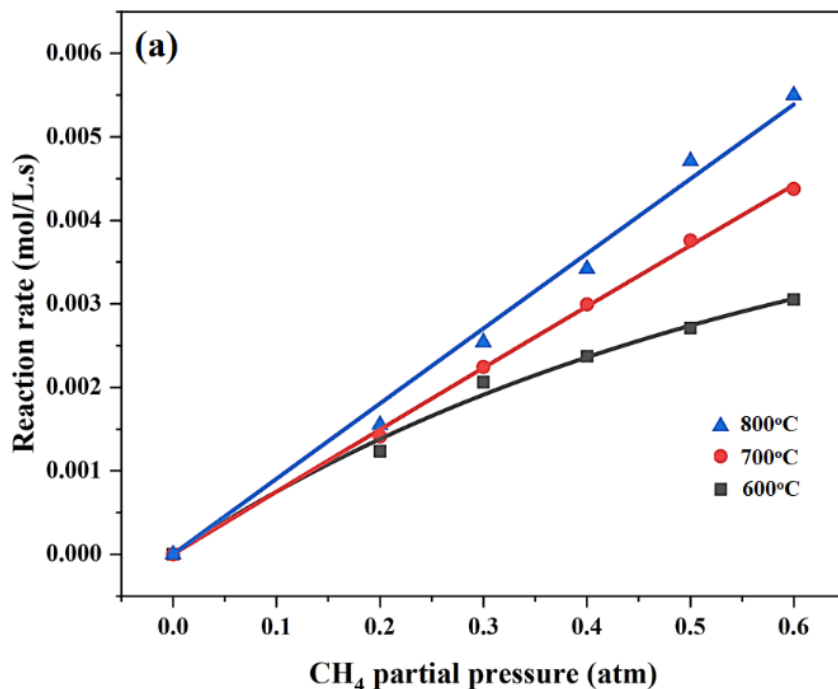
where $R = 8.314$ J/mol.K

Table 4.14. The activation energies (E_A) over different catalysts for DRM reaction.

Catalyst	Reactor	Flowrate (ml/min)	E_{CH_4} (kJ/mol)	E_{CO_2} (kJ/mol)	References
Ni/MgOSiO ₂ (700°C)	Fixed Bed	-	41.87	-	[259]
Ni/Al ₂ O ₃ (500-700°C)	Fixed Bed (ID = 10 mm)	360	50.9	56.1	[260]
0.3Pt–10Ni (580-620°C)	Fixed Bed (ID = 6 mm)	100	26.9	23.6	[165]
LaSrNiO ₄ (450-800°C)	Fixed Bed (ID = 10 mm)	60	41.8	12.4	[248]
Ni-W/Al ₂ O ₃ -MgO (600-800°C)	Fixed Bed (ID = 10 mm)	70	45.94	31.92	(This work)

4.5.3 Effect of process variables on reaction rate

The effect of partial pressure of reactant gases (i.e., CH_4 and CO_2) on the rate of DRM reaction was investigated over the $\text{Ni-W/Al}_2\text{O}_3\text{-MgO}$ catalyst at a flow rate of 70 ml/min, 1 atm pressure in the temperature range of 600°C-800°C. The flow rate of one reactant gas was fixed at 24 ml/min and that of another is varied simultaneously, to get partial pressures varying from 0.2 to 0.6. The effect of CH_4 partial pressure at different temperatures was investigated by keeping a constant CO_2 partial pressure as shown in in Figure 4.30 (a). It is evident from the analysis that reforming rate was influenced by varying the partial pressure of CH_4 during the experiment in the range of 0.2-0.6. The acceleration of reforming rate slowly decreased with the increase in CH_4 partial pressure at a constant CO_2 partial pressure. Similarly, the effect of CO_2 partial pressure at different temperatures was investigated by keeping a constant CH_4 partial pressure as shown in in Figure 4.30 (b). It has been observed that at lower temperatures, the effect of CO_2 partial pressure was substantial to a lesser extent compared to that at elevated temperatures. On comparing the trends obtained by varying the partial pressure as shown in Figure 4.30 (a) and 4.30 (b), it appeared that the DRM reaction rate was more susceptible towards partial pressure of CH_4 than that of CO_2 . It can be attributed due to stronger adsorption of CH_4 towards catalyst's surface compared to that of CO_2 at elevated partial pressures.



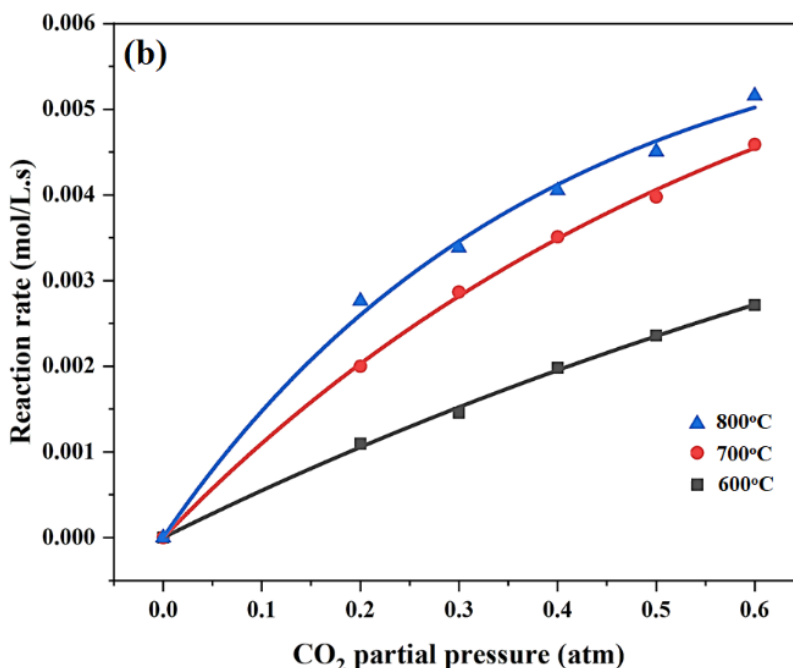


Figure 4.30. The rate of consumption as a function of temperature vs. partial pressure of (a) CH₄ and (b) CO₂ from experimental data of Ni-W bimetallic catalyst. The curve fitting carried out by employing the LH model.

4.5.4 General applicable kinetic models

4.5.4.1 Power-Law Model

The power law model is the simplest model that is used to illustrate the reforming rate of DRM over Ni-W/Al₂O₃-MgO catalyst. A typical power law model can be described as eqn. 4.18. The activation energies of reaction and the pre-exponential factors were attained from Arrhenius equations (eqn. 4.23). The Arrhenius plot for the attained k values was depicted in Figure 4.29, i.e., acquired from data fitting of Figure 4.28. The adsorption equilibrium constant of different reaction gas and reaction rate constants calculated according to the slope and intercept of fitted lines in Figure 4.28, (cf. APPENDIX F, Tables A.11). A comparison of estimated and experimental reaction rate is shown in Figure 4.31, and an R^2 value of 0.936 has been predicted by the power-law model. The m and n values varied from 0.72-1.07 and 0.707-0.678, respectively and agree with the existing literature [261]. The power law model may not be significant due to its lack of considering various the mechanistic steps of DRM reaction [159, 262].

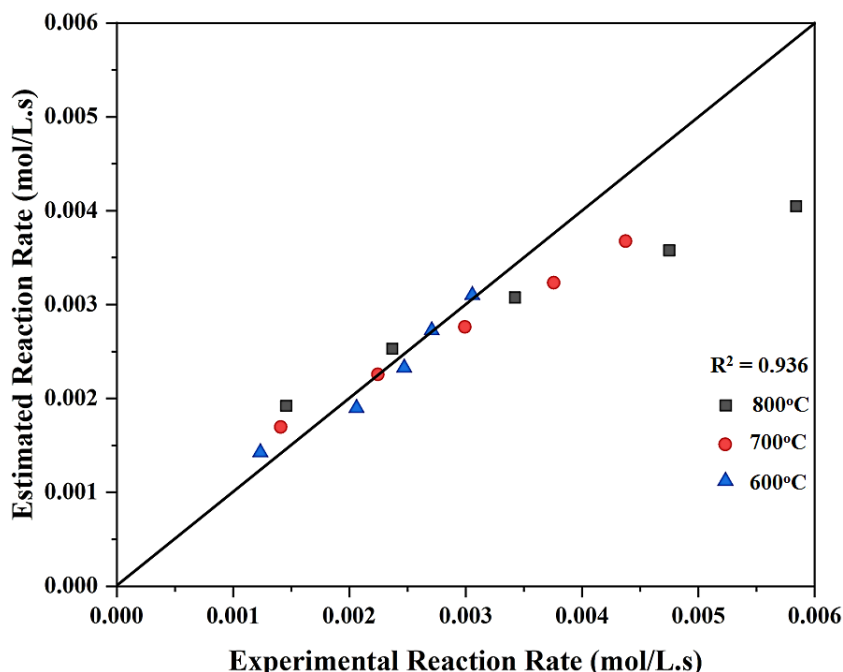


Figure 4.31. Comparison between experimental and estimated reaction rates of DRM based on Power-Law model.

4.5.4.2 Langmuir-Hinshelwood Model

The LH-model is the most widely and accepted approach to describe surface adsorption phenomena of reforming reactions, and hence used for data fitting of DRM over Ni-W/Al₂O₃-MgO catalyst. The pre-exponential factors and activation energies were obtained from Arrhenius equations whereas the experimental reaction rate data points are obtained from APPENDIX F (cf. Table A.9 and Table A.10). A comparison of estimated and experimental reaction rate is depicted in Figure 4.32. The LH-model (eqn. 4.21) fitting resulted in prediction of R^2 value equal to 0.983, which is highly satisfactory. The LH-model fitting curve has been shown in Figure 4.32.

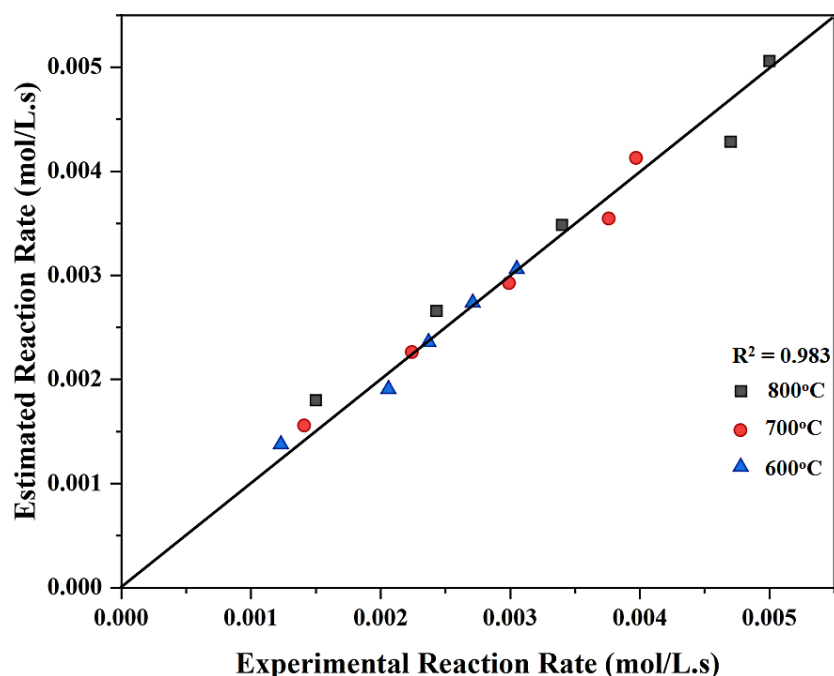


Figure 4.32. Comparison between experimental and estimated reaction rates of DRM based on Langmuir-Hinshelwood model.

4.5.4.3 Eley Rideal Models

The experimental reaction rates were also compared with the ER models (i.e., ERI, ERII), to determine the goodness of fit of kinetic data. The kinetic parameters (i.e., K and k) were computed and tabulated for all the kinetic models in Table 4.15. The kinetic parameters were then fitted in the ER1 and ER2 kinetic models for analysis as in eqns. 4.19 and 4.20, respectively. The ER1 and ER2 model gave the R^2 values of 0.958 and 0.957, respectively which is however lower as compared to the LH-model fitting. The ER I and ER II kinetic model fitting curve has been shown in Figure 4.33 (a-b). The R^2 value for PL model was found to be minimum amongst all the kinetic models studied for DRM over Ni-W/Al₂O₃-MgO catalyst.

Table 4.15. Kinetic parameters attained by the applied kinetic models.

Temperature (°C)	PL Model	ER I Model		ER II Model	
	k (mol/L.s)	k (mol/L.s)	K_{CO_2} (atm ⁻¹)	k (mol/L.s)	K_{CH_4} (atm ⁻¹)
600	1.06×10^{-2}	4.328×10^{-2}	0.4525	2.684×10^{-2}	1.059
700	1.55×10^{-2}	4.042×10^{-2}	1.0377	8.144×10^{-2}	0.347
800	2.08×10^{-2}	3.135×10^{-2}	1.999	2×10^{-1}	0.148

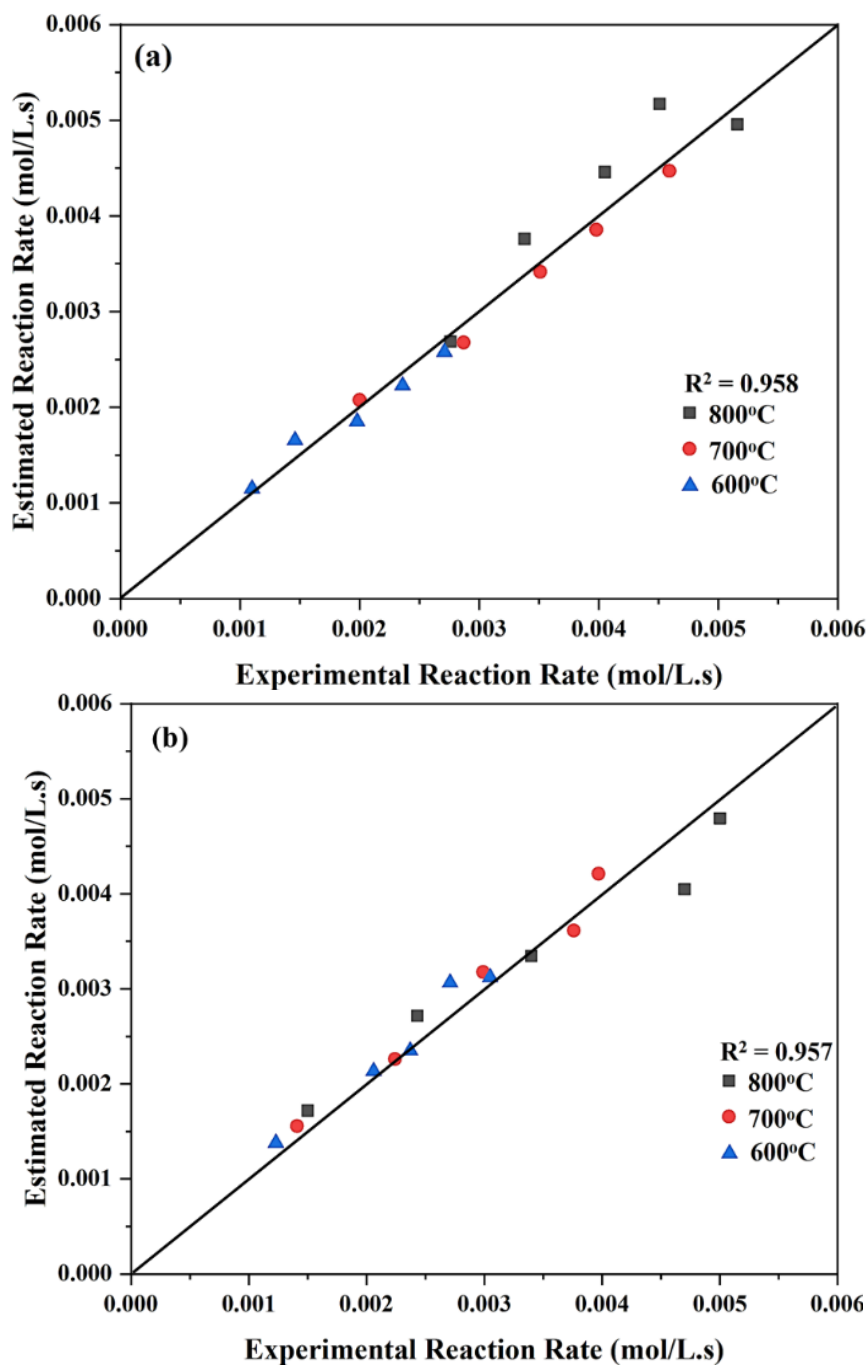


Figure 4.33. Comparison between experimental and estimated reaction rates of DRM based on (a) ERI and (b) ERII models

Therefore, from the kinetic modelling analysis of DRM reaction over Ni-W/ Al_2O_3 -MgO catalyst it can be inferred that the Langmuir-Hinshelwood model provided the best fit and prediction of data with an R^2 value of 0.983.

4.6 Summary

A series of differently Ni-loaded (i.e., 10, 12, 14, and 16 wt.%) catalysts supported on $\text{Al}_2\text{O}_3\text{-MgO}$ ($\text{Al}_2\text{O}_3\text{:MgO}=1\text{:}2$) were prepared via co-precipitation and impregnation method. The 12 wt.% Ni is screened as the best performing and stable catalyst. The XRD and TEM and results of the spent catalyst confirmed the formation of carbon nanosheets, which were responsible for the declined activity of catalyst over time. Thereafter, 12 wt.% Ni catalyst is studied further to determine the effect of W loading (2-8wt.%) as a bimetal on Ni-W bimetallic catalyst. It has been found that 12 wt.% Ni + 4 wt.% W catalyst showed very stable performance and activity. The rigorous characterization of the fresh Ni-W/ $\text{Al}_2\text{O}_3\text{-MgO}$ catalysts via XRD, BET, FESEM, EDX, elemental mapping, TPR and TPD has been done. The characterization of the synthesized catalysts revealed the enhanced surface area, morphology, metallic dispersion, and enriched degree of reduction. Further, the spent catalyst has been characterized again via FESEM, EDX, elemental mapping, TEM, TPO- O_2 and RAMAN analysis. The characterizations revealed the formation of MWCNTs for Ni-W bimetallic catalyst, which was responsible for the prolonged stability of catalyst. The MWCNTs does not shroud the active sites of the catalyst like the carbon nanosheets, and hence remain active even after 24 h of DRM reaction. The Ni_f catalyst showed lower CH_4 and CO_2 conversion of 84% and 90.6% respectively when compared to W_b catalyst, i.e., 95% and 95.6% for CH_4 and CO_2 respectively, even after 6 h of DMR reaction. The W_b catalyst showed excellent stability, as the CH_4 and CO_2 conversions were still high (after 24 h DRM stability test) at 88.8%, and 91.5%, respectively, and the $\text{H}_2\text{:CO}$ ratio was 0.9. The optimum Ni-W high-performance catalyst has used for optimization of process parameters (i.e., temperature and feed partial pressure) for DRM via CCD tool of RSM software. The optimum input conditions for temperature and feed ratio were found to be 777.29 °C and of 1.11 with the desirability of 0.723. The predicted conversions of CH_4 and CO_2 were 87.6% and 93.3%, were found in close agreement with the experimentally obtained conversions, i.e., 85.5% and 90.1%. Further a syngas ($\text{H}_2\text{:CO}$) ratio of 0.96 is attained, which is also agree with the predicted syngas ratio of 1. Finally, the kinetic modelling of DRM reaction over Ni-W bimetallic catalyst has been conducted via four main kinetic models, i.e., PL, LH, ERI and ERII models. The results concluded that the order of prediction of reaction rates for DRM followed the order as $\text{PL} < \text{ER II} < \text{ERI} < \text{LH}$. Moreover, as per the LH model the activation energies of CH_4 and CO_2 consumption were 45.94 kJ/mol and 31.92 kJ/mol, respectively.

CHAPTER 5

CONCLUSION AND RECOMMENDATION

5.1 Conclusion

1. The 12wt.% Ni loading on Al_2O_3 -MgO support with Al_2O_3 :MgO of 1:2 gave the optimum catalytic activity and stability. Further, addition of W, as a bimetal to 12wt.% Ni loaded catalyst, has displayed improved catalytic properties for DRM reactions. The properties obtained for Ni-W bimetallic catalysts are enhanced thermal stability, BET surface area, reducibility, more uniform morphology, reactant conversion, and stability. The XRD analysis of the freshly synthesized Ni-W bimetallic catalyst confirmed the existence of Ni-W alloy (i.e., NiWO_4) which is thermally very stable and responsible for stable performance of the catalyst. The TPR- H_2 results validated better Ni dispersion and enhanced number of active sites for Ni-W bimetallic catalyst compared to Ni_f . The FESEM analysis highlighted that on adding W to Ni catalyst a comparatively fine-grained Pacific-elkhorn corals morphology is obtained. The EDX and elemental mapping results verified the composition of all the prepared catalysts and enhanced metallic distribution for bimetallic catalysts, respectively. The TPD- CO_2 analysis confirmed the basicity of the prepared catalysts. The XPS analysis reported that BE of Ni for Ni_f and W_b catalysts, and also confirmed the oxidation states of Ni, W and O as +2, +6 and -2 respectively. The additional peak at 530.8 eV is ascribed to NiWO_4 (i.e., O-[Ni-W] bond) and WO_3 (i.e., W-O bond) which confirmed the existence of NiWO_4 and WO_3 in W_b catalyst.
2. The different synthesized catalysts have been tested for DRM reaction at CH_4 : CO_2 : N_2 of 1:1:1 at 800°C in the tubular reactor. The Ni-W bimetallic catalysts have shown significantly better activity and enhanced stability during the 6 h of DRM reaction test. The Ni-W bimetallic catalyst with 12wt.% Ni and 4wt.% W loading (i.e., W_b) showed the optimum performance. W_b catalyst stayed active even after 24h of stability test with CH_4 and CO_2 conversions of 88.8%, and 91.5%, respectively. This is mainly due to the formation of WC for $\text{W}_{b,\text{sp}}$ catalyst during the DRM reaction. The average Ni crystallite size for $\text{W}_{b,\text{sp}}$ catalyst remained almost constant even after 6 h of DRM reaction (i.e.,

from 22.9nm to 23.1nm). Whereas for monometallic Ni_{sp} catalyst the Ni crystallite size grew from 46.1nm to 53.4nm. The formation of amorphous carbon on Ni_{sp} catalyst and MWCNTs has been confirmed by FESEM, TEM, TPO-O₂ and RAMAN analysis of the spent catalysts.

3. The optimum Ni-W/Al₂O₃-MgO catalyst (i.e., W_b) was further used for optimization of parameters using the RSM tool of design expert. The optimization process investigated the effect of reaction temperature and feed gas ratio (i.e., CH₄:CO₂) on the percentage conversion of CH₄ and CO₂ and syngas (H₂:CO) ratio. The CCD tool of RSM is found to be best suited for the experimental design of optimization studies (as obtained from ANOVA). The suggested set of 13 experiments by CCD for the optimization of temperature and feed ratio (i.e., in the temperature range of 600°C - 800°C and CH₄: CO₂ of 0.5-1.5) was conducted. The optimum input parameters for DRM were found to be a reaction temperature of 777.29°C and a feed ratio of 1.11 with the desirability of 0.723. The experimental and predicted values were found in close proximity after the experimental analysis with insignificant error.
4. Finally, the micro kinetic modelling of DRM reaction over Ni-W/Al₂O₃-MgO catalyst has been carried out at atmospheric pressure. The four different kinetic models (i.e., PL model, LH model, ERI model and ERII model) were employed and the curve fitting is done using the attained kinetics data for DRM reaction. The LH model yielded the best fit between experimental and estimated reaction rates when compared to other models. Further, the activation energies of CH₄ and CO₂ consumption as calculated via LH model found to be 45.94 kJ/mol and 31.92 kJ/mol, respectively. CH₄ is required to overcome considerably higher energy barrier (than CO₂) during DRM reaction as indicated by the elevated value of activation energy for CH₄. Lastly, the results concluded that the order of prediction of reaction rates (i.e., experimental vs predicted) for DRM followed the order as PL<ER II<ERI<LH, which is evident from their respective R² values.

5.2 Recommendations

The development of composite bimetallic catalysts may help in the commercialization of DRM process in the future. Since every catalyst go through different reaction mechanism for DRM reaction, hence testing and exploring new metallic combinations may help in the journey to

achieve an ideal catalyst. As per the available literature and based on the conclusions of this study, following remarks can be made to improve the DRM reaction:

- A comparative study on the effect of catalyst synthesis route (such as microwave-assisted micro-emulsion, one- pot synthesis, hydrotalcite route, surfactant induced method etc.) on the performance and catalytic properties may be studied to adopt the best route for catalyst synthesis.
- The oxidative DRM (ODRM) may be studied to investigate the efficiency of the process while burning the coke formed in situ. Further, the regeneration of catalyst may be studied to reuse the spent catalyst in case it is thermally stable.
- The raw natural gas contains several other gases such as H_2S and mercaptans along with CH_4 and CO_2 . The effect of such impurities on the performance of catalyst may be investigated to minimize the catalyst deactivation, and usage of raw natural gas from the well head directly for DRM.
- The reaction mechanism may be studied in the very beginning by employing the use of software tools such as density functional theory (DFT). This practice will help to avoid the loss of material and better prediction of reaction mechanisms.

REFERENCES

- [1] U. Nations, S. Affairs, and P. Division, “World Population Prospects,” 2019.
- [2] S. Bhattar, M. A. Abedin, S. Kanitkar, and J. J. Spivey, “A review on dry reforming of methane over perovskite derived catalysts,” *Catal. Today*, vol. 365, no. October 2020, pp. 2–23, 2021, doi: 10.1016/j.cattod.2020.10.041.
- [3] B. Abdullah, N. A. Abd Ghani, and D. V. N. Vo, “Recent advances in dry reforming of methane over Ni-based catalysts,” *J. Clean. Prod.*, vol. 162, pp. 170–185, 2017, doi: 10.1016/j.jclepro.2017.05.176.
- [4] A. S. Al-Fatesh, Y. Arafat, S. O. Kasim, A. A. Ibrahim, A. E. Abasaeed, and A. H. Fakeeha, “In situ auto-gasification of coke deposits over a novel Ni-Ce/W-Zr catalyst by sequential generation of oxygen vacancies for remarkably stable syngas production via CO₂-reforming of methane,” *Appl. Catal. B Environ.*, vol. 280, no. June 2020, p. 119445, 2021, doi: 10.1016/j.apcatb.2020.119445.
- [5] N. H. Darman and A. R. B. Harun, “Technical challenges and solutions on natural gas development in Malaysia,” *Proc. Pet. Policy Manag. Proj. Work. China-Sichuan Basin Case Study*, 2006, doi: 10.1126/science.1071776\n296/5576/2203.
- [6] E. Global, M. Division, G. Greenhouse, and G. Reference, “Global Monitoring Division (/gmd /) Trends in Atmospheric Methane Global CH₄ Monthly Means,” no. September 2018, pp. 1–6, 2020.
- [7] B. Dudley, “BP Statistical Review of World Energy,” no. June, 2015.
- [8] C. Le Quéré, R. M. Andrew, P. Friedlingstein, S. Sitch, J. Hauck, J. Pongratz, P. A. Pickers, J. I. Korsbakken, G. P. Peters, and J. G. Canadell, “Global Carbon Budget 2018,” pp. 2141–2194, 2018.
- [9] V. Talyan, R. P. Dahiya, S. Anand, and T. R. Sreekrishnan, “Quantification of methane emission from municipal solid waste disposal in Delhi,” vol. 50, no. 236, pp. 240–259, 2007, doi: 10.1016/j.resconrec.2006.06.002.
- [10] D. J. Wuebbles and K. Hayhoe, “Atmospheric methane and global change,” vol. 57, no. x,

pp. 177–210, 2002.

- [11] R. B. Jackson, M. Saunio, P. Bousquet, J. G. Canadell, B. Poulter, A. R. Stavert, P. Bergamaschi, Y. Niwa, A. Segers and A. Tsuruta. “Increasing anthropogenic methane emissions arise equally from agricultural and fossil fuel sources,” *Environ. Res. Lett.*, vol. 15, no. 7, p. 071002, 2020.
- [12] R. O. Yusuf, Z. Z. Noor, A. H. Abba, M. Ariffin, and A. Hassan, “Methane emission by sectors : A comprehensive review of emission sources and mitigation methods,” *Renew. Sustain. Energy Rev.*, vol. 16, no. 7, pp. 5059–5070, 2012, doi: 10.1016/j.rser.2012.04.008.
- [13] J. Hansen, M. Sato “Ice melt , sea level rise and superstorms : evidence from paleoclimate data , climate modeling , and modern observations that 2° C global warming could be dangerous,” pp. 3761–3812, 2016, doi: 10.5194/acp-16-3761-2016.
- [14] W. Steffen, L. Hughes, A. Pearce "C. Council, *Climate Change 2015 : Growing Risks , Critical Choices*" 2015.
- [15] F. Fayaz, H. T. Danh, C. Nguyen-huy, K. B. Vu, and B. Abdullah, “Promotional Effect of Ce-dopant on Al₂O₃ -supported Co Catalysts for Syngas Production via CO₂ Reforming of Ethanol,” *Procedia Eng.*, vol. 148, pp. 646–653, 2016, doi: 10.1016/j.proeng.2016.06.530.
- [16] Y.-S. Lin, J.-Y. Tu, and D.-H. Tsai, “Steam-promoted Methane-CO₂ reforming by NiPdCeO_x@SiO₂ nanoparticle clusters for syngas production,” *Int. J. Hydrogen Energy*, pp. 1–11, 2021, doi: 10.1016/j.ijhydene.2021.05.053.
- [17] Y. J. O. Asencios and E. M. Assaf, “Combination of dry reforming and partial oxidation of methane on NiO–MgO–ZrO₂ catalyst : Effect of nickel content,” *Fuel Process. Technol.*, vol. 106, pp. 247–252, 2013, doi: 10.1016/j.fuproc.2012.08.004.
- [18] W. Jang, J. Shim, H. Kim, S. Yoo, and H. Roh, “A review on dry reforming of methane in aspect of catalytic properties,” *Catal. Today*, vol. 324, no. June 2018, pp. 15–26, 2019, doi: 10.1016/j.cattod.2018.07.032.
- [19] M. A. A. Aziz, H. D. Setiabudi, L. P. Teh, N. H. R. Annuar, and A. A. Jalil, “A review of

- heterogeneous catalysts for syngas production via dry reforming,” *J. Taiwan Inst. Chem. Eng.*, vol. 101, pp. 139–158, 2019, doi: 10.1016/j.jtice.2019.04.047.
- [20] M. Motak, T. Grzybek, M. E. Galvez, and P. Da Costa, “A Short Review on the Catalytic Activity of Hydrotalcite-Derived Materials for Dry Reforming of Methane,” no. 1, pp. 1–25, 2017, doi: 10.3390/catal7010032.
- [21] C. M. Damaskinos, J. Zavašnik, P. Djinović, and A. M. Efstathiou, “Dry reforming of methane over Ni/Ce_{0.8}Ti_{0.2}O_{2-δ}: The effect of Ni particle size on the carbon pathways studied by transient and isotopic techniques,” *Appl. Catal. B Environ.*, vol. 296, no. 120321, pp. 1–20, 2021, doi: 10.1016/j.apcatb.2021.120321.
- [22] H. Wu, G. Pantaleo, V. La, A. M. Venezia, X. Collard, C. Aprile, and L. F. Liotta, “Bi- and trimetallic Ni catalysts over Al₂O₃ and Al₂O₃-MO_x (M= Ce or Mg) oxides for methane dry reforming : Au and Pt additive effects,” *Appl. Catal. B Environ.*, vol. 156–157, pp. 350–361, 2014, doi: 10.1016/j.apcatb.2014.03.018.
- [23] V. García, J. J. Fernández, W. Ruíz, F. Mondragón, and A. Moreno, “Effect of MgO addition on the basicity of Ni/ZrO₂ and on its catalytic activity in carbon dioxide reforming of methane,” *Catal. Commun.*, vol. 11, no. 4, pp. 240–246, 2009, doi: 10.1016/j.catcom.2009.10.003.
- [24] Z. Alipour, M. Rezaei, and F. Meshkani, “Effect of alkaline earth promoters (MgO, CaO, and BaO) on the activity and coke formation of Ni catalysts supported on nanocrystalline Al₂O₃ in dry reforming of methane,” *J. Ind. Eng. Chem.*, vol. 20, pp. 2858–2863, 2014.
- [25] B. M. Al-Swai, N. Osman, M. S. Alnarabiji, A. A. Adesina, and B. Abdullah, “Syngas Production via Methane Dry Reforming over Ceria-Magnesia Mixed Oxide-Supported Nickel Catalysts,” *Ind. Eng. Chem. Res.*, vol. 58, no. 2, pp. 539–552, 2019, doi: 10.1021/acs.iecr.8b03671.
- [26] F. Mirzaei, M. Rezaei, F. Meshkani, and Z. Fattah, “Journal of Industrial and Engineering Chemistry Carbon dioxide reforming of methane for syngas production over Co – MgO mixed oxide nanocatalysts,” *J. Ind. Eng. Chem.*, vol. 21, pp. 662–667, 2015, doi: 10.1016/j.jiec.2014.03.034.

- [27] I. V. Yentekakis, P. Panagiotopoulou, and G. Artemakis, “A review of recent efforts to promote dry reforming of methane (DRM) to syngas production via bimetallic catalyst formulations,” *Appl. Catal. B Environ.*, vol. 296, no. February, p. 120210, 2021, doi: 10.1016/j.apcatb.2021.120210.
- [28] R. De, M. Elena, F. Launay, M. Motak, T. Grzybek, and P. Da, “Low temperature dry methane reforming over Ce , Zr and CeZr promoted Ni e Mg e Al hydrotalcite- derived catalysts,” vol. 1, pp. 0–7, 2016, doi: 10.1016/j.ijhydene.2016.02.074.
- [29] J. Spivey, “Chem Soc Rev noble metal catalysts,” 2014, doi: 10.1039/c3cs60395d.
- [30] A. Movasati, S. Mehdi, and G. Mazloom, “CO₂ reforming of methane over Ni / ZnAl₂O₄ catalysts : Influence of Ce addition on activity and stability,” *Int. J. Hydrogen Energy*, vol. 42, no. 26, pp. 16436–16448, 2017, doi: 10.1016/j.ijhydene.2017.05.199.
- [31] Y. X. Zeng, L. Wang, C. F. Wu, J. Q. Wang, B. X. Shen, and X. Tu, “Applied Catalysis B : Environmental Low temperature reforming of biogas over K- , Mg- and Ce-promoted Ni/Al₂O₃ catalysts for the production of hydrogen rich syngas : Understanding the plasma-catalytic synergy,” vol. 224, no. September 2017, pp. 469–478, 2018, doi: 10.1016/j.apcatb.2017.10.017.
- [32] H. Arbag, S. Yasyerli, N. Yasyerli, T. Dogu, and G. Dogu, “Coke minimization in dry reforming of methane by ni based mesoporous alumina catalysts synthesized following different routes: Effects of W and Mg,” *Top. Catal.*, vol. 56, no. 18–20, pp. 1695–1707, 2013, doi: 10.1007/s11244-013-0105-3.
- [33] A. R. M. M. Bagheri-mohagheghi, “Comparison of sol-gel and co-precipitation methods on the structural properties and phase transformation of γ and α -Al₂O₃ nanoparticles,” pp. 176–182, 2013, doi: 10.1007/s40436-013-0018-1.
- [34] J. Lavoie and F. G. Labiano, “Review on dry reforming of methane , a potentially more environmentally-friendly approach to the increasing natural gas exploitation,” vol. 2, no. November, pp. 1–17, 2014, doi: 10.3389/fchem.2014.00081.
- [35] L. Daza, “Influence of the operating parameters over dry reforming of methane to

- syngas,” *Int. J. Hydrogen Energy*, vol. 39, no. 8, pp. 4089–4094, 2013, doi: 10.1016/j.ijhydene.2013.05.135.
- [36] O. Omoregbe, H. T. Danh, C. Nguyen-huy, H. D. Setiabudi, S. Z. Abidin, Q. Duc, and D. N. Vo, “Syngas production from methane dry reforming over Ni/SBA-15 catalyst : Effect of operating parameters,” *Int. J. Hydrogen Energy*, vol. 42, no. 16, pp. 11283–11294, 2017, doi: 10.1016/j.ijhydene.2017.03.146.
- [37] M. Yusuf, A. S. Farooqi, L. K. Keong, K. Hellgardt, and B. Abdullah, “Contemporary trends in composite Ni-based catalysts for CO₂ reforming of methane,” *Chem. Eng. Sci.*, vol. 229, p. 116072, 2021, doi: 10.1016/j.ces.2020.116072.
- [38] F. Sharifianjazi, A. Esmaeilkhanian, L. Bazli, S. Eskandarinezhad, S. Khaksar, P. Shafiee, M. Yusuf, B. Abdullah, P. Salahshour, and F. Sadeghi, “A review on recent advances in dry reforming of methane over Ni- and Co-based nanocatalysts,” *Int. J. Hydrogen Energy*, 2021, doi: 10.1016/j.ijhydene.2021.11.172.
- [39] U. Arunachalam, P. Veeramani, and N. S. V. Moorthi, “A Review on Thermal Behavior Aspects of Nickel-Tungsten Alloy Coating,” *Int. Rev. Mech. Eng. (IREME); Vol 7, No 1*, 2013.
- [40] W. L. Dai, M. H. Qiao, and J. F. Deng, “XPS studies on a novel amorphous Ni-Co-W-B alloy powder,” *Appl. Surf. Sci.*, vol. 120, no. 1–2, pp. 119–124, 1997, doi: 10.1016/S0169-4332(97)00223-7.
- [41] M. P. Quiroga Argañaraz, S. B. Ribotta, M. E. Folquer, G. Benítez, A. Rubert, L. M. Gassa, M. E. Vela, and R. C. Salvarezza, “The electrochemistry of nanostructured Ni-W alloys,” *J. Solid State Electrochem.*, vol. 17, no. 2, pp. 307–313, 2013, doi: 10.1007/s10008-012-1965-3.
- [42] F. Z. et Al., “Water-Gas Shift Reaction on Ni–W–Ce Catalysts Catalytic Activity and Structural Characterization,” *J. Phys. Chem. C*, vol. 118, pp. 2528–2538, 2014, doi: doi.org/10.1021/jp410790z.
- [43] S. Das, J. Ashok, Z. Bian, N. Dewangan, M. H. Wai, Y. Du, A. Borgna, K. Hidajat, and S.

- Kawi, “Silica–Ceria sandwiched Ni core–shell catalyst for low temperature dry reforming of biogas: Coke resistance and mechanistic insights,” *Appl. Catal. B Environ.*, vol. 230, no. November 2017, pp. 220–236, 2018, doi: 10.1016/j.apcatb.2018.02.041.
- [44] M. Yusuf, A. Salaam Farooqi, M. Azad Alam, L. Kok Keong, K. Hellgardt, and B. Abdullah, “ Performance of Ni/Al₂O₃-MgO catalyst for Dry Reforming of Methane: Effect of preparation routes ,” *IOP Conf. Ser. Mater. Sci. Eng.*, vol. 1092, no. 1, p. 012069, 2021, doi: 10.1088/1757-899x/1092/1/012069.
- [45] Y. Zhu, S. Zhang, B. Chen, Z. Zhang, and C. Shi, “Effect of Mg/Al ratio of NiMgAl mixed oxide catalyst derived from hydrotalcite for carbon dioxide reforming of methane,” *Catal. Today*, vol. 264, pp. 163–170, 2016, doi: 10.1016/j.cattod.2015.07.037.
- [46] M. Radlik, M. Adamowska-Teyssier, A. Krztoń, K. Koziel, W. Krajewski, W. Turek, and P. Da Costa, “Dry reforming of methane over Ni/Ce_{0.62}Zr_{0.38}O₂ catalysts: Effect of Ni loading on the catalytic activity and on H₂/CO production,” *Comptes Rendus Chim.*, vol. 18, no. 11, pp. 1242–1249, 2015, doi: 10.1016/j.crci.2015.03.008.
- [47] S. Zhang, C. Shi, B. Chen, Y. Zhang, and J. Qiu, “An active and coke-resistant dry reforming catalyst comprising nickel-tungsten alloy nanoparticles,” *Catal. Commun.*, vol. 69, pp. 123–128, 2015, doi: 10.1016/j.catcom.2015.06.003.
- [48] A. Salam, B. M. Al-swai, F. Hamimi, N. Asmawati, M. Zabidi, R. Saidur, S. Anuar, and S. Muhammad, “Catalytic conversion of greenhouse gases (CO₂ and CH₄) to syngas over Ni-based catalyst : Effects of Ce-La promoters,” *Arab. J. Chem.*, vol. 13, no. 6, pp. 5740–5749, 2020, doi: 10.1016/j.arabjc.2020.04.012.
- [49] M. A. Hossain, B. V. Ayodele, C. K. Cheng, and M. R. Khan, “Optimization of renewable hydrogen-rich syngas production from catalytic reforming of greenhouse gases (CH₄ and CO₂) over calcium iron oxide supported nickel catalyst,” *J. Energy Inst.*, vol. 92, no. 1, pp. 177–194, 2019, doi: 10.1016/j.joei.2017.10.010.
- [50] S. Li, X. Qin, G. Zhang, Y. Xu, and Y. Lv, “Optimization of content of components over activated carbon catalyst on CO₂ reforming of methane using multi-response surface methodology,” *Int. J. Hydrogen Energy*, vol. 45, no. 16, pp. 9695–9709, 2020, doi:

10.1016/j.ijhydene.2020.01.226.

- [51] M. V. Iyer, L. P. Norcio, E. L. Kugler, and D. B. Dadyburjor, “Kinetic modeling for methane reforming with carbon dioxide over a mixed-metal carbide catalyst,” *Ind. Eng. Chem. Res.*, vol. 42, no. 12, pp. 2712–2721, 2003, doi: 10.1021/ie020677q.
- [52] P. Gangadharan, K. C. Kanchi, and H. H. Lou, “Evaluation of the economic and environmental impact of combining dry reforming with steam reforming of methane,” *Chem. Eng. Res. Des.*, vol. 90, no. 11, pp. 1956–1968, 2012, doi: 10.1016/j.cherd.2012.04.008.
- [53] M. A. Nieva, M. M. Villaverde, A. Monzón, T. F. Garetto, and A. J. Marchi, “Steam-methane reforming at low temperature on nickel-based catalysts,” *Chem. Eng. Jour.*, vol. 235, pp. 158–166, 2014, doi: 10.1016/j.cej.2013.09.030.
- [54] L. S. Carvalho, A. R. Martins, P. Reyes, M. Oportus, A. Albonoz, V. Vicentini, and M. do C. Rangel, “Preparation and characterization of Ru/MgO-Al₂O₃ catalysts for methane steam reforming,” *Catal. Today*, vol. 142, no. 1–2, pp. 52–60, 2009, doi: 10.1016/j.cattod.2009.01.010.
- [55] P. Djinović, I. G. Osojnik črnivec, B. Erjavec, and A. Pintar, “Influence of active metal loading and oxygen mobility on coke-free dry reforming of Ni-Co bimetallic catalysts,” *Appl. Catal. B Environ.*, vol. 125, pp. 259–270, 2012, doi: 10.1016/j.apcatb.2012.05.049.
- [56] A. S. Larimi and S. M. Alavi, “Ceria-Zirconia supported Ni catalysts for partial oxidation of methane to synthesis gas,” *Fuel*, vol. 102, no. 3, pp. 366–371, 2012, doi: 10.1016/j.fuel.2012.06.050.
- [57] H. Y. Wang and E. Ruckenstein, “Carbon dioxide reforming of methane to synthesis gas over supported rhodium catalysts : the effect of support,” vol. 204, pp. 143–152, 2000.
- [58] N. Yang and R. Wang, “Sustainable technologies for the reclamation of greenhouse gas CO₂,” *J. Clean. Prod.*, vol. 103, pp. 784–792, 2015, doi: 10.1016/j.jclepro.2014.10.025.
- [59] M. A. Pefia, “New catalytic routes for syngas and hydrogen production,” vol. 144, pp. 7–57, 1996.

- [60] K. Selvarajah, N. H. H. Phuc, B. Abdullah, F. Alenazey, and D.-V. N. Vo, "Syngas production from methane dry reforming over Ni/Al₂O₃ catalyst," *Res. Chem. Intermed.*, vol. 42, no. 1, pp. 269–288, 2016, doi: 10.1007/s11164-015-2395-5.
- [61] J. Xu, W. Zhou, Z. Li, J. Wang, and J. Ma, "Biogas reforming for hydrogen production over nickel and cobalt bimetallic catalysts," *Int. J. Hydrogen Energy*, vol. 34, no. 16, pp. 6646–6654, 2009, doi: 10.1016/j.ijhydene.2009.06.038.
- [62] M. K. Nikoo and N. A. S. Amin, "Thermodynamic analysis of carbon dioxide reforming of methane in view of solid carbon formation," *Fuel Process. Technol.*, vol. 92, no. 3, pp. 678–691, 2011, doi: 10.1016/j.fuproc.2010.11.027.
- [63] S. Perry, R. H. Perry, D. W. Green, and J. O. Maloney, *CHEMICAL ENGINEERS' HANDBOOK SEVENTH*.
- [64] M. Wullenkord, "Determination of Kinetic Parameters of the Thermal Dissociation of Methane," *PhD Thesis, Ger. Aerosp. Cent. Col. Ger.*, p. 259, 2011.
- [65] Y. Kathiraser, U. Oemar, E. T. Saw, Z. Li, and S. Kawi, "Kinetic and mechanistic aspects for CO₂ reforming of methane over Ni based catalysts," *Chem. Eng. J.*, vol. 278, pp. 62–78, 2015, doi: 10.1016/j.cej.2014.11.143.
- [66] S. Zhao, Y. Sun, X. Lü, and Q. Li, "Kinetics and thermodynamics evaluation of carbon dioxide enhanced oil shale pyrolysis," *Sci. Rep.*, vol. 11, no. 1, pp. 1–14, 2021, doi: 10.1038/s41598-020-80205-4.
- [67] W. Chen and N. Cheng, "Thermodynamic analysis of hydrogen production from methane via autothermal reforming and partial oxidation followed by water gas shift reaction," 2010, doi: 10.1016/j.ijhydene.2010.08.126.
- [68] W. J. Jang, D. W. Jeong, J. O. Shim, H. M. Kim, H. S. Roh, I. H. Son, and S. J. Lee, "Combined steam and carbon dioxide reforming of methane and side reactions: Thermodynamic equilibrium analysis and experimental application," *Appl. Energy*, vol. 173, pp. 80–91, 2016, doi: 10.1016/j.apenergy.2016.04.006.
- [69] W. Jang, D. Jeong, J. Shim, H. Kim, H. Roh, I. Hyuk, and S. Jae, "Combined steam and

- carbon dioxide reforming of methane and side reactions : Thermodynamic equilibrium analysis and experimental application,” *Appl. Energy*, vol. 173, pp. 80–91, 2016, doi: 10.1016/j.apenergy.2016.04.006.
- [70] S. Wang, G. Q. Lu, and G. J. Millar, “Carbon dioxide reforming of methane to produce synthesis gas over metal-supported catalysts: State of the art,” *Energy and Fuels*, vol. 10, no. 4, pp. 896–904, 1996, doi: 10.1021/ef950227t.
- [71] P. K. Chaudhary, N. Koshta, and G. Deo, “Effect of O₂ and temperature on the catalytic performance of Ni/Al₂O₃ and Ni/MgAl₂O₄ for the dry reforming of methane (DRM),” *Int. J. Hydrogen Energy*, vol. 47, no. 7, pp. 4490–4500, 2019, doi: 10.1016/j.ijhydene.2019.12.053.
- [72] C. Tanios, C. Gennequin, M. Labaki, and H. L. Tidahy, “Evaluation of a Catalyst Durability in Absence and Presence of Toluene Impurity : Case of the Material Co₂Ni₂Mg₂Al₂ Mixed Oxide Prepared by Hydrotalcite Route in Methane Dry Reforming to Produce Energy,” *Materials (Basel)*, vol. 12, no. 1362, pp. 1–20, 2019, doi: 10.3390/ma12091362.
- [73] B. M. Al-swai, N. Osman, M. S. Alnarabiji, A. A. Adesina, and B. Abdullah, “Syngas Production via Methane Dry Reforming over Ceria – Magnesia Mixed Oxide-Supported Nickel Catalysts,” *Ind. Eng. Chem. Res.*, vol. 58, pp. 539–552, 2018, doi: 10.1021/acs.iecr.8b03671.
- [74] Y. Zhu, S. Zhang, B. Chen, Z. Zhang, and C. Shi, “Effect of Mg/Al ratio of NiMgAl mixed oxide catalyst derived from hydrotalcite for carbon dioxide reforming of methane,” vol. 264, pp. 163–170, 2016.
- [75] Z. Rong-jun, X. I. A. Guo-fu, L. I. Ming-feng, W. U. Yu, N. I. E. Hong, and L. I. Da-dong, “Effect of support on the performance of Ni-based catalyst in methane dry reforming,” vol. 43, no. 11, 2015, doi: 10.1016/S1872-5813(15)30040-2.
- [76] A. Djaidja, H. Messaoudi, D. Kaddeche, and A. Barama, “Study of Ni-M/MgO and Ni-M-Mg/Al (M = Fe or Cu) catalysts in the CH₄-CO₂ and CH₄-H₂O reforming,” *Int. J. Hydrogen Energy*, pp. 1–7, 2015, doi: 10.1016/j.ijhydene.2014.12.106.

- [77] J. Feng, Y. Ding, Y. Guo, X. Li, and W. Li, “Calcination temperature effect on the adsorption and hydrogenated dissociation of CO₂ over the NiO/MgO catalyst,” *Fuel*, vol. 109, pp. 110–115, 2013, doi: 10.1016/j.fuel.2012.08.028.
- [78] S. Sokolov, E. V Kondratenko, M. Pohl, A. Barkschat, and U. Rodemerck, “Applied Catalysis B : Environmental Stable low-temperature dry reforming of methane over mesoporous La₂O₃-ZrO₂ supported Ni catalyst,” *Applied Catal. B, Environ.*, vol. 113–114, pp. 19–30, 2012, doi: 10.1016/j.apcatb.2011.09.035.
- [79] C. Fauteux-lefebvre, N. Abatzoglou, and J. Blanchard, “Steam reforming of liquid hydrocarbons over a nickel – alumina spinel catalyst,” vol. 195, pp. 3275–3283, 2010, doi: 10.1016/j.jpowsour.2009.11.121.
- [80] B. T. Egelske, J. M. Keels, J. R. Monnier, and J. R. Regalbuto, “An analysis of electroless deposition derived Ni-Pt catalysts for the dry reforming of methane,” *J. Catal.*, vol. 381, pp. 374–384, 2020, doi: 10.1016/j.jcat.2019.10.035.
- [81] M. Zhang, J. Zhang, Z. Zhou, S. Chen, T. Zhang, and F. Song, “Effects of the surface adsorbed oxygen species tuned by rare-earth metal doping on dry reforming of methane over Ni/Zr₂ catalyst,” *Appl. Catal. B Environ.*, vol. 264, no. December 2019, p. 118522, 2020, doi: 10.1016/j.apcatb.2019.118522.
- [82] Y. Sun, G. Zhang, J. Liu, Y. Xu, and Y. Lv, “Production of syngas via CO₂ methane reforming process : Effect of cerium and calcium promoters on the performance of Ni-MSO catalysts,” *Int. J. Hydrogen Energy*, vol. 45, no. 1, pp. 640–649, 2019, doi: doi.org/10.1016/j.ijhydene.2019.10.228.
- [83] P. D. C. Katarzyna Świrk, Maria Elena Gálvez, Monika Motak, Teresa Grzybek, Magnus Rønning, “Syngas production from dry methane reforming over yttrium-promoted nickel-KIT-6 catalysts,” *Int. J. Hydrogen Energy*, vol. 44, no. 1, pp. 274–286, 2019, doi: 10.1016/j.ijhydene.2018.02.164.
- [84] M. Chotirach and S. Tungasmita, “Titanium nitride promoted Ni-based SBA-15 catalyst for dry reforming of methane,” *Int. J. Hydrogen Energy*, vol. 43, no. 46, pp. 21322–21332, 2018, doi: 10.1016/j.ijhydene.2018.09.205.

- [85] S. C. P. Maina, A. D. Ballarini, J. I. Vilella, and S. R. De Miguel, “Study of the performance and stability in the dry reforming of methane of doped alumina supported iridium catalysts,” *Catal. Today*, vol. 344, no. April, pp. 1–14, 2018, doi: 10.1016/j.cattod.2018.11.023.
- [86] N. Azeanni, A. Ghani, A. Azapour, A. Faua, and B. Abdullah, “Dry reforming of methane for hydrogen production over Ni-Co catalysts: Effect of Nb-Zr promoters,” *Int. J. Hydrogen Energy*, vol. 44, no. 37, pp. 20881–20888, 2018, doi: 10.1016/j.ijhydene.2018.05.153.
- [87] L. Yao, M. Elena, C. Hu, and P. Da, “Mo-promoted Ni/Al₂O₃ catalyst for dry reforming of methane,” *Int. J. Heat Mass Transf.*, vol. 42, no. 37, pp. 23500–23507, 2017, doi: 10.1016/j.ijhydene.2017.03.208.
- [88] I. S. and A. H. M. Németh, D. Srankó, J. Károlyi, F. Somodi, Z. Schay, G. Sáfrán, “Na-promoted Ni/ZrO₂ dry reforming catalyst with high efficiency: details of Na₂O–ZrO₂–Ni interaction controlling activity and coke formation,” *Catal. Sci. Technol.*, vol. 7, pp. 5386–5401, 2017, doi: 10.1039/c7cy01011g.
- [89] Y. Cao, H. Li, J. Zhang, L. Shi, and D. Zhang, “Promotional effects of rare earth elements (Sc, Y, Ce, and Pr) on NiMgAl catalysts for dry reforming of methane,” *RSC Adv.*, vol. 6, no. 113, pp. 112215–112225, 2016, doi: 10.1039/c6ra19139h.
- [90] R. Alotaibi, F. Alenazey, F. Alotaibi, and N. Wei, “Ni catalysts with different promoters supported on zeolite for dry reforming of methane,” *Appl. Petrochemical Res.*, vol. 5, no. 4, pp. 329–337, 2015, doi: 10.1007/s13203-015-0117-y.
- [91] A. K. Monika Radlik, Małgorzata Adamowska-Teyssier and P. D. C. Krzysztof Kozieł, Waldemar Krajewski, Wincenty Turek, “Dry reforming of methane over NiCe_{0.62}Zr_{0.38}O₂ catalysts Effect of Ni loading on the catalytic activity and on H₂:CO production,” *Comptes Rendus Chim.*, vol. 18, pp. 1242–1249, 2015, doi: 10.1016/j.crci.2015.03.008.
- [92] Y. Turap, I. Wang, T. Fu, Y. Wu, Y. Wang, and W. Wang, “Co–Ni alloy supported on CeO₂ as a bimetallic catalyst for dry reforming of methane,” *Int. J. Hydrogen Energy*, vol. 45, no. 11, pp. 6538–6548, 2020, doi: 10.1016/j.ijhydene.2019.12.223.

- [93] R. Y. Aybuke Leba, “Determining most effective structural form of nickel-cobalt catalysts for dry reforming of methane,” *Int. J. Hydrogen Energy*, vol. 45, no. 7, pp. 4268–4283, 2019, doi: 10.1016/j.ijhydene.2019.12.020.
- [94] F. R. Shamskar, F. Meshkani, and M. Rezaei, “Preparation and characterization of ultrasound-assisted co-precipitated nanocrystalline La-, Ce-, Zr – promoted Ni-Al₂O₃ catalysts for dry reforming reaction,” *J. CO₂ Util.*, vol. 22, pp. 124–134, 2017, doi: 10.1016/j.jcou.2017.09.014.
- [95] Y. M. Dai, C. Y. Lu, and C. J. Chang, “Catalytic activity of mesoporous Ni/CNT, Ni/SBA-15 and (Cu, Ca, Mg, Mn, Co)-Ni/SBA-15 catalysts for CO₂ reforming of CH₄,” *RSC Adv.*, vol. 6, no. 77, pp. 73887–73896, 2016, doi: 10.1039/c6ra07635a.
- [96] S. Zhang, C. Shi, B. Chen, Y. Zhang, and J. Qiu, “An active and coke-resistant dry reforming catalyst comprising nickel – tungsten alloy nanoparticles,” *CATCOM*, vol. 69, pp. 123–128, 2015, doi: 10.1016/j.catcom.2015.06.003.
- [97] K. Young, S. Lee, U. Ho, H. Roh, and W. Lai, “Syngas production via combined steam and carbon dioxide reforming of methane over Ni–Ce/MgAl₂O₄ catalysts with enhanced coke resistance,” *Fuel Process. Technol.*, vol. 119, pp. 151–157, 2014, doi: 10.1016/j.fuproc.2013.11.005.
- [98] C. Shi, A. Zhang, X. Li, S. Zhang, A. Zhu, Y. Ma, and C. Au, “Ni-modified Mo₂C catalysts for methane dry reforming,” *Appl. Catal. A Gen.*, vol. 432, pp. 164–170, 2012, doi: 10.1016/j.apcata.2012.04.035.
- [99] T. Huang, W. Huang, J. Huang, and P. Ji, “Methane reforming reaction with carbon dioxide over SBA-15 supported Ni – Mo bimetallic catalysts,” *Fuel Process. Technol.*, vol. 92, no. 10, pp. 1868–1875, 2011, doi: 10.1016/j.fuproc.2011.05.002.
- [100] Y. Lu, D. Guo, Y. Ruan, Y. Zhao, S. Wang, and X. Ma, “Facile one-pot synthesis of Ni@HSS as a novel yolk-shell structure catalyst for dry reforming of methane,” *J. CO₂ Util.*, vol. 24, no. January, pp. 190–199, 2018, doi: 10.1016/j.jcou.2018.01.003.
- [101] C. C. Chong, S. N. Bukhari, Y. W. Cheng, H. D. Setiabudi, A. A. Jalil, and C.

- Phalakornkule, “Robust Ni/Dendritic fibrous SBA-15 (Ni/DFSBA-15) for methane dry reforming: Effect of Ni loadings,” *Appl. Catal. A Gen.*, vol. 584, no. April, 2019, doi: 10.1016/j.apcata.2019.117174.
- [102] J. Feng, Y. Ding, Y. Guo, X. Li, and W. Li, “Calcination temperature effect on the adsorption and hydrogenated dissociation of CO₂ over the NiO/MgO catalyst,” *Fuel*, vol. 109, no. 2013, pp. 110–115, 2013, doi: 10.1016/j.fuel.2012.08.028.
- [103] Y. Zhan, K. Song, Z. Shi, C. Wan, J. Pan, D. Li, C. Au, and L. Jiang, “Influence of reduction temperature on Ni particle size and catalytic performance of Ni/Mg(Al)O catalyst for CO₂ reforming of CH₄,” *Int. J. Hydrogen Energy*, vol. 45, no. 4, pp. 2794–2807, 2019, doi: 10.1016/j.ijhydene.2019.11.181.
- [104] A. S. A. Al-Fatish, A. A. Ibrahim, A. H. Fakeeha, M. A. Soliman, M. R. H. Siddiqui, and A. E. Abasaeed, “Coke formation during CO₂ reforming of CH₄ over alumina-supported nickel catalysts,” *Appl. Catal. A Gen.*, vol. 364, no. 1–2, pp. 150–155, 2009, doi: 10.1016/j.apcata.2009.05.043.
- [105] S. Das, S. Thakur, A. Bag, M. Singh, and P. Mondal, “Support interaction of Ni nanocluster based catalysts applied in CO₂ reforming,” *J. Catal.*, vol. 330, pp. 46–60, 2015.
- [106] P. Hoan, D. Ngoc, T. Dung, and Q. Tran, “Paper-structured catalyst containing CeO₂ - Ni flowers for dry reforming of methane,” *Int. J. Hydrogen Energy*, vol. 45, no. 36, pp. 18363–18375, 2019, doi: 10.1016/j.ijhydene.2019.10.247.
- [107] V. G. de la Cruz-Flores, A. Martinez-Hernandez, and M. A. Gracia-Pinilla, “Deactivation of Ni-SiO₂ catalysts that are synthesized via a modified direct synthesis method during the dry reforming of methane,” *Appl. Catal. A Gen.*, vol. 594, p. 117455, 2020, doi: 10.1016/j.apcata.2020.117455.
- [108] W. Liu, X. Wang, N. Zhang, Z. Wang, P. Wu, and H. Zhu, “Catalysts in Coronas: A Surface Spatial Confinement Strategy for High-Performance Catalysts in Methane Dry Reforming,” *ACS Catal.*, vol. 9, no. 10, pp. 9072–9080, 2019, doi: 10.1021/acscatal.9b00968.

- [109] L. A. Salazar Hoyos, B. M. Faroldi, and L. M. Cornaglia, "A coke-resistant catalyst for the dry reforming of methane based on Ni nanoparticles confined within rice husk-derived mesoporous materials," *Catal. Commun.*, vol. 135, no. October 2019, p. 105898, 2020, doi: 10.1016/j.catcom.2019.105898.
- [110] H. Umar, A. Abdul, A. A. Abdulrasheed, T. Ji, and D. N. Vo, "Enhanced dry reforming of methane over mesostructured fibrous Ni / MFI zeolite : Influence of preparation methods," *J. Energy Inst.*, vol. 93, no. 4, pp. 1535–1543, 2020, doi: 10.1016/j.joei.2020.01.016.
- [111] R. K. Singha, A. Yadav, A. Shukla, M. Kumar, and R. Bal, "Low temperature dry reforming of methane over Pd-CeO₂ nanocatalyst," *Catal. Commun.*, vol. 92, pp. 19–22, 2017, doi: 10.1016/j.catcom.2016.12.019.
- [112] S. Das, J. Ashok, Z. Bian, N. Dewangan, M. H. Wai, Y. Du, A. Borgna, K. Hidajat, and S. Kawi, "Silica – Ceria sandwiched Ni core – shell catalyst for low temperature dry reforming of biogas : Coke resistance and mechanistic insights," *Appl. Catal. B Environ.*, vol. 230, no. November 2017, pp. 220–236, 2018, doi: 10.1016/j.apcatb.2018.02.041.
- [113] O. Uyi, H. Dina, and R. Abdul, "Journal of Natural Gas Science and Engineering Syngas production via methane dry reforming : A novel application of SmCoO₃ perovskite catalyst," *J. Nat. Gas Sci. Eng.*, vol. 37, pp. 435–448, 2017, doi: 10.1016/j.jngse.2016.11.060.
- [114] T. Wei, L. Jia, J. Luo, B. Chi, J. Pu, and J. Li, "CO₂ dry reforming of CH₄ with Sr and Ni co-doped LaCrO₃ perovskite catalysts," *Appl. Surf. Sci.*, vol. 506, p. 144699, 2019, doi: 10.1016/j.apsusc.2019.144699.
- [115] X. Lin, R. Li, M. Lu, C. Chen, D. Li, Y. Zhan, and L. Jiang, "Carbon dioxide reforming of methane over Ni catalysts prepared from Ni – Mg – Al layered double hydroxides : Influence of Ni loadings," *Fuel*, vol. 162, pp. 271–280, 2015, doi: 10.1016/j.fuel.2015.09.021.
- [116] A. Al-fatesh, "Suppression of carbon formation in CH₄–CO₂ reforming by addition of Sr into bimetallic Ni–Co/ γ -Al₂O₃ catalyst," *J. KING SAUD Univ. - Eng. Sci.*, vol. 27, no. 1, pp. 101–107, 2013, doi: 10.1016/j.jksues.2013.09.006.

- [117] A. Jawad, F. Rezaei, and A. A. Rownaghi, “Highly efficient Pt/Mo-Fe/Ni-based Al_2O_3 - CeO_2 catalysts for dry reforming of methane,” *Catal. Today*, vol. 350, no. February, pp. 80–90, 2019, doi: 10.1016/j.cattod.2019.06.004.
- [118] F. A. J. Al-doghachi and Y. Hin, “Investigation of Ce(III) promoter effects on the tri-metallic Pt, Pd, Ni / MgO catalyst in dry-reforming of methane,” *RSC Adv.*, vol. 6, pp. 10372–10384, 2016, doi: 10.1039/C5RA25869C.
- [119] S. R. De Miguel, I. M. J. Vilella, S. P. Maina, D. S. José-alonso, M. C. Román-martínez, and M. J. Illán-gómez, “Influence of Pt addition to Ni catalysts on the catalytic performance for long term dry reforming of methane,” *Applied Catal. A, Gen.*, vol. 435–436, pp. 10–18, 2012, doi: 10.1016/j.apcata.2012.05.030.
- [120] N. Azeanni, A. Ghani, A. Azapour, S. Anuar, S. Muhammad, and N. Mohamed, “Dry reforming of methane for syngas production over Ni–Co supported Al_2O_3 – MgO catalysts,” *Appl. Petrochemical Res.*, vol. 8, no. 4, pp. 263–270, 2018, doi: 10.1007/s13203-018-0218-5.
- [121] W. Yong, J. Suk, E. Cheol, K. Young, E. Hyup, and J. Sung, “Reduced perovskite LaNiO_3 catalysts modified with Co and Mn for low coke formation in dry reforming of methane,” *Appl. Catal. A Gen.*, vol. 575, no. February, pp. 198–203, 2019, doi: 10.1016/j.apcata.2019.02.029.
- [122] A. G. Bhavani, W. Y. Kim, J. Y. Kim, and J. S. Lee, “Applied Catalysis A : General Improved activity and coke resistance by promoters of nanosized trimetallic catalysts for autothermal carbon dioxide reforming of methane,” *Applied Catal. A, Gen.*, vol. 450, pp. 63–72, 2013, doi: 10.1016/j.apcata.2012.10.008.
- [123] N. Abdel, K. Aramouni, J. Zeaiter, W. Kwapinski, J. J. Leahy, and M. N. Ahmad, “Eclectic trimetallic Ni-Co-Ru catalyst for the dry reforming of methane,” *Int. J. Hydrogen Energy*, vol. 45, no. 35, pp. 17153–17163, 2020, doi: 10.1016/j.ijhydene.2020.04.261.
- [124] C. Ruocco, B. De Caprariis, V. Palma, A. Petrullo, A. Ricca, M. Scarsella, and P. De Filippis, “Methane dry reforming on Ru perovskites, AZrRuO_3 : Influence of preparation

- method and substitution of A cation with alkaline earth metals,” *J. CO₂ Util.*, vol. 30, no. December 2018, pp. 222–231, 2019, doi: 10.1016/j.jcou.2019.02.009.
- [125] W. Y. Kim, B. J. Lee, H. Park, Y. H. Choi, J. H. Kim, and J. S. Lee, “Ultrapervious Nickel–Cobalt–Manganese/Alumina Inverse Opal as a Coke-Tolerant and Pressure-Drop-Free Catalyst for the Dry Reforming of Methane,” *ChemCatChem*, vol. 10, no. 10, pp. 2214–2218, 2018, doi: doi:10.1002/cctc.201702038.
- [126] A. Jawad, F. Rezaei, and A. A. Rownaghi, “Highly efficient Pt/Mo-Fe/Ni-based Al₂O₃-CeO₂ catalysts for dry reforming of methane,” *Catal. Today*, vol. 350, no. February, pp. 80–90, 2020, doi: 10.1016/j.cattod.2019.06.004.
- [127] C. Cheng, Y. Wang, H. D. Setiabudi, N. Ainirazali, D. N. Vo, and B. Abdullah, “Dry reforming of methane over Ni / dendritic fibrous and regeneration studies,” vol. 15, pp. 1–19, 2020.
- [128] V. Polshettiwar, D. Cha, X. Zhang, and J. M. Basset, “High-Surface-Area Silica Nanospheres (KCC-1) with a Fibrous Morphology,” *Angew. Chemie*, vol. 49, no. 50, pp. 9652–9656, 2010, doi: 10.1002/anie.201003451.
- [129] E. Febriyanti, V. Suendo, R. R. Mukti, A. Prasetyo, M. A. Akbar, S. Triwahyono, and I. N. Marsih, “Further Insight into the Definite Morphology and Formation Mechanism of Mesoporous Silica KCC - 1,” *Langmuir*, vol. 32, no. 23, pp. 5802–5811, 2016, doi: 10.1021/acs.langmuir.6b00675.
- [130] C. C. Chong, Y. W. Cheng, H. D. Setiabudi, N. Ainirazali, D. V. N. Vo, and B. Abdullah, “Dry reforming of methane over Ni/dendritic fibrous SBA-15 (Ni/DFSBA-15): Optimization, mechanism, and regeneration studies,” *Int. J. Hydrogen Energy*, vol. 45, no. 15, pp. 8507–8525, 2020, doi: 10.1016/j.ijhydene.2020.01.056.
- [131] P. Rosha, S. Kumar, S. Kumar, and A. Dhir, “Hydrogen enrichment of biogas via dry and autothermal-dry reforming with pure nickel (Ni) nanoparticle,” *Energy*, vol. 172, pp. 733–739, 2019, doi: 10.1016/j.energy.2019.02.006.
- [132] C. D. Moura-nickel, C. Gaspodini, R. Landers, A. De Noni, E. Virmond, M. Peterson, R.

- De Fátima, P. Muniz, and H. Jorge, “Syngas production by dry reforming of methane using lyophilized nickel catalysts,” *Chem. Eng. Sci.*, vol. 205, pp. 74–82, 2019, doi: 10.1016/j.ces.2019.04.035.
- [133] J. Dou, R. Zhang, X. Hao, Z. Bao, T. Wu, and B. Wang, “Sandwiched $\text{SiO}_2\text{@Ni @ ZrO}_2$ as a coke resistant nanocatalyst for dry reforming of methane,” *Appl. Catal. B Environ.*, vol. 254, pp. 612–623, 2019, doi: 10.1016/j.apcatb.2019.05.021.
- [134] W. Liu, L. Li, X. Zhang, Z. Wang, X. Wang, and H. Peng, “Design of $\text{Ni-ZrO}_2\text{@SiO}_2$ catalyst with ultra-high sintering and coking resistance for dry reforming of methane to prepare syngas,” *J. CO₂ Util.*, vol. 27, pp. 297–307, 2018, doi: 10.1016/j.jcou.2018.08.003.
- [135] A. Rajaeiyan and M. M. Bagheri-Mohagheghi, “Comparison of sol-gel and co-precipitation methods on the structural properties and phase transformation of γ and α - Al_2O_3 nanoparticles,” *Advances in Manufacturing*, vol. 1, no. 2, pp. 176–182, 2013, doi: 10.1007/s40436-013-0018-1.
- [136] D. Jeong, W. Jang, J. Shim, H. Roh, I. Hyuk, and S. Jae, “The effect of preparation method on the catalytic performance over superior MgO -promoted,” *Int. J. Hydrogen Energy*, vol. 38, no. 31, pp. 13649–13654, 2013, doi: 10.1016/j.ijhydene.2013.08.026.
- [137] A. Arora, S. S. Cameotra, R. Kumar, C. Balomajumder, A. K. Singh, B. Santhakumari, P. Kumar, and S. Laik, “Biosurfactant as a Promoter of Methane Hydrate Formation: Thermodynamic and Kinetic Studies,” *Sci. Rep.*, vol. 6, no. February, pp. 1–13, 2016, doi: 10.1038/srep20893.
- [138] E. Meloni, M. Martino, and P. Vincenzo, “A Short Review on Ni Based Catalysts and Related Engineering Issues for Methane Steam Reforming,” *Catalysts*, vol. 10, no. 3, p. 352, 2020.
- [139] M. Usman, W. M. A. Wan Daud, and H. F. Abbas, “Dry reforming of methane: Influence of process parameters - A review,” *Renew. Sustain. Energy Rev.*, vol. 45, pp. 710–744, 2015, doi: 10.1016/j.rser.2015.02.026.

- [140] Q. Ma, D. Wang, M. Wu, T. Zhao, Y. Yoneyama, and N. Tsubaki, "Effect of catalytic site position: Nickel nanocatalyst selectively loaded inside or outside carbon nanotubes for methane dry reforming," *Fuel*, vol. 108, pp. 430–438, 2013, doi: 10.1016/j.fuel.2012.12.028.
- [141] A. Ochoa, J. Bilbao, A. G. Gayubo, and P. Casta, "Coke formation and deactivation during catalytic reforming of biomass and waste pyrolysis products : A review," *Renew. Sustain. Energy Rev.*, vol. 119, p. 109600, 2020, doi: 10.1016/j.rser.2019.109600.
- [142] A. S. Berenblyum, T. A. Podoplelova, E. A. Katsman, R. S. Shamsiev, and V. Y. Danyushevsky, "Kinetics and mechanism of the deoxygenation of stearic acid in the presence of palladium catalysts on alumina," *Kinet. Catal.*, vol. 53, no. 5, pp. 595–609, 2012, doi: 10.1134/S0023158412050023.
- [143] G. E. P. Box and K. B. Wilson, "On the Experimental Attainment of Optimum Conditions," *J. R. Stat. Soc. Ser. B*, vol. 13, no. 1, pp. 1–38, 1951, doi: 10.1111/j.2517-6161.1951.tb00067.x.
- [144] M. A. Alam, H. H. Ya, M. Azeem, P. Bin Hussain, M. S. bin Salit, R. Khan, S. Arif, and A. H. Ansari, "Modelling and optimisation of hardness behaviour of sintered Al/SiC composites using RSM and ANN: a comparative study," *J. Mater. Res. Technol.*, vol. 9, no. 6, pp. 14036–14050, 2020, doi: 10.1016/j.jmrt.2020.09.087.
- [145] K. Jenišťová, I. Hachemi, P. Mäki-Arvela, N. Kumar, M. Peurla, L. Čapek, J. Wärnå, and D. Y. Murzin, "Hydrodeoxygenation of stearic acid and tall oil fatty acids over Ni-alumina catalysts: Influence of reaction parameters and kinetic modelling," *Chem. Eng. J.*, vol. 316, pp. 401–409, 2017, doi: 10.1016/j.cej.2017.01.117.
- [146] A. Witek-Krowiak, K. Chojnacka, D. Podstawczyk, A. Dawiec, and K. Pokomeda, "Application of response surface methodology and artificial neural network methods in modelling and optimization of biosorption process," *Bioresour. Technol.*, vol. 160, pp. 150–160, 2014, doi: 10.1016/j.biortech.2014.01.021.
- [147] F. Ghorbani, H. Younesi, S. M. Ghasempouri, A. A. Zinatizadeh, M. Amini, and A. Daneshi, "Application of response surface methodology for optimization of cadmium

- biosorption in an aqueous solution by *Saccharomyces cerevisiae*,” *Chem. Eng. J.*, vol. 145, no. 2, pp. 267–275, 2008, doi: 10.1016/j.cej.2008.04.028.
- [148] E. Rodríguez, J. L. Arqués, *et al.*, “An Overview of Response Surface Methodology Approach to Optimization of Hydrogen and Syngas Production by Catalytic Reforming of Greenhouse Gases (CH₄ and CO₂),” *Intech*, vol. 32, no. tourism, pp. 137–144, 1989, [Online]. Available: <https://www.intechopen.com/books/advanced-biometric-technologies/liveness-detection-in-biometrics>
- [149] F. Torrades and J. García-Montaña, “Using central composite experimental design to optimize the degradation of real dye wastewater by Fenton and photo-Fenton reactions,” *Dye. Pigment.*, vol. 100, no. 1, pp. 184–189, 2014, doi: 10.1016/j.dyepig.2013.09.004.
- [150] R. F. Gunst, “Response surface methodology: process and product optimization using designed experiments,” *Technometrics*, vol. 38, no. 3, pp. 285–286, Jan. 2021, doi: 10.2307/1270613.
- [151] T. P. Braga, R. C. R. Santos, B. M. C. Sales, B. R. da Silva, A. N. Pinheiro, E. R. Leite, and A. Valentini, “CO₂ mitigation by carbon nanotube formation during dry reforming of methane analyzed by factorial design combined with response surface methodology,” *Cuihua Xuebao/Chinese J. Catal.*, vol. 35, no. 4, pp. 514–523, 2014, doi: 10.1016/s1872-2067(14)60018-8.
- [152] M. S. Fan, A. Z. Abdullah, and S. Bhatia, “Hydrogen production from carbon dioxide reforming of methane over Ni-Co/MgO-ZrO₂ catalyst: Process optimization,” *Int. J. Hydrogen Energy*, vol. 36, no. 8, pp. 4875–4886, 2011, doi: 10.1016/j.ijhydene.2011.01.064.
- [153] S. M. Sidik, S. Triwahyono, A. A. Jalil, Z. A. Majid, N. Salamun, N. B. Talib, and T. A. T. Abdullah, “CO₂ reforming of CH₄ over Ni-Co/MSN for syngas production: Role of Co as a binder and optimization using RSM,” *Chem. Eng. J.*, vol. 295, pp. 1–10, 2016, doi: 10.1016/j.cej.2016.03.041.
- [154] A. A. Abdulrasheed, A. A. Jalil, M. Y. S. Hamid, T. J. Siang, and T. A. T. Abdullah, “Dry reforming of CH₄ over stabilized Ni-La@KCC-1 catalyst: Effects of la promoter and

- optimization studies using RSM,” *J. CO₂ Util.*, vol. 37, no. October 2019, pp. 230–239, 2020, doi: 10.1016/j.jcou.2019.12.018.
- [155] B. V. Ayodele, M. R. Khan, S. S. Nooruddin, and C. K. Cheng, “Modelling and optimization of syngas production by methane dry reforming over samarium oxide supported cobalt catalyst: response surface methodology and artificial neural networks approach,” *Clean Technol. Environ. Policy*, vol. 19, no. 4, pp. 1181–1193, 2017, doi: 10.1007/s10098-016-1318-5.
- [156] B. V. Ayodele and C. K. Cheng, “Modelling and optimization of syngas production from methane dry reforming over ceria-supported cobalt catalyst using artificial neural networks and Box-Behnken design,” *J. Ind. Eng. Chem.*, vol. 32, pp. 246–258, 2015, doi: 10.1016/j.jiec.2015.08.021.
- [157] A. K. Mageed, B. V. Ayodele, and S. I. Mustapa, “Response Surface Optimization of Hydrogen-Rich Syngas Production by Greenhouse Gases Reforming,” *Chem. Eng. Technol.*, vol. 43, no. 4, pp. 742–751, 2020, doi: 10.1002/ceat.201900475.
- [158] H. Y. Wang and A. C. Lua, “Deactivation and kinetic studies of unsupported Ni and Ni – Co – Cu alloy catalysts used for hydrogen production by methane decomposition,” *Chem. Eng. J.*, vol. 243, pp. 79–91, 2014, doi: 10.1016/j.cej.2013.12.100.
- [159] Z. L. Zhang and X. E. Verykios, “Carbon dioxide reforming of methane to synthesis gas over supported Ni catalysts,” *Catal. Today*, vol. 21, no. 2–3, pp. 589–595, 1994.
- [160] M. F. Mark, F. Mark, and W. F. Maier, “Reaction kinetics of the CO₂ reforming of methane,” *Chem. Eng. Technol.*, vol. 20, no. 6, pp. 361–370, 1997, doi: 10.1002/ceat.270200602.
- [161] K. Nagaoka, K. Seshan, J. A. Lercher, and K. Aika, “Activation mechanism of methane-derived coke (CH_x) by CO₂ during dry reforming of methane – comparison for Pt/Al₂O₃ and Pt/ZrO₂,” *Catal. Letters*, vol. 70, pp. 109–116, 2000.
- [162] J. Niu, F. Guo, J. Ran, W. Qi, and Z. Yang, “Methane dry (CO₂) reforming to syngas (H₂/CO) in catalytic process: From experimental study and DFT calculations,” *Int. J.*

- Hydrogen Energy*, vol. 45, no. 55, pp. 30267–30287, 2020, doi: 10.1016/j.ijhydene.2020.08.067.
- [163] T. Zhang, Z. Liu, Y. Zhu, Z. Liu, Z. Sui, and K. Zhu, “Dry reforming of methane on Ni-Fe-MgO catalysts : Influence of Fe on carbon-resistant property and kinetics,” *Appl. Catal. B Environ.*, vol. 264, no. February 2019, p. 118497, 2020, doi: 10.1016/j.apcatb.2019.118497.
- [164] C. Fan, Y. Zhu, M. Yang, Z. Sui, X. Zhou, and D. Chen, “Density Functional Theory-Assisted Microkinetic Analysis of Methane Dry Reforming on Ni Catalyst,” *Ind. Eng. Chem. Res.*, vol. 54, pp. 5901–5913, 2015, doi: 10.1021/acs.iecr.5b00563.
- [165] A. E. Aksoylu, “A comparative study on the kinetics of carbon dioxide reforming of methane over Pt–Ni/Al₂O₃ catalyst : Effect of Pt/Ni Ratio,” *Chem. Eng. J. J.*, vol. 216, pp. 542–549, 2013, doi: 10.1016/j.cej.2012.11.034.
- [166] N. F. Khairudin, M. Farid, F. Sukri, M. Khavarian, and A. R. Mohamed, “Understanding the performance and mechanism of Mg-containing oxides as support catalysts in the thermal dry reforming of methane,” pp. 1162–1183, 2018, doi: 10.3762/bjnano.9.108.
- [167] A. S. A. Al-Fatesh and A. H. Fakeeha, “Effects of calcination and activation temperature on dry reforming catalysts,” *J. Saudi Chem. Soc.*, vol. 16, no. 1, pp. 55–61, 2012, doi: 10.1016/j.jscs.2010.10.020.
- [168] W. Khaodee, B. Jongsomjit, P. Praserttham, S. Goto, and S. Assabumrungrat, “Impact of temperature ramping rate during calcination on characteristics of nano-ZrO₂ and its catalytic activity for isosynthesis,” *J. Mol. Catal. A Chem.*, vol. 280, pp. 35–42, 2008, doi: 10.1016/j.molcata.2007.10.020.
- [169] Z. Bao, Y. Zhan, J. Street, W. Xu, F. To, and F. Yu, “Insight into the phase evolution of a NiMgAl catalyst from the reduction stage to the post-reaction stage during the dry reforming of methane,” *Chem. Commun.*, vol. 53, no. 44, pp. 6001–6004, 2017, doi: 10.1039/c7cc03094k.
- [170] R. Krishna, A. N. Jones, R. Edge, and B. J. Marsden, “Residual stress measurements in

- polycrystalline graphite with micro-Raman spectroscopy,” *Radiat. Phys. Chem.*, vol. 111, pp. 14–23, 2015, doi: 10.1016/j.radphyschem.2015.02.007.
- [171] F. Tuinstra and J. Koenig, “Raman Spectrum of Graphite,” *J. Chem. Phys.*, vol. 53, no. 3, pp. 1126–1130, 1970, doi: 10.1063/1.1674108.
- [172] K. Nagaoka, K. Takanabe, and K. I. Aika, “Influence of the reduction temperature on catalytic activity of Co/TiO₂ (anatase-type) for high pressure dry reforming of methane,” *Appl. Catal. A Gen.*, vol. 255, no. 1, pp. 13–21, 2003, doi: 10.1016/S0926-860X(03)00631-8.
- [173] J. G. G. Jr., S. Kim, and W. D. Rhodes, “Turnover frequencies in metal catalysis: Meanings, functionalities and relationships,” vol. 17, pp. 320–348, 2007, doi: 10.1039/9781847553294-00320.
- [174] S. Kozuch and J. M. L. Martin, “‘Turning over’ definitions in catalytic cycles,” *ACS Catal.*, vol. 2, no. 12, pp. 2787–2794, 2012, doi: 10.1021/cs3005264.
- [175] S. Sengupta, K. Ray, and G. Deo, “Effects of modifying Ni/Al₂O₃ catalyst with cobalt on the reforming of CH₄ with CO₂ and cracking of CH₄ reactions,” *Int. J. Hydrogen Energy*, vol. 39, no. 22, pp. 11462–11472, 2014, doi: 10.1016/j.ijhydene.2014.05.058.
- [176] K. Ray, S. Sengupta, and G. Deo, “Reforming and cracking of CH₄ over Al₂O₃ supported Ni, Ni-Fe and Ni-Co catalysts,” *Fuel Process. Technol.*, vol. 156, pp. 195–203, 2017, doi: 10.1016/j.fuproc.2016.11.003.
- [177] A. Erdöhelyi, “Catalytic reaction of carbon dioxide with methane on supported noble metal catalysts,” *Catalysts*, vol. 11, no. 2, pp. 1–30, 2021, doi: 10.3390/catal11020159.
- [178] H. U. Hambali, A. A. Jalil, A. A. Abdurashed, T. J. Siang, A. H. K. Owgi, and F. F. A. Aziz, “CO₂ reforming of methane over Ta-promoted Ni/ZSM-5 fibre-like catalyst: Insights on deactivation behavior and optimization using response surface methodology (RSM),” *Chem. Eng. Sci.*, p. 116320, 2020, doi: 10.1016/j.ces.2020.116320.
- [179] M. Yusuf, A. Salam, M. A. Alam, L. K. Keong, K. Hellgardt, and B. Abdullah, “Response surface optimization of syngas production from greenhouse gases via DRM over high

- performance Ni-W catalyst,” *Int. J. Hydrogen Energy*, 2021, doi: 10.1016/j.ijhydene.2021.05.153.
- [180] G. Derringer and R. Suich, “Simultaneous Optimization of Several Response Variables,” *J. Qual. Technol.*, vol. 12, no. 4, pp. 214–219, 1980, doi: 10.1080/00224065.1980.11980968.
- [181] M. and Montgomery, *RESPONSE SURFACE METHODOLOGY- Process and Product Optimization Using Designed Experiments*. Wiley.
- [182] F. Mark and F. Wilhelm, “Reaction Kinetics of the CO₂ Reforming of Methane,” *Chem. Eng. Technol.*, vol. 20, pp. 361–370, 1997.
- [183] U. Oemar, Y. Kathiraser, L. Mo, X. K. Ho, and S. Kawi, “CO₂ reforming of methane over highly active La-promoted Ni supported on SBA-15 catalysts: Mechanism and kinetic modelling,” *Catal. Sci. Technol.*, vol. 6, no. 4, pp. 1173–1186, 2016, doi: 10.1039/c5cy00906e.
- [184] A. G. Gayubo, B. Valle, B. Aramburu, C. Montero, and J. Bilbao, “Kinetic model considering catalyst deactivation for the steam reforming of bio-oil over Ni/La₂O₃-Al₂O₃,” *Chemical Engineering Journal*, vol. 332, pp. 192–204, 2018, doi: 10.1016/j.cej.2017.09.063.
- [185] N. A. K. Aramouni, J. G. Touma, B. A. Tarboush, J. Zeaiter, and M. N. Ahmad, “Catalyst design for dry reforming of methane: Analysis review,” *Renew. Sustain. Energy Rev.*, vol. 82, no. June 2017, pp. 2570–2585, 2018, doi: 10.1016/j.rser.2017.09.076.
- [186] Y. Zhu, S. Zhang, B. Chen, Z. Zhang, and C. Shi, “Effect of Mg/Al ratio of NiMgAl mixed oxide catalyst derived from hydrotalcite for carbon dioxide reforming of methane,” *Catal. Today*, vol. 264, pp. 163–170, 2016, doi: 10.1016/j.cattod.2015.07.037.
- [187] V. R. Bach, A. C. de Camargo, T. L. de Souza, L. Cardozo-Filho, and H. J. Alves, “Dry reforming of methane over Ni/MgO–Al₂O₃ catalysts: Thermodynamic equilibrium analysis and experimental application,” *Int. J. Hydrogen Energy*, vol. 45, no. 8, pp. 5252–5263, 2020, doi: 10.1016/j.ijhydene.2019.07.200.

- [188] M. D. Donohue and G. L. Aranovich, "Classification of Gibbs adsorption isotherms," *Adv. Colloid Interface Sci.*, vol. 76–77, pp. 137–152, 1998, doi: 10.1016/S0001-8686(98)00044-X.
- [189] A. S. Farooqi, M. Yusuf, N. A. M. Zabidi, R. Saidur, M. U. Shahid, B. V. Ayodele, and B. Abdullah, "Hydrogen-rich syngas production from bi-reforming of greenhouse gases over zirconia modified Ni/ MgO catalyst ," *Int. J. Energy Res.*, no. June, pp. 1–17, 2021, doi: 10.1002/er.7325.
- [190] Z. Jiang, Y. Liu, L. Huang, W. H. Gong, and P. K. Shen, "A Facile Method to Synthesize Pt–Ni Octahedral Nanoparticles with Porous and Open Structure Features for Enhanced Oxygen Reduction Catalysis," *ACS Sustain. Chem. Eng.*, vol. 7, pp. 8109–8116, 2019, doi: 10.1021/acssuschemeng.8b05444.
- [191] S. Ali, M. M. Khader, M. J. Almarri, and A. G. Abdelmoneim, "Ni-based nano-catalysts for the dry reforming of methane," *Catal. Today*, vol. 343, no. April 2019, pp. 26–37, 2020, doi: 10.1016/j.cattod.2019.04.066.
- [192] J. Xu, W. Zhou, J. Wang, Z. Li, and J. Ma, "Characterization and analysis of carbon deposited during the dry reforming of methane over Ni/La₂O₃/Al₂O₃ catalysts," *Cuihua Xuebao/Chinese J. Catal.*, vol. 30, no. 11, pp. 1076–1084, 2009, doi: 10.1016/s1872-2067(08)60139-4.
- [193] B. Li, Y. Luo, B. Li, X. Yuan, and X. Wang, "Catalytic performance of iron-promoted nickel-based ordered mesoporous alumina FeNiAl catalysts in dry reforming of methane," *Fuel Process. Technol.*, vol. 193, no. May, pp. 348–360, 2019, doi: 10.1016/j.fuproc.2019.05.033.
- [194] A. S. Al-Fatesh, A. H. Fakeeha, A. A. Ibrahim, and A. E. Abasaeed, "Ni supported on La₂O₃+ZrO₂ for dry reforming of methane: The impact of surface adsorbed oxygen species," *Int. J. Hydrogen Energy*, vol. 46, no. 5, pp. 3780–3788, 2021, doi: 10.1016/j.ijhydene.2020.10.164.
- [195] S. Yu, Y. Hu, H. Cui, Z. Cheng, and Z. Zhou, "Ni-based catalysts supported on MgAl₂O₄ with different properties for combined steam and CO₂ reforming of methane," *Chem. Eng.*

- Sci.*, vol. 232, p. 116379, 2021, doi: 10.1016/j.ces.2020.116379.
- [196] H. Li, H. Y. Wei, Y. Cui, R. L. Sang, J. L. Bu, Y. N. Wei, J. Lin, and J. H. Zhao, "Synthesis and characterisation of MgAl_2O_4 spinel nanopowders via nonhydrolytic sol-gel route," *J. Ceram. Soc. Japan*, vol. 125, no. 3, pp. 100–104, 2017, doi: 10.2109/jcersj2.16297.
- [197] H. Zhang, X. Jia, Z. Liu, and Z. Li, "The low temperature preparation of nanocrystalline MgAl_2O_4 spinel by citrate sol-gel process," *Mater. Lett.*, vol. 58, no. 10, pp. 1625–1628, 2004, doi: 10.1016/j.matlet.2003.09.051.
- [198] S. M. M. Zawawi, R. Yahya, A. Hassan, H. N. M. E. Mahmud, and M. N. Daud, "Structural and optical characterization of metal tungstates (MWO_4 ; $\text{M}=\text{Ni, Ba, Bi}$) synthesized by a sucrose-templated method," *Chem. Cent. J.*, vol. 7, no. 1, p. 1, 2013, doi: 10.1186/1752-153X-7-80.
- [199] F. J. O. Rosal, A. F. Gouveia, J. C. Sczancoski, P. S. Lemos, E. Longo, B. Zhang, and L. S. Cavalcante, "Electronic structure, growth mechanism, and sonophotocatalytic properties of sphere-like self-assembled NiWO_4 nanocrystals," *Inorg. Chem. Commun.*, vol. 98, no. July, pp. 34–40, 2018, doi: 10.1016/j.inoche.2018.10.001.
- [200] S. Mani, V. Vedyappan, S. M. Chen, R. Madhu, V. Pitchaimani, J. Y. Chang, and S. Bin Liu, "Hydrothermal synthesis of NiWO_4 crystals for high performance non-enzymatic glucose biosensors," *Sci. Rep.*, vol. 6, pp. 2–9, 2016, doi: 10.1038/srep24128.
- [201] J. Sheng, X. Yi, F. Li, and W. Fang, "Effects of tungsten on the catalytic activity of Ni-W catalysts for the hydrogenation of aromatic hydrocarbons," *React. Kinet. Mech. Catal.*, vol. 99, no. 2, pp. 371–379, 2010, doi: 10.1007/s11144-009-0133-y.
- [202] C. N. Panagopoulos, G. D. Plainakis, and M. G. Tsoutsouva, "Corrosion of Nanocrystalline Ni-W Coated Copper," *J. Surf. Eng. Mater. Adv. Technol.*, vol. 05, no. 02, pp. 65–72, 2015, doi: 10.4236/jsemat.2015.52007.
- [203] S. Echeandia, P. L. Arias, V. L. Barrio, B. Pawelec, and J. L. G. Fierro, "Synergy effect in the HDO of phenol over Ni-W catalysts supported on active carbon: Effect of tungsten

- precursors,” *Appl. Catal. B Environ.*, vol. 101, no. 1–2, pp. 1–12, 2010, doi: 10.1016/j.apcatb.2010.08.018.
- [204] A. S. Al-Fatesh, S. O. Kasim, A. A. Ibrahim, A. H. Fakeeha, A. E. Abasaeed, R. Alrasheed, R. Ashamari, and A. Bagabas, “Combined magnesia, ceria and nickel catalyst supported over γ -alumina doped with titania for dry reforming of methane,” *Catalysts*, vol. 9, no. 2, 2019, doi: 10.3390/catal9020188.
- [205] S. Khajeh Talkhoncheh and M. Haghghi, “Syngas production via dry reforming of methane over Ni-based nanocatalyst over various supports of clinoptilolite, ceria and alumina,” *J. Nat. Gas Sci. Eng.*, vol. 23, pp. 16–25, 2015, doi: 10.1016/j.jngse.2015.01.020.
- [206] M. Yao, D. Wang, and M. Zhao, “Element Analysis Based on Energy-Dispersive X-Ray Fluorescence,” *Adv. Mater. Sci. Eng.*, vol. 2015, no. 1, 2015, doi: 10.1155/2015/290593.
- [207] D. E. Newbury* and N. W. M. Ritchie, “Is Scanning Electron Microscopy/Energy Dispersive X-ray Spectrometry (SEM/EDS) Quantitative?” *Scanning*, vol. 35, no. 3, pp. 141–168, May 2013, doi: <https://doi.org/10.1002/sca.21041>.
- [208] L. Hu and A. Urakawa, “Continuous CO₂ capture and reduction in one process: CO₂ methanation over unpromoted and promoted Ni/ZrO₂,” *J. CO₂ Util.*, vol. 25, no. February, pp. 323–329, 2018, doi: 10.1016/j.jcou.2018.03.013.
- [209] Q. Pan, J. Peng, T. Sun, S. Wang, and S. Wang, “Insight into the reaction route of CO₂ methanation: Promotion effect of medium basic sites,” *Catal. Commun.*, vol. 45, pp. 74–78, 2014, doi: 10.1016/j.catcom.2013.10.034.
- [210] A. Awad, M. S. Alnarabiji, M. A. Salam, D. V. N. Vo, H. D. Setiabudi, and B. Abdullah, “Synthesis, Characterisation, and Performance Evaluation of Promoted Ni-Based Catalysts for Thermocatalytic Decomposition of Methane,” *ChemistrySelect*, vol. 5, no. 37, pp. 11471–11482, 2020, doi: 10.1002/slct.202001998.
- [211] B. M. Al-Swai, N. B. Osman, A. Ramli, B. Abdullah, A. S. Farooqi, B. V. Ayodele, and D. O. Patrick, “Low-temperature catalytic conversion of greenhouse gases (CO₂ and CH₄)

- to syngas over ceria-magnesia mixed oxide supported nickel catalysts,” *Int. J. Hydrogen Energy*, 2020, doi: 10.1016/j.ijhydene.2020.04.233.
- [212] S. Singh, M. B. Bahari, B. Abdullah, P. T. T. Phuong, Q. D. Truong, D. V. N. Vo, and A. A. Adesina, “Bi-reforming of methane on Ni/SBA-15 catalyst for syngas production: Influence of feed composition,” *Int. J. Hydrogen Energy*, vol. 43, no. 36, pp. 17230–17243, 2018, doi: 10.1016/j.ijhydene.2018.07.136.
- [213] A. A. Ibrahim, A. S. Al-fatesh, N. S. Kumar, A. E. Abasaeed, S. O. Kasim, and A. H. Fakeeha, “Dry Reforming of Methane Using Ce-modified Ni,” *Catalysts*, vol. 10, p. 242, 2020.
- [214] C. Wang, N. Sun, N. Zhao, W. Wei, and Y. Zhao, “Template-free preparation of bimetallic mesoporous Ni-Co-CaO-ZrO₂ catalysts and their synergetic effect in dry reforming of methane,” *Catal. Today*, vol. 281, pp. 268–275, 2017, doi: 10.1016/j.cattod.2016.03.026.
- [215] M. Ding, J. Tu, Q. Zhang, M. Wang, N. Tsubaki, T. Wang, and L. Ma, “Enhancement of methanation of bio-syngas over CeO₂-modified Ni/Al₂O₃ catalysts,” *Biomass and Bioenergy*, vol. 85, pp. 12–17, 2016, doi: 10.1016/j.biombioe.2015.11.025.
- [216] S. L. Suib, Ed., “New and Future Developments in Catalysis,” in *New and Future Developments in Catalysis*, Amsterdam: Elsevier, 2013, p. iii. doi: <https://doi.org/10.1016/B978-0-444-53870-3.00023-X>.
- [217] C.-Y. Wang, P. K. Shen, H. Eltejaei, H. Reza Bozorgzadeh, J. Towfighi, M. Reza Omidkhah, M. Rezaei, R. Zanganeh, A. Zamaniyan, and A. Zarrin Ghalam, “Methane dry reforming on Ni/Ce_{0.75}Zr_{0.25}O₂-MgAl₂O₄ and Ni/Ce_{0.75}Zr_{0.25}O₂- γ -alumina: Effects of support composition and water addition,” *International Journal of Hydrogen Energy*, vol. 37, no. 5, pp. 4107–4118, 2012..
- [218] J. W. Han, J. S. Park, M. S. Choi, and H. Lee, “Uncoupling the size and support effects of Ni catalysts for dry reforming of methane,” *Appl. Catal. B Environ.*, vol. 203, pp. 625–632, 2017, doi: 10.1016/j.apcatb.2016.10.069.

- [219] W. Grünert, E. S. Shpiro, R. Feldhaus, K. Anders, G. V. Antoshin, and K. M. Minachev, "Reduction behavior and metathesis activity of $\text{WO}_3\text{-Al}_2\text{O}_3$ catalysts. I. An XPS investigation of $\text{WO}_3\text{-Al}_2\text{O}_3$ catalysts," *J. Catal.*, vol. 107, no. 2, pp. 522–534, 1987, doi: 10.1016/0021-9517(87)90316-2.
- [220] U. Pramod Kumar, T. Liang, C. J. Kennady, R. Nandha Kumar, and J. Prabhu, "Influence of Positional Isomeric Spacers of Naphthalene Derivatives on Ni-W Alloy Electrodeposition: Electrochemical and Microstructural Properties," *ACS Omega*, vol. 5, no. 7, pp. 3376–3388, 2020, doi: 10.1021/acsomega.9b03599.
- [221] A. F. Pérez-Cadenas, C. Moreno-Castilla, F. J. Maldonado-Hódar, and J. L. G. Fierro, "Tungsten oxide catalysts supported on activated carbons: Effect of tungsten precursor and pretreatment on dispersion, distribution, and surface acidity of catalysts," *J. Catal.*, vol. 217, no. 1, pp. 30–37, 2003, doi: 10.1016/S0021-9517(03)00059-9.
- [222] S. Ardizzone, C. L. Bianchi, M. Fadoni, and B. Vercelli, "Magnesium salts and oxide: An XPS overview," *Appl. Surf. Sci.*, vol. 119, no. 3–4, pp. 253–259, 1997, doi: 10.1016/S0169-4332(97)00180-3.
- [223] I. Isomäki, M. Hämäläinen, M. H. Braga, and M. Gasik, "First principles, thermal stability and thermodynamic assessment of the binary Ni-W system," *Int. J. Mater. Res.*, vol. 108, no. 12, pp. 1025–1035, 2017, doi: 10.3139/146.111557.
- [224] N. F. Karpovich, N. V. Lebukhova, V. G. Zavodinsky, and K. S. Makarevich, "Mechanism of the single-crystal tungsten whiskers growth in the process of the NiWO_4 reduction by CO," *J. Phys. Chem. C*, vol. 112, no. 47, pp. 18455–18458, 2008, doi: 10.1021/jp805430b.
- [225] N. A. Lima, L. D. S. Alencar, M. Siu-Li, C. A. C. Feitosa, A. Mesquita, J. C. M'peko, and M. I. B. Bernardi, " NiWO_4 powders prepared via polymeric precursor method for application as ceramic luminescent pigments," *J. Adv. Ceram.*, vol. 9, no. 1, pp. 55–63, 2020, doi: 10.1007/s40145-019-0347-z.
- [226] S. Zhang, C. Shi, B. Chen, Y. Zhang, and J. Qiu, "An active and coke-resistant dry reforming catalyst comprising nickel-tungsten alloy nanoparticles," *Catal. Commun.*, vol.

- 69, pp. 123–128, 2015, doi: 10.1016/j.catcom.2015.06.003.
- [227] M. D. Obradović, B. M. Babić, A. Kowal, V. V. Panić, and S. L. J. Gojković, “Electrochemical properties of mixed WC and Pt-black powders,” *J. Serbian Chem. Soc.*, vol. 73, no. 12, pp. 1197–1209, 2008, doi: 10.2298/JSC0812197O.
- [228] A. S. Rajan, S. Sampath, and A. K. Shukla, “An in situ carbon-grafted alkaline iron electrode for iron-based accumulators,” *Energy Environ. Sci.*, vol. 7, no. 3, pp. 1110–1116, 2014, doi: 10.1039/c3ee42783h.
- [229] R. T. K. Baker, P. S. Harris, R. B. Thomas, and R. J. Waite, “Formation of filamentous carbon from iron, cobalt and chromium catalyzed decomposition of acetylene,” *J. Catal.*, vol. 30, no. 1, pp. 86–95, 1973, doi: 10.1016/0021-9517(73)90055-9.
- [230] M. Usman and W. M. A. Wan Daud, “An investigation on the influence of catalyst composition, calcination and reduction temperatures on Ni/MgO catalyst for dry reforming of methane,” *RSC Adv.*, vol. 6, no. 94, pp. 91603–91616, 2016, doi: 10.1039/c6ra15256b.
- [231] H. O. Seo, “Recent scientific progress on developing supported Ni catalysts for dry (CO₂) reforming of methane,” *Catalysts*, vol. 8, no. 3, pp. 16–22, 2018, doi: 10.3390/catal8030110.
- [232] L. He, S. Hu, L. Jiang, S. S. A. Syed-Hassan, Y. Wang, K. Xu, S. Su, J. Xiang, L. Xiao, H. Chi, and X. Chen, “Opposite effects of self-growth amorphous carbon and carbon nanotubes on the reforming of toluene with Ni/A-Al₂O₃ for hydrogen production,” *Int. J. Hydrogen Energy*, vol. 42, no. 21, pp. 14439–14448, 2017, doi: 10.1016/j.ijhydene.2017.04.230.
- [233] M. Yusuf, A. Salam, and B. Al-kahtani A, Ubaidullah M, Alam M A, Keong L K, Hellgardt K, Abdullah, “Syngas production from greenhouse gases using Ni-W bimetallic catalyst via dry methane reforming: Effect of W addition,” *Int. J. Hydrogen Energy*, 2021, doi: 10.1016/j.ijhydene.2021.05.186.
- [234] C. Hammond, J. Straus, M. Righettoni, S. E. Pratsinis, and I. Hermans, “Nanoparticulate

- tungsten oxide for catalytic epoxidations,” *ACS Catal.*, vol. 3, no. 3, pp. 321–327, 2013, doi: 10.1021/cs300826c.
- [235] H. Ay and D. Üner, “Dry reforming of methane over CeO₂ supported Ni, Co and Ni-Co catalysts,” *Appl. Catal. B Environ.*, vol. 179, pp. 128–138, 2015, doi: 10.1016/j.apcatb.2015.05.013.
- [236] H. Bin Zhang, G. D. Lin, Z. H. Zhou, X. Dong, and T. Chen, “Raman spectra of MWCNTs and MWCNT-based H₂-adsorbing system,” *Carbon N. Y.*, vol. 40, no. 13, pp. 2429–2436, 2002, doi: 10.1016/S0008-6223(02)00148-3.
- [237] N. D. Charisiou, L. Tzounis, V. Sebastian, S. J. Hinder, M. A. Baker, K. Polychronopoulou, and M. A. Goula, “Investigating the correlation between deactivation and the carbon deposited on the surface of Ni/Al₂O₃ and Ni/La₂O₃-Al₂O₃ catalysts during the biogas reforming reaction,” *Appl. Surf. Sci.*, vol. 474, no. May 2018, pp. 42–56, 2019, doi: 10.1016/j.apsusc.2018.05.177.
- [238] S. ullah Rather, “Preparation, characterization and hydrogen storage studies of carbon nanotubes and their composites: A review,” *Int. J. Hydrogen Energy*, vol. 45, no. 7, pp. 4653–4672, 2020, doi: 10.1016/j.ijhydene.2019.12.055.
- [239] A. Iqbal, A. Saeed, and A. Ul-Hamid, “A review featuring the fundamentals and advancements of polymer/CNT nanocomposite application in aerospace industry,” *Polym. Bull.*, vol. 78, no. 1, pp. 539–557, 2021, doi: 10.1007/s00289-019-03096-0.
- [240] N. Anzar, R. Hasan, M. Tyagi, N. Yadav, and J. Narang, “Carbon nanotube - A review on Synthesis, Properties and plethora of applications in the field of biomedical science,” *Sensors Int.*, vol. 1, no. December 2019, p. 100003, 2020, doi: 10.1016/j.sintl.2020.100003.
- [241] H. U. Hambali, A. A. Jalil, A. A. Abdulrasheed, T. J. Siang, A. H. K. Owgi, and F. F. A. Aziz, “CO₂ reforming of methane over Ta-promoted Ni/ZSM-5 fibre-like catalyst: Insights on deactivation behavior and optimization using response surface methodology (RSM),” *Chem. Eng. Sci.*, vol. 231, p. 116320, 2020, doi: 10.1016/j.ces.2020.116320.

- [242] C. H. Kim and Y. C. Kim, “Combined Steam-Carbon Dioxide Reforming of Methane: Modeling Using Response Surface Methodology (RSM),” *J. Nanosci. Nanotechnol.*, vol. 20, no. 9, pp. 5720–5724, 2020, doi: 10.1166/jnn.2020.17628.
- [243] P. Rosha, R. Singh, S. K. Mohapatra, S. K. Mahla, and A. Dhir, “Optimization of Hydrogen-Enriched Biogas by Dry Oxidative Reforming with Nickel Nanopowder Using Response Surface Methodology,” *Energy and Fuels*, vol. 32, no. 6, pp. 6995–7001, 2018, doi: 10.1021/acs.energyfuels.8b00819.
- [244] B. V. Ayodele, M. R. Khan, S. S. Nooruddin, and C. K. Cheng, “Modelling and optimization of syngas production by methane dry reforming over samarium oxide supported cobalt catalyst: response surface methodology and artificial neural networks approach,” *Clean Technol. Environ. Policy*, vol. 19, no. 4, pp. 1181–1193, 2017, doi: 10.1007/s10098-016-1318-5.
- [245] B. V. Ayodele, S. B. Abdullah, and C. K. Cheng, “Kinetics and mechanistic studies of CO-rich hydrogen production by CH₄/CO₂ reforming over Praseodymia supported cobalt catalysts,” *Int. J. Hydrogen Energy*, vol. 42, no. 47, pp. 28408–28424, 2017, doi: 10.1016/j.ijhydene.2017.09.037.
- [246] J. Wei and E. Iglesia, “Isotopic and kinetic assessment of the mechanism of reactions of CH₄ with CO₂ or H₂O to form synthesis gas and carbon on nickel catalysts,” *J. Catal.*, vol. 224, no. 2, pp. 370–383, 2004, doi: 10.1016/j.jcat.2004.02.032.
- [247] J. Z. Luo, Z. L. Yu, C. F. Ng, and C. T. Au, “CO₂/CH₄ reforming over Ni-La₂O₃/5A: An investigation on carbon deposition and reaction steps,” *J. Catal.*, vol. 194, no. 2, pp. 198–210, 2000, doi: 10.1006/jcat.2000.2941.
- [248] C. Pichas, P. Pomonis, D. Petrakis, and A. Ladavos, “Kinetic study of the catalytic dry reforming of CH₄ with CO₂ over La_{2-x}Sr_xNiO₄ perovskite-type oxides,” *Applied Catalysis A: General*, vol. 386, no. 1–2, pp. 116–123, 2010, doi: 10.1016/j.apcata.2010.07.043.
- [249] J. Zhang, H. Wang, and A. K. Dalai, “Kinetic studies of carbon dioxide reforming of methane over Ni-Co/Al-Mg-O bimetallic catalyst,” *Industrial and Engineering Chemistry Research*, vol. 48, no. 2, pp. 677–684, 2009, doi: 10.1021/ie801078p.

- [250] Z. Zhang and X. E. Verykios, “Mechanistic aspects of carbon dioxide reforming of methane to synthesis gas over Ni catalysts,” *Catal. Letters*, vol. 38, no. 3–4, pp. 175–179, 1996, doi: 10.1007/BF00806565.
- [251] I. M. D. Ase Slagtern, Unni Olsbye, Richard Blom, “The Influence of Rare Earth Oxides on Ni/Al₂O₃ Catalysts during CO₂ Reforming of CH₄,” *Stud. Surf. Sci. Catal.*, vol. 107, pp. 497–502, 1997.
- [252] Y. H. Hu and E. Ruckenstein, “Transient response analysis via a broadened pulse combined with a step change or an isotopic pulse. Application to CO₂ reforming of methane over NiO/SiO₂,” *J. Phys. Chem. B*, vol. 101, no. 38, pp. 7563–7565, 1997, doi: 10.1021/jp971711v.
- [253] V. A. Tsipouriari and X. E. Verykios, “Kinetic study of the catalytic reforming of methane with carbon dioxide to synthesis gas over Ni/La₂O₃ catalyst,” *Catal. Today*, vol. 64, no. 1–2, pp. 83–90, 2001, doi: 10.1016/S0920-5861(00)00511-3.
- [254] J. Xu and G. F. Froment, “Methane steam reforming, methanation and water-gas shift: I. Intrinsic kinetics,” *AIChE Journal*, vol. 35, no. 1, pp. 88–96, 1989. doi: 10.1002/aic.690350109.
- [255] Z. Wang, X. M. Cao, J. Zhu, and P. Hu, “Activity and coke formation of nickel and nickel carbide in dry reforming: A deactivation scheme from density functional theory,” *J. Catal.*, vol. 311, pp. 469–480, 2014, doi: 10.1016/j.jcat.2013.12.015.
- [256] Y. Sun, G. Zhang, H. Cheng, and J. Liu, “Kinetics and mechanistic studies of methane dry reforming over Ca promoted 1Co-1Ce/AC-N catalyst,” pp. 1–12, 2020, doi: 10.1016/j.ijhydene.2020.09.192.
- [257] R. J. Baxter and P. Hu, “Insight into why the Langmuir-Hinshelwood mechanism is generally preferred,” *J. Chem. Phys.*, vol. 116, no. 11, pp. 4379–4381, 2002, doi: 10.1063/1.1458938.
- [258] N. Braidy, S. Bastien, J. Blanchard, C. Fauteux-Lefebvre, I. E. Achouri, and N. Abatzoglou, “Activation mechanism and microstructural evolution of a YSZ/Ni-alumina

- catalyst for dry reforming of methane,” *Catal. Today*, vol. 291, pp. 99–105, 2017, doi: 10.1016/j.cattod.2017.03.006.
- [259] A. Takano, T. Tagawa, and S. Goto, “Carbon dioxide reforming of methane on supported nickel catalysts,” *Journal of Chemical Engineering of Japan*, vol. 27, no. 6. pp. 727–731, 1994. doi: 10.1252/jcej.27.727.
- [260] S. Wang and G. Q. Lu, “A comprehensive study on carbon dioxide reforming of methane over Ni/ γ -Al₂O₃ catalysts,” *Ind. Eng. Chem. Res.*, vol. 38, no. 7, pp. 2615–2625, 1999, doi: 10.1021/ie980489t.
- [261] S. Y. Foo, C. K. Cheng, T. H. Nguyen, and A. A. Adesina, “Syngas production from CH₄ dry reforming over Co-Ni/Al₂O₃ catalyst: Coupled reaction-deactivation kinetic analysis and the effect of O₂ co-feeding on H₂:CO ratio,” *Int. J. Hydrogen Energy*, vol. 37, no. 22, pp. 17019–17026, 2012, doi: 10.1016/j.ijhydene.2012.08.136.
- [262] M. A. Alsaffar, B. V. Ayodele, J. M. Ali, M. A. Abdel Ghany, S. I. Mustapa, and C. K. Cheng, “Kinetic modeling and reaction pathways for thermo-catalytic conversion of carbon dioxide and methane to hydrogen-rich syngas over alpha-alumina supported cobalt catalyst,” *Int. J. Hydrogen Energy*, 2021, doi: 10.1016/j.ijhydene.2021.04.158.

LIST OF PUBLICATIONS

Journals

Lit. Review	1. Yusuf M , Farooqi AS, Keong LK, Hellgardt K, Abdullah B. Contemporary trends in composite Ni-based catalysts for CO ₂ reforming of methane. Chem Eng Sci 2021; ;229:116072 (Q1, IF=4.311, published).
Objective 1	2. Yusuf M , Farooqi AS, Keong LK, Hellgardt K, Abdullah B. Syngas Production Employing Ni on Alumina-Magnesia Supported Catalyst Via Dry Methane Reforming. Materialwissenschaft und Werkstofftechnik 2021(Q3, IF=0.854, published).
Objective 1-2	3. Yusuf M , Salam A, Al-kahtani A, Ubaidullah M, Alam M A, Keong L K, Hellgardt K, Abdullah B. Syngas production from greenhouse gases using Ni-W bimetallic catalyst via dry methane reforming : Effect of W addition. Int J Hydrogen Energy 2021(Q2, IF=5.816, published).
Objective 3	4. Yusuf M , Salam A, Alam MA, Keong LK, Hellgardt K, Abdullah B. Response surface optimization of syngas production from greenhouse gases via DRM over high performance Ni-W catalyst. Int J Hydrogen Energy 2021(Q2, IF=5.816, published).
Objective 4	5. Yusuf M , Beg M, Keong LK, Hellgardt K, Abdullah B. Kinetic studies for DRM over high performance Ni-W/Al ₂ O ₃ -MgO catalyst. Int J Hydrogen Energy 2021(Q2, IF=5.816, published).

Conferences

- | | |
|-------------|--|
| Lit. Review | 1. Yusuf M , Farooqi AS, Keong LK, Hellgardt K, Abdullah B. Latest trends in Syngas production employing compound catalysts for methane dry reforming. I O P Conf Ser Mater Sci 2020. 5th International Conference of Chemical Engineering & Industrial Biotechnology (ICCEIB 2020), 9th -11th August 2020, Kuala Lumpur, Malaysia (published) . |
| Methodology | 2. Yusuf M , Farooqi AS, Alam MA, Keong LK, Hellgardt K, Abdullah B. Performance of Ni/Al ₂ O ₃ -MgO catalyst for dry reforming of methane: effect of preparation routes. IOP Conf Ser Mater Sci Eng 2021;1092:1-9. The 2 nd International Conference on Innovative Technology, Engineering and Sciences 2020 (iCITES 2020) (published) . |
| Lit. Review | 3. Yusuf M , Bazli L, Alam MA, Keong LK, Noor A, Masood F, Hellgardt K, Abdullah B. Hydrogen production via natural gas reforming: A comparative study between DRM, SRM and BRM techniques. IEEE Xplore. Third International Sustainability and Resilience Conference: Climate Change - The Sustainability and Resilience 2021 (SRC 21) (published) . |

Book Chapters

Lit. Review	1. Yusuf M , Alnarabiji MS, Abdullah B. Clean Hydrogen Production Technologies. <i>Advances in Sustainable Energy: Policy, Materials, and Devices</i> , Springer 2020 (published) .
Lit. Review	2. Yusuf M , Bazli L, Abdullah B. Challenges and Remediation for Global Warming and Sustainable Development. <i>Artificial Intelligence for Renewable Energy Systems</i> , Elsevier 2021 (In production) .
Lit. Review	3. Yusuf M , Farooqi AS, Keong LK, Hellgardt K, Abdullah B. Dry Reforming of Methane: Quest Towards Ideal Catalyst for Syngas Production. UTP Press. 2020 (In production) .

APPENDIX A
SAMPLE CALCULATIONS FOR CATALYST SYNTHESIS

Table A. 1 Precursor chemical salts used for catalyst synthesis

Chemical Name	Linear Formula	Supplier	Mass Fraction Purity	Molecular Weight (g/mol)
Nickel Nitrate Hexahydrate	$\text{Ni}(\text{NO}_3)_2 \cdot 6\text{H}_2\text{O}$	Sigma Aldrich	>99.9%	290.80
Ammonium Tungstate	$((\text{NH}_4)_{10}(\text{H}_2\text{W}_{12}\text{O}_{42}) \cdot 4\text{H}_2\text{O})$	Sigma Aldrich	>99.9%	3,132.2
Magnesium Nitrate Hexahydrate	$\text{Mg}(\text{NO}_3)_2 \cdot 6\text{H}_2\text{O}$	Sigma Aldrich	>99%	256.41
Aluminium Nitrate Nonahydrate	$\text{Al}(\text{NO}_3)_3 \cdot 9\text{H}_2\text{O}$	Sigma Aldrich	>99%	374.985
Ammonia solution	NH_4OH	Sigma Aldrich	28 wt%	35.04
Distilled Water	H_2O	Labmart Supplier, Malaysia	pH 5.5 to 6.0	18.015

Catalyst Support:

The binary metal oxide support was prepared by taking stoichiometric amounts of precursor salts for Al ($\text{Al}(\text{NO}_3)_3 \cdot 9\text{H}_2\text{O}$) and Mg ($\text{Mg}(\text{NO}_3)_2 \cdot 6\text{H}_2\text{O}$). The calculations for preparation of 18 gm of binary metal oxide catalyst support ($\text{Al}_2\text{O}_3:\text{MgO}=1:2$) are as follow:

For 18 gm of binary metal oxide catalyst support with $\text{Al}_2\text{O}_3:\text{MgO}=1:2$, 6 gm of Al_2O_3 and 12 gm of MgO are required.

2 mols of $\text{Al}(\text{NO}_3)_3 \cdot 9\text{H}_2\text{O}$ produce \rightarrow 1 mol of Al_2O_3

Therefore,

$2 \times \{26.982 + [14.007 + (15.999 \times 3)3] + 9[(1 \times 2) + 15.999]\}$ gm salt \rightarrow 101.961 gm alumina

Hence, applying the unitary method and calculating the amount of ($\text{Al}(\text{NO}_3)_3 \cdot 9\text{H}_2\text{O}$) salt required for 6 gm of Al_2O_3 :

1 gm Al_2O_3 is produces from $\rightarrow (2 \times 374.985/101.961)$ gm salt

6 gm Al_2O_3 is produces from $\rightarrow 6 \times (2 \times 374.985/101.961)$ gm salt

i.e., 44.13 gm of ($\text{Al}(\text{NO}_3)_3 \cdot 9\text{H}_2\text{O}$) salt is required.

Similarly, 1 mols of $\text{Mg}(\text{NO}_3)_2 \cdot 6\text{H}_2\text{O}$ produce \rightarrow 1 mol of MgO

Therefore,

$24.31 \times \{14 + [(16 \times 3)2] + 6[(2 \times 1) + 16]\}$ gm salt \rightarrow 40.3 gm Magnesia

Hence, applying the unitary method and calculating the amount of ($\text{Mg}(\text{NO}_3)_2 \cdot 6\text{H}_2\text{O}$) salt required for 12 gm of MgO:

1 gm MgO is produces from $\rightarrow (256.41/40.3)$ gm salt

12 gm MgO is produces from $\rightarrow 12 \times (256.41/40.3)$ gm salt

i.e., 76.347gm of ($\text{Mg}(\text{NO}_3)_2 \cdot 6\text{H}_2\text{O}$) salt is required.



The precursor chemicals for support (i.e., Aluminum and Magnesium Nitrate salts) are mixed and stirred 10 hours at a pH of 9 and 80°C

The precipitate formed is washed with distilled water and placed in Oven maintained at 110°C for 12 hours

The dried catalyst support is placed in the furnace for calcination at 850°C for 4 hours.

The calcined catalyst support from the furnace is taken out after cooling to room temperature and crushed into powdered form which is further impregnated with Ni.

Figure A. 1. Different steps of Al_2O_3 -MgO support preparation by Co-precipitation method.

Ni Loading:

The 12wt.% Ni loaded catalyst on the above prepared Al_2O_3 -MgO catalyst support is done via impregnation method. The calculations for preparation of 2 gm of 12wt.%Ni/ Al_2O_3 :MgO catalyst sample are as follow:

For 2 gm of 12wt.%Ni/ Al_2O_3 :MgO catalyst sample, 0.24 gm of Ni loading is required on 1.76 gm of support.

1 mols of $\text{Ni}(\text{NO}_3)_2 \cdot 6\text{H}_2\text{O}$ produce \rightarrow 1 mol of Ni

Therefore,

290.80 gm salt produce \rightarrow 58.69 gm Ni

Hence, applying the unitary method and calculating the amount of $\text{Ni}(\text{NO}_3)_2 \cdot 6\text{H}_2\text{O}$ salt required for 0.24 gm of Ni:

1gm Ni is produces from \rightarrow (290.8/58.69) gm salt

0.24 gm Ni is produces from \rightarrow $0.24 \times (290.8/58.69)$ gm salt

i.e., 1.1892 gm of $(\text{Ni}(\text{NO}_3)_2 \cdot 6\text{H}_2\text{O})$ salt is required.

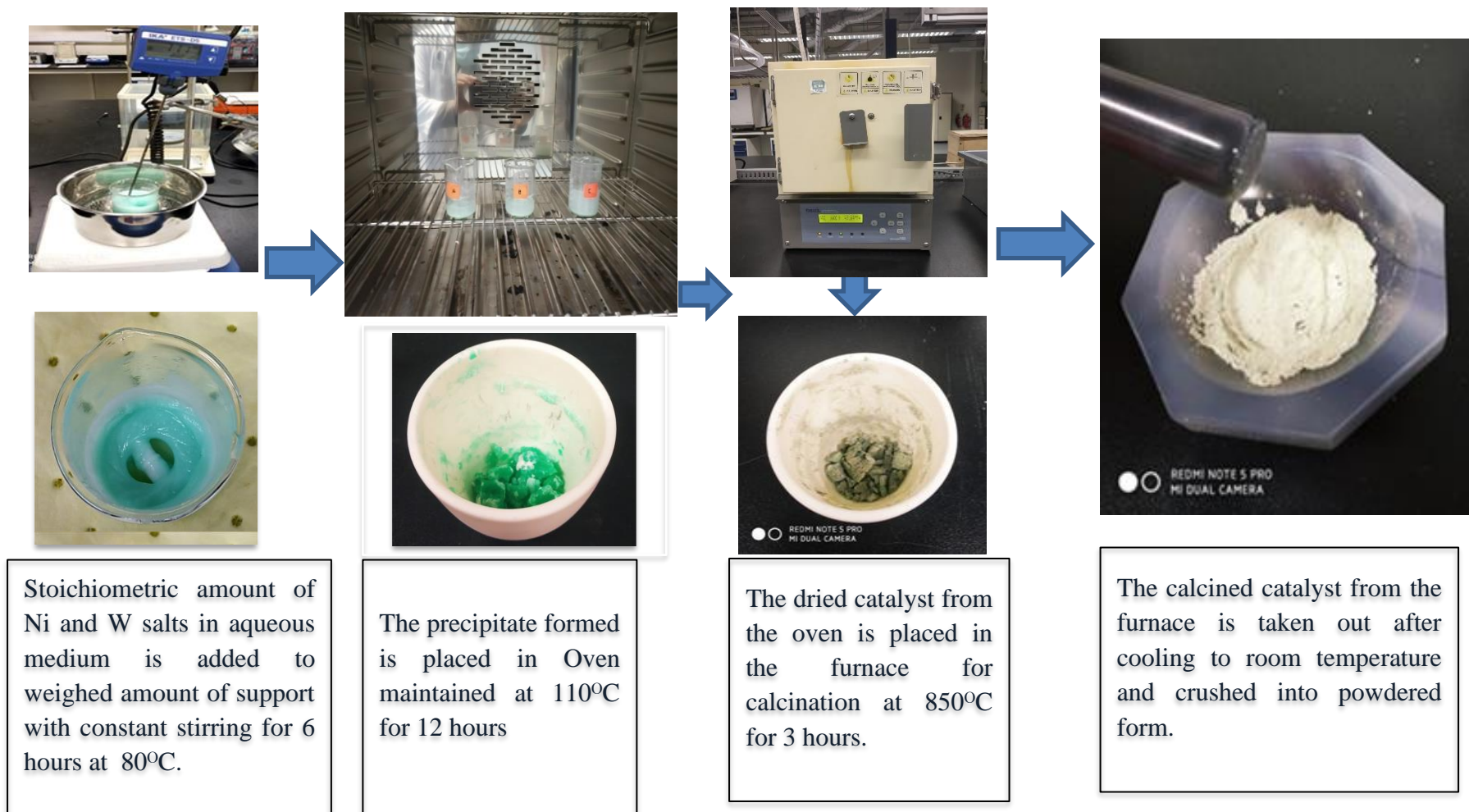


Figure A. 2. Different steps of Ni and W impregnation in the prepared $\text{Al}_2\text{O}_3\text{-MgO}$ support.



Figure A. 3. The Al_2O_3 -MgO support and different Ni loaded catalyst samples.

Ni-W bimetallic Loading:

The 12wt.% Ni and 4wt.% W loaded catalyst on the above prepared Al_2O_3 -MgO catalyst support is done via impregnation method. The calculations for preparation of 2 gm of 12wt.%Ni-4wt.%W/ Al_2O_3 :MgO catalyst sample are as follow:

For 2 gm of 12wt.%Ni-4wt.%/ Al_2O_3 :MgO catalyst sample, 12wt.% (i.e., 0.24 gm) of Ni and 0.08 gm of W loading are required on 1.68 gm of support.

1 mols of $(\text{NH}_4)_{10}(\text{H}_2\text{W}_{12}\text{O}_{42}) \cdot 4\text{H}_2\text{O}$ produce \rightarrow 12 mol of W

Therefore,

3132.2 gm salt produce \rightarrow 12×183.84 gm W

Hence, applying the unitary method and calculating the amount of $(\text{NH}_4)_{10}(\text{H}_2\text{W}_{12}\text{O}_{42}) \cdot 4\text{H}_2\text{O}$ salt required for 4wt.% (i.e., 0.08 gm) of W:

1 gm W is produces from \rightarrow $(3132.2/12 \times 183.84)$ gm salt

0.08 gm W is produces from \rightarrow $0.08 \times (3132.2/12 \times 183.84)$ gm salt

i.e., 0.1136 gm of $(\text{NH}_4)_{10}(\text{H}_2\text{W}_{12}\text{O}_{42}) \cdot 4\text{H}_2\text{O}$ salt is required.



Figure A. 4. The differently W loaded Ni-W bimetallic catalyst samples.

APPENDIX B
CALIBRATION OF GAS CHROMATOGRAPHY

- Calibration curve for H₂ (area vs concentration percent)

Table A. 2. GC calibration data for H₂

Retention time (min)	Level	Concentration	Area
1.66	1	10.00	5428.80
1.66	2	20.00	10633.00
1.66	3	30.00	15824.00
1.66	4	40.00	20940.00

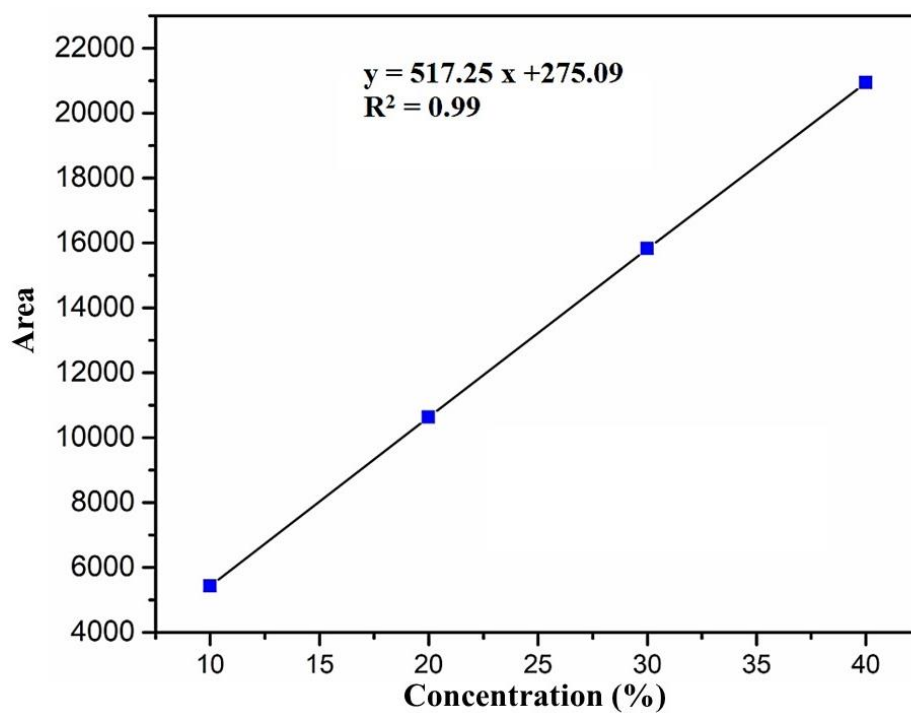


Figure A. 5. GC calibration curve for H₂

- Calibration curve for N₂ (area vs concentration percent)

Table A. 3. GC calibration data for N₂

Retention time (min)	Level	Concentration	Area
4.25	1	10.00	234.25
4.25	2	20.00	516.64
4.25	3	40.00	1083.60
4.25	4	60.00	1645.30
4.25	5	80.00	2210.40

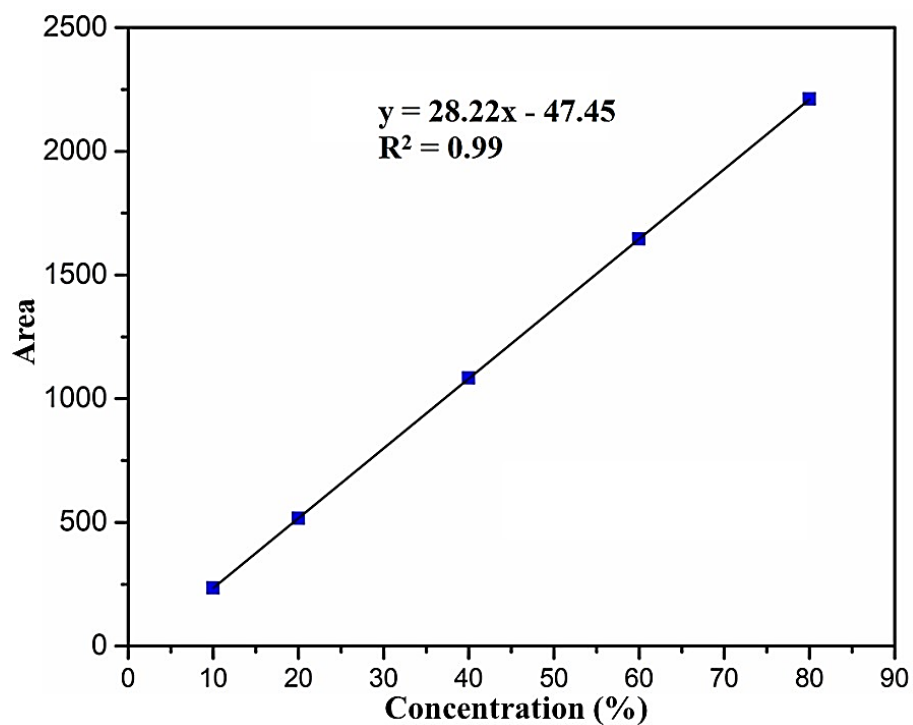


Figure A. 6. GC calibration curve for N₂

- Calibration curve for CO (area vs concentration percent)

Table A. 4. GC calibration data for CO

Retention time (min)	Level	Concentration	Area
5.14	1	10.00	263.32
5.14	2	20.00	527.49
5.14	3	30.00	791.74
5.14	4	40.00	1054.20

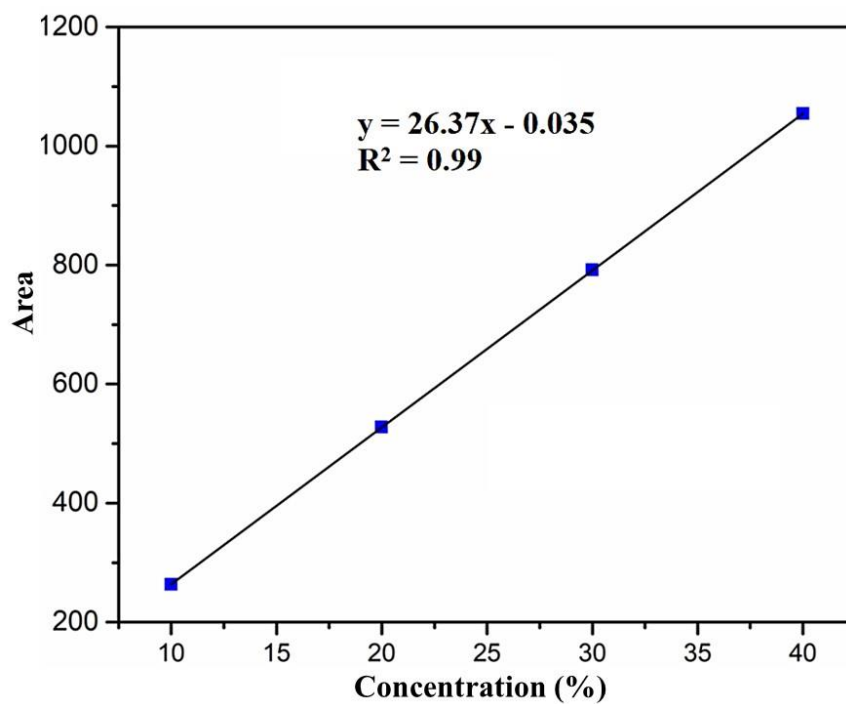


Figure A. 7. GC calibration curve for CO

- Calibration curve for CH₄ (area vs concentration percent)

Table A. 5. GC calibration data for CH₄

Retention time (min)	Level	Concentration	Area
8.49	1	10.00	1286.30
8.49	2	20.00	2520.70
8.49	3	30.00	3762.40
8.49	4	40.00	4988.80
8.49	5	45.00	5609.60

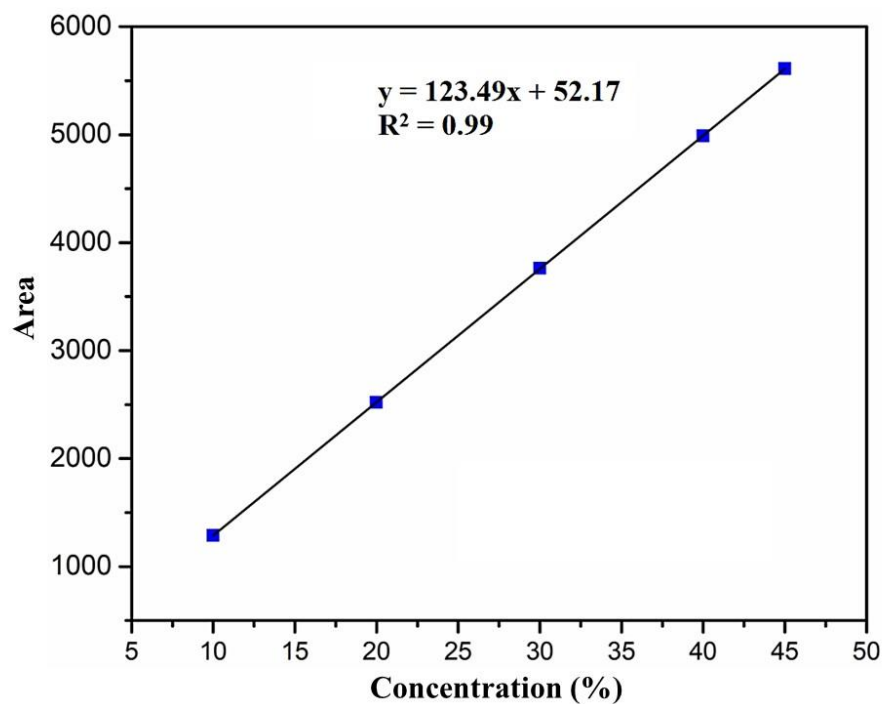


Figure A. 8. Calibration curve for CH₄

Calibration curve for CO₂ (area vs concentration percent)

Table A. 6. GC calibration data for CO₂

Retention time (min)	Level	Concentration	Area
12.12	1	10.00	448.69
12.12	2	20.00	863.44
12.12	3	30.00	1260.6
12.12	4	40.00	1659.60
12.12	5	45.00	1861.80

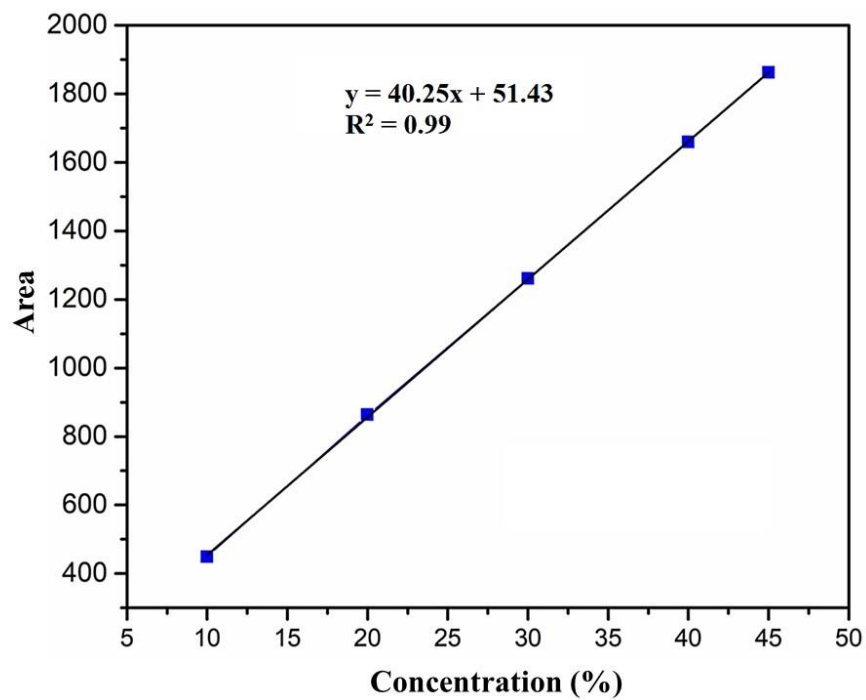


Figure A. 9. Calibration curve for CO₂

APPENDIX C
GC ANALYSIS RESULTS

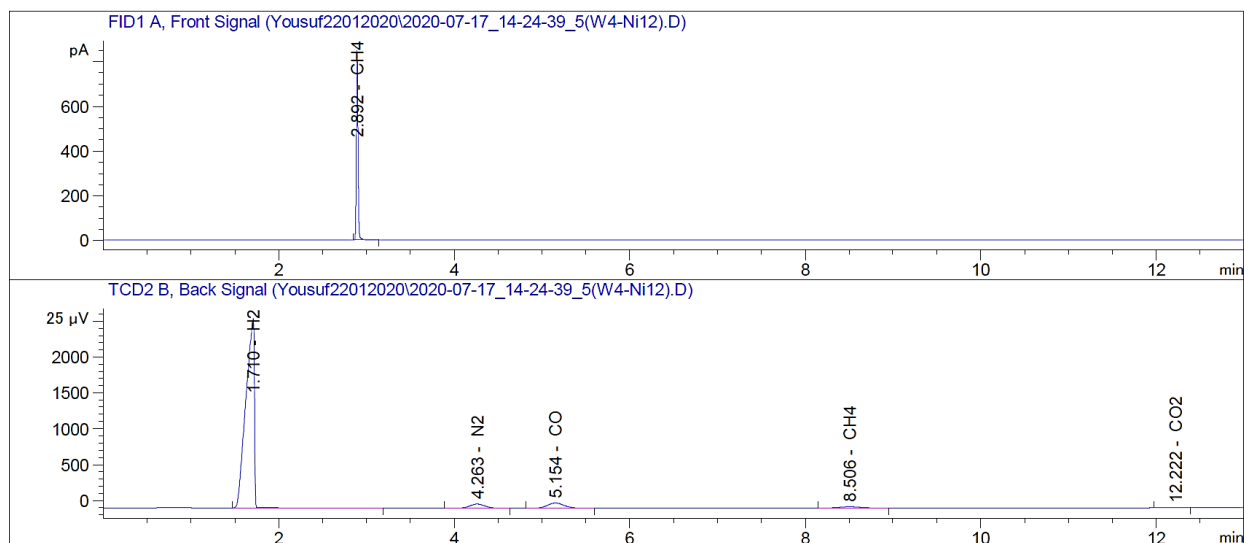


Figure A. 10. GC-TCD spectrum of the outlet gases from the tubular reactor over Ni-W bimetallic catalyst at 800°C, confirming the occurrence of the DRM reaction.

APPENDIX D
MASS TRANSFER LIMITATION

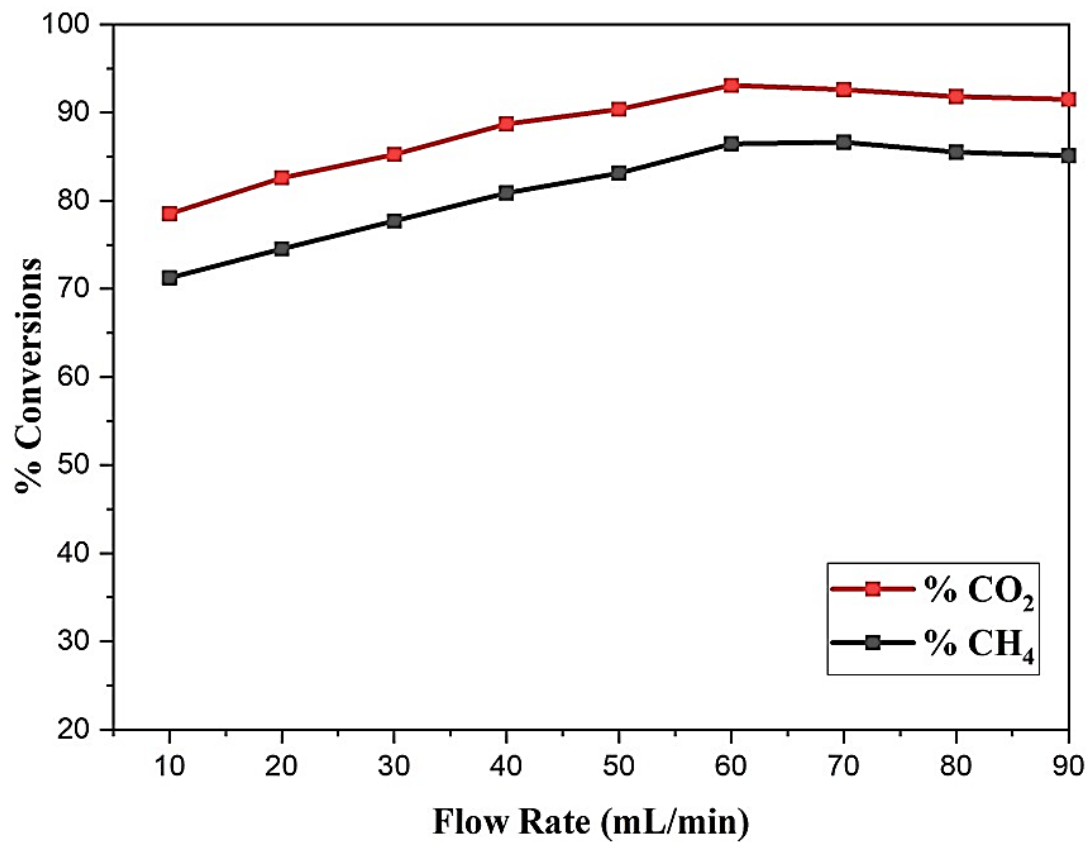


Figure A. 11. Effect of flow rate of feed gases mixture (i.e., CH₄:CO₂:N₂) on the percentage conversion to determine the optimal flow rate at which external mass transfer are negligible (Reactor's ID = 10mm).



Figure A. 12. The fixed bed tubular reactor jacketed with furnace used for DRM reaction.

APPENDIX E

SAMPLE CALCULATIONS FOR DRM REACTION AND CHARACTERIZATION

Table A. 7. The process parameters used for DRM reaction test for prepared catalyst.

	Reaction Conditions	Gaseous Species	Inlet Flow Rate (mL/min)
Catalyst	12wt.%Ni-4wt%W/Al ₂ O ₃ -MgO	CH ₄	20
Catalyst Wt. (gm)	0.1	CO ₂	20
Reaction Temperature	800°C	N ₂	20
Total Flow Rate (mL/min)	60	H ₂	0
Total Pressure (bar)	1.01325	CO	0

Table A. 8. DRM reaction test over the binary oxide ($\text{Al}_2\text{O}_3\text{-MgO}$) catalyst support at 800°C , showing almost negligible conversion of H_2 and CO .

Time (hr)	CH_4 content in exit stream	CO_2 content in exit stream	H_2 content in exit stream	CO content in exit stream	CH_4 Conversion (%)	CO_2 Conversion (%)	H_2/CO
0.5	27.624	29.032	0.801	2.277	17.1262	12.90307	0.351735
1	27.313	32.807	1.19	2.214	18.06115	1.58038	0.537428
2	27.341	32.64589	0.377	1.550	17.97766	2.06233	0.243113
3	27.595	28.718	0.206	1.552	17.21482	13.8451	0.132738
4	27.599	28.789	0	1.639	17.20294	13.63408	0

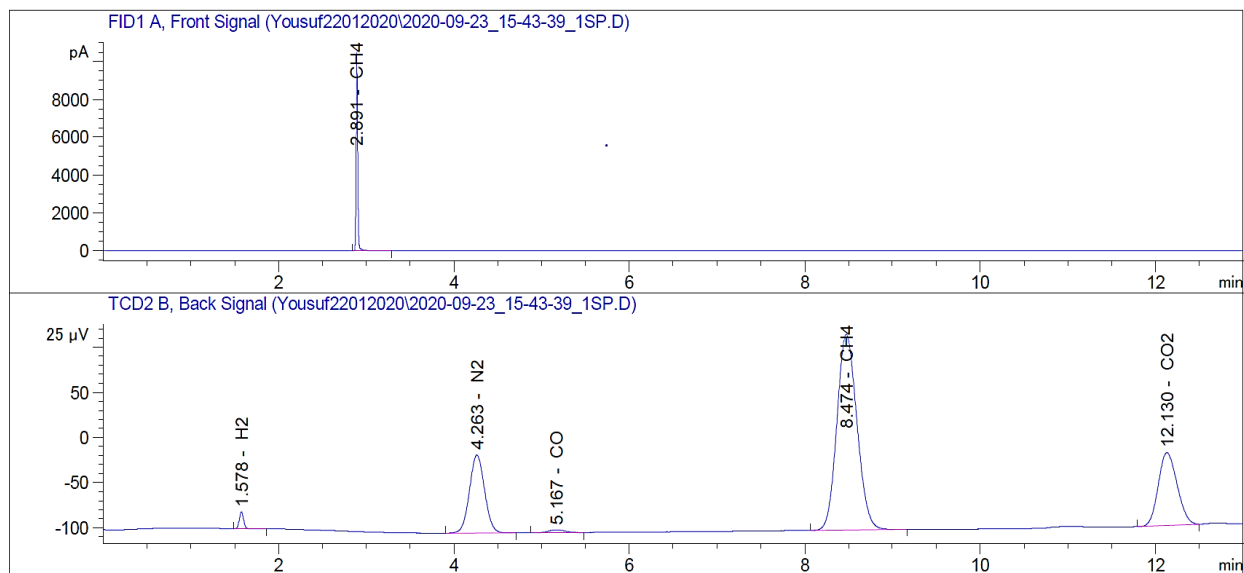
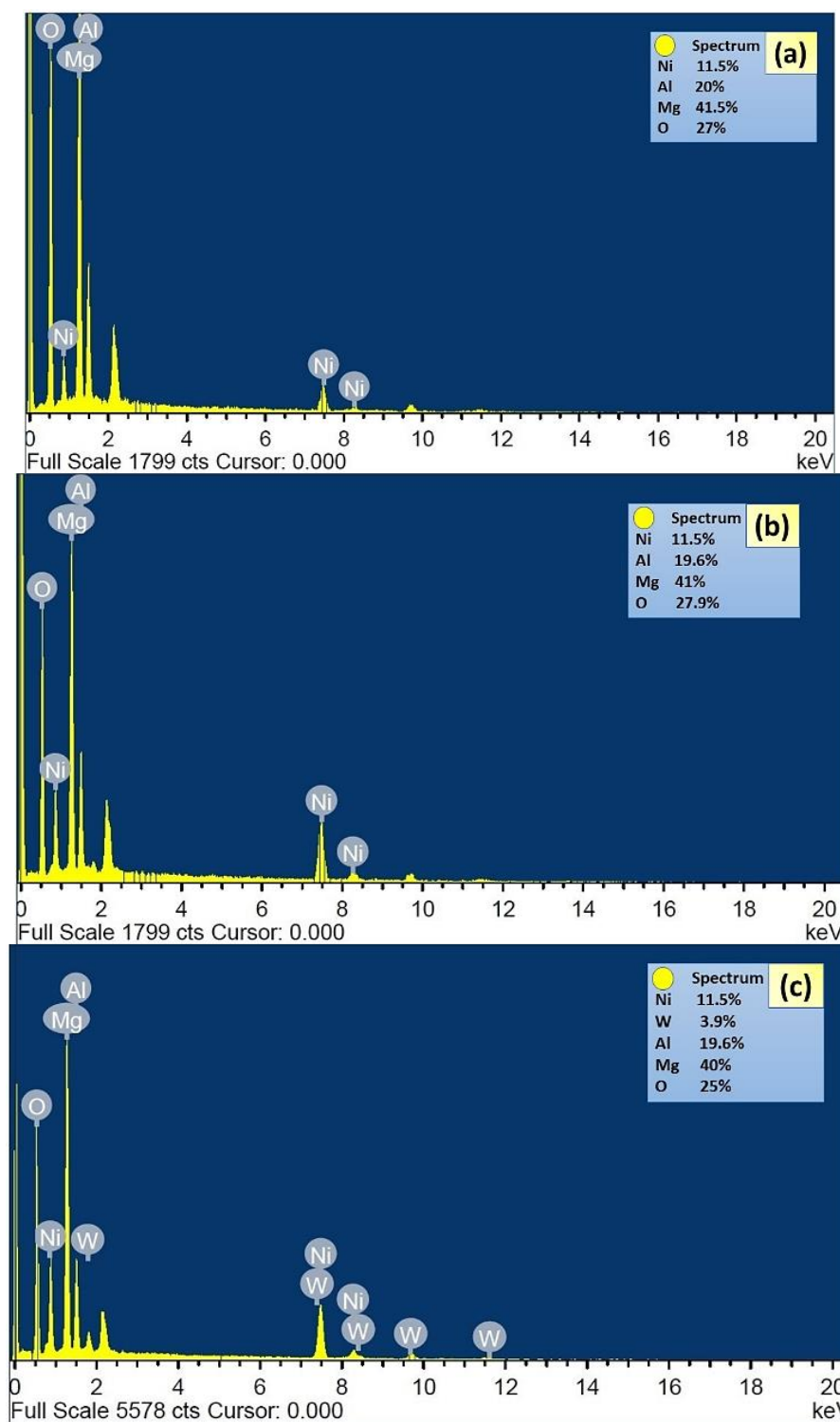


Figure A. 13. GC-TCD spectrum of the outlet gases from the tubular reactor over the binary oxide (Al_2O_3 - MgO) catalyst support at 800°C , depicting high peaks of unconverted feed gases (CH_4 and CO_2).

Time (hr)	CH₄ content in exit stream	CO₂ content in exit stream	H₂ content in exit stream	CO content in exit stream	CH₄ Conversion (%)	CO₂ Conversion (%)	H₂/CO
0.5	1.667	0.671	30.908	31.245	95	98	0.99
1	1.667	0.66	30.908	31.245	95	98.02	0.99
1.5	2.11	1.248	34.681	35.278	93.7	96.3	0.98
2	2.101	1.371	29.714	34.79	93.7	95.9	0.85
2.5	2.18	0	33.915	35.746	93.5	100	0.95
3	2.255	1.442	31.075	36.022	93.2	95.7	0.86
3.5	2.082	0.583	30.841	33.185	93.8	98.2	0.93
4	2.234	0.898	33.139	35.052	93.3	97.3	0.95
4.5	2.27	0.955	33.825	35.314	93.2	97.1	0.96
5	2.346	1.17	32.979	35.364	93	96.5	0.93
5.5	2.359	1.137	32.551	34.887	92.9	96.6	0.93
6	2.336	1.187	30.421	32.714	93.0	96.4	0.93
7	2.383	1.442	30.269	32.899	92.9	95.7	0.92
8	2.667	1.633	31.001	33.78	92.0	95.1	0.92
9	2.708	1.793	30.505	33.44	91.9	94.6	0.91
10	2.921	1.967	30.025	32.994	91.2	94.1	0.91
11	3.039	2.096	30.021	32.988	90.9	93.7	0.91

Time (hr)	CH₄ content in exit stream	CO₂ content in exit stream	H₂ content in exit stream	CO content in exit stream	CH₄ Conversion (%)	CO₂ Conversion (%)	H₂/CO
12	3.221	2.3	30.1	33.077	90.3	93.1	0.91
13	3.233	2.333	30.4	33.407	90.3	93.0	0.91
14	3.267	2.367	29.88	32.835	90.2	92.9	0.91
15	3.3	2.4	29.245	32.032	90.1	92.8	0.91
16	3.333	2.433	29.78	32.618	90.0	92.7	0.91
17	3.333	2.5	29.529	32.343	90.0	92.5	0.91
18	3.4	2.5	29.345	32.212	89.8	92.5	0.91
19	3.433	2.533	29.192	32.044	89.7	92.4	0.91
20	3.5	2.567	29.114	31.958	89.5	92.3	0.91
21	3.567	2.667	29.034	31.87	89.3	92.0	0.91
22	3.633	2.733	29.2	32.053	89.1	91.8	0.91
23	3.7	2.767	29.105	31.984	88.9	91.7	0.91
24	3.733	2.833	29.145	32.383	88.8	91.5	0.90

Table A. 9. GC analysis for exit gas composition during the stability test of 12wt%Ni-4wt%W/Al₂O₃-MgO catalyst for DRM.



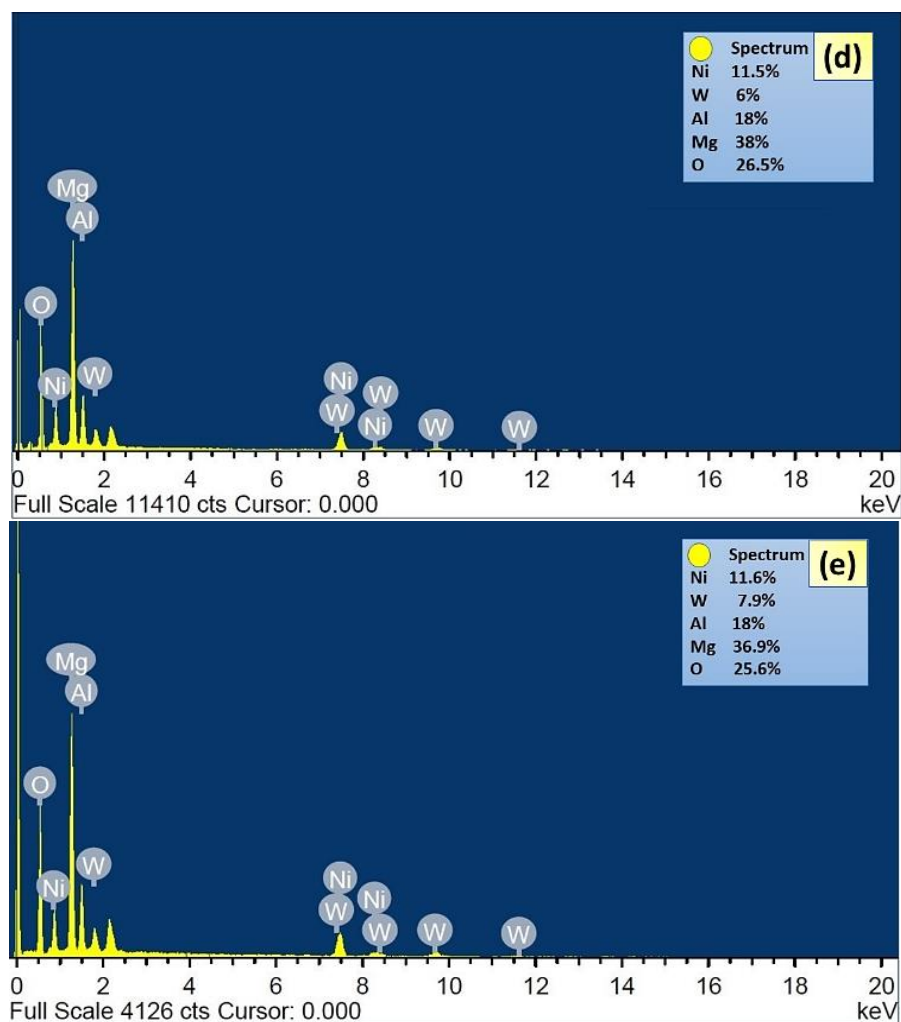


Figure A. 14. The EDX spectrum showing different peaks for elemental composition of (a) Ni_f , (b) W_a , (c) W_b , (d) W_c , (e) W_d catalysts.

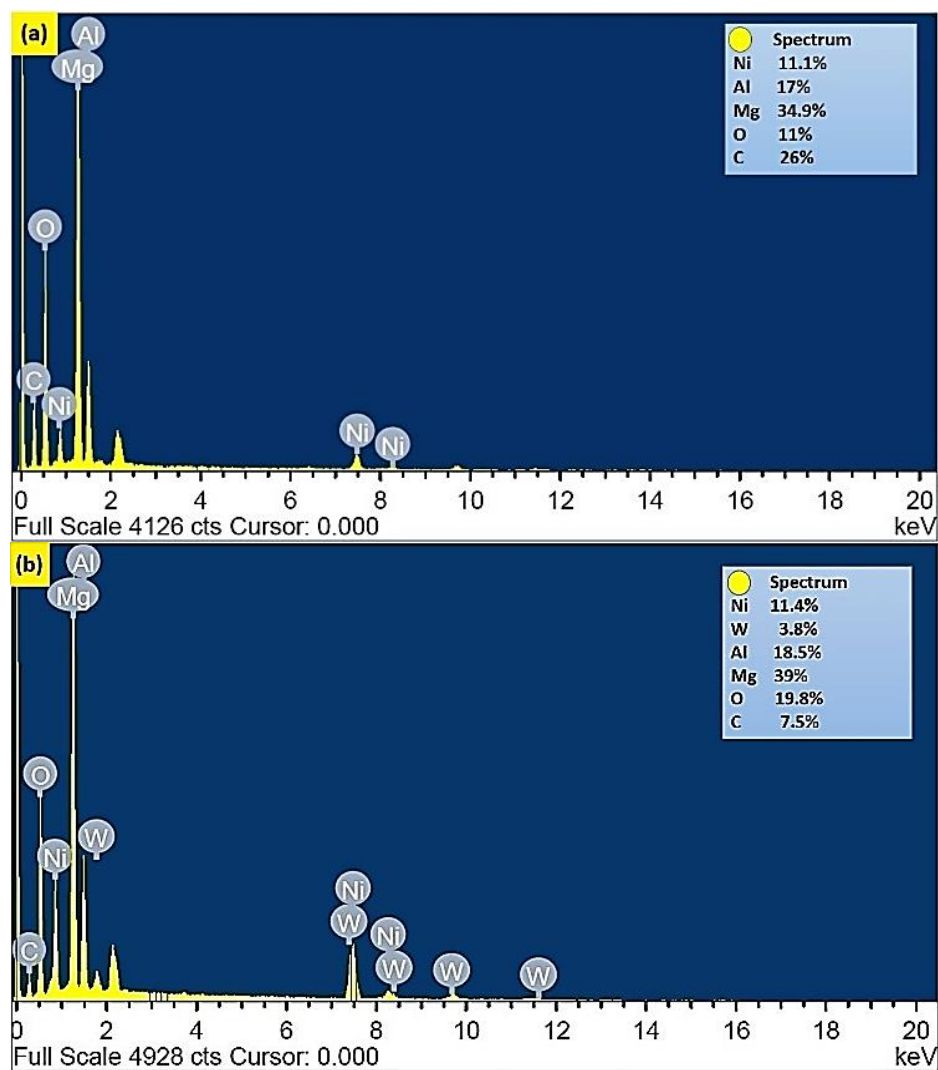


Figure A. 15. The EDX spectrum showing different peaks for elemental composition of (a) Ni_{Sp} and (b) W_{b.sp} catalysts after 6h of DMR reaction.

APPENDIX F
KINETIC MODELLING CALCULATIONS

Table A. 10. Kinetic parameters for DRM reaction obtained from experiments (partial pressure of CO₂ was kept constant and that of CH₄ was varied between 0.2-0.6).

Temperature (°C) ^a	P _{CO2} ^b	x _{CO} ^c	X _{CH4} ^d	V (m ³) ^e	F _{CH4} (mol/s)	R (mol/(L.s))
600	0.2	0.1722887	0.01552857	3.93 × 10 ⁻⁴	0.00028628	1.234 × 10 ⁻³
	0.3	0.21395186	0.02659445		0.00050576	2.061 × 10 ⁻³
	0.4	0.22118842	0.0632722		0.00076341	2.471 × 10 ⁻³
	0.5	0.21487522	0.12375746		0.00114511	2.708 × 10 ⁻³
	0.6	0.21540439	0.20025326		0.00171767	3.057 × 10 ⁻³
700	0.2	0.24787697	0.0041425		0.00028628	1.409 × 10 ⁻³
	0.3	0.26766138	0.01965122		0.00050576	2.244 × 10 ⁻³
	0.4	0.28427216	0.0423652		0.00076341	2.993 × 10 ⁻³
	0.5	0.29582141	0.0814965		0.00114511	3.757 × 10 ⁻³
	0.6	0.28349259	0.14144955		0.00171767	4.375 × 10 ⁻³
800	0.2	0.27824007	0		0.00028628	1.457 × 10 ⁻³
	0.3	0.27257694	0.01179834		0.00050576	2.369 × 10 ⁻³
	0.4	0.30688902	0.02073859		0.00076341	3.422 × 10 ⁻³
	0.5	0.31197847	0.0353931		0.00114511	4.750 × 10 ⁻³
	0.6	0.31114532	0.07724486		0.00171767	5.841 × 10 ⁻³

^a Reaction temperature of experimental analysis for DRM reaction kinetics.

^b Partial pressure (P_{CH4}) of reaction gas CH₄.

^c Molar fraction (x_{CO}) of CO in the product gas.

^d Molar fraction (x_{CH4}) of CH₄ in the product gas.

^e Volume of catalyst (in m³).

Table A. 11. Kinetic parameters for DRM reaction obtained from experiments (partial pressure of CH₄ was kept constant and that of CO₂ was varied between 0.2-0.6).

Temperature (°C) ^a	P _{CO2} ^b	x _{CO} ^c	X _{CH4} ^d	V (m ³) ^e	F _{CH4} (mol/s)	R (mol/(L.s))
600	0.2	0.025212	0.181457011	3.93 × 10 ⁻⁴	0.001145113	1.10 × 10 ⁻³
	0.3	0.028432	0.175531628		0.001145113	1.46 × 10 ⁻³
	0.4	0.03031	0.16382125		0.001145113	1.98 × 10 ⁻³
	0.5	0.036047	0.159803187		0.001145113	2.36 × 10 ⁻³
	0.6	0.040877	0.15380135		0.001145113	2.71 × 10 ⁻³
700	0.2	0.036923	0.11430423		0.001145113	2.00 × 10 ⁻³
	0.3	0.050606	0.084097057		0.001145113	2.87 × 10 ⁻³
	0.4	0.062708	0.067262848		0.001145113	3.51 × 10 ⁻³
	0.5	0.075408	0.058441599		0.001145113	3.98 × 10 ⁻³
	0.6	0.093329	0.044688675		0.001145113	4.59 × 10 ⁻³
800	0.2	0.036843	0.070502958		0.001145113	2.76 × 10 ⁻³
	0.3	0.063309	0.072683873		0.001145113	3.38 × 10 ⁻³
	0.4	0.075552	0.053678143		0.001145113	4.05 × 10 ⁻³
	0.5	0.091819	0.036220972		0.001145113	4.51 × 10 ⁻³
	0.6	0.107964	0.02490138		0.001145113	5.16 × 10 ⁻³

^a Reaction temperature of experimental analysis for DRM reaction kinetics.

^b Partial pressure (P_{CH4}) of reaction gas CH₄.

^c Molar fraction (x_{CO}) of CO in the product gas.

^d Molar fraction (x_{CH4}) of CH₄ in the product gas.

^e Volume of catalyst (in m³).

Table A. 12. Reaction rate and adsorption equilibrium constants as obtained from Figure 4.29

Temperature (°C)	Adsorption equilibrium or reaction constants		
	K_{CH_4} (atm ⁻¹) ^a	K_{CO_2} (atm ⁻¹) ^b	k (mol/L.s) ^c
600	5.509582901	4.57336377	1.0213×10 ⁻¹
700	2.683974325	2.533160705	1.4984×10 ⁻¹
800	1.755234449	1.893199008	1.8874×10 ⁻¹

^a Adsorption equilibrium constant of CH₄ (atm⁻¹).

^b Adsorption equilibrium constant of CO₂ (atm⁻¹).

^c Rate constant of DRM reaction (mol/L.s).

Table A. 13. The experimental and estimated reaction rate by Power Law Model at different temperatures.

Experimental Rate (mol/s. L)	Estimated PL Rate (mol/s. L)	Temperature
0.0015	0.00192	800 °C
0.00254	0.00253	
0.00342	0.00308	
0.00471	0.00358	
0.0055	0.00405	
0.00141	0.0017	700 °C
0.00224	0.00226	
0.00299	0.00276	
0.00376	0.00323	
0.00438	0.00368	
0.00123	0.00143	600 °C
0.00206	0.0019	
0.00237	0.00233	
0.00271	0.00273	
0.00305	0.0031	

Table A. 14. The experimental and estimated reaction rate by Langmuir-Hinshelwood Model at different temperatures.

Experimental Rate (mol/s. L)	Estimated LH Rate (mol/s. L)	Temperature
0.0015	0.0018	800 °C
0.00254	0.0027	
0.00342	0.0036	
0.00471	0.0045	
0.0055	0.00539	
0.00141	0.00149	700 °C
0.00224	0.00223	
0.00299	0.00297	
0.00376	0.0037	
0.00438	0.00442	
0.00123	0.00138	600 °C
0.00206	0.00191	
0.00237	0.00236	
0.00271	0.00274	
0.00305	0.00306	

Table A. 15. The experimental and estimated reaction rate by Eley Rideal Model I at different temperatures (CH₄ varied).

Experimental Rate (mol/s. L)	Estimated ERI Rate (mol/s. L)	Temperature
0.0015	0.00264	800 °C
0.00254	0.00345	
0.00342	0.0041	
0.00471	0.00461	
0.0055	0.00503	
0.00141	0.00204	700 °C
0.00224	0.00282	
0.00299	0.00348	
0.00376	0.00405	
0.00438	0.00456	
0.00123	0.00106	600 °C
0.00206	0.00152	
0.00237	0.00195	
0.00271	0.00235	
0.00305	0.00272	

Table A. 16. The experimental and estimated reaction rate by Eley Rideal Model II at different temperatures (CO₂ varied).

Experimental Rate	Estimated ERII Rate	Temperature
0.00276	0.00172	800 °C
0.00338	0.00255	
0.00405	0.00334	
0.00451	0.00404	
0.00516	0.00479	
0.002	0.00156	700 °C
0.00287	0.00226	
0.00351	0.00297	
0.00398	0.00360	
0.00459	0.00421	
0.0011	0.00138	600 °C
0.00146	0.00213	
0.00198	0.00235	
0.00236	0.003065	
0.00271	0.00312	